Biochemical and structural characterization of the NLRP3 inflammasome

Dissertation
zur
Erlangung des Doktorgrades (Dr. rer. nat.)
der
Mathematisch-Naturwissenschaftlichen Fakultät
der
Rheinischen Friedrich-Wilhelms-Universität Bonn

vorgelegt von

Hildegard Maria Rebecca Brinkschulte
aus
Lünen

Bonn, 2019

Angefertigt mit Genehmigung der
Mathematisch-Naturwissenschaftlichen Fakultät der
Rheinischen Friedrich-Wilhelms-Universität Bonn

1. Gutachter: Prof. Dr. rer. nat. Matthias Geyer
2. Gutachterin: Prof. Dr. rer. nat. Irmgard Förster

Tag der Promotionsprüfung: 04.07.2019

Erscheinungsjahr: 2020

Table of contents

1 Abstract

The innate immune system utilizes inflammasome proteins to recognize danger signals and to fight invading pathogens. To date, the most studied inflammasome protein is NLRP3 - a multidomain protein, composed of a N-terminal Pyrin (PYD) domain, a central NACHT-domain and a C-terminal leucine-rich-repeat (LRR) domain. NLRP3 was further grouped into the family of AAA+ ATPases, due to its sequence homology and ATP-binding ability. NLRP3 inflamasome formation has previously been shown to depend on a two-step mechanism: A priming event, initiating the transcriptional upregulation of NLRP3, and an activation event. Nontheless, the molecular mechanisms underlying self-regulation and activation of NLRP3 remain illusive.

NLRP3 has been identified as a sensor for the fibrillar peptide amyloid-beta (Aβ) in the pathogenesis of Alzheimer's disease. In this study, we clearly show that filamentous ASC forms a seed for the assembly of pathogenic Aβ (1-42). Moreover, the seeding of ASC was shown to be dependent on its ability to form filaments mediated by the PYD-domain.

The present biochemical characterization sheds light on the structural and functional aspects of the human NLRP3 activation mechanism. Recombinant human MBP-NLRP3 was found to assemble into two oligomeric entities, with deviating biochemical characteristics. A larger protein complex, that elutes in the void volume, was shown to possess ATP hydrolysis activity, whereas a second species assembled into an inactive octameric to decameric oligomer complex. Moreover, the ATP hydrolysis activity of NLRP3 was shown to go along with a phosphorylation of Ser198, previously identified to regulate NLRP3 inflammasome activation. Characterization of the ATP-binding site by *in-silico* analysis, followed by a mutational approach, confirmed and revealed amino-acid residues involved in ATP-binding and hydrolysis of NLRP3. The Lysine residue of the Walker A motif (K232) and the sensor 1 motif (R351) have been confirmed to be crucial for the ATPase activity of NLRP3. Moreover, the Walker B residues G303, D305 and E306 have been shown to be equally important for maintaining ATP hydrolysis activity. The highly conserved histidine residue (H522) was also identified to be essential to the ATP hydrolysis activity of NLRP3 and is thus assumed to take over the function of sensor 2 in NLRP proteins. The amino acids identified as crucial to ATP-hydrolysis in NLRP3 suggest a hydrolysis mechanism, deviating from the classical mechanism described for AAA+ ATPases. Intruingly, in control experiments, adenylate kinase (AK) activity was identified as a new function. Human NLRP3 was shown to convert 2 ADP into 1 AMP and 1 ATP and also to mediate the reverse reaction. Amino acid residues involved in the process could be identified by introduction of point mutations. Furthermore, a connection between the CAPS disease and NLRP3 mediated AK-activity was identified. Altogether, the present study supports the model of NLRP3 being an intracellular ANP-sensor and provides new insights into the activation mechanism of NLRP3.

2 Zusammenfassung

Inflammasom-bildende Proteine dienen dem angeborenen Immunsystem zur Erkennung und zur Abwehr von Krankheitserregern. Das bis heute bestuntersuchte Inflammasomprotein ist NLRP3 – ein Multidomänenprotein, bestehend aus einer N-terminalen Pyrin (PYD) Domäne, einer zentral gelegenen NACHT-Domäne, sowie einer C-terminalen Leucin-reichen-Repeat (LRR) Domäne. Aufgrund seiner ATP-Bindungseigenschaft und Sequenzhomologie wurde NLRP3 der Familie der AAA+ ATPase zugeordnet. Bislang konnte gezeigt werden, dass die Entstehung des NLRP3-Inflammasoms auf einem zweistufigen Aktivierungsmechanismus fußt: Einem ‚priming-event', welches die vermehrte NLRP3 Transkription initiiert, sowie einem darauf folgenden ‚activation-event'. Nichtsdestotrotz bleiben die molekularen Mechanismen, die der Aktivierung von NLRP3 zu Grunde liegen, bislang weitgehend ungeklärt.

NLRP3 wurde bereits als Sensor für das fibrillierende Amyloid-beta (Aβ) Peptid in der Pathogenese der Alzheimer Krankheit identifiziert. In dieser Studie konnten wir deutlich zeigen, dass filamentierendes ASC einen Keim für die Aneinanderlagerung des pathogenen Aβ (1-42) bildet. Des Weiteren wurde gezeigt, dass die Bildung des ASC-Keims von der Möglichkeit PYD-Domänen vermittelte Filamente zu formen, abhängt.

Die vorliegende Studie beleuchtet sowohl die biochemische Charakterisierung als auch strukturelle und funktionelle Aspekte der humanen NLRP3-Aktivierung. Es konnte gezeigt werden, dass rekombinantes, humanes MBP-NLRP3 zwei verschiedene oligomere Stadien einnimmt, welche unterschiedliche biochemische Charakteristiken aufweisen. Für den größeren Proteinkomplex, der im Ausschlussvolumen eluiert, konnte ATP-Hydrolyseaktivität nachgeweisen werden, während sicheine zweite, inaktive, Spezies bildet, welche eine Größe im Bereich eines Okta-, Nona- oder Dekameres aufweist. Darüber hinaus konnte gezeigt werden, dass die ATP-Hydrolyseaktivität von NLRP3 mit einer Phosphorylierung an Position Ser198 einhergeht, welche zuvor bereits als für die Regulation des NLRP3 Inflammasoms essentiell nachgewiesen wurde. Durch eine in-silico Analyse der ATP-Bindestelle, sowie eine darauf folgende Mutationsanalyse, konnten mehrere an der ATP-Hydrolyse beteiligte Aminosären identifiziert oder bestätigt werden. Es konnte gezeigt werden, dass sowohl das Lysin des Walker A motifs (K232) sowie das Sensor 1 Motif (R351) für die ATPase Aktivität von NLRP3 essentiell sind. Auch die im Walker B Motiv konservierten Reste G303, D305 und E306 wurden als für die ATP Hydrolyseaktivität essentiell bestätigt. Darüber hinaus konnte gezeigt werden, dass das hochkonservierte His522 für die ATP Hydrolyseaktivität unerlässlich ist, und somit potentiell die Funktion des Sensor 2 in NLRP Proteinen übernimmt. Die hier als für die ATPase

Aktivität von NLRP3 essentiell identifizierten Aminosäurereste suggerieren somit einen von den klassischen AAA+ ATPase abweichenden Hydrolysemechanismus.

Faszinierenderweise konnte in Kontrollexperimenten eine neue Funktion, die Adenylatkinase Aktivität für NLRP3 ermittelt werden. Hier zeigte sich, dass NLRP3 sowohl die Synthese von einem Molekül AMP und einem Molekül ATP aus zwei Molekülen ADP vermittelt, sowie die Rückreaktion. Durch das Einfügen von Punktmutationen konnten die an der Adenylatkinasereaktion beteiligte Amminosäurereste identifiziert werden. Außerdem konnte eine Verbindung zwischen der CAPS Krankheit und der von NLRP3 vermittelten AK-Aktivität ermittelt werden. Die vorliegende Arbeit unterstützt somit das Modell des NLRP3 Proteins als intrazellulärem ANP-Sensor und bietet neue Einblicke in den Aktivierungsmechanismus von NLRP3.

3 List of Abbreviations

Å	Ångström (10^{-10} m)
AAA+ ATPases	ATPases associated with various cellular activities
AD	Alzheimer's disease
AD	acidic transcriptional activation domain
ADP	adenosine diphosphate
ADPβS	adenosine-5'-(β-thio)-diphosphate
AK	adenylate kinase
al.	lat.: alii
AMP	adenosine monophosphate
Amp	ampicillin
Ap5A	P1-(5'-Adenosyl) P5-(5'-adenosyl) pentaphosphate
ApCpp	adenosine-5'-[(α,β)-methyleno]triphosphate
ApNHp	adenosine-5'-[(α,β)-imido]diphosphate
APP	amyloid-precursor protein
AppNHp	adenosine-5'-[(β,γ)-imido]triphosphate
APS	ammonium persulfate
ASC	apoptosis-associated speck-like protein containing a CARD
ASCE	Additional Strand Catalytic E group
ATP	adenosine triphosphate
Aβ	amyloid-β
β-ME	β-mercaptoethanol
BIR	Baculovirus Inhibitor of apoptosis protein repeat
bp	base pair
cAMP	cyclic AMP
CAPS	cryopyrin-associated periodic syndrome
CARD	caspase-recruitment domain
CASR	calcium-sensing receptor
CDR	complementarity determining region
cGMP	cyclic GMP
CINCA	Chronic Infantile Neurological Cutaneous and Articular syndrome
CLR	C-type lectin receptors
COP	CARD-only protein
CRD	carbohydrate recognition domain
CTP	cytidine triphosphate
Da	Dalton
DAMP	damage/danger-associated molecular pattern
DC	dendritic cell
DD	death domains
DED	death effector domain
DMSO	dimethyl sulfoxide
DNA	deoxyribonucleic acid (DNA)

dNTP	deoxynucleotide
DSF	Differential Scanning Fluorimetry
E.coli	*Escherichia coli*
ER	endoplasmic reticulum
FCAS	Familial Cold Autoinflammatory Syndrome
FIIND	function to find domain
FISNA	Fish-specific NACHT associated domain
GBP	guanylate binding protein
GSDMD	Gasdermin D
GSH	glutathione
GST	glutathione S-transferase
GTP	guanosine-5'-triphosphate
HD	helical domain
HEPES	4-(2-hydroxyethyl)-1-piperazineethanesulfonic acid
HPLC	high performance liquid chromatography
HSP90	heat-shock protein 90
IFN	type I interferons
IKK-β	IκB kinase
IPS-1	IFN-β promoter stimulator-1
IPTG	isopropyl β-D-1-thiogalactopyranoside
IRAK	IL-1R-associated kinase
IRF	IFN regulatory factor
ITAM	immunoreceptor tyrosine-based activation motif
ITIM	tyrosine-based inhibition motif
JNK1	c-Jun N-terminal kinase 1
K_a	association constant
kan	kanamycin
kb	kilo base
K_D	binding affinity
K_d	dissociation constant
LB	lysogeny broth
LGP2	Laboratory of Genetics and Physiology 2
LMW	low molecular weight
LPS	lipopolysaccharide
LRR	leucine-rich-repeat
MAM	mitochondria-associated membrane
MAVS	mitochondrial antiviral signalling
MBP	maltose-binding protein
MDA5	Melanoma Differentiation Associated gene 5
MDP	muramyl dipeptide
Mg	magnesium
MWS	Muckle–Wells syndrome
NACHT	nucleotide-binding domain
NAD	NACHT-associated domain
NAIP	NLR family apoptosis inhibitory protein
NEMO	NF-κB essential modulator
NLR	NOD-like receptor
NO	nitric oxide
NOMID	Neonatal-Onset Multisystem Inflammatory Disease

OD	optical density
P2X7	P2X purinoceptor 7
PAMP	pathogen-associated microbial pattern
PBS	phosphate buffered saline
PCR	polymerase chain reaction
PDB	Protein Data Bank
PKR	protein kinase R
PLCγ	phospholipase C-γ
POP	Pyrin-only protein
pred.	predicted
PRR	pattern recognition receptors
PTK	protein tyrosine kinase
PTM	posttranslational modifications
PTP	phosphotyrosine phosphatase
RD	repressor domain
RIG-I	Retinoic acid Inducible Gene I
RIP-kinase	Receptor-interacting protein kinase
RLR	Retinoic acid-inducible gene (RIG)-I-like receptors
RNA	ribonucleic acid
ROS	reactive oxygen species
rpm	revolutions per minute
RT	room temperature
RU	resonance units
S.pombe	*Schizosaccharomyces pombe*
SARM	Sterile-alpha and Armadillo motif-containing protein
SCK	single cycle kinetics
SDS	sodium dodecyl sulfate
Sen1	sensor-1
Sf	*Spodoptera frugiperda*
SDS-PAGE	sodium dodecyl sulfate–polyacrylamide gel electrophoresis
SPR	Surface Plasmon Resonance
STAND	Signal Transduction ATPases with Numerous Domains
T3SS	bacterial type III secretion system
TAB	TAK1-binding protein
TAK	TGF-β-activated kinase
TCEP	tris(2-carboxyethyl)phosphine
TEMED	tetramethylethylenediamine
TEV	Tobacco Etch Virus
TIR	intracellular Toll/interleukin-1 receptor
TLR	Toll-like receptor
T_m	melting temperature
TRAF	TNFR-associated factor
TRAM	TRIF-related adaptor molecule
TRIF	TIR domain-containing adaptor inducing IFN-β
Tris	tris(hydroxymethyl)aminomethane
TTP	deoxythymidine triphosphate
TXNIP	thioredoxin (TRX)-interacting protein
v/v	volume per volume
VHH	variable domain fragment

VISA	virus-induced signalling adapter
WA	Walker A
WB	Walker B
WHD	winged helix domain
WT	wild-type

Regular units of measurement as well as amino acids are abbreviated according to the IUPAC nomenclature.

4 List of Figures

5 List of Tables

6 Introduction

Every higher organism has evolved a strategy to recognize stressors and invading pathogens: the immune system. The innate immune system focusses on the recognition of common pathogenic or stressful patterns and molecules whereas after a period of 4-7 days the adaptive immune system establishes a more specific line of defence (Murphy & Weaver, 2012). Pathogens invading the epithelial barrier are recognized by phagocytic macrophages, which engulf the invading pathogen and cause a first immune response. The activated macrophage then releases chemokines and cytokines to recruit monocytes and neutrophils and starts an inflammation reaction. The released cytokines lead to a local reaction on the surrounding blood vessel, the five main signs of inflammation: heat, pain, redness, swelling and the loss of tissue function (Takeuchi & Akira, 2010). The increased dilation and permeability of the vascular endothelium results in migration of neutrophils to the site of infection.

Specific cells are present in the epithelial barrier, which are in contact with the external environment, like dendritic cells. Others like neutrophils are present predominantly in the blood stream and are recruited to the site of infection by following cytokines and chemokines to fulfil their phagocytic function. Also, monocytes migrate through the blood stream to the infected tissue and can further differentiate into tissue resident macrophages or dendritic cells (DCs). DCs are antigen-presenting cells, which connect the innate and the adaptive immune system, by presenting antigens to T-cells.

The immune system mainly ensures the recognition of invading pathogens and repair of tissue damage by pattern recognition receptors (PRRs) (Akira *et al.*, 2006; Beutler *et al.*, 2006). To facilitate the detection of pathogens, the innate immune system makes use of conserved microbial patterns, so called pathogen-associated microbial patterns (PAMPs) (Takeuchi & Akira, 2010). Further, PRRs sense so called damage/danger-associated molecular patterns (DAMPs). These are either of proteinatious origin or endogenous molecules, like for example heat-shock proteins or ATP, uric acid and deoxyribonucleic acid (DNA).

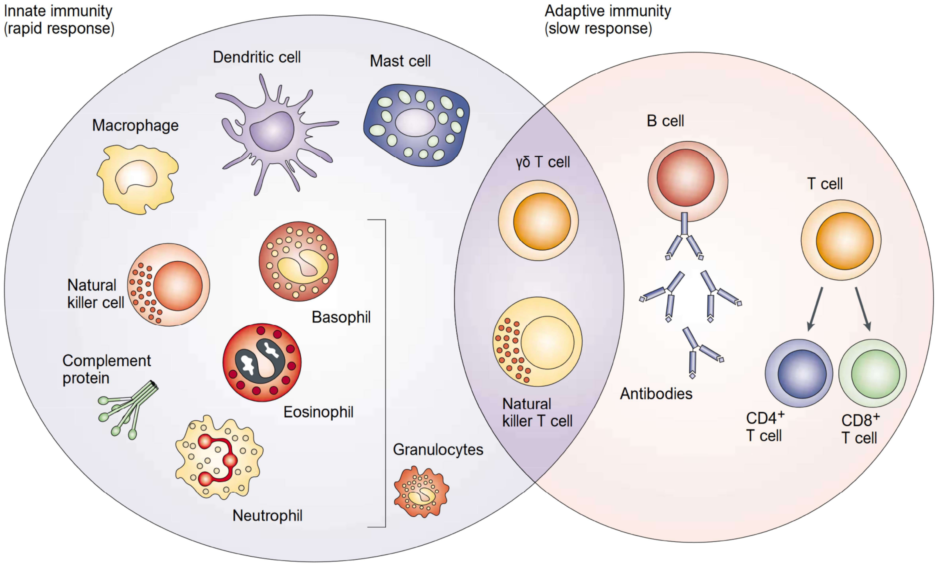

Figure 1: Responding cells of the adaptive and innate immune system. The innate immune system builds up the first line of defense against infection. It consists of granulocytes (basophils, eosinophils and neutrophils), mast cells, macrophages, dendritic cells and natural killer cells. The adaptive immune system consists of consists of antibodies, B cells as well as $CD4^+$ and $CD8^+$ T lymphocytes. Natural killer cells are build up the interface between the adaptive and the innate immune system. Figure taken from Dranoff, 2004.

6.1 Pattern-recognition receptors

Germline-encoded pattern-recognition receptors are expressed by cells of the immune system such as macrophages, dendritic cells, monocytes and neutrophils as well as by epithelial cells, which build up the first barrier against pathogen invasion. PRRs are thus either found as transmembrane-proteins or they are found as cytosolic receptors. The family of Toll-like receptors (TLRs) and C-type lectin receptors (CLRs) are transmembrane-receptors, whereas the remaining two PRR families, Retinoic acid-inducible gene (RIG)-I-like receptors (RLRs) and NOD-like receptors (NLRs), comprise cytosolic receptors. Downstream of the sensing event of PAMPs and DAMPs, inflammatory response genes are transcriptionally upregulated, resulting among others in the expression of proinflammatory cytokines, type I interferons (IFNs), chemokines and antimicrobial proteins.

6.1.1 Toll-like receptors (TLRs)

TLRs are mostly specified to the sensing of PAMPs on cell membranes, thus these receptors detect pathogen invasion accounting the cell from the extracellular space or after pathogen uptake in endosomes and lysosomes. Until now, 10 different TLRs have been identified in humans, and 12 in mice. The PAMPs vary greatly with respect to the specific TLR ranging from lipoproteins and LPS, to flagellin and ssRNA or CpG-DNA from several different species like, protozoan, bacteria, fungi or viruses. An even higher variation in ligand sensing is achieved by the oligomeric assembly of the TLRs. TLR2, for example, forms a heterodimeric complex with either TLR1 or TLR6, thus recognizing triacyl or diacyl lipoproteins, respectively. In comparison, TLR3, TLR7, TLR8 and TLR9 are known to recognize bacterial and fungal DNA as well as single-stranded RNA and host DNA (Akira *et al.*, 2006). The following downstream effect of TLR activation varies, depending on the receptor involved. TLRs follow a defined domain organization. They contain an extracellular N-terminal glycoprotein ectodomain leucine-rich-repeat (LRR) domain, followed by a single transmembrane helix and an intracellular Toll/interleukin-1 receptor (TIR) homology domain. The TLR receptors are localized to cellular membrane compartments, more specifically, TLR 1, 2, 4, 5 and 6 are localized on the plasma membrane whereas TLR 3,7 and 9 are found on the membrane of the endoplasmic reticulum (ER). The nucleotide sensing TLRs are recruited to the endolysosomes by UNC93B, which binds to the uncharged, hydrophobic transmembrane helix of the TLR receptor to encounter their specific ligand (Botos *et al.*, 2011). Upon ligand binding and activation, the TLRs dimerize and signal via the MyD88- and TRIF-dependent pathway. Dimerization of the TLRs is initiated by the TIR domain (Botos *et al.*, 2011). Further, homotypic interactions of the TIR domain of TLRs and adaptor proteins like MyD88, TIR domain-containing adaptor inducing IFN-β (TRIF), TIRAP/Mal, TRIF-related adaptor molecule (TRAM), and Sterile-alpha and Armadillo motif-containing protein (SARM) are the first step in downstream signalling (Takeuchi & Akira, 2010). The MyD88 signalling pathway is used by the TLRs with exception of TLR3. MyD88 binds to IL-1R-associated kinase (IRAK)-4 via homotypic death domain interactions and IRAK-4 in turn activates IRAK-1 and IRAK-2. The dissociated IRAK complex binds to the TNFR-associated factor 6 (TRAF6), leading to the activation of IϰB kinase (IKK)-β and MAP kinase kinase 6 by binding of the TGF-β-activated kinase 1 (TAK1), TAK1-binding protein 1 (TAB1), TAB2, and TAB3 protein complex. Finally, the IKK complex and NF-κB essential modulator (NEMO), phosphorylates IϰBa, an NF-ϰB inhibitory protein, which leads in turn to the release of NF-κB and its recruitment to the nucleus and subsequently, the expression of proinflammatory cytokine genes (Takeuchi & Akira, 2010).

Besides the MyD88 pathway, TLRs also signal via the TRIF dependent pathway. TRIF interacts with TRAF6 and TRAF3. Interaction with TRAF6 results in the recruitment of the kinase RIP-1, which in turn activates NF-κB and MAPKs via the TAK1 complex. In contrast, trafficking of TRAF3 works similar to the MyD88 pathway. TRAF3 binds the kinases TBK1 and IKKi along with NEMO, which lead to the phosphorylation of the transcription factor IFN regulatory factor 3 (IRF3) and further leads to the expression of type I IFN genes. Additionally, the activation of MAP kinases results in the formation of the transcription factor complex, AP-1, leading to the expression of further cytokines.

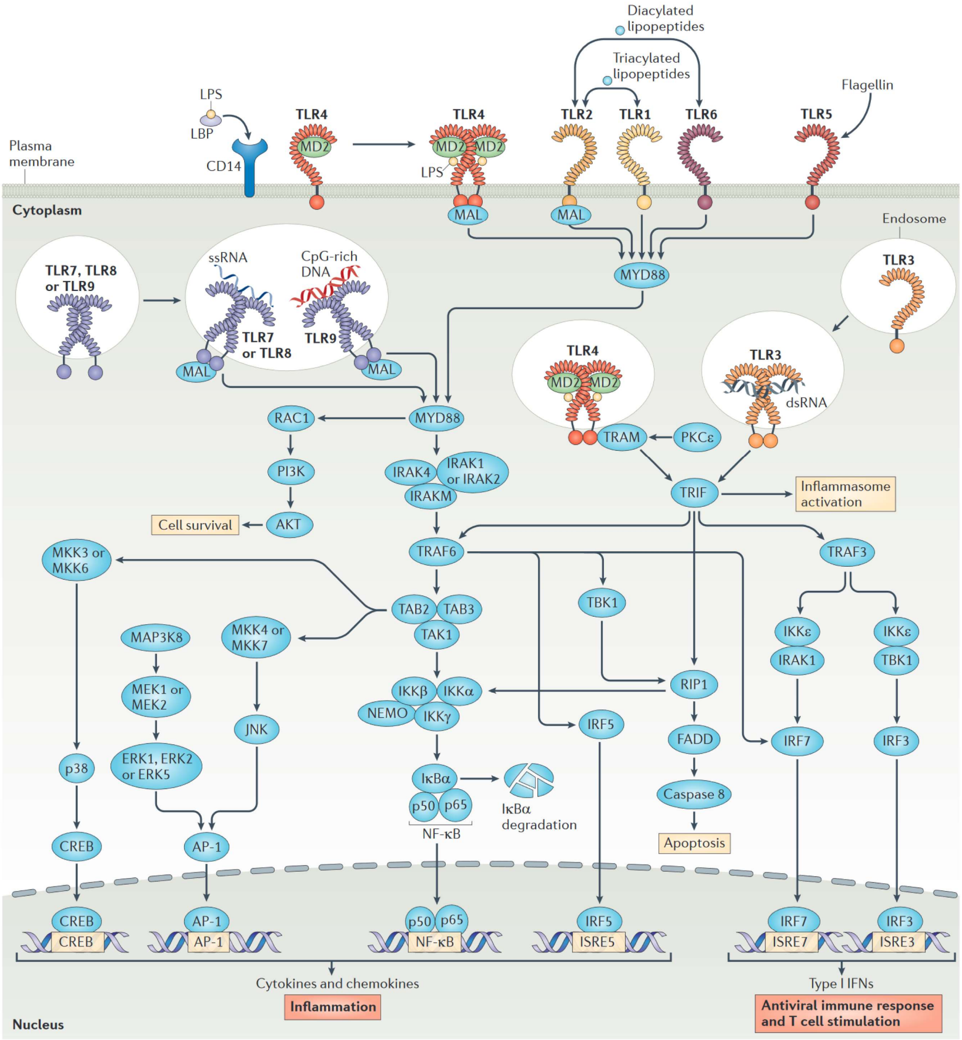

Figure 2: TLR signalling pathways. TLRs are either presented on the cell wall or on endosomes. Upon recognition of microbial cell-wall components, non-self nucleic acids or danger-associated self molecules two types of pathways are activated. TLRs either cause the activation of myeloid differentiation primary response protein 88 (MYD88) and/or TIR domain-containing adaptor protein inducing IFNβ (TRIF). Downstream signalling leads to the transcription of pro-inflammatory cytokines and chemokines as well as type I interferons (IFNs). Figure taken from Gay *et al.*, 2014.

6.1.2 C-type lectin receptors (CLRs)

CLRs comprise a family of transmembrane receptors which contain an extracellular carbohydrate recognition domain (CRD) and a calcium-binding site. These receptors are divided into two distinct clusters, the Dectin-1 cluster which contains MICL, CLEC-2, CLEC9A, CLEC12B, CLEC-1, Dectin-1, LOX-1 and the Dectin-2 cluster which is composed of BDCA-2, DCAR, DCIR, Dectin-2, Clecsf8 and Mincle (Kingeter & Lin, 2012). CLRs of the Dectin-1 and Dectin-2 cluster differ with respect to the cytoplasmic domain. Proteins of the Dectin-1 cluster contain an extracellular CRD, a stalk region and a transmembrane region. In comparison, the proteins belonging to the Dectin-2 cluster contain a short cytoplasmic domain.

Typically, β-glucan is recognized by the CRD domain of the Dectin-1 cluster, whereas the CRD of the Dectin-2 cluster binds mannose (Kingeter & Lin). Further proteins of the Dectin-1 cluster harbour an intracellular signal transduction domain, which for Dectin-1, CLEC-2, CLEC9A and LOX1 is identified as immunoreceptor tyrosine-based activation motif (ITAM), an important interaction site for downstream signalling. The consensus ITAM motif YxxI/Lx(6–12)YxxI/L is phosphorylated upon ligand recognition and receptor clustering by protein tyrosine kinase (PTK), leading to several downstream effects like activation of Ras, recruitment of phospholipase C-γ (PLCγ), and activation of calcium signalling and the ERK pathway. Negative regulation is mediated by receptors containing a tyrosine-based inhibition motif (ITIM), showing the consensus sequence S/I/V/LxYxxI/V/L (Barrow & Trowsdale, 2006). Activation of an ITIM motif by phosphorylation results in the recruitment of a phosphotyrosine phosphatase (PTP), which in turn counteract the effect of the ITAM motif (Barrow & Trowsdale). The CLR Dectin-1 cluster members MICL, CLEC12B, and DCIR harbour an ITIM motif, resulting in the inhibition of transcription factor activation (Kingeter & Lin).

For BDCA-2, DCAR, Mincle, Clecsf8 and Dectin-2 no signal transduction activity is known, but a positively charged residue in the transmembrane domain of these receptors is known to interact with FcRγ, which transmits the signal via an ITAM motif (Kingeter & Lin). Finally, downstream signalling cascades unite in the activation of NF-κB and the subsequent expression of proinflammatory cytokines.

6.1.3 Retinoic acid-inducible gene (RIG)-I-like receptors (RLRs)

Another class of cytoplasmic pattern-recognition receptors are Retinoic acid-inducible gene (RIG)-I-like receptors (RLRs). This family comprises three RNA-helicases, Retinoic acid Inducible Gene I (RIG-I), Melanoma Differentiation Associated gene 5 (MDA5), and Laboratory of Genetics and Physiology 2 (LGP2). These receptors sense for viral invasion by recognition of viral RNA, leading to the production of IFNγ as antiviral response (Kato & Fujita, 2015). RLRs are expressed in a variety of cell types and trigger an antiviral response in myeloid cells, epithelial cells, and cells of the central nervous system. Expression of these receptors is increased upon cell stimulation with IFNγ and upon virus infection (Loo & Gale, 2011). The members of the RLR family differ with respect to the virus family they recognize. Hepaciviruses and members of the Paramyxoviridae, Rhabdoviridae, and Orthomyxoviridae are recognized by RIG-I, whereas MDA5 responses to Picornaviridae. Further, some viruses are detected by both RLRs like Dengue virus, West Nile virus and reovirus.

RLRs share a similar domain organization. N-terminally, RIG-I and MDA5 possess a tandem caspase-recruitment domain (CARD) and further a DExD/H-box helicase domain, followed by a C-terminal domain, including a repressor domain (RD). The helicase domain has the capacity to hydrolyse ATP and further binds RNA (Loo & Gale, 2011). LGP2 lacks the N-terminal CARD domain (Kato & Fujita). In order to avoid autoimmunity, one major challenge of these receptors is to discriminate self from non-self RNA. The nucleotide sensing TLRs, TLR3, TLR7 and TLR8 are located at endosomes or the plasma membrane, locations that usually do not encounter endogenous RNA or DNA molecules, whereas RLRs are located in the cytosol. These receptors discriminate self from non-self RNA by the length of the dsRNA molecule. Furthermore, RIG-I was found to recognize 5'-triphosphate single and double stranded RNA molecules (Schlee *et al.*, 2009). Activation of RLRs is studied best for the receptor RIG-I. The protein is thought to be held in an autoinhibited conformation between the CARD domains and the C-terminal RD domain, in absence of viral RNA (Loo & Gale, 2011). Upon ligand recognition, RIG-I opens and is thought to multimerize. In this state, the CARD domains interact with the adaptor IFN-β promoter stimulator-1 (IPS-1), also called mitochondrial antiviral signalling (MAVS), CARD adapter inducing IFN-β (CARDIF), and virus-induced signalling adapter (VISA), in the mitochondrial membrane via homotypic CARD-CARD interactions (Schlee *et al.*, 2009). This leads to the activation of the transcription factors IRF3, IRF7 and NF-κB and subsequently the expression of type I IFN and proinflammatory cytokines.

6.1.4 NOD-like receptors (NLRs)

The family of NLRs comprises 22 cytoplasmic receptors in humans, that can be further classified into 3 subfamilies, NOD, NLRP and IPAF, dependent on the phylogenetic relationship and the molecular domain architecture (Figure 3). Additionally, the NLR proteins can be classified into 4 subgroups according to the N-terminal effector domains, NLRA, NLRB, NLRC and NLRX (Ting *et al.*, 2008). The NLRs contain a central nucleotide-binding domain (NACHT) or NACHT-associated domain (NAD) and an N-terminal effector domain. Four different effector domains can be distinguished. The family members NOD1, NOD2, NLRC3, 4 and 5 as well as an isoform of CIITA contain an N-terminal Caspase activation and recruitment domain (CARD), whereas a second isoform of CIITA harbours an acidic transcriptional activation domain (AD). Further, the NOD-family member NLRX1, which does not show a strong homology to the other NLR members, contains a N-terminal mitochondrial addressing sequence (Ting *et al.*, 2008; Arnoult *et al.*, 2009). The only member of the NLR family containing a Baculovirus Inhibitor of apoptosis protein repeat (BIR) domain is NAIP, which shows a tripartite BIR domain at the N-terminus. The largest subfamily, consisting of 14 members, is build up by the NLRP proteins. All of these proteins have a N-terminal PYD domain but differ in parts with respect to the C-terminal domain. NLRP1 and NLRP10 are the only members of the NLR family which do not contain a C-terminal leucine-rich repeat domain (LRR).

Instead, the domain architecture of NLRP10 ends in the nucleotide-binding domain, whereas NLRP1 is extended by a function to find domain (FIIND) and a C-terminal CARD domain. Additionally, NLRX1 contains a N-terminal and a C-terminal helical bundle flanking the LRR domain, thus underlining the dissimilarity of NLRX1 (Hong *et al.*, 2012).

The IPAF subfamily is composed of the nucleotide-binding domain, leucine-rich repeat-containing family, apoptosis inhibitory proteins (NAIPs) as well as the nucleotide-binding domain, leucine-rich repeat-containing family, CARD domain-containing protein 4 (NLRC4). In mice, NAIP proteins were found to specifically activate the NLRC4 inflammasome, after recognition of specific ligands. NAIPs recognize ligands of the bacterial type III secretion system (T3SS), as for example the T3SS needle protein activated NAIP1, NAIP2 recognizes the T3SS inner rod protein and the component flagellin is bound by NAIP5 and NAIP6 (Reyes Ruiz *et al.*, 2017).

In contrast, the only human NAIP protein detected so far recognizes multiple ligands like: T3SS inner rod protein PrgJ of *Salmonella typhimurium*, needle protein and flagellin (Reyes Ruiz *et al.*, 2017). Upon recognition of the respective ligand, NAIP proteins bind NLR4, forming the NLRC4 inflammasome by recruiting and subsequent activation of Caspase-1.

The NOD-subfamily is the most divergent subfamily, consisting of six different receptors. The member NLRX1, deviating from all other mentioned receptors, is anchored to the mitochondrial outer membrane and does not exhibit inflammasome function (Jo *et al.*, 2016). In contrast, NLRX1 was found to act as a tumor suppresor, attenuates NF-κB signalling and promotes virus-induced autophagy (Jo *et al.*, 2016).

The NOD-family member CIITA, is a trancriptional co-activator, which regulates the transcription of MHC class II genes. Binding of CIITA to the the transcription factor TFIID, leads to the initiation of an enhancer complex. Moreover, CIITA was found to possess kinase activity, utilizing both GTP and ATP, whereas inflammasome function is not reported (Soe *et al.*, 2013).

A similar mode of action is supposed to hold true for NLRC5. The receptor was found to shuttle to the nucleus, leading to the induction of the transcription of MHC class I genes (Benkő *et al.*, 2017). Whether NLRC5 also forms an inflammasome complex is still to be elucidated, whereas changes in IL-1β expression levels are reported in response to NLRC5 activation (Benkő *et al.*, 2017).

In contrast, the immune receptor NLRC3, is known to negatively regulate inflammatory signalling pathways, like the NF-κB- and STING-pathway and was further shown to regulate the adaptive immune response following *Mycobacterium tuberculosis* infection (Hu *et al.*, 2018).

The cytosolic receptor NOD2 is activated upon recognition of bacterial peptidoglycan, like muramyl dipeptide (MDP) (Negroni *et al.*, 2018). Upon ligand binding to the LRR-domain of NOD2, the kinase receptor interacting protein 2 (RIP2) is recruited via homophilic CARD-CARD interactions. This leads to downstream signalling via NF-κB and subsequently, to the expression of proinflammatory genes, including cytokines and growth factors (Negroni *et al.*, 2018). Moreover, NOD2 was shown to directly interact with the zymogen pro-caspase-1 again via CARD-CARD domain interactions, leading to the activation of pro-IL-1β (Negroni *et al.*, 2018).

Simillarly, NOD1 was also found to recruit RIP2 and leads to the downstream activation of the NF-κB pathway in teleost fish (Bi *et al.*, 2018). Moreover, NOD1 was also found to be activated by peptidoglycans (γ-tri-DAP), as well as bacterial cell wall components from gram-negative bacteria (Xu *et al.*, 2018).

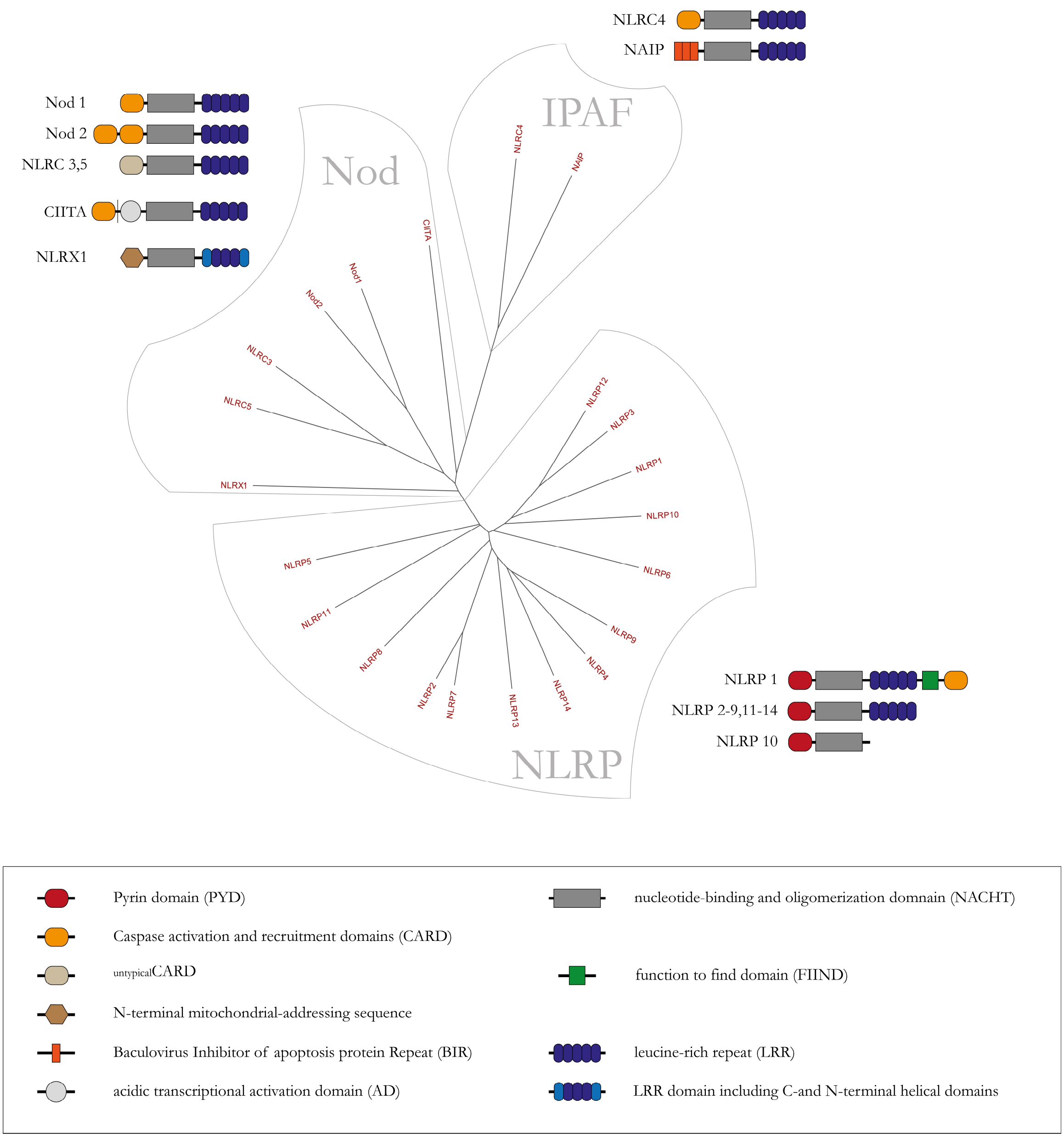

Figure 3: Phylogenetic tree of human NOD-like receptor family. The NOD-like receptor family is subdivided in three families: NOD, IPAF and NLRP. The subfamilies are distinguished based on the domain architecture. NLRP family members possess an N-terminal PYD domain, whereas the members of the NOD-family either contain an N-terminal CARD-domain or a mitochondrial-adressing sequence. Moreover, the IPAF family member NLRC4 contains an N-terminal CARD-domain. In contrast, NAIP possesses an N-terminal BIR-domain. Moreover, each receptor harbours a central NACHT domain as well as a LRR-domain, except for NLRP10. The phylogenetic tree was determined using CLC-Sequence Viewer 8.

6.2 Protein domains mediating NLRP3-inflammasome assembly

Most of the NLR-members like NLRP3, show a tripartite domain architecture: an N-terminal Pyrin domain, a central NACHT domain and a C-terminal LRR domain. The superfamily of death domains can be subdivided into four subfamilies. Besides the largest subfamily, the pyrin domain (PYD) family, further the death effector domain (DED) family, the caspase recruitment domain (CARD) family, and the death domains (DD) family can be distinguished (Park *et al.*, 2007). Death domains were identified as the critical domains, mediating homotypic domain/domain interactions in apoptosome, necrosis and immune receptor signalling (Park, 2011). The main function of these domains is the recruitment of adaptor proteins, like ASC and/or the direct interaction with pro-Caspase zymogens. The adaptor protein ASC fulfils a specialized role, as it contains two death domains, an N-terminal PYD domain and a C-terminal CARD domain, thus facilitating the bridging between other death domain containing protein families. Homotypic PYD/PYD interactions have been identified for a multitude of different proteins like ASC, AIM2, Pyrin, NLRP1, NLRP2, NLRP3, NLRP7, NLRP10, NLRP12, POP1 and POP2, as well as IFI16 (Kwon *et al.*, 2012). Furthermore, homotypic CARD/CARD interactions have been shown for the following proteins: ASC, CARD12, CARD16, Caspase-1, RIPK2 and NLRC4 (Kwon *et al.*, 2012; Li *et al.*, 2018).

All death domains of the DD subfamily exhibit a six-helical bundle fold, but differ with respect to the helix length and orientation. Low sequence homology was detected among the death domains, going along with completely different surface features (Park, 2011). In comparison to the DD subfamily, the CARD subfamily also forms a six-helical bundle fold, with a separated helix1. Both, an acidic and basic surface of the CARD domain are thought to mediate protein/protein interactions, as shown for the structure of APAF1-CARD with the CARD domain of Caspase-9 (Park *et al.*, 2007; Hu *et al.*, 2014).

Caspases are recruited to the inflammasome platform via CARD/CARD interactions. Most likely, the activation of Caspase-1 is facilitated by an increase in the local protein concentration, that favours dimerization and autocatalytic processing (Boucher *et al.*, 2018). Caspase-1 undergoes autoproteolytic cleavage, thus forming a p33/p10 dimer. In association with the inflammasome, the dimer is processed to a p20/p10 dimeric fragment, which upon release from the inflammasome becomes inactive (Boucher *et al.*, 2018).

The active Caspase-1 tetramer cleaves pro-IL-1β, pro-IL-18 and Gasdermin D (GSDMD) into their active forms, leading to the induction of pyroptosis. Upon cleavage, e.g. by Caspase-1 and Caspase-11, the N-terminal fragment of GSDMD is released from the inhibitory C-terminal fragment, thus forming pores in the cell membrane by binding to the inner leaflet (Liu *et al.*, 2016). Besides GSDMD, Caspase-1 also cleaves pro-IL-1β and pro-IL-18 into their active forms. Inflammation, vasodilatation and immune-cell extravasation is mediated by IL-1β, whereas Il-18 secretion leads to local inflammation and IFN-γ production in Th1 cells, NK cells and cytotoxic T cells (Yuan *et al.*, 2018).

Deviating from the typical fold of DDs and CARD domains, the PYD domains show an altered assembly. As an example, helix 3 of the ASC-PYD domain is shortened to four residues, whereas it is completely missing in NLRP1 (Park *et al.*, 2007). Nonetheless, the ASC-PYD assembled into a filament structure, which was shown to be nucleated by either NLRP3 or AIM2 (Lu *et al.*, 2014). Three assymetric interfaces have been described to form the homotypic interactions in the ASC-PYD filament, which are also thought to mediate heterotypic PYD/PYD interactions (Lu *et al.*, 2014).

A family of proteins that possess a single PYD or CARD domain was shown to negatively regulate inflammasome formation by direct inhibition of the adaptor ASC or interaction with the NLR-complexes: the Pyrin-only proteins (POPs) and CARD-only proteins (COPs) (Matusiak *et al.*, 2015). POP2 was shown to directly inhibit NLRP2-inflammasome formation and was further able to inhibit NLRP3-inflammasome assembly by directly interacting with the adaptor protein ASC (Matusiak *et al.*, 2015).

The NLRP3 protein possesses a central NACHT domain. This domain is composed of a nucleotide-binding domain (NBD), followed by a helical domain 1 (HD1), winged helix domain (WHD) and helical domain 2 (HD2) (Hauenstein *et al.*, 2015). The WHD domain was found to be associated with the ADP binding site in the closed NLRC4ΔCARD structure, whereas its position varies strongly between APAF1 and Ced-4 (Hu *et al.*, 2013). The HD1 and HD2 domains both form helical bundles flanking the WHD. For NLRC4, the HD2 domain was shown to negatively regulate a Arg-containing helix in the NBD. Furthermore, the HD2 was also found to cap the N-terminal part of the LRR domain (Hu *et al.*, 2013). The HD1 was also found to associate with the NBD domain of NLRC4ΔCARD in its autoinhibited conformation (Hu *et al.*, 2013). The NBD is explained in more detail below.

The C-terminal Leucine-Rich-Repeat (LRR) motif, usually consists of a 22-29 residue sequence, which fulfills diverse functions (Park *et al.*, 2015). Typically, LRR domains are involved in protein/protein interaction and ligand binding. The conserved 11-residue sequence of LxxLxLxxN/CxL, consisting of a short β-strand-loop-α-helix motif.

Dependent on the amount of LRRs, ranging from 2-45 LRRs, it forms into a nonglobular, horseshoe-shaped molecule (Kobe & Kajava, 2001; Ng & Xavier, 2011). For most of the LRR-containing proteins, like the RNAse-RNAse inhibitor interaction, ligand binding occurs on the inner, concave surface of the horseshoe-shaped structure (Botos *et al.*, 2011). A characteristic of the LRR domains of TLRs is the occurrence of extensions in the LRR-sequence as well as the presence of N- and C-terminal structures, capping the LRR domain (Botos *et al.*, 2011). Further, binding of dsRNA was shown to take place in the capping structures of the TLR3-LRR domain (Botos *et al.*, 2011). Moreover, LPS and MD-2 were found to localize in the inner surface of the LRR domain of TLR4. Until now, no direct ligand interaction was determined with any LRR domain of NLRs. In particular, the structures solved for NLRC4 in its autoinhibited and activated state suggest sequestering of murine NLRC4ΔCARD in a monomeric state, whereas the LRR also builds an interaction surface in the activated multimer (Hu *et al.*, 2013; Diebolder *et al.*, 2015; Zhang *et al.*, 2015; Tenthorey *et al.*, 2017). Whether the LRR is involved in ligand binding of NLRs, still remains elusive.

6.3 Structural aspects of inflammasomes

The first multimeric inflammasome complex was discovered in 2002, as a platform containing NLRP1 and Apoptosis-associated speck-like protein containing a CARD (ASC), leading to the activation of Capsase-1 and Caspase-5 (Martinon *et al.*, 2002). During the following years, canonical inflammasome formation has been shown for the following receptors: NLRP1, NLRP3, NLRC4 and AIM2 (Kesavardhana & Kanneganti, 2017). Furthermore, NLRP6, NLRP12, IFI16 and Pyrin have been identified as inflammasome-forming proteins (Vanaja *et al.*, 2015). Canonical inflammasomes are multiprotein complexes consisting of a receptor, contingently the adaptor protein ASC and pro-Caspase-1. Upon assembly on the inflammasome-receptor platform, the zymogen pro-Caspase-1 gets activated by dimerization and autoprocessing (Elliott *et al.*, 2009). Thereafter, Caspase-1 cleaves pro-IL1β, pro-IL18 and GSDMD into their active forms, thus inducing a specified form of cell death called pyroptosis.

The assembly of each inflammasome is dependent on the subdomain organization of the receptors, as well as the ligands involved. Until now, only a few direct ligands have been identified.
Two isoforms of the murine NLRP1b variant are activated by Anthrax lethal toxin from *B. anthracis*, whereas for the human NLRP1 protein, no ligand could be identified so far.

Nonetheless, the NLRP1 protein of both species was found to be activated by cleavage in the N-terminal linker region between the PYD- and the NACHT domain (Kesavardhana & Kanneganti, 2017). Autoproteolytic cleavage was found to occur in the FIIND domain, also resulting in the activation of the NLRP1 inflammasome (D'Osualdo *et al.*, 2011). The adaptor ASC, was found to associate with the C-terminal CARD domain that becomes accessible upon autocatalytic processing (Finger *et al.*, 2012).

The NLRC4 inflammasome forms a heterogenous assembly of NLRC4 and an associated NLR apoptosis inhibitory protein (NAIP). In absence of a NAIP protein, the crystal structure of NLRC4 (PDB accession code: 4KXF) showed an auto-inhibited form, which was bound to ADP (Hu *et al.*, 2013). An autoinhibited conformation was detected in the ADP-bound APAF1 (PDB: IZ6T) crystal structure (Riedl *et al.*, 2005). Upstream of NLRC4, NAIP 5 and 6 bind to the ligand flagellin, and NAIP 1 and 2 were found to bind rod and needle proteins of the bacterial type III secretion system (T3SS) (Kesavardhana & Kanneganti, 2017). The NLRC4-inflammasome was the first, that was structurally determined in a multiprotein complex. Cryo-electron tomography as well as Cryo-electron microscopy revealed a disc-like structure of NLRC4. Ligand-bound NAIP2 was found to catalyze the propagation of a wheel-like assembly by the activation of inactive NLRC4ΔCARD proteins (Diebolder *et al.*, 2015; Hu *et al.*, 2015; Zhang *et al.*, 2015). Furthermore, also NAIP5 was identified to propagate NLRC4 inflammasome formation in a multimeric assembly (Tenthorey *et al.*, 2017). The active NAIP/NLRC4 disc-assembly forms a multimer of 10-12 subunits, that form interaction interfaces between two molecules in the following domains: LRR-/LRR domain, WHD/HD1 and NBD-/NBD domain (Hu *et al.*, 2015). The assembly of the NLRC4 inflammasome is a unidirectional process, initiated by the catalytic surface on the activated NAIP molecule, that mediates progressive intermolecular autoactivation of the following NLRC4 subunit (Hu *et al.*, 2015). The NLRC4 inflammasome is thought to form upon CARD-CARD interactions of ASC and NLRC4 and subsequent Caspase-1 activation, again by CARD-CARD interactions with ASC or by direct interaction of the NLRC4-CARD with the Caspase-1 CARD domain (Zhang *et al.*, 2015). The disc-like assembly of the NLRC4ΔCARD/NAIP complex was formed in absence of the NLRC4 CARD domain, thus the spatial arrangement of the ASC adaptor domain, remains to be elucidated.

Recently, the self-assembly of the ASC-CARD domain and the NLRC4-CARD domain was investigated by Cryo-EM (Li *et al.*, 2018). Comparable to the structures determined for the ASC-PYD filament (PDB: 3J63) and the Caspase-CARD-filament (PDB: 5FNA), the ASC-CARD (PDB: 6DRN) as well as the NLRC4-CARD (PDB: 6DRP) structure equally revealed a filamentous arrangement, each consisting of a homo-8mer (Lu *et al.*, 2014; Lu *et al.*, 2016; Li *et al.*, 2018). Strikingly, the structures revealed for the oligomeric assembly of the NLRC4ΔCARD/NAIP inflammasome, mostly showed a 10-12mer assembly.

Thus, the exact arrangement and the interaction mechanism of NLRC4-CARD and Caspase-1-CARD as well as the ASC-CARD domain, remains elusive. Moreover, the structures of two additional pattern-recognition-receptors were determined. The crystal structure of the NOD-like receptor NOD2 (PDB: 5IRL) revealed an open conformation in the ADP-bound state (Maekawa *et al.*, 2016). Whereas the crystal structure determined for the CED4 apoptosome (PDB: 3LQQ) from *C. elegans* showed a homo-oligomer, formed by a tetramer of an asymmetric dimer (Qi *et al.*, 2010). The associated Caspase Ced-3, which shows homology to the mammalian Caspase-3, was found to interact with the octameric Ced-4 apoptosome complex. Interestingly, only two molecules of Ced3 instead of eight, were found to bind the formed apoptosome (Qi *et al.*, 2010).

6.4 The NLRP3 inflammasome

Among all studied inflammasomes, the NLRP3 inflammasome is the most-studied and at the same time the least understood inflammasome. NLRP3 can be activated via the canonical or the non-canonical pathway.

In the non-canonical pathway identified in mice, Caspase-11 is activated by direct interaction with cytosolic lipopolysaccharide (LPS) via the CARD domain (Vanaja *et al.*, 2015). Caspase-4 and 5 were identified to form the human counterpart to Caspase-11 in mice, as these caspases were also found to bind LPS directly (Shi *et al.*, 2014). Caspase-11 was shown to license the formation of the NLRP3-inflammasome in a TRIF-dependent pathway, although it is not itself recruited to the inflammasome complex (Rathinam *et al.*, 2012).
For the activation of NLRP3 and subsequently Caspase-1 via the canonical pathway, a two-step mechanism is required. In a first priming step LPS is used to upregulate the expression of NLRP3 and pro-IL-1β in a TLR4-MD2 dependent way (Vanaja *et al.*, 2015). A huge variety of secondary activating stimuli has been identified for the canonical pathway until now.

Several DAMPs like extracellular ATP, nucleic acids, uric acid crystals, silica, asbestos as well as aluminium hydroxide, amyloid-β fibrils, UV irradiation or PAMPs like *S.aureus*, *L.monocytogenes*, and *N.gonorrhoeae* have been shown to activate the NLRP3 inflammasome (Jo *et al.*, 2016; Kesavardhana & Kanneganti, 2017). NLRP3 is thought to preassemble into an inactive oligomeric complex, which is activated upon a decrease in extracellular osmolarity (Compan *et al.*, 2012). Instead of a direct interaction and activation of these stimuli these factors converge on a still unknown intrinsic signal which in turn activates the NLRP3 inflammasome.

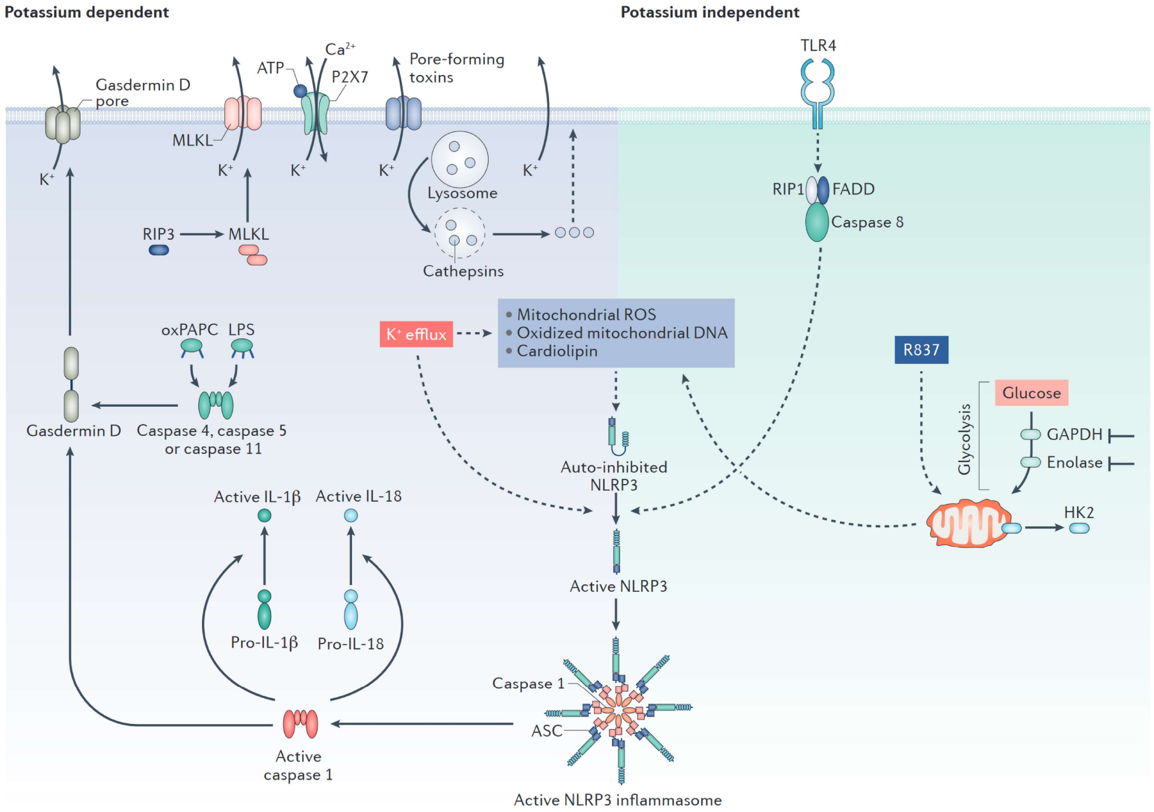

Figure 4: NLRP3 activation pathways. NLRP3 is activated either in a potassium dependent or potassium independent pathway. Potassium efflux is mediated by membrane pore formation through either Gasdermin D or bacterial pore-forming toxins. Furthermore, mixed lineage kinase domain-like protein (MLKL) activation, as well as the opening of the P2X purinoceptor 7 (P2X7) channel mediate potassium efflux. Moreover, NLRP3 is activated via the potassium independent TLR4-Caspase-8 pathway. Figure taken from Mangan *et al.*, 2018.

One potential convergence point is the production of reactive oxygen species (ROS). In several pathologies, ROS production goes along with mitochondrial damage and was found to be involved in redox signalling to the cytosol and nucleus (Murphy, 2009).

It has been shown previously, that mitochondrial ROS lead to the activation of the NLRP3 inflammasome, by NLRP3-dependent lysosomal membrane permeabilization (Areschoug & Gordon, 2008). Moreover, mitochondrial apoptosis and dysfunction was shown to induce NLRP3 activiation by the interaction with mitochondrial oxidized DNA (Shimada *et al.*, 2012). Liposome induced NLRP3 activation, was also found to converge on ROS production, mediated by calcium influx via the TRPM2 channel (Zhong *et al.*, 2013). The ROS production in response to stimulation with increased extracellular ATP levels, was also shown to go along with a decrease in intracellular ATP concentration (Cruz *et al.*, 2007; Heid *et al.*, 2013).

A second, widely excepted, feasible underlying mechanism is potassium efflux. *In vitro*, spontaneous NLRP3-inflammasome formation occurred at K^+ concentrations below 90 mM, whereas physiological K^+ concentrations (143 mM) inhibited inflammasome assembly. Of note, NLRP1-inflammasome formation is also dependent on low intracellular K^+ concentrations (Pétrilli *et al.*, 2007). Well-established NLRP3 activators like ATP, nigericin and gramicidin are known to influence the K^+ homeostasis. Nigericin as a K^+/H^+ exchanger and gramicidin as a cation channel both can lead to an intracellular potassium depletion. Moreover, ATP is known to act via P2X7 receptors, which upon ATP binding open within milliseconds to gate small cations, thus leading to the influx of Ca^{2+} and Na^+ and the efflux of K^+. In the following seconds, the channel opens a larger pore, which is selective to small molecules with a size of 900 Da. In humans, P2X7 receptors are found predominantly in immune cells like, macrophages, microglia, and certain lymphocytes, suggesting an important immune-modulating role (Volonté *et al.*, 2012). Several NLRP3 activating factors like, hydroxyapatite crystals as well as PAMPs secreted by *C.albicans* and *A.hyphae* were shown to activate both, K^+ efflux and ROS production, pointing to a combined underlying pathway (Jo *et al.*, 2016). Further, these stimuli, also lead to a third mechanism of NLRP3 activation, lysosomal rupture.

Lysosomal rupture, is observed in cells triggered with ATP and nigericin, whereas, it is a late event, following NLRP3 activation (Jo *et al.*, 2016). In comparison, direct induction of lysosomal rupture, using the agents Leu-Leu-OMe and alum, also leads to NLRP3 activation (Jo *et al.*, 2016). Lysosomal dysfunction and cathepsin release are already observed in the priming step, following LPS treatment. Further, chlosterol-crystal induced NLRP3 activation is dependent on the phagolysosomal damage (Jo *et al.*, 2016). Moreover, lysosomal rupture-dependent NLRP3 activation was connected to the TAK1-JNK pathway and more upstream, the calcium-dependent calcium/calmodulin-dependent protein kinase type II function (Okada *et al.*, 2014).

Besides these molecular mechanisms, NLRP3 activation was also shown to be dependent on the spatial arrangement of organelles inside the cell. Microtubule association of the adaptor ASC, was found to be a crucial prerequisite for proper NLRP3 inflammasome assembly.

Prior to activation, NLRP3 is localized at the endoplasmic reticulum (ER), whereas upon activation, NLRP3 and ASC move to the perinuclear space and co-localize to ER- and mitochondrial clusters, respectively (Zhou *et al.*, 2011; Misawa *et al.*, 2013). Upon NLRP3 activation, a decrease in NAD^+ was identified to cause an accumulation of acetylated α-tubulin, caused by an inactive NAD^+-dependent α-tubulin deacetylase sirtuin 2. Mitochondria are subsequently transported to the perinuclear region in a dynein-dependent way, mediated by acetylated α-tubulin, thus allowing for the translocation of ASC to the perinuclear space (Misawa *et al.*, 2013). NLRP3 is recruited to mitochondria via the mitochondria-associated adapter molecule, MAVS (Subramanian *et al.*, 2013).

An intracellular, spatial bridge between the ER and mitochondria is the mitochondria-associated membrane (MAM), which interconnects protein folding and synthesis to the mitochondrial metabolism, thus potentially building a place for NLRP3 inflammasome assembly (Raturi & Simmen, 2013). Additionally, it is concluded that the thioredoxin (TRX)-interacting protein (TXNIP) upon detachment of TRX, localizes to the MAM and directly interacts with NLRP3 (Zhou *et al.*, 2011; Jo *et al.*, 2016).

NLRP3 was also shown to be influenced by changes in Ca^{2+} homeostasis as well as the concentration of cAMP. An increase in intracellular Ca^{2+}, which goes along with a decrease in cellular cyclic AMP (cAMP), is mediated by the murine calcium-sensing receptor (CASR), which leads to activation of the NLRP3 inflammasome (Lee *et al.*, 2012). In presence of the second messenger cAMP, NLRP3 inflammasome activation is inhibited, whereas the Ca^{2+}-dependent drop in intracellular cAMP results in the termination of this inhibition mechanism (Lee *et al.*, 2012). NLRP3 was shown to directly bind cAMP but not cGMP via the NACHT domain. Moreover, ATP binding of the NACHT domain was not inhibited in the presence of cAMP (Lee *et al.*, 2012).

Various interaction partners of NLRP3 have been identified to date, in which the molecular interplay still needs to be revealed. The interaction of NLRP3 with the ubiquitin ligase-associated protein SGT1 and the heat-shock protein 90 (HSP90) chaperone machinery has been shown to be crucial for inflammasome activation (Mayor *et al.*, 2007). Besides NLRP3 binding, SGT1 was also found to interact with further members of the NLR family like NLRP2, NLRP4, and NLRP12, as well as NOD1, NOD2 and IPAF. Thus an evolutionarily conserved mechanism underlying inflammasome activation, is proposed (Mayor *et al.*, 2007).

NLRP3 was shown to directly interact with HSP90 via 2 binding sites in the NACHT and LRR domain, respectively, and additionally with a single binding site in the LRR domain to SGT1 (Mayor *et al.*, 2007).

Recently it was shown that the LRR-domain of NLRP3 is not needed for its activation, as a minimal variant is fully responsive to activating signals in macrophages (Hafner-Bratkovič *et al.*, 2018). Moreover, it is stated, that the LRR domain does not stabilize the inactive conformation of NLRP3 (Hafner-Bratkovič *et al.*, 2018).

In mouse, another factor was identified, that interacts directly with NLRP3 via the LRR domain and mediates inflammasome assembly: the NIMA-related serine/threonine kinase Nek7 (He *et al.*, 2016b; Shi *et al.*, 2016). In association with Nek9 and Nek6, Nek7 regulates mitotic spindle formation as well as centrosome separation during mitosis (Shi *et al.*, 2016). Nek7 is thought to form a cellular checkpoint, deciding between mitosis and the activation of the immune system.

The Nek7/NLRP3 interaction was shown to be dependent on K^+ efflux, thus representing a consequence of NLRP3 activation (He *et al.*, 2016b; Schmid-Burgk *et al.*, 2016).

The assembly of the NLRP3 inflammasome, including the formation of ASC-Specks is dependent on NEK7, which associates with the complex (He *et al.*, 2016b). Activation of the NLRP3 inflammasome by Nek7 is thought to be irrespective of its kinase activity (He *et al.*, 2016b).

Several additional factors were shown to directly interact with the inflammasome forming receptor NLRP3.
The murine guanylate binding protein (GBP) GBP5 was shown to directly interact with the PYD-domain of NLRP3 (Shenoy *et al.*, 2012). Moreover, GBP5 was shown to specifically activate NLRP3 upon administration of bacterial stimuli and soluble activating agents (Shenoy *et al.*, 2012).
The double-stranded RNA dependent protein kinase (PKR) was also shown to directly interact with NLRP3 (Lu *et al.*, 2012). A more global influence on the clearance of the cellular bacterial burden is suggested, as PKR was also shown to directly interact with the inflammasome components NLRP1, AIM2, and NLRC4 (Lu *et al.*, 2012).
NLRP3 is known to respond to multiple activation signals, among these are dsRNA as well as bacterial RNA molecules. The DExD/H-box RNA helicase family member DHX33 was shown to specifically bind dsRNA and subsequently bound to NLRP3, leading to the formation of the NLRP3 inflammasome (Mitoma *et al.*, 2013).
A diversity of factors and stimuli was shown to interact with the inflammasome component NLRP3, but until now, no correlation between the different binding partners was found.

6.4.1 Posttranslational modifications of NLRP3

Posttranslational modifications (PTM) like phosphorylation, ubiquitination, alkylation, and S-nitrosylation have been investigated with respect to an activating and inhibiting function in NLRP3 inflammasome formation. Until now, six different phosphorylation sites have been identified in human NLRP3 (Table 1). Posttranslational phosphorylation of NLRP3 is a key event in the regulation of inflammasome activation and inhibition. Phosphorylation of S5 leads to an inactive NLRP3 variant, which is activated upon dephosphorylation by PP2A (Stutz et al., 2017). Phosphorylation is already a critical event during priming. C-Jun N-terminal kinase 1 (JNK1) was identified as kinase, which phosphorylates NLRP3 at position S198, during a prolonged priming phase (Song et al., 2017). In this case, the self-association of NLRP3 is facilitated due to NLRP3 deubiquitination (Song et al., 2017).

Table 1: Phosphorylation sites of human NLRP3. The effect on NLRP3 inflammasome formation and the responsible kinases and phosphatases are shown. [1] (Stutz *et al.*, 2017), [2] (Song *et al.*, 2017), [3](Mortimer *et al.*, 2016), [4] (Zhang *et al.*, 2017), [5] (Spalinger *et al.*, 2016)

position	kinase / phosphatase	effect
S5	Protein-phosphatase 2A (PPTA)	Desphosphorylation of NLRP3-PYD domain is needed for inflammasome activation [1]
S161	N/A	N/A [1]
S198	Jun-N-terminal kinase 1 (JNK1)	Phosphorylation of NLRP3 is critical for NLRP3 deubiquitination and activation [2]
S295	Protein-kinase A (PKA), Protein-kinase D (PKD)	Phosphorylation of NLRP3 (PKA, PKD), reduced ATPase function (PKA), activation (PKD) [3,4]
S728	N/A	N/A [1]
Y861	tyrosine phosphatase non-receptor 22 (PTPN22)	Phosphorylated during priming, dephosphorylation of NLRP3 by PPT [5]

Ubiquitination is a further critical posttranslational modification that regulates NLRP3 inflammasome activity. Two different Lysine residues are reported to be ubiquitinated on NLRP3: K63 and K84. Ubiquitination of K84 leads to proteasomal degradation, whereas ubiquitination of both residues leads to inactivation of NLRP3 (Shim & Lee, 2018).

The deubiquitinase BRCC3 was shown to act on NLRP3, subsequently leading to its activation (Py *et al.*, 2013).

Moreover, NLRP3 inhibiting compounds were identified to regulate inflammasome activity by alkylation. The inhibitors Parthenolide and Bay11-7082, alkylate NLRP3 and subsequently lead to a decreased ATPase activity (Juliana *et al.*, 2010). Moreover, thiol-nitrosylation mediated by nitric oxide (NO) was found to inhibit NLRP3 inflammasome assembly, thus potentially mediating the crosstalk between the adaptive and innate immune system (Mishra *et al.*, 2013).

6.4.2 NLRP3 Inflammasomopathies

The cryopyrin-associated periodic syndrome (CAPS) is a disease caused by mutations in the *CIAS1* gene, encoding for the NLRP3 protein (Hoffman *et al.*, 2001). CAPS can be divided into three subforms: (i) Muckle–Wells syndrome (MWS), showing the mildest phenotype, (ii) Chronic Infantile Neurological Cutaneous and Articular syndrome (CINCA) also known as Neonatal-onset multisystem inflammatory disease (NOMID), which is showing the most severe form; and (iii) Familial Cold Autoinflammatory Syndrome (FCAS), as an intermediate phenotype (Tran, 2017). Either inherited or de-novo-gain of function mutations in the NLRP3 gene lead to increased levels of IL-1β, caused by the activation of the NLRP3-inflammasome, even in the absence of an infection (Tran, 2017). Until now, 210 sequence variants have been identified in the human NLRP3 gene, in which the vast majority is positioned in exon 3 (Sarrauste de Menthière *et al.*, 2003).

The inflammasomopathies differ greatly with respect to the severeness of the occurring symptoms, thus besides the presence of raised inflammatory markers, two or more of the following symptoms are mandatory for the diagnosis of CAPS: Urticaria-like rash, cold/stress-triggered episodes, sensorineural hearing loss, musculoskeletal symptoms like arthralgia, arthritis or myalgia, chronic aseptic meningitis and skeletal abnormalities (Tran, 2017). To date, six point-mutations have been identified that show a prevalence of 75%, in the diagnosed patients. The remaining 25% of casses are caused by either no mutations identified in the NLRP3 gene or by rare mutations (Tran, 2017). The most frequently occurring mutations, R260W (25%) and T348M (15%) are both located in close proximity to the nucleotide-binding domain of NLRP3. Less frequently occuring mutations are: V198M (10%), A439V (10%), E311K (7%) and Q703K (7%) (Tran, 2017). Nonetheless, the underlying mechanism, that causes a hyperactive NLRP3 inflammasome, is still to be elucidated.

6.5 ATPases

The domain architecture of the animal NLRs shows a strong convergence with its plants analogues, the R-proteins (Urbach & Ausubel, 2017). A common ancestor for plant and animal NLRs was suggested due to the similarity in domain organization and function but is highly questionable since phylogenetic analysis revealed that either protein families evolved independently, or the genes were acquired by horizontal gene transfer (Urbach & Ausubel, 2017).

The function of ATPases associated with various cellular activities (AAA+ ATPases) is diverse, ranging from proteases, like the 26S proteasome, over proteins involved in vesicular fusion as well as helicases and transcriptional activators, found among all kingdoms of life (Ammelburg *et al.*, 2006; Snider & Houry, 2008; Sysoeva, 2017). Classification of this protein family starts with the discrimination of P-loop NTPases into the two major groups of either Kinase GTPases and the Additional Strand Catalytic E group (ASCE) (Snider & Houry, 2008). Typically, these two major classes can be distinguished by their substrate specificity, thus showing higher affinity towards ATP for the family members belonging to the ASCE division. The family of ASCE can then be further subdivided into AAA+ -, KAP-, RecA/F1, ABC-ATPases, SF1/2 helicases and VirD/PilT ATPases and HerA-FtsK (Figure 5) (Leipe *et al.*, 2004; Snider & Houry, 2008). The family of AAA+ ATPases further branches into five groups, the extended AAA group including representatives like FtSH and Katanin, the HEC group including the Clamp loader clade, the PACTT group, including e.g. MoxR and dynein, as well as the ExeA group and the STAND group, which comprises the family of NLRs (Ammelburg *et al.*, 2006; Erzberger & Berger, 2006; Snider & Houry, 2008). The STAND family (signal transduction ATPases with numerous domains) includes NB-ARC and NACHT NTPases respectively consisting of multidomain proteins (Leipe *et al.*, 2004; Ammelburg *et al.*, 2006; Wendler *et al.*, 2012).

AAA ATPases are known to convert the energy generated during ATP binding and hydrolysis into mechanical force, used to evoke conformational changes of their substrates like nucleic acids and proteins (Sysoeva, 2017; Yedidi *et al.*, 2017). A typical feature of AAA+ ATPases is the assembly into multiprotein complexes or at least into dimers. The clamploader and initiator clade proteins characteristically form closed hexameric complexes, whereas DnaA and RFC form open ring structures (Erzberger & Berger, 2006). Hexameric rings are also formed by the eukaryotic 26S proteasome as well as its prokaryotic ancestors like HsIU (Yedidi *et al.*, 2017). In the archaeal kingdom, representatives like proteasome-alike proteases were found to assemble into four heptameric rings (Yedidi *et al.*, 2017).

Comparing the proteasomal AAA ATPases, the prokaryotic variants form a homohexamer, whereas the eukaryotic proteasome forms a heterohexamer, in which the six ATPase subunits follow a particular order (Yedidi *et al.*, 2017). Besides the differences in the structural assembly of AAA ATPases, they also differ with respect to the ATP hydrolysis cycle. Usually, ATP hydrolysis takes place in the assembled oligomer, predominantly a hexameric structure (Monroe & Hill, 2016). For some AAA ATPases the processs of hexamerization was found to be concentration dependent *in vitro*, showing most of the proteins being present in a monomeric or dimeric state at low concentrations (Monroe & Hill, 2016). Further, substrate dependent recruitment of the monomers could lead to a local increase in concentration and thus favors oligomer formation (Monroe & Hill, 2016).

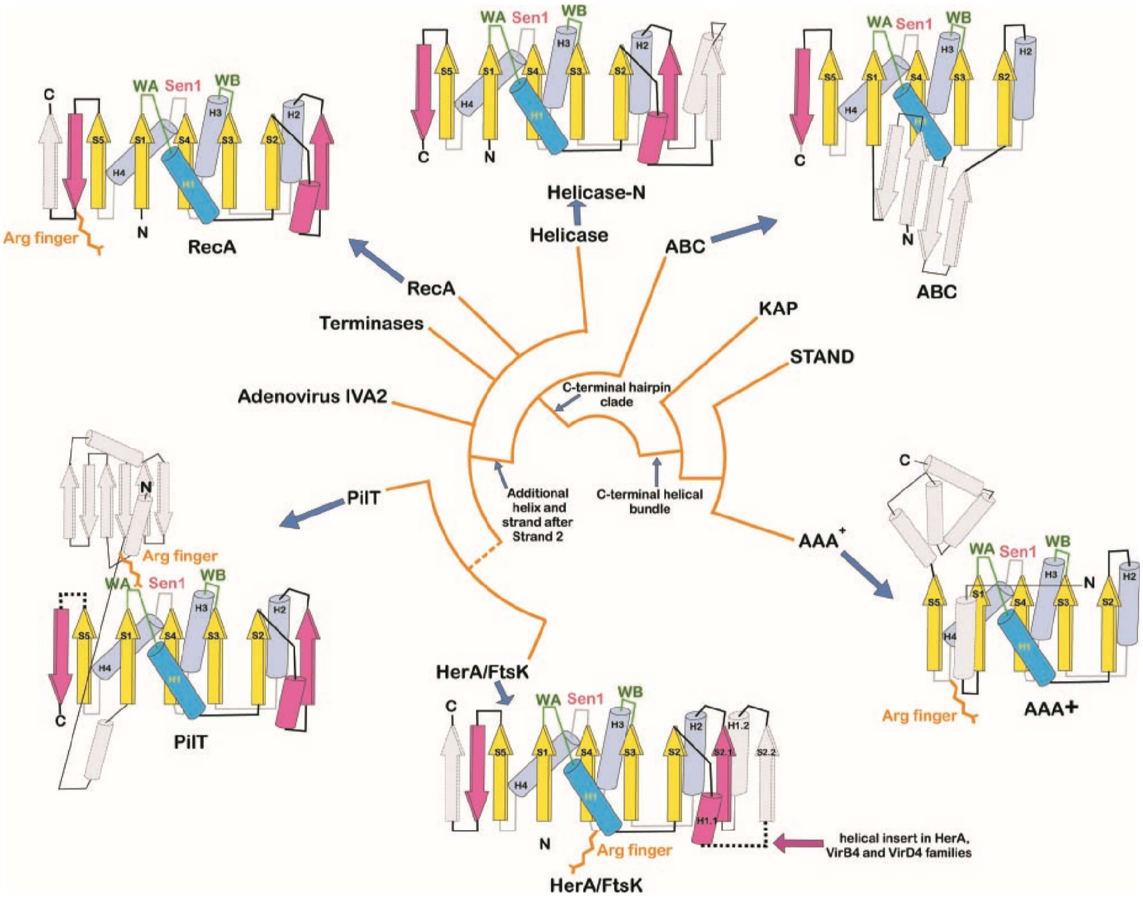

Figure 5: Topology diagram showing the relationship between ASCE ATPases. Numbered strands and helices are conserved across the group of ASCE ATPases, colored yellow and blue, respectively. Secondary structural elements, which are not cnserved between the members of the ASCE family are colored in white. Conserved motifs are indicated: Walker A (WA); Walker B (WB), Sensor-1 (Sen1). Insertions in the topology diagram are displayed by a dotted line. Figure taken from Iyer *et al.*, 2004.

The process of oligomerization follows different mechanisms, dependent on the single AAA ATPases. The active sites of the ATPases are typically located at the interfaces of the individual subunits (Sysoeva, 2017). Another difference between AAA ATPases is the way these proteins bind their substrates. On the one hand, substrates are known to bind close to the ring pore, as e.g. papillomavirus replication helicase E1 and the unfoldase ClpX, whereas proteins like dynein and IstB show lateral substrate binding (Sysoeva, 2017). Further, AAA+ ATPases differ with respect to their multimeric assembly. The oligomerization state ranges from pentamers to octamers in the family of AAA+ ATPase motors including opened and closed conformations (Sysoeva, 2017). The secondary arrangement varies further from helical filaments (DnaA) over single and double ring structures identified by crystallography and electron microscopy (Sysoeva, 2017). Variable assemblies were also found in dependence of the substrates, e.g. RuvB was found to assemble into hexamers in the presence of its substrate whereas it forms a heptamer in its absence (Sysoeva, 2017). Further, simultaneous populations of either hexamers or heptamers were found for several different AAA+ ATPases like NtrC1, HsIU and T7 helicase (Sysoeva, 2017). As another example, the NLR-related apoptosis inducing protein CED-4 assembles into a closed octameric ring structure (Qi *et al.*, 2010). Moreover, multiple ATPase domains are either provided on the same or on different polypeptide chains (Wendler *et al.*, 2012; Sysoeva, 2017). For proteins that harbor two ATPase modules on one polypeptide chain, like NSF and p97, it was shown that these proteins assemble into a two-tiered ring.

The mechanistic cycle of ATP hydrolysis comes at hand with the assembly into large oligomeric structures of the AAA+ motor proteins (Figure 6). Several different mechanisms of transfer from an inactive to an active state upon ATP hydrolysis are proposed, like a symmetrical, rotary, sequential and stochastic activation model. The symmetrical mechanism was proposed for proteins like F1-ATPase that forms a hexameric ring, with three different substates of the protein during ATP hydrolysis, that lead to a rotating hydrolysis mechanism (Sysoeva, 2017). Sequential or rotary hydrolysis mechanisms were suggested for proteins like HsIU, which shows different populations. Here the ATP hydrolysis is synchronized for only two opposite subunits at the same time. Furthermore, it was shown, that some AAA+ motors hydrolyze ATP in a more random than directed way supporting a stochastic mechanism (Sysoeva, 2017).

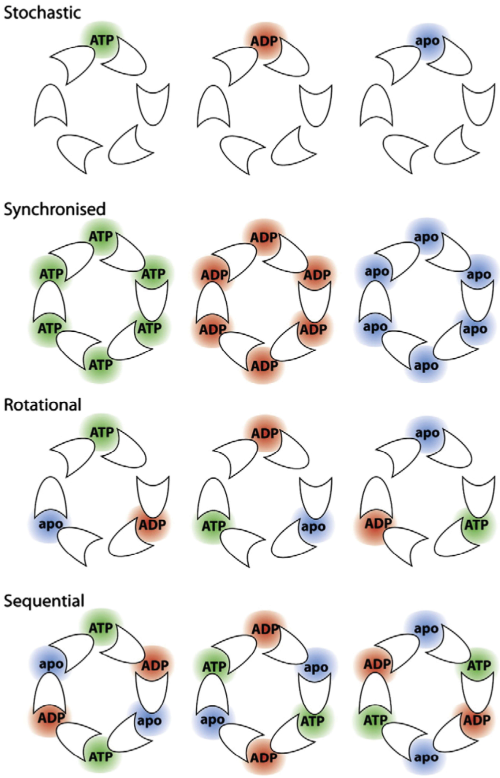

Figure 6: ATP hydrolysis cycle in hexameric ATPases. The stochastic model suggests an independent function of each protomer, whereas in the sychronized model, the protomers are supplemented with the same nucleotides simultaneously. Three pairs of dimers in different nucleotide states form the functional unit in the rotational model. In the sequential model, each protomer is supplemented by a nucleotide, whereas opposite protomers are occupied by the same nucleotide. Figure taken from Joly *et al.*, 2012.

In its ATPase domain, the family of ASCE ATPases contains a conserved αβα fold. Herein, five parallel β-strands build the central element, arranged in a distinct order (N-term-5-1-4-3-2-C-term) (Ogura & Wilkinson, 2001; Hanson & Whiteheart, 2005; Wendler *et al.*, 2012). The β-strands are interconnected by loops and alpha helices, harboring the main ATPase elements like the Walker A and Walker B motif, respectively. Among the subfamilies of ASCE ATPases, the core fold is extended by individual C-terminal extensions, like an additional helical bundle in AAA+ ATPases, the C domain or additional β-strands in RecA-like ATPases (Ammelburg *et al.*, 2006; Erzberger & Berger, 2006; Sysoeva, 2017). The C domain was the main feature identified to group STAND ATPases, including the NLRs, into the family of AAA+ ATPases (Ammelburg *et al.*, 2006). A main difference to other ATPases is the lack of additional β-strands N-terminal to the β2 strand of the ATP core (Hanson & Whiteheart, 2005).

The Walker A motif (GxxGxGK[T/S]), located at the tip of β1, interacts with the phosphate group of the nucleotide, whereas the Walker B motif (hhhhDE), which is located at the tip of β3, is responsible for nucleotide hydrolysis (Figure 7) (Wendler *et al.*, 2012; Sysoeva, 2017). Both motifs are known to be involved in ATP binding and hydrolysis (Walker *et al.*, 1982). Here, the Mg^{2+} ion is coordinated by the aspartate, whereas the glutamate is often thought to serve as the catalytic base for hydrolysis, by coordinating the water molecule (Hanson & Whiteheart, 2005; Sysoeva, 2017). Mutations of the lysine located in the Walker A motif typically abolished nucleotide binding and protein activity as well as dissociation of the oligomeric complex (Hanson & Whiteheart, 2005; Wendler *et al.*, 2012).

Mutations of the glutamate residue in the Walker B motif do not influence nucleotide binding, but impair nucleotide hydrolysis (Hanson & Whiteheart, 2005; Wendler *et al.*, 2012). It was stated, that the mutation of glutamic acid to glutamine in the Walker B motif leads to an impaired substrate release (substrate trap) (Hanson & Whiteheart, 2005). Some motifs have been indentified, to be involved in ATP hydrolysis, but are not identified in any of the AAA+ ATPases.

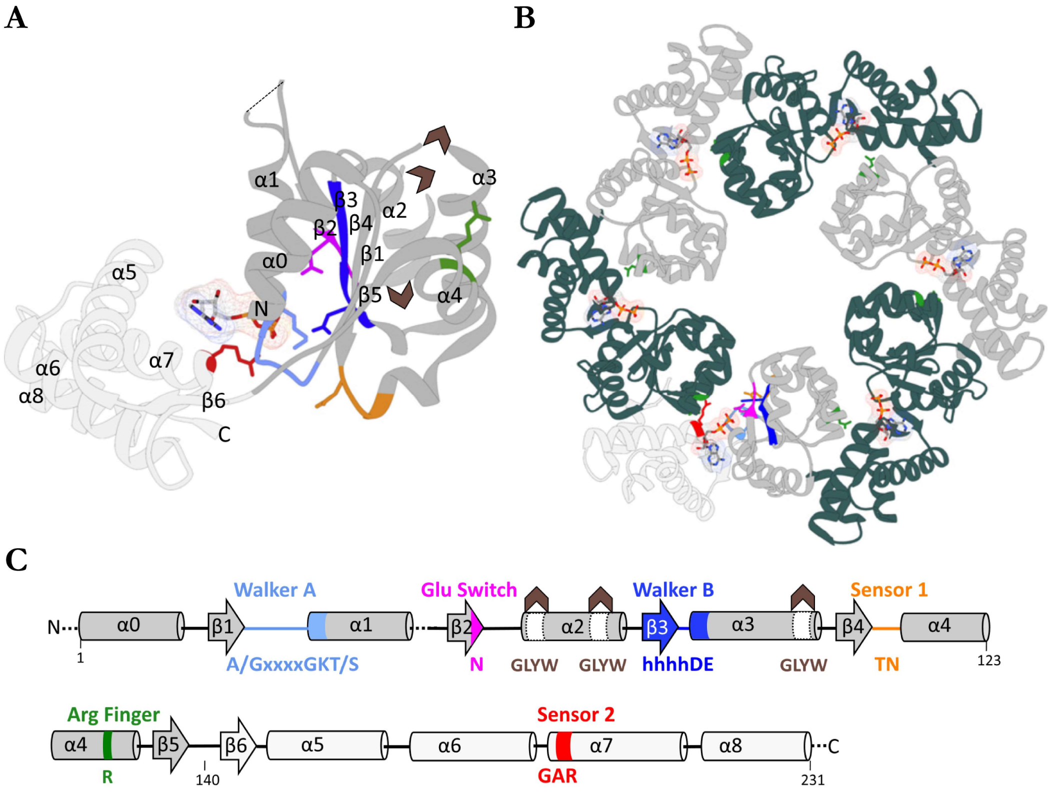

Figure 7: Structural arrangement of hexameric AAA+ ATPase. A: ATPase module **B:** Structural assembly of toLon bound to ADP (PDB ID: 3K1J), showing hexameric assembly and involved interface residues. Alternating protomers are alternatingly coloured. **C:** Consensus sequence of AAA+ ATPase module. Conserved residues are indicated. Figure taken from Wendler *et al.*, 2012.

The second region of homology (SRH), ranging from β4, α4 until the beginning of β5, harbors two distinct elements, the sensor-1 motif and the arginine-finger (R-finger) (Hanson & Whiteheart, 2005). The R-finger, only one conserved polar residue for AAA+ ATPases, which is located on α4, is involved in the formation of the symmetric hexamer by interaction with the ATPase subunit of the neighboring molecule (Iyer *et al.*, 2004; Hanson & Whiteheart, 2005; Ammelburg *et al.*, 2006; Zhang & Wigley, 2008; Sysoeva, 2017). It is thought, that it coordinates the leaving phosphate group during ATP hydrolysis (Sysoeva, 2017). However, the R-finger is not identified in any of the members of the STAND family of AAA+ ATPases.

The γ-phosphate of ATP is sensed by an additional crucial amino acid, the sensor-1 motif (Ammelburg *et al.*, 2006). Typically, it is located at the C-terminal tip of the β-strand 4 (Erzberger & Berger, 2006). This motif is further termed BoxVII, second region of homology (SRH) and SRC motif (Hanson & Whiteheart, 2005; Erzberger & Berger, 2006). Mutation of this residue to alanine was found to impair ATP hydrolysis (Hanson & Whiteheart, 2005). For some ASCE ATPases it was shown that the sensor-1 residue is involved in the formation of hydrogen bonds, that position the attacking water molecule in relation to the γ-phosphate (Wendler *et al.*, 2012). Another motif present in AAA+ ATPases is the sensor-2 arginine located at the tip of helix α7 and it was found to directly interact with the γ-phosphate of the bound ATP (Iyer *et al.*, 2004; Hanson & Whiteheart, 2005). Mutational analysis revealed, that sensor-2 is involved in ATP hydrolysis (HsIU, CLpX, RuvB) and complex formation, by contacting the ATP core of the adjacent ATPase protomer (Wendler *et al.*, 2012). The SRH region as well as the sensor-2/α7 helix are thought to build the interface between two subunits in the hexameric assembly (Hanson & Whiteheart, 2005).

The Glutamate switch is another conserved motif found in AAA+ ATPases (Zhang & Wigley, 2008). Substantial movement of the glutamate side-chain located in the Walker B motif is related to an "on and off" switch of the ATPase identified by investigation of the AAA+ATPase PspF. Here, in an ATP bound state, the glutamate is hold in place by a hydrogen bond formed with an asparagine residue located on β2 (Zhang & Wigley, 2008). Hence, upon ATP binding, the ATPase is switched off, as the glutamate changed to a position where it is no longer able to activate the incoming water molecule (Zhang & Wigley, 2008). The asparagine, which is responsible for the hydrogen bond with the glutamate residue in PspF, is not strictly conserved in the family of AAA+ ATPases, thus can be exchanged by serine, threonine or lysine found on the β2 strand of other AAA+ ATPases (Zhang & Wigley, 2008). The glutamate switch can also fulfil the opposite function as e.g. in the case of HsIU, where it is found in a locked state, when ADP is bound, but is free to bind the incoming water molecule in the ATP bound state (Zhang & Wigley, 2008). Also the binding of substrates seems to have an impact on the glutamate switch state (Zhang & Wigley, 2008). Sensor-1, Sensor-2 as well as the Glutamate-switch are not conserved among all AAA+ ATPases.

The family of STAND AAA+ ATPases, including NLRP3, contains some more distinct motifs and conserved residues besides the already mentioned ones (Leipe *et al.*, 2004). Similar to the AAA+ ATPase family of the ASCE division, the STAND family also contains five parallel β-strands in the central NTPase domain and a helix motif, N-terminally of the central core, typically consisting of the sequence GR[DE] (Leipe *et al.*, 2004). The C domain, a helical bundle, located C-terminally of the ATP binding site contains a conserved GxP motif. Moreover, N-terminally to the Walker A motif another conserved motif is detectable, the hhGRExE motif, which is located on the helix N-terminally to β1 (Leipe *et al.*, 2004). Besides these similarities, the STAND family strongly differs to the family of AAA+ ATPases as no Arginine-finger is found in these proteins. Typically, the Arginine-finger mediates the oligomerization and ring-formation by acting in trans on the neighboring molecule. Although several STAND family members were found to oligomerize, the residues involved in signal transduction from one protein to the next have to be elucidated as the Arginine-finger is missing in these molecules.
Until now, the activation mechanism of the NLRP3 inflammasome was shown to rely on ATP as well as dATP binding, whereas its ATP-hydrolysis activity was not yet proven to be a prerequisite for inflammasome formation (Duncan *et al.*, 2007).

7 Materials and Methods

7.1 Materials

7.1.1 Reagents, chemicals and kits

The reagents and materials used in this study, were purchased from the following companies: Abcam (Cambridge, UK), Agilent Technologies, Inc. (Santa Clara, USA), AppliChem (Darmstadt, Germany), BioRad (München, Germany), Carl Roth GmbH (Karlsruhe, Germany), Cayman Chemicals (Ann Arbor, USA), Eppendorf (Hamburg, Germany), Fermentas (St. Leon-Rot, Germany), GE-Healthcare (München, Germany), Invitrogen (Karlsruhe, Germany), Merck (Darmstadt, Germany), Roche (Basel, Switzerland), Millipore (Schwalbach, Germany), MWG Biotech (Ebersberg, Germany), New England Biolabs (Frankfurt, Germany), Novagen, Merck (Darmstadt, Germany), Qiagen (Hilden, Germany), Sarstedt (Nümbrecht, Germany), Sigma-Aldrich (München, Germany), Thermo Fisher Scientific Inc. (Waltham, USA), Waters Corporation (Milford, USA)

All solutions were prepared using Millipore filtered water or doubled-distilled water. The solutions were sterilized by autoclavation if needed and/or filtered using 0.22 µm Millipore syringe filters.

Marker / standards	Company
LMW marker	GE Healthcare, München, Germany
Page Ruler Plus Prestained protein ladder	Thermo Fisher Scientific, Waltham, USA
DNA ladder 100bp	CarlRoth, Karlsruhe, Germany
DNA ladder 1kb	CarlRoth, Karlsruhe, Germany
Gel filtration standard	Bio-Rad, München, Germany

Kits	Company
QIAquick Gel Extraction Kit	Qiagen, Hilden, Germany
QIAprep Spin Miniprep Kit	Qiagen, Hilden, Germany
PCR Purification Kit	Qiagen, Hilden, Germany
Malachite Green Phophate Assay Kit	Cayman Chemicals
Luminescence ATP detection Assay Kit	Abcam, Cambridge, UK

7.1.2 Cell culture media

Medium	Components / Company
Sf-900TM III SFM 1x	Invitrogen, Karlsruhe, Germany
LB-Medium (Lennox)	Roth, Karlsruhe, Germany
LB-Agar plates – *E.coli* DH10	100 µg/mL Ampicillin, 50 µg/mL Kanamycin, 7 µg/mL Gentamycin, 10 µg/mL Tetracyclin, 100 µg/mL X-Gal, 40 µg/mL IPTG
LB-Agar plates and medium, single differentiation	Ampicillin (100 mg/L Medium), Kanamycin (50 mg/L Medium), Gentamycin (7 mg/L Medium)

7.1.3 Devices

Devices	**Company**
Agarose gel chamber, DNA-SUB-Cell	Bio-Rad, München, Germany
Autoclave 5075 EL	Systec, Linden, Germany
Biacore T200	GE Healthcare, München, Germany
Biophotometer	Eppendorf, München, Germany
Centrifuge, Avanti J265 XP	Beckman and Coulter, Brea, California, USA
Centrifuge, Eppendorf 5810	Eppendorf, München, Germany
Centrifuge, Eppendorf 5810R	Eppendorf, München, Germany
Electroporator, Eporator	Eppendorf, München, Germany
FPLC-System Äkta Avant	GE Healthcare, München, Germany
FPLC-System Äkta micro	GE Healthcare, München, Germany
FPLC-System Äkta prime plus	GE Healthcare, München, Germany
FPLC-System Äkta Pure	GE Healthcare, München, Germany
FPLC-System Äkta Start	GE Healthcare, München, Germany
Freezer (-80°C)	Thermo Scientific, Corston, UK
HPLC system, Agilent 1260 Infinity II	Agilent, Stevens Creek, USA
Incubator Heratherm	Thermo Scientific, Waltham, USA
Incubator Innova 40	New Brunswick Scientific, Jersey, USA
Incubator Multitron pro	Infors HAT, Bottmingen, Switzerland
Incubator, Heraeus CO2 Auto zero	Heraeus Instruments, Hanau, Germany
Magnetic stirrer MR 2000	Heidolph, Schwabach, Germany
Magnetic stirrer MR 3002	Heidolph Instruments, Schwabach
Mastercycler nexus SX1	Eppendorf, München, Germany
Microbalance CPA324S	Sartorius, Göttingen, Germany
Microplate reader	Tecan Trading AG, Männedorf, Switzerland
Microscope Axiolab	Carl Zeiss, Jena, Germany
Millipore	Thermo Scientific, Corston, UK
Mini protean Tetra Cell	Bio-Rad, München, Germany
Nanodrop 2000/c UV-Spectrometer	Thermo Scientific, Wilmington, USA
Odyssey, gel documentation system	Li-Cor Biosciences, Bad Homburg, Germany
pH meter lab 850	Schott Instruments, Mainz, Germany
Sonifier Vibra cell	Sonics, Newton, USA
Sonifier W-250	Branson, Danbury, USA
Tabletop centrifuge Eppendorf 3424	Eppendorf, München, Germany
Tabletop centrifuge Eppendorf 3424 R	Eppendorf, München, Germany
Tabletop centrifuge Eppendorf 5804	Eppendorf, München, Germany
Thermomixer comfort	Eppendorf, München, Germany
Ultracentrifuge Optima Max-TL	Beckman and Coulter, Brea, California, USA
Vortexer Vortex Genie 2	Bender & Hobein, Bruchsal, Germany
Waage Sartorius BP110S	Sartorius, Göttingen, Germany
Water bath Julabo 5	Julabo, Seelbach, Germany

7.1.4 Enzymes

Enzyme	Company
Restriction endonucleases	New England Biolabs, Ipswich, USA
T4 DNA polymerase	New England Biolabs, Ipswich, USA
Q5 High Fidelity DNA polymerase	New England Biolabs, Ipswich, USA
T4 DNA Ligase	New England Biolabs, Ipswich, USA
Tev protease	UKB, Bonn (own)

7.1.5 Cells and bacterial strains

Insect cell line	Company
Sf9 insect cells (clonal isolates derived from *Spodoptera frugiperda* cell line IPLB-*Sf21*-AE)	Thermo Fisher Scientific, Waltham, USA

E.coli strain	Genotype
Top10	TOP10 F- mcrA Δ(mrr-hsdRMS-mcrBC) Φ80lacZΔM15 ΔlacX74 nupG recA1 araD139 Δ(ara-leu)7697 galE15 galK16 rpsL(StrR) endA1 nupG λ-
ß10 (NEB)	Δ(ara-leu) 7697 araD139 fhuA ΔlacX74 galK16 galE15 e14- ϕ80dlacZΔM15 recA1 relA1 endA1 nupG rpsL (StrR) rph spoT1 Δ(mrr-hsdRMS-mcrBC)
DH10 MultiBac$^{\text{Turbo}}$	F– mcrA Δ(mrr-hsdRMS-mcrBC) Φ80lacZΔM15 ΔlacX74 recA1 endA1 araD139 Δ(ara, leu)7697 galU galK λ– rpsL nupG /pMON14272 v-cath::Ampr chiA::LoxP */ pMON7124
BL21 (DE3)	F–, ompT, hsdSB(rB-, mB-), dcm, gal, λ(DE3)
XL1Gold	TetrD(mcrA)183 D(mcrCBhsdSMR-mrr)173 endA1 supE44 thi-1 recA1 gyrA96 relA1 lac The [F'proAC lacIqZDM15 Tn10 (Tetr) Amy Camr

7.1.6 Primer and Vectors

Vector description	Expression -tag	Expression species	Company
pGEX-4T1-TEV (mod.)	GST	*E.coli*	GE Healthcare, München, Germany
pET23a-his(mod)	HIS	*E.coli*	Novagen, Darmstadt, Germany
pET28a-MBP-TEV (mod.)	MBP	*E.coli*	Novagen, Darmstadt, Germany
pACEBac1-MBP-TEV (mod.)	MBP	*Sf9*	ATG Biosynthetics, Merzhausen, Germany
pACEBac1-mMBP (mod.)	mMBP	*Sf9*	Addgene, Watertown, USA

Primers are purchased from Metabion International AG**,** Planegg, Steinkirchen, Germany. Cloning of mMBP-vectors and the generation of appropriate vectors, which are compatible with the used *E.coli* and *Sf9* expression system, were generated using the mMBP-template vector pHLmMBP-6 (Bokhove *et al.*, 2016).

7.1.7 Chromatography Columns

Chromatography columns	Company
HisTrap FF	GE Healthcare, München, Germany
GSTrap FF	GE Healthcare, München, Germany
MBPTrap HP	GE Healthcare, München, Germany
Superdex 75 Increase 10/300 GL	GE Healthcare, München, Germany
HiLoad 16/600 Superdex 75 prep grade	GE Healthcare, München, Germany
Superdex 200 Increase 10/300 GL	GE Healthcare, München, Germany
HiLoad 16/600 Superdex 200 prep grade	GE Healthcare, München, Germany
Superose 6 3.2/300 GL	GE Healthcare, München, Germany
Superose 6 10/300 GL increase	GE Healthcare, München, Germany
XK 16/70 Superose 6 prep grade	GE Healthcare, München, Germany

7.1.8 Buffers

Application	**Buffer**	**Composition**
Column regeneration	GSTrap buffer	6 M Gdn-HCl
	HIStrap buffer	6 M Gdn-HCl, 200 mM acetic acid
	MBPtrap buffer	0.5 M NaOH
SDS-PAGE	Running buffer (10x)	250 mM Tris, 1.94 M glycine, 1% (w/v) SDS
	SDS sample buffer (4x)	240 mM Tris pH 6.8, 8% (w/v) SDS, 40% (v/v) glycerol, 0.04% bromphenol blue, 5% (v/v) βME
	Native gel Running buffer (10x)	Tris base (60.6 g), MOPS (104.6 g), EDTA (3.0 g), deionized H_2O ad 1000 mL
	Native gel sample buffer (5x)	Tris base (150 mg), glycerol (5.0 mL), bromphenol blue (25 mg), β-mercaptoethanol (1.0 mL), deionized H_2O ad 10 mL, pH adjusted to 6.8
	Coomassie staining solution	40% (v/v) ethanol, 10% (v/v) acetic acid, 0.1% (w/v) Coomassie Brilliant Blue R 250
	Coomassie destain solution	10% (v/v) ethanol, 5% (v/v) acetic acid
	Stacking gel buffer	0.5 M Tris pH 6.8, 0.4% (w/v) SDS
	Running gel buffer	1.5 M Tris pH 8.8, 0.4% (w/v) SDS
HPLC	Running buffer	20 mM TBA-Br pH6.5, 30 mM K_2HPO_4, 70 mM KH_2PO_4, 0.2 mM Sodiumazide 4% Acetonitrile
	Reaction buffer (10x)	200 mM HEPES pH 8.0, 1.5 M NaCl, 50 mM $MgCl_2$
TEV digestion	TEV cleavage buffer (10x)	500 mM Tris, pH 8.0 1.5 M NaCl, 5 mM EDTA
Cell harvesting	PBS	150 mM NaCl, 25 mM sodium phosphate, 2 mM EDTA, pH 8.0

7.1.8.1 SDS-PAGE composition

	12% running gel		15% running gel		18% running gel	
	4 gels	**2 gels**	**4 gels**	**2 gels**	**4 gels**	**2 gels**
H_2O	6.75 mL	3.38 mL	4.65 mL	2.33 mL	1.65 mL	825.0 µL
30% acrylamide	8.40 mL	4.20 mL	10.50 mL	5.25 mL	13.5 mL	6.75 mL
running gel buffer	5.85 mL	2.93 mL	5.85 mL	2.93 mL	5.85 mL	2.92 mL
10% SDS	235.5 µL	117.8 µL	235.5 µL	117.8 µL	235.5 µL	117.8 µL
10% APS	235.5 µL	117.8 µL	235.5 µL	117.8 µL	235.5 µL	117.8 µL
TEMED	7.05 µL	3.53 µL	7.1 µL	3.5 µL	7.1 µL	3.5 µL

	5% stacking gel	
	4 gels	**2 gels**
H_2O	3.60 mL	1.80 mL
30% acrylamide	0.90 mL	0.45 mL
stacking gel buffer	0.70 mL	0.35 mL
10% SDS	53.0 µL	26.5 µL
10% APS	53.0 µL	26.5 µL
TEMED	5.3 µL	2.7 µL

7.1.8.2 Buffers for protein purification

Application	Buffer	Composition
MBP-trap (NLRP3)	Lysis buffer	20 mM Tris pH 8.0, 150 mM NaCl, 5 mM ßME
	Elution buffer	20 mM Tris pH 8.0, 150 mM NaCl, 10 mM maltose, 5 mM ßME
GSTrap (NLRP3-PYD)	Lysis buffer	50 mM HEPES pH 7.5, 300 mM NaCl, 5 mM ßME
	Wash buffer	20 mM HEPES pH 7.5, 1 M NaCl, 5 mM ßME
	Elution buffer	20 mM HEPES pH 7.5, 300 mM NaCl, 10 mM GSH, 5 mM ßME

Application	Buffer	Composition
ASC-mCherry$_{His}$ purification	Lysis buffer	20 mM Tris pH 8.0, 500 mM NaCl, 5 mM Imidazole
	Resuspension buffer	20 mM Tris pH 8.0, 500 mM NaCl, 5 mM Imidazole, 2 M Gdn-HCl
	Wash buffer	20 mM Tris pH 8.0, 500 mM NaCl, 20 mM Imidazole
	Elution buffer	20 mM Tris pH 8.0, 500 mM NaCl, 200 mM Imidazole
	Dialysis buffer I	20mM Tris pH 8.0, 500 mM NaCl
	Dialysis buffer II	20mM Tris pH 8.0, 300 mM NaCl
VHH purification	TES buffer (1x)	200 mM Tris pH 8.0, 0.65 mM EDTA, 0.5 M sucrose
	Wash buffer	50 mM Tris pH 7.5, 150 mM NaCl, 10 mM imidazole
	Elution buffer	50 mM Tris pH 7.5, 150 mM NaCl, 500 mM imidazole
Size-exclusion chromatography	Gel filtration (PYD)	20 mM HEPES pH 7.5, 150 mM NaCl, 1 mM TCEP
	Gel filtration I	20 mM HEPES pH 8.0, 150 mM NaCl, 1 mM TCEP
	Gel filtration II	20 mM TCEP pH 7.4, 140 mM KCl, 10 mM NaCl, 1 mM TCEP
	Gel filtration III	20 mM HEPES pH 8.0, 150 mM NaCl, 3 mM $MgCl_2$, 1 mM TCEP

All buffers were prepared using either MilliPore filtered H_2O or ddH_2O.

7.1.9 Nucleotides

Nucleotide	Company
ATP, ADP, AMP	Jena Bioscience, Jena, Germany
AppNHp, ApNHpp	Jena Bioscience, Jena, Germany
ApCpp	Jena Bioscience, Jena, Germany
ADPβS	Jena Bioscience, Jena, Germany
Ap4A, Ap5A	Jena Bioscience, Jena, Germany
ATP, CTP, GTP, TTP (NTP Bundle)	Jena Bioscience, Jena, Germany
dNTPs	Roche, Mannheim, Germany

The nucleotides were purchased in HPLC grade (purity: ≥95%).

7.2 Molecular genetics

7.2.1 Polymerase chain reaction

The polymerase chain reaction (PCR) is applied for the amplification of double stranded DNA fragments from a template. This method is based on a 3-step mechanism, starting with a primary denaturation step at 95-98°C to separate the double stranded DNA. In a second step, complementary oligonucleotides (20-50 bp), flanking the region to be amplified, anneal to the template strands at temperatures ranging from 50-72°C. The annealing temperature is calculated according to the lowest melting temperature (T_m), matching both primers. In a final elongation step carried out at 72°C, the heat-stable polymerase extends the oligonucleotide primers complementary to the template strand in 5' to 3' direction. Numerous replications of the PCR cycle thus lead to the amplification of the DNA region of interest. The primer sequences are typically equipped with restriction endonuclease recognition sites to facilitate directional cloning.

The PCR reactions were carried out using Q5 High-Fidelity DNA Polymerase (New England Biolabs, Frankfurt, Germany) according to the manufacturer's protocol.

Table 2: Preparation of PCR reaction

Component	**Final concentration**
reaction buffer (5x)	1x
dNTPs	200 µM
forward primer	0.6 µM
reverse primer	0.6 µM
template DNA	100-500 ng
Q5 DNA polymerase	0.02 U/µL
Q5 High GC enhancer	1x
H_2O	ad 50 µL

The PCR reaction was carried out in a thermocycler (Eppendorf, Hamburg, Germany), using the standard PCR program shown in Table 3.

Table 3: Standard PCR conditions

Step	Temperature	Time
initial denaturation	98°C	30 sec
25-35 cycles	98°C 50-72°C 72°C	10 sec 30 sec 30 sec /kb
final elongation	72°C	2 min
hold	8°C	

Following the PCR reaction, the amplified DNA fragment was purified using a PCR clean up kit (Qiagen, Hilden, Germany) according to the manufacturer's instructions.

7.2.2 Restriction digest

Restriction endonucleases are a class of prokaryotic enzymes, which are responsible for the recognition and sequence specific cleavage of foreign double stranded RNA and DNA. Prokaryotes distinguish foreign from self DNA, by making use of a specific methylation pattern. Type II restriction endonucleases recognize both asymmetric or symmetric, so called palindromic, DNA motifs and cleave the phosphodiester bond within these sequences. The resulting either sticky or blunt ends can be further ligated according to the cohesive ends. Double digests are used in directional cloning to define the orientation of the cleaved DNA fragment.

Restriction digests were carried out at 37°C for 1h using high fidelity restriction enzymes (New England Biolabs, Frankfurt, Germany) according to the manufacturer's protocol.

7.2.3 Agarose gel electrophoresis

The PCR reaction mixture or digested DNA fragments were loaded onto an agarose gel to estimate the size and separate it from the cleaved overhangs. In agarose gel electrophoresis, the DNA molecules are separated according to their negative charge and the molecule's size as well as their secondary structure. Applied to an electric field, small DNA molecules migrate farthest when loaded onto an agarose gel, while larger fragments are retained.

The DNA mixtures were mixed with 6x loading dye and separated on a 1% agarose gel supplemented with 1:20,000 PeqGreen (VWR International, Vienna, Austria) in 1x TBE buffer. Electrophoresis was performed at constant voltage (120V) for 30-60 min. To determine the relative DNA fragment size, a standard (100 bp or 1 kb DNA ladder) was added (CarlRoth, Karlsruhe, Germany). The agarose gel was analysed using a UV-lamp or blue led-light to visualize the DNA intercalating agent PeqGreen.

Following agarose gel electrophoresis, the band representing the separated DNA fragment of interest was cut out and further purified using a gel extraction kit (Qiagen, Hilden, Germany) according to the manufacturer's instructions. The concentration of the purified DNA fragment was determined at 260 nm using a NanoDrop 2000/c (Thermo Fisher Scientific Inc. (Waltham, USA).

7.2.4 Ligation of DNA fragments

The T4 DNA ligase from T4 bacteriophage origin catalyses the formation of a phosphodiester bond between a 3'-hydroxyl group and a 5'-phosphate group under consumption of ATP. The T4 DNA ligase is used to ligate digested DNA fragments into a vector pretreated with equivalent restriction enzymes. The amount of insert DNA used for the ligation mixture was calculated according to the following equation, assuming a 3:1 ratio of insert to vector.

Equation 1: Calculation of ligation mixture

$$\frac{(50\, ng_{vector} \times kb_{insert})}{kb_{vector}} \times \frac{3}{1} = ng_{\ insert}$$

Typically, the ligation was performed over night at RT, using T4 DNA ligase (New England Biolabs, Frankfurt, Germany), according to the manufacturer's protocol.

7.2.5 Transformation of *E.coli* cells and plasmid amplification

Chemical competent *E.coli* cells were transformed with DNA-plasmids using either heat-shock or electroporation. Either NEBß10, XL1gold, Top10, DH10, DH5α cells were used for amplification of the plasmid DNA, whereas BL21 (DE3) Rosetta cells were used for protein expression. The cells were thawn on ice and incubated with 50-200 ng of DNA for 10 min. prior to transformation. The heat shock was performed at 42°C for 60 sec in a water bath. Subsequently, the cells were incubated on ice for 5 min. Electroporation was carried out using an electroporation cuvette in an Eporator (Eppendorf, Hamburg, Germany) and subjected to a pulsation of 1.5 kV. The cells were regenerated for 60 min at 37°C, 1100 rpm in 800 μL LB-medium. Finally, the cell suspension was streaked out on prewarmed agar-plates supplemented with the corresponding antibiotics and incubated at 37°C over night.

Plasmid amplification was achieved by transfer of single colonies in 4 mL LB-medium supplemented with the appropriate antibiotic, incubated over night at 37°C at 150 rpm. The plasmid DNA was extracted using a plasmid isolation kit (Qiagen, Hilden, Germany) according to the manufacturer's recommendations. The ligation efficiency was analysed by a restriction digest using appropriate restriction endonucleases and subsequently administered to an agarose gel. Reaction mixtures showing bands at the expected height were sent for Sanger sequencing at GATC Biotech AG, Konstanz, Germany.

7.2.6 Purification of recombinant bacmid-DNA

The baculovirus containing pACEBac1 acceptor vector carries a late polyhedrin baculoviral promotor and is equipped with a Tn7 transposition acceptor site (mini-attTn7). Transformation was carried out into *E.coli* DH10 MultiBac$^{\text{Turbo}}$ cells, harbouring the corresponding Tn7 transposase and the recipient baculovirus, thus enable the integration of the pACEBac1 vector into the recipient baculovirus. The Tn7 transposition site is located on a lacZα peptide, which is disrupted upon successful transposition allowing for blue/white screening.

The plasmid DNA ligated into a pACEBac1 vector, either modified to allow GST-tag or MBP-tag fusion protein expression, was transformed in *E.coli* DH10MultiBac$^{\text{Turbo}}$ cells and plated on agar plates supplemented with 100 μg/mL Ampicillin, 50 μg/mL Kanamycin, 7 μg/mL Gentamycin, 10 μg/mL Tetracyclin, 100 μg/mL X-Gal and 40 μg/mL IPTG and incubated for 24-48 h at 37°C.

Single white colonies were used to inoculate 4 mL of LB-medium supplemented with Ampicillin (100 µg/mL), Kanamycin (50 µg/mL), Gentamycin (7 µg/mL) und Tetracyclin (10 µg/mL) and further incubated for 24 h at 37°C and 150 rpm.
The recombinant bacmid DNA was used for transfection of *Sf9* insect cells to generate the initial virus stock V_0. Transformed *E.coli* DH10 cells were pelleted by centrifugation at 4,000xg for 10 min and subsequently subjected to alkaline lysis. Lysis was performed using a standard plasmid Miniprep Kit, according to the manufacturer's instructions, until the plasmid DNA is supposed to be administered to a miniprep column. Instead, the supernatant was precipitated using 800 µL of ice-cold isopropanol and centrifuged for 1 h at 15,000xg at 4°C. The resulting pellet was washed twice with ice-cold 70% ethanol for 10 min at 15,000xg at 4°C. The precipitated bacmid DNA pellet was air-dried and resuspended in 20 µL of sterile H_2O.

7.2.7 Insect cell culture

The insect cell lines *Sf9* and *Sf21* are typically used for transfection and amplification of recombinant baculovirus. These cells originate from the pupal ovarian tissue of the fall army worm, *Spodoptera frugiperda* and more specifically, from the cell line PLBSF-21. A single isolated clone of the cell line IPLB*SF21*-AE (*Sf21*) was further used to generate the insect cell line *Sf9*.

7.2.8 Continuous culture of *Sf9* insect cells

Passaging and subculturing of *Sf9* insect cells was carried out as suspension culture in *Sf*-900TM III SFM medium (Thermo Fisher Scientific Inc., Waltham, USA) at 27°C and 80 rpm, lacking antibiotics. The cell density and viability were continuously monitored using an automated cell counter EVE (VWR International, Vienna, Austria) and maintained at 0.3-3.0x10^6 cells/mL.

7.2.9 Transfection of *Sf9* insect cells

The recombinant bacmid DNA was transfected into *Sf9* insect cells using the transfection reagent Cellfectin (Thermo Fisher Scientific Inc., Waltham, USA). Cellfectin consists of cationic lipids, present in a unilamellar liposomal structure, which interacts with the DNA's phosphate backbone via its positive surface charge when dissolved in water.

Thus, the endocytotic uptake of the negatively charged DNA is facilitated due to the interaction with positively charged liposomes. For transfection of the isolated bacmid DNA, 2 mL of *Sf9* cells, grown to a cell density of 0.35x10^6 cells/mL, was plated onto a 6-well plate and incubated at 27°C for 1h. Under sterile conditions, 8 µL of the Cellfectin reagent as well as 10 µL of the isolated bacmid DNA solution were mixed with 100 µL of Sf-900TM III SFM medium (Thermo Fisher Scientific Inc., Waltham, USA) each, combined and incubated for 30 min at RT. The suspension was added dropwise to the plated *Sf9* cells and incubated at 27°C. After 3-5 h, the medium was exchanged, and the cells were incubated for 72 h at 27°C. The supernatant, which contained the initial virus stock V_0, was filtered using a 0.22 µm filter and stored at 4°C.

7.2.10 Virus amplification

For amplification of the baculovirus, 50 mL of *Sf9* cells, grown to a cell density of 0.6x10^6 cells/mL, were supplemented with the initial virus stock V_0. The cell suspension was incubated at 27°C at 80 rpm for 96 h. Cells were harvested by centrifugation at 500xg for 20 min and the supernatant, containing the amplified virus V_1, was filtered using a 0.22 µm filter and stored at 4°C. Further amplification of the recombinant baculovirus was achieved by inoculation of 200 mL of *Sf9* cell suspension, grown to a cell density of 1.0x10^6 cells/mL, with 3 mL of the V_1 virus stock. The cells were again cultured for 96 h under standard conditions and harvested by centrifugation at 2000 rpm for 20 min. The supernatant containing the amplified baculovirus stock V_2 was filtered using a 0.22 µm filter and stored at 4°C.

7.3 Protein expression, purification and characterization

7.3.1 Protein expression in *E.coli* cells

The protein expression constructs were transformed in *E.coli* BL21 (DE3) Rosetta cells. A preculture was generated by inoculating 100-200 mL LB-medium provided with the appropriate antibiotic with single colonies, followed by an incubation over night at 37°C and 150 rpm. Subsequently, the preculture was used to inoculate a large-scale expression of 1-6 L of LB-medium to OD_{600}=0.1, again supplemented with the required antibiotics.

The cells were incubated at 37°C and 110 rpm until an OD_{600} of 0.7-0.9 was reached and subsequently supplemented with 0.3-1.0 mM isopropyl-1-thio-β-D-galactopyranoside (IPTG), for the induction of protein expression. The cultures were incubated at 20°C for 16-20 h. The bacteria were harvested by centrifugation at 4,000xg for 20 min. The cells pellets were washed with pre-chilled PBS and again administered to centrifugation at 4,000xg for 20 min. Finally, the cell pellets were frozen in liquid nitrogen and stored at -20°C.

7.3.2 Protein expression in *Sf9* insect cells

The *Sf9* insect cells were grown in suspension culture to a cell density of $1.5x10^6$cells/mL, supplemented with 4% Virus V_2 and incubated for further 72 h at 27°C at 80 rpm. Subsequently, the cells were harvested by centrifugation at 1,000xg for 15 min at 10°C and the cell pellets were washed with pre-chilled PBS. The cells were again centrifuged at 1,000xg for 15 min at 4°C, frozen in liquid nitrogen and stored at -20°C.

7.3.3 Cell lysis

The cell pellets generated by protein expression in *E.coli* or *Sf9* cells, were resuspended in lysisbuffer supplemented with a spatula tip of DNase and Lysozyme under constant stirring at 4°C. A cell pellet originating from a cell suspension of 1-1.5 L was lysed in 40 mL of lysis buffer. The cells were lysed on ice by sonication using a Sonifier W-250 (Branson, Danbury, USA) at an amplitude of 40% for 4 min, 5 sec on/off. The lysate was centrifuged to separate the soluble fraction from the insoluble particles and the cell membrane fraction at 25,000 rpm for 30-60 min at 10°C. The supernatant was filtered through a 0.45 μm filter to further clarify the lysate prior to administration to an affinity column.

7.3.4 Protein purification from inclusion bodies

Overexpression of recombinant protein in *E.coli* cells can lead to the accumulation of inactive protein in inclusion bodies. There are several reasons which promote the formation of inclusion bodies, like a high copy number of the gene of interest, a strong promoter system or a high inducer concentration, as well as the lack of eukaryotic chaperones and post-translational modifications. Partly folded or misfolded proteins tend to aggregate and due to an imbalance in the amount of soluble to insoluble protein, inclusion bodies are formed. In order to isolate protein from inclusion bodies, the inclusion body fraction is isolated, denatured and refolded, to gain soluble protein from the aggregated fraction. Inclusion body purification was performed for the recombinant proteins ASC-mCherry. Initially, the harvested cell pellets were lysed according to the standard lysis protocol, described in 7.3.2. . Subsequently, the cell pellet including ASC-mCherry was lysed for 30-60 min at 4°C in buffers including the denaturing agent guanidine hydrochloride (GdnHCl) to dissolve the inclusion bodies containing the aggregated protein. The buffers used for protein purification are shown 7.1.8.2. The protein solution was centrifuged at 25,000 rpm at 10°C for 1 h. The ASC-mCherry protein was dialysed twice in order to reduce the amount of imidazole and NaCl to facilitate fibril formation.

7.3.5 Protein dialysis

Protein dialysis was carried out to perform a buffer exchange using the regenerated cellulose Spectra/Por dialysis membranes (Carl Roth GmbH, Karlsruhe, Germany) with an exchange limit of 3,000 Da or 14,000 Da, respectively. The appropriate dialysis membranes were boiled twice in H_2O, prior to filling the protein solution into the membranes. The dialysis membranes were sealed and immersed in 100-200 fold excess of a buffer suitable for affinity purification. The proteins were dialysed for 16-24 h at 4°C under constant stirring. Finally, the protein solution was centrifuged at 25,000 rpm at 10°C for 15 min and filtered trough a 45 µm filter, following the administration to an affinity purification column.

7.3.6 Affinity purification

Affinity purification is a method to extract proteins and macromolecules from crude extracts. The protein of interest is in most cases fused to a specific tag like a poly-histidine-(His_6), Glutathione-S-Transferase- (GST-), or a maltose-binding-protein- (MBP-) tag, which is interacting specifically with the stationary phase of the chromatography column. This strategy allows for separation of a protein of interest from non-tagged proteins. The non-covalent interaction between the tag and the stationary phase is detached in an elution step, that includes chemicals or proteins to compete for the binding on the stationary phase.

7.3.6.1 Immobilized metal affinity chromatography (IMAC)

A widely used method for the purification of polyhistidine affinity-tagged proteins is Immobilized Metal Affinity Chromatography (IMAC). Chelators like nitrilotriacetic acid (NTA) are coupled to an agarose-resin and loaded with divalent transition metal ions (Co^{2+}, Ni^{2+}, Cu^{2+}, Zn^{2+}) to prepare an appropriate stationary phase. The polyhistidine affinity-tag is used, as directly, coordination bonds are formed between the electron donor groups on the histidine imidazole ring and the transition metal ion. Elution of the tagged protein from the Ni^{2+}-NTA-resin is achieved by competition with the reagent imidazole.

The cell lysate including the N-terminally His_6-tagged proteins of interest, was loaded onto a Histrap FF crude column (GE Healthcare, München, Germany), previously equilibrated with the corresponding lysisbuffer including 5 mM imidazole to lower unspecific interactions with the Ni^{2+}-NTA-resin. After protein loading, the chromatography column was washed with at least 5 column volumes (CV) of washbuffer including 20 mM of imidazole, followed by elution of the protein of interest in a buffer containing 200 mM imidazole. Subsequently the proteins were either subjected to further purification methods like size-exclusion chromatography or dialysed. All buffers used are shown in 7.1.8.2.

7.3.6.2 Maltose binding protein (MBP) purification

Maltose binding protein (MBP) is a commonly used tag to purify proteins, as it greatly enhances the solubility of the fusion-protein in aqueous solution, but is comparatively big in size with about 42 kDa. Typically, the protein of interest is inserted downstream of the *E.coli malE* gene, which encodes for periplasmic MBP, resulting in a MBP-fusion protein.

MBP is an *E.coli* host protein which belongs to the maltose system, responsible for the uptake and metabolism of maltodextrins. Due to their specific interaction with maltodextrins, MBP-tagged proteins can be easily purified using a sepharose resin coupled to dextrin or amylose. Besides the MBP-tag also a mutant MBP-tag can be used which is optimized for crystallographic approaches (Bokhove *et al.*, 2016).

The cell lysate containing the MBP-tagged protein of interest was loaded onto a MBPtrap column (GE Healthcare, München, Germany), pre-equilibrated with the corresponding lysis buffer. The column was washed with at least 6 CV of lysis buffer and the protein was subsequently eluted in a buffer containing 10 mM maltose, which directly binds to the MBP-tag, thus competing for the interaction sites used for binding to the dextrin column. The proteins were subjected to further purification using size-exclusion chromatography. All buffers used are shown in 7.1.8.2.

7.3.6.3 Glutathione S-transferase (GST) purification

Glutathione S-transferases are a class of enzymes which harbor detoxification and toxification ability. This is achieved by promoting the formation of GS^- from GSH and subsequent conjugation to the adjacently binding hydrophobic and electrophilic compounds. Typically, the cytosolic GST is found as a dimer of two subunits. Sepharose-resins coupled to Glutathione (GSH) can be used to specifically purify GST-tagged proteins because of its high binding affinity to GSH.

The cell lysate containing the GST-tagged protein of interest was loaded onto a GSTrap FF column (GE Healthcare, München, Germany), pre-equilibrated with an appropriate lysis buffer. The column was washed with at least 6 CV of a wash buffer containing high salt, to reduce unspecific interaction with the stationary phase, followed by an additional washing step with the lysis buffer. The protein of interest was eluted in a buffer containing 10 mM GSH, to detach the protein of interest from the GSH-resin. The proteins were subjected to further purification using size-exclusion chromatography. All buffers used are shown in 7.1.8.2.

7.3.7 Protein sample concentration

Proteins purified via affinity chromatography or size-exclusion chromatography were subjected to ultrafiltration. The protein solution was centrifuged in Amicon Ultra Centrifugal filters (Sigma-Aldrich, München, Germany) with the appropriate molecular weight cut-off at 4°C according to the manufacturer's instructions.

The filter units, pre-equilibrated with the corresponding size-exclusion buffer, consist of Ultracel (Merck Millipore, Burlington, USA) regenerated cellulose membranes, which retain proteins exceeding the molecular weight cut-off inside the filter unit and let the remaining solution and small molecules pass, leading to a concentrated sample in a smaller volume. The protein solution was concentrated until the desired protein concentration or volume was reached.

7.3.8 Determination of protein concentration

Protein concentration can be determined by measuring absorbance in a spectrophotometer. The aromatic amino acids tyrosine, tryptophan, cysteine and phenylalanine show absorption at 280 nm. Furthermore, to a small extent, also disulfide bonds formed between cysteine residues contribute to the specific absorption of a protein at 280 nm. The protein concentration was continuously monitored during purification using a NanoDrop 2000/c Spectrophotometer (Thermo Fisher Scientific Inc., Waltham, USA). Dependent on the amino acid composition of each protein, the specific extinction coefficient was determined using ProtParam (Wilkins *et al.*, 1999). An extinction coefficient describes the weighed sum of the molar absorptivities of the amino acids tryptophan (W), tyrosine (Y), cysteine (C) and phenylalanine (F) at 280 nm.

Equation 2: Calculation of molar absorption coefficient

$$\varepsilon = (n_W \times 5500\ \mathrm{M^{-1}\ cm^{-1}}) + (n_Y \times 1490\ \mathrm{M^{-1}\ cm^{-1}}) + (n_C \times 125\ \mathrm{M^{-1}\ cm^{-1}})$$

ε = molar extinction coefficient at 280 nm in ($\mathrm{M^{-1}cm^{-1}}$)
n_x = number of particular amino acid in protein

According to Lambert-Beer's law, a linear relationship is assumed between the absorption of a solution and the concentration of the absorbing species. Thus, the protein concentration can be determined by measuring the absorbance according to the following formula:

Equation 3: Lambert-Beer's law

$$c = \frac{A_{280}}{\varepsilon \times d}$$

A = absorption at 280nm,
ε = molar extinction coefficient at 280 nm in ($\mathrm{M^{-1}cm^{-1}}$),
d = path length in (cm)
c = protein concentration mol $\mathrm{L^{-1}}$

Considering the proteins molecular weight (MW), the protein concentration can be recalculated to a value in mg/mL.

7.3.9 Size-exclusion chromatography (SEC)

Size-exclusion chromatography (SEC), also called gel filtration (GF), is a chromatography technique to separate proteins according to their hydrodynamic radius. The hydrodynamic radius, more specifically Stokes-Einstein radius, describes the radius of a hard sphere, that diffuses with the same rate as the analysed molecule. Proteins of equivalent molecular weight can have different hydrodynamic radii as usually proteins are not perfectly spherical, thus the Stokes-Einstein radius is also dependent on the shape and hydration of a molecule. In SEC, the stationary phase of a chromatography column is made of a porous matrix that the macromolecules interact with and a mobile phase, composed of an aqueous buffer system. Small molecules interact with the pores of a stationary phase and are retained, whereas bigger molecules which cannot diffuse into the porous matrix elute first. Different materials and pore sizes can be chosen as stationary phase to aquire desired separation conditions. SEC is used for separation of proteins according to size and for desalting and buffer exchange approaches. The separation resolution can be influenced by several different factors like the bed material, the size of a column and protein amount as well as the flow rate. Different bed materials are available that deviate in pore size and composition. Three typical stationary phase materials are: Sephacryl, a cross-linked co-polymer of allyl dextran and N, N'-methylenebisacrylamide, the Superdex material, cross-linked agarose and dextran as well as the Superose material, which is composed of highly cross-linked beaded agarose. Typically, the particle size of these materials determines the separation range.

7.3.9.1 Preparative size-exclusion chromatography

Preparative SEC was performed as an additional purification step in using an Äkta Prime and Äkta Pure FPLC System (GE Healthcare, München, Germany). Typically, 0.5-10 mg of protein were loaded onto the column and the eluted proteins were detected at 280 nm, fractionated and subsequently analysed by SDS-PAGE. A HiLoad 16/600 Superdex 75 prep grade column was used to separate proteins of a size ranging from 3 kDa to 70 kDa. Proteins in a range from 10 kDa to 600 kDa were separated using a HiLoad 16/600 Superdex 200 prep grade and Superdex 200 Increase 10/300 GL. Large protein complexes with a size of 5 kD to 5000 kDa were separated using XK 16/70 Superose 6 prep grade and Superose 6 10/300 GL increase column. Further a Sephacryl S-400 HR column was used to separate proteins in a range of 20 kD to 8000 kDa. All columns used were supplied by GE Healthcare (München, Germany) and pursued according to the manufacturer's instructions. The buffers used are shown in 7.1.8.2. SEC performed with MBP-NLRP3 and mMBP-NLRP3 proteins, was carried out exclusively at 0.2 mL/min.

7.3.9.2 Analytical size exclusion chromatography

Analytical SEC is a technique to perform qualitative and quantitative analyses of a protein of interest and further to determine its oligomerization state. A gel filtration standard (BioRad, München, Germany) was used to estimate the molecular weight of the analyzed protein. Thus, the molecular weight of a protein can be calculated according to the elution profile of known molecular weight standards. Further, the void volume, the total geometric volume of a column and the specific elution volume of the analyte are used.

Equation 4: Calculation of molecular weight in analytical SEC

$$\frac{V_{e\,(analyte)} - V_0}{V_c - V_0} = K_{av\,(analyte)}$$

$V_{e\,(analyte)}$= elution volume of analyte [mL]
V_0 = void volume of the column [mL]
V_c = total geometric volume of the column [mL]
$K_{av\,(analyte)}$ = proportion of pores available to the analyte

The molecular weight of an analyte is determined by using a linear regression curve generated by plotting the K_{av} values of the gel filtration standards to the logarithmic values of the corresponding molecular weights. The generated calibration curve is used to calculate the molecular weight of the analyte according to the specific $K_{av\ (analyte)}$ value.
The analytical SEC columns Superose 6 3.2/300 and Superdex 75 3.2/300 using MBP-NLRP3, mMBP-LRR variants as well as nanobodies, were pursued at a flow rate of 0.3 mL/min at RT using an Äkta micro FPLC system (GE Healthcare, München, Germany), according to the manufacturer's instructions. The buffers used are shown in 7.1.8.2.
Further, analytical gel filtration was performed for the analysis of NLRP3-PYD variants. For each individual measurement, the protein samples were diluted to 100 µM in 100 µL sample volume, in the following running buffer: 20 mM Tris, pH 7.5, 150 mM NaCl and 0.5 mM TCEP. The measurements were performed using a Superdex 75 3.2/300 column (GE Healthcare, Munich, Germany) coupled to an HPLC system. The samples were eluted at RT using a flowrate of 0.5 mL/min. These measurements were performed by Dr. S. Lülf at the Max Planck Institute of Molecular Physiology in Dortmund, Germany.

7.3.10 Sodium dodecyl sulfate - polyacrylamide gel electrophoresis (SDS-PAGE)

Discontinous denaturing and reducing polyacrylamide gel electrophoresis (PAGE) is a standard separation technique for proteins based on the protein's mass. The proteins are separated in a polyacrylamide gel in an electric field, dependent on the size of a protein. Thus, smaller proteins travel faster through the gel than bigger proteins, as they are retained in the gel pores. Polyacrylamide gels are prepared by mixing acrylamide and the crosslinker N, N'-methylenediacrylamide (bis-acrylamide) in different ratios to allow for diverse pore sizes. A higher percentage of polymer results in a smaller pore size, thus the percentage of polymer decides for the separation efficiency. The polymerization of acrylamide and the crosslinker bis-acrylamide is initiated by ammonium persulfate (APS). Further tetramethylethylenediamine (TEMED) is added as a catalyst. A discontinuous electrophoresis system separates the proteins in two different gels and buffer systems, a low-percentage stacking gel and a resolving gel made of smaller pores. Thus, the loaded protein samples are alligned and concentrated prior to entering the resolving gel.

The anionic detergent SDS binds to the denatured proteins and masks its intrinsic charge, leading to a uniformly negatively charged protein. SDS binds to the protein with a constant ratio of 1.4 g of SDS to 1 g of protein. The polyacrylamide gel is mounted in SDS containing buffer, hence applying of an electric field leads to migration of the charged proteins towards the anode (Laemmli, 1970). During protein purification, the protein purity was monitored using SDS-PAGE. Electrophoresis was performed using the Mini Protean Tetra Cell system (Bio-Rad, München, Germany) at 35 mA for 40-70 min at RT. Subsequently, the gels were stained using Coomassie staining solution and destained using Coomassie destain solution. The protein markers LMW marker (GE Healthcare, München, Germany) or Page Ruler Plus Prestained protein ladder (Thermo Fisher Scientific, Waltham, USA) were loaded to estimate the protein's molecular weight. The buffers used for SDS-PAGE are shown in 0.

7.3.11 Native PAGE

Native PAGE was used to determine the oligomerization state of purified proteins. Native PAGE underlies the same electrophoresis mechanism as SDS-PAGE but differs with respect to the sample preparation and the buffer system. In native PAGE, the proteins are separated according to their native structure and mass-to-charge ratio. The protein loading dye lacks SDS but is supplemented with Coomassie G-250 or R250, which confers a net negative charge. As the proteins retain their native state, besides the charge of the protein, also the shape and the oligomeric state determine the migration behavior.

Native PAGE was performed using manually, stepwise casted gradient gels, ranging from 4-20%. Running buffer and sample buffer were prepared according to the manufacturer's instructions (GenScript USA Inc., NY, USA). Electrophoresis was performed using the Mini Protean Tetra Cell system (Bio-Rad, München, Germany) at 100 mA for 180 min at RT. Subsequently, the gels were stained using Coomassie staining solution and destained using Coomassie destain solution.

7.3.12 ATP hydrolysis measurements

Adenosine triphosphate (ATP) consists of an adenine base, which is attached to a ribose moiety by a N-glycosidic linkage. Further, a triphosphate group is attached to the 5’ carbon atom of the ribose moiety. In cells, at pH 7.0, the ATP dianion is predominantly complexed with Mg^{2+}. The hydrolysis of ATP to adenosine diphosphate (ADP) and inorganic free phosphate (P_i) is driven by a nucleophilic attack of a water molecule, thus destabilazing the terminal phosphoanhydride bond between the β- and the γ- phosphate of ATP. At pH 7.0, the hydrolysis of ATP releases a negative, free energy of -32.2 kJ mol^{-1}.

Equation 5: ATP hydrolysis reaction

$$ATP^{4-} + H_2O \rightleftharpoons ADP^{3-} + HPO_4{}^{2-} + H^+ \qquad \Delta G^0 = -32.2 kJ\, mol^{-1}$$

7.3.12.1 Malachite Green Phosphate Assay

The Malachite Green Phosphate Assay kit (Cayman Chemical, Ann Arbor, USA) was used to measure the amount of inorganic phosphate (P_i) generated during an ATP hydrolysis reaction. In the presence of sulfuric acid, the P_i is complexed with ammonium molybdate. In a second step, a malachite green phosphomolybdate complex is formed. The absorbance of the formed complex is specifically measurable at 620 nm and is further proportional to the amount of generated free inorganic phosphate. The proteins to be tested were diluted to a final concentration of 0.4 µM using a 10x buffer containing 200 mM HEPES pH 8.0, 1.5 M NaCl, 50 mM $MgCl_2$, and incubated with ATP (Jena Bioscience, Jena, Germany) for 75 min at 25°C. The protein solution was subjected to the Malachite Green Phosphate Assay kit, recalculated to a sample volume of 25 µL, according to the manufacturer’s instructions. Absorbance at 620 nm was measured using a Tecan plate reader (Tecan Trading AG, Männedorf, Switzerland). The standard curve was measured in technical duplicates and the protein samples were measured in technical triplicates. The determined values were averaged. Outliers deviating by ≥50% from average were excluded.

7.3.12.2 Luminescence ATP detection Assay kit

The Luminescence ATP detection Assay kit (Abcam, Cambridge, UK) is typically used to determine the amount of intracellular ATP. Instead of measuring the amount of intracellular ATP, the assay was used to determine the amount of ATP during an ATP hydrolysis reaction. In the presence of ATP and Mg^{2+} the firefly enzyme luciferase converts luciferin and O_2 into oxyluciferin, CO_2, AMP, PP_i and light. The amount of emitted light is directly proportional to the amount of ATP in the solution. The protein solution was incubated with ATP (Jena Bioscience, Jena, Germany) in the presence of 5 mM $MgCl_2$ for 60 min at 25°C. The protein solution was subjected to the Luminescence ATP detection Assay kit, according to the manufacturer's instructions. Deviating from that, the cell lysis step was omitted. Luminescence was measured using a Tecan plate reader (Tecan Trading AG, Männedorf, Switzerland).

7.3.12.3 Nucleotide separation using Ion-paired Reverse Phase HPLC

High-performance liquid chromatography (HPLC) is a chromatography method to separate molecules with respect to polarity. Under high pressure conditions, ranging from about 50-400 bar, analytes are separated according to their retention time. To separate polar from non-polar molecules, the stationary and mobile phase are chosen with different polarity properties. Polar molecules tend to interact with a polar stationary phase and are retained, whereas non-polar analytes interact with a non-polar mobile-phase and elute faster. Typical solvents used for a mobile phase, ordered from polar to non-polar, are: water, alcohol, acetonitrile and hexane. The stationary phase is commonly made of silica, a hydrophilic and polar material. To increase its polarity, silica is routinely modified with covalently bound alkyl chains of varying length, like cyanopropylsilyl- (CN), n-octylsilyl- (C8), and n-octadecylsilyl- (C18). Normal-Phase HPLC (NP-HPLC) typically consists of a polar stationary phase and a non-polar mobile phase. In contrast, in Reversed-Phase HPLC (RP-HPLC) the mobile phase is composed of a polar, mostly aqueous solvent and the stationary phase consists of a non-polar, e.g. C18-coupled silica material. Because of sterical hindrance between the attached alkyl chains, some silanol groups are unmodified, thus in RP-HPLC additionally, endcapping is used. Endcapping describes the binding of trimethylsilyl groups to free silanol groups, increasing its hydrophobicity. An additional modification of RP-HPLC is Ion-paired Reverse Phase HPLC (IPC). In this isocratic chromatography method, ion-pairing reagents are used as additives in the mobile phase to allow for the separation of ionic analytes like nucleotides.

Typically, the ion-pairing reagent contains a hydrophobic region to interact with the stationary phase and a charge, which is opposite to the analyte's charge, and enables binding of the analyte to the stationary phase. An ion-pairing reagent facilitates the binding of an ionic reagent to the stationary phase, as ionic analytes are usually hydrophilic and thus have very low retention times when subjected to a RP-HPLC. Nucleotides are negatively charged at a neutral pH, thus an acidic ion-pair reagent like tetrabutylammonium bromide (TBA-Br), which is positively charged under the same conditions, is used. A mixture of nucleotides consisting e.g. of ATP, ADP and AMP separates according to its charge and polarity, thus AMP elutes first, followed by ADP and ATP is retained the longest due to the highest charge at neutral pH.

IPC was used to analyse the amount of nucleotide released upon an ATP hydrolysis reaction. Nucleotides and nucleotide analogues were separated using an Chromolith Performance RP-18 endcapped 100-4.6 HPLC column and the corresponding guard cartridge Chromolith RP-18 (Merck, Darmstadt, Germany). The measurement was performed using an Agilent 1260 infinity PSS bio-inert HPLC System (Agilent Technologies, Inc., Santa Clara, USA). The mobile phase was composed of the following: 10 mM TBA-Br, 30 mM K_2HPO_4, 70 mM KH_2PO_4, 0.2 mM sodiumazide, 4% acetonitrile, pH 6.5. The proteins to be tested were diluted to a final concentration of 3 µM in a 10x buffer containing 200 mM HEPES pH 8.0, 1.5 M NaCl, 50 mM $MgCl_2$ and were incubated with nucleotide or nucleotide analogues at a concentration ranging from 0.1-200 µM at 25°C. The samples were incubated in glass vials (Waters Corporation, Milford, USA). The measurement was performed at 25°C at a flow rate of 1 mL/min and the absorbance was continuously detected at 280 nm and 254 nm, respectively. The peak borders were set manually, and the peak areas were integrated using the PSS-xxx software.

7.3.13 Mass spectrometry

In order to identify protein samples as well as post-translational modifications, like phosphorylations, the protein samples were analysed by peptide mass fingerprint. SDS-PAGE separated and Coomassie stained protein bands were cut out, under sterile conditions and subsequently sent for analysis to the Max Planck Institute for Biophysical Chemistry, Göttingen, Germany (Prof. Dr. H. Urlaub). The protein samples were subjected to a proteolytic digest using chymotrypsin and analysed in a mass-spectrometer.

7.3.14 SEC-DLS and SEC-MALS

Multi-angle light scattering (MALS) combined with size-exclusion chromatography, is used to determine the molar mass and concentration as well as the oligomeric state of protein samples in solution. This method allows for online molecular mass determination without the use of internal calibration standards (Hsieh & Wyatt, 2017). The interaction of light with matter, results in oscillating polarization, which is in turn dependent on the matter's refractive index. Subsequently, the intensity of the scattered light is directly proportional to the product of molar mass and concentration, whereas the RMS radius of the scatterer is proportional to the angular variation of scattered light (Hofmann *et al.*, 2014). In comparison, DLS is used to measure the fluctuations in scattered light, thus the hydrodynamic radius and the hydrodynamic diameter of a protein sample can be calculated. SEC-DLS and MALS was used to determine the molecular weight of MBP-NLRP3 Peak 1 and Peak 2, previously purified by SEC. An Agilent 1260 Infinity II system was coupled to a DAWN TREOS II (3 angle light scattering detector), a Wyatt QELS (online DLS at 135 °) and an Optilab T-rEX (refractive index detector) (Wyatt Technology Europe GmbH, Dernbach, Germany). Further, a Superose 6 10/300 GL increase gel filtration column (GE Healthcare) was connected to the system. As mobile phase, the following gel filtration buffer was used: 20 mM HEPES pH 7.4, 140 mM KCl, 10 mM $NaCl_2$, 1 mM TCEP. Besides the SEC-DLS measurement, the proteins were measured in a batch device DynaPro Nanostar (DLS) using a Quartz cuvette.

7.3.15 Protein stability and thermal unfolding – Prometheus

The stability of purified protein was monitored by nano Differential Scanning Fluorimetry (nanoDSF) in a Prometheus NT.48 device (NanoTemper, Munich, Germany). This technique determines the melting temperature (T_m) of a protein sample under native conditions. The change in intrinsic fluoresence, mediated by Tryptophan residues, is measured in dependence of the temperature applied to determine T_m. Varying protein concentrations of eg. MBP-NLRP3 were tested in the following buffer system, using a temperature ramp of 2°C: 20 mM HEPES, pH 8.0, 150 mM NaCl, 1 mM TCEP. For the experiments, 18.82 µM of MBP-NLRP3 Peak 2 and MBP were used, as well as 9.41 µM of MBP-NLRP3 Peak 1. The nanobodies were added in a 2-fold molar excess. Moreover, the experiments including nucleotides were carried out in the presence of 5 mM $MgCl_2$ and 100 µM ADP or ATP, respectively.

The inhibitor Ap5A was added in a concentration of 1 mM to the samples MBP and MBP-NLRP3 Peak 2 and 0.25 µM Ap5A was added to MBP-NLRP3 Peak 1. The measurement was performed in a temperature range of 20-90°C and an excitation power of 10%. The intrinsic fluorescence was measured at 330 nm and 350 nm simultaneously. For evaluation, the ratio of 350 nm to 330 nm was calculated and integrated automatically. The T_m value was determined by the maximum of the first derivative of the unfolding curve. The protein samples were mixed prior to freezing in liquid nitrogen and subsequently subjected to the nanoDSF measurement. The measurements were performed by Dr. V. Misetic in the NanoTemper laboratories in Munich, Germany.

7.3.16 Electron microscopic analysis

Negative-stain electron microscopy was used for the analysis of the tertiary structures of (MBP)-NLRP3 and NLRP3-PYD variants as well as ASC-mCherry mutants.

The respective samples were negative-stained using uranyl acetate and subjected to EM-grids. Typically, a volume of protein sample (5 µL) at a suitable concentration, individually determined for each sample, was loaded onto the carbon-coated side of an EM grid, followed by an incubation time of 1 min. The grid was washed 3-times by emersion into the respective gel filtration buffer, prior to drying the grid, using a filter paper. The sample slide was subsequently dipped twice into the uranyl acetate staining solution and incubated for 30 sec. The sample slide was again dried, by using a filter paper and an additional air-drying step. The following protein concentrations were used for EM-analysis of the NLRP3-PYD mutants: C108S (0.6 mg/mL), S5E, C108S (3.7 mg/mL), K23E, C108S (2.7 mg/mL), D50K, C108S (1.0 mg/mL) and D53K, C108S (1.0 mg/mL).

The analysis of (MBP)-NLRP3 and NLRP3-PYD variants was performed by I. Hochheiser and Dr. H. Behrmann at the Center of advanced european studies and research (caesar) in Bonn, Germany.

Furthermore, ASC-mCherry was analysed using transmission electron microscopy in the absence and presence of Aβ (1-42). For these experiments, 1 mg of lyophilized Aβ (1-42) peptide (PSL) was dissolved in 250 µl NaOH and 750 µl Tris–HCl (pH 7.6) buffer to a final concentration of 1 mg/ml. The sample was incubated for 2 h at 37 °C and afterwards centrifuged at 20,000xg for 5 min. Aβ was mixed with ASC protein and incubated in time course experiments up to 72 h. Samples of either ASC–mCherry or Aβ alone, or ASC–mCherry together with Aβ were bound to carbon-coated grids and stained with 1% uranyl acetate.

Pictures were taken at 72,000× magnification on a CM120 microscope with a 4,096 × 4,096 pixel TemCam F416 CMOS camera (TVIPS, Gauting) (Venegas *et al.*, 2017). These experiments were performed by Dr. D. Riedel (Electron Microscopy Group) at the Max Planck Institute for Biophysical Chemistry, Göttingen, Germany.

7.3.17 Crystallographic analysis

The purified protein samples were subjected to crystallographic trials using the hanging drop vapor diffusion method. Here, the protein solution is mixed in a one to one ratio with the precipitation reagent and applied upside down to a cover slip, sealing a reservoir. The reservoir is filled with the same but higher concentrated precipitation reagent. Over time, water evaporates from the hanging drop, thus increasing the protein concentration and causing precipitation and potentially leading to crystallization of the protein (McPherson & Gavira, 2014).
Crystallographic trials were performed by Dr. Kanchan Anand at the Karlsruher institute of technology, KIT, Germany.

In the following, the protein concentrations and precipitant reagents are listed:

Protein	**Precipitation reagent**
NLRP3-LRR F1 (aa 712-1036, C838S)	0.1 M Sodium acetate pH 4.6-5.5 + 25-40% PEG 400 + different sulfate ions (Li, Mg, Am, Na etc.)
mMBP-NLRP3 (3-1036) batch 2 (10.22 mg/ml)	imidazole pH 8.0 + 20-30% of medium weight PEG mix + 5% MPD + 0.1-0.2 M ammonium and lithium sulfates ions + 0.2 M $MgCl_2$
mMBP-NLRP3 (3-1036) batch 3 (13.44 mg/ml)	same as above with little differences of concentration of sulfate ions
mMBP-NLRP3 (3-1036) batch 4 (15.78 mg/ml)	0.1 M sodium acetate ph 5.5 + 20-35% MPD + 5% ethanol + 0.1 M $LiSO_4$. Also: 0.1 M Tris-HCl pH 8-8.5 + medium weight PEG mix 15-20% + 0.2 M $MgCl_2$ + 0.1 M sodium fluoride + 5% MPD
mMBP-NLRP3 (3-1036) batch 5 (14.8 mg/ml)	0.1M Bis-Tris propane pH 7.5 + 0.05 M ammonium sulfate + 0.1 M $MgCl_2$ + 0.05 M $NiSO_4$ + different PEG mixes 25-30%
mMBP-NLRP3 (3-1036) batch 7 (24.9 mg/ml)	including Ap5A inhibitor: HEPES pH 7.5 + 50% PEG mix (mix of PEG 3350 + 1k + mpd) + mix of divalent cations Also: incubated with ADP and $MgCl_2$: 0.1 M sodium acetate pH 4.6 + 0.2 M $LiSO_4$ + 0.1 M sodium acetate pH 8.4 + 60% PEG 400

7.3.18 Generation of MBP-NLRP3 specific VHH antibodies

Antibodies are well-established and well-studied tools for the investigation of protein-protein interactions, protein targeting in cells as well as in functional screens. One of the major drawbacks using antibodies in cellular screens, is the unpredictable behaviour of antibodies when studied in intracellular compartments (Gargano & Cattaneo, 1997). Naturally, several different subsets of antibodies are generated: IgG, IgM, IgA, IgD, and IgE, whereas IgG is the most abundant isotype. It consists of two heavy and two light chains, which are further composed of two variable domains (VL and VH). Nevertheless, IgGs as well as its subdomain structures have an impaired hydrodynamic stability, thus often require biochemical engineering (Helma *et al.*, 2015). This uncertainty can be overcome by using camelid heavy chain-only antibodies, more specifically the single variable domain fragment (VHH) (Figure 8). These antibody fragments (about 14 kDa) are composed of only one variable region, thus binding to the target protein is mediated only by three complementarity determining regions (CDRs) located on the VHH fragment (Helma *et al.*, 2015).

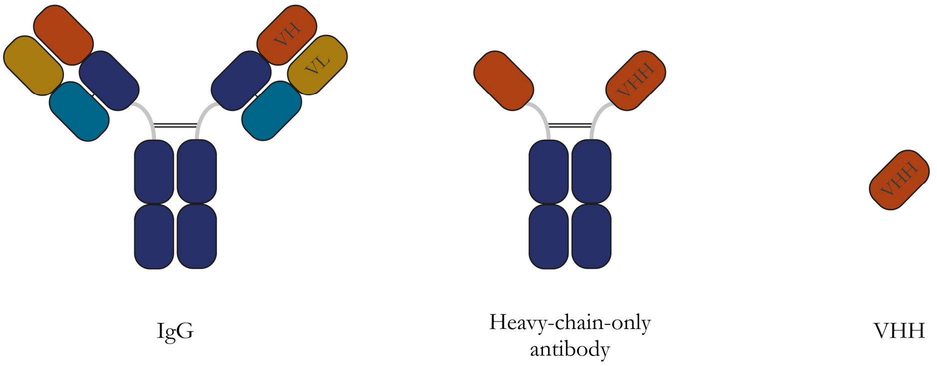

Figure 8: Comparison of immunoglobulin derivatives. A conventional IgG antibody is composed of two heavy and two light chains. The three heavy chain constant domains are shown in blue and the corresponding variable domains in red. The light chain in shown in light blue and its corresponding variable domain in yellow. Heavy-chain-only antibodies (right) are found in *Camelidae*, and consist of only two heavy chain constant domains, but lack the light chain. Further, they comprise a single, antigen binding domain, the VHH domain.

Compared to conventional antibodies, VHH-antibodies show a higher stability and solubility due to framework exchanges of hydrophobic to hydrophilic residues (Helma *et al.*, 2015). Besides its improved stability, VHH-antibodies mediate epitope binding in a different way, compared to IgG antibodies. Heavy-chain-only antibodies typically form a convex paratope, which is prone to bind cavity-structured epitopes, whereas conventional IgG paratopes either forms cavities, grooves or flat surfaces to interact with the respective epitope (Helma *et al.*, 2015).

As the folding of VHH-antibodies is independent of glycolysation and disulfide-bond formation they can be expressed in the cytosol, without losing the ability to bind to the corresponding epitope. Therefore, cameloid VHH-antibodies are an improved tool for studying intracellular protein-protein interactions, besides conventional biochemical approaches.

Specific VHH-antibodies directed against MBP-NLRP3 Peak 2 as well as mMBP-NLRP3 LRR4 were generated in Alpacas to yield a tool to improve crystallization trials. The immunization as well as the isolation and identification of VHH-antibodies was performed in collaboration with Dr. F. Schmidt at the Institute of Innate Immunity, University Clinics Bonn.

7.3.18.1 Alpaca immunization using NLRP3 variants

In order to generate specific VHH-antibodies against MBP-NLRP3 Peak 2 and mMBP-NLRP3 LRR4, two individual female Alapacas were immunized with purified protein. Whereas the animal, which was injected with the NLRP-LRR variant was simultaneously immunized with a bundle of additional antigens. The immunization was performed by a veterinarian at the preclinics research farm in Bruchhausen-Vilsen (Preclinics GmbH, Potsdam, Germany).

For both immunizations, four s.c. injections were applied over a time range of 8 weeks. Accompanied by the first injection of 625 µg of purified MBP-NLRP3 Peak 2 (animal: June) and 500 µg of mMBP-NLRP3 LRR4 (animal: Alice), a pre-immune serum was taken for validation. Beforehand, both animals were tested negatively for already generated MBP-directed antibodies.

Figure 9: Picture of alpaca animals used for immunization. The female alpaca Alice was used for immunization with mMBP-NLRP3 LRR4 (left), whereas the female alpaca June (right) was used for immunization with MBP-NLRP3 Peak 2.

The second immunization took place after 28 days, using 515 µg of freshly purified MBP-NLRP3 Peak 2 and 500 µg of frozen mMBP-NLRP3 LRR4. For both immunizations, the protein samples were mixed with the adjuvant GERBU FAMA in a 1:1 ratio, prior to injection. The third immunization was performed after additional 14 days, using 625 µg of freshly purified MBP-NLRP3 Peak 2 and 500 µg of frozen mMBP-NLRP3 LRR4. The immunization was carried out as tandem injection, thus the adjuvant and the antigen were injected seperately in a distance of 5 cm. An intermediate serum sample of 2-4 mL was taken 50 days after the first immunization injection. The last immunisation step was performed in a tandem emulsion procedure after additional 16 days. This time, two injections were performed for each of the antigens. Again, 625 µg of MBP-NLRP3 Peak 2 were injected as well as 500 µg of mMBP-NLRP3 LRR4 in a tandem approach. The adjuvant GERBU FAMA was mixed with the protein samples in a 1:1 ratio prior to injection. The final bleeding was performed 60 days after the first immunization injection. Thus, 100 mL of whole blood were taken as well as an additional serum sample of 2-4 mL.

7.3.18.2 VHH library generation

The following steps were performed by the lab members of Dr. F. Schmidt at the Institute of Innate Immunity, University Clinics Bonn.

VHH library generation in the M13 phagemid vector pJSC was generated as previously described (Schmidt *et al.*, 2016). According to that, peripheral blood mononuclear cells (PBMCs) are isolated from the alpaca whole blood samples, by centrifugation in order to isolate the RNA. The isolated RNA is used for generation of cDNA, by three primer subsets: random hexamers, oligo[dT]s, and primers specific for the constant region of the alpaca heavy chain gene. Furthermore, specific primers were used to amplify the codon region, specific for VHHs by PCR. Subsequently, these PCR fragments were ligated into the vector pJSC. *E.coli* TG1 (Agilent) cells were used for amplification and stored in glycerol stocks (Schmidt *et al.*, 2016).

7.3.18.3 VHH phage display and panning

The following steps were performed by the lab members of Dr. F. Schmidt at the Institute of Innate Immunity, University Clinics Bonn.

The perviously generated *E.coli* TG1 cells, used for cloning of the VHH-library, were cultured and infected with the helper phage line VCSM13. Subsequently, the phages display the VHH-antibodies encoded by the VHH-library as a pIII fusion protein (Schmidt *et al.*, 2016). The minor coat protein pIII, targets the *E.coli* pilus and is thus required for the initiation of bacterial infection (Deng *et al.*, 1999). The resulting phages were isolated by centrifugation steps, washed with PBS and subsequently negatively selected for binding to amylose-beads, that were previously bound to either MBP or mMBP. The negatively-selected phages were further incubated to amylose-beads coupled to the target protein. Phages resulting from VHH-library generated from blood samples of the alpaca June, which was immunized with MBP-NLRP3 Peak 2 were incubated with amylose-beads coupled to mMBP-NLRP3 LRR1 and MBP-NLRP3 Peak 2, respectively. In contrast, the phages resulting from the VHH-library generated from blood samples isolated from the alpaca Alice, immunized with mMBP-NLRP3 LRR4, were tested against amylose-beads coupled to the respective antigen as well as biotinylated NLRP3 extracted from HEK cells. Mainly two different strategies were applied to elute the bound phages from the amylose-beads coupled to the target protein. Either, glycine at pH 2.2 or 10 mM maltose was used for the elution step (Table 4).

The isolated phages were used to infect *E.coli* ER2738 cells which were subsequently plated on agar plates including the respective antibiotic and incubated over night. The resulting colonies were pooled and stored in glycerol and subsequently subjected to a second panning procedure. Following the second panning round, single colonies were picked and incubated in 96-well-plates using the appropriate antibiotics. The individual cultures were further tested in an ELISA approach using coupled MBP-NLRP3 Peak 2 or mMBP-NLRP3 LRR1 as well as MBP and mMBP in a control ELISA experiment. Positive samples were detected by using an anti-E-HRP secondary antibody. Further correlation with the (m)MBP-ELISA control values accounts for unspecific MBP interaction. Positively selected VHHs were recultured in the appropriate antibiotics and subcloned into the *E.coli* expression vector pHEN6, encoding a C-terminal sortase recognition site (LPETG), followed by a His$_6$-tag and a periplasmic localisation signal (Schmidt *et al.*, 2016).

The identified VHH-antibody SN-04A-D08 and PK-03-C09 were shown to be identical, thus further the label SN-04A-D08 is used.

Table 4: Panning of generated VHH-antibodies. The proteins used for the panning of the VHH-antibodies generated against MBP-NLRP3 Peak 2 and mMBP-NLRP3 LRR4, the respective elution strategy and the corresponding VHH-label are shown.

Antigen	Panning	Elution	VHH-label
MBP-NLRP3 (Peak 2) WT, 3-1036	MBP-NLRP3 Peak 2	glycine pH 2.2	FS-01A
		10 mM maltose	FS-01B
	mMBP-NLRP3 LRR1	glycine pH 2.2	FS-02A
		10 mM maltose	FS-02B
mMBP-NLRP3 LRR4	mMBP-NLRP3 LRR1	10 mM maltose	PK-03
	NLRP3-SH (derived from cell lysates using Streptactin)	biotin	SN-04 A/B

7.3.18.4 Purification of VHH-antibodies

In order to analyse the binding capability and binding affinity of the generated VHH-antibodies towards their antigen MBP-NLRP3 Peak 2 and mMBP-NLRP3 LRR4, the isolated VHHs were expressed in and purified from *E.coli* WK6 cells.

The VHH-constructs were transformed into electrocompetent *E.coli* WK6 cells by electroporation as described in 7.2.5. Subsequently, a preculture was inoculated from a single colony and protein expression was performed according to 7.3.1. Deviating from that, 1 M of IPTG was used for the induction of protein expression, which was carried out at 30°C over night. The pelleted cells were resuspended in 15 mL/L culture TES buffer and incubated at 4°C for 1 h. Subsequently, the suspension was split in half and supplemented each with 35 mL of 0.25x TES buffer and incubated over night and shakened at 4°C. The cell suspension was centrifuged twice at 4°C for 20 min at 20,000 rpm using a JA 25.50 rotor (Beckman and Coulter, Brea, California, USA). The clarified cell lysate was then subjected to affinity purification via the His_6-tag, followed by gel filtration in gel filtration buffer I using a HiLoad 16/600 Superdex 75 pg column (GE Healthcare, Munich, Germany). The detailed procedure is described in 7.3.6.1 and 7.3.9.1.

In order to simplify the nomenclature and thus to avoid mistakes during handling the generated and analysed VHH-antibodies, the tested proteins have been renamed according to Table 5. To dispel uncertainties, the VHH-antibodies were generated in alpacas, the animal names assigned do not have any relevance concerning the species they were raised in.

Table 5: List of tested VHH-antibodies. The table shows the list of tested VHH-antibodies as well as the correspondig antigen and the assigned common names.

VHH label	Common name	Antigen
FS-01A-B07	whale	MBP-NLRP3 (Peak 2) WT, 3-1036
FS-01A-B08	seal	
FS-01A-C06	fox	
FS-01B-C06	rabbit	
FS-02A-H05	goose	
FS-02B-E02	horse	
FS-01A-C07	elephant	
FS-01B-C08	hen	
FS-01A-C09	mosquito	
FS-01A-D07	emu	
FS-01A-C10	hedgehog	
FS-01B-B09	lugworm	
FS-01B-E06	deer	
SN-04A-D08 / PK-03-C09	wolf	mMBP-NLRP3 LRR4

7.3.19 SPR analysis

Surface plasmon resonance (SPR) is a label-free technique, used to study protein-protein interactions, as well as interactions of proteins with small molecules in a surface-oriented method (Homola, 2008).

The phenomenon of SPR was initially observed in 1902, but was first used in 1983 by Liedberg and Nylander, in a biomolecular sensing approach (Liedberg *et al.*, 1995). The main principle of surface plasmon resonance is based on an opto-electronic phenomenon, which is dependent on a nobel metal surface like silver or gold (Mitchell, 2010). A surface plasmon is an oscillation of electrons setting up an electromagnetic field, initiated by photons, which interact with the metal surface. A prerequisite of the coupling event is, that the wavelength of the photon equals the resonance wavelength of the metal used (Mitchell, 2010). The resulting plasmon resonance waves propagate parallel to the interface between the metal surface and the external medium, as for example, a liquid (Richens *et al.*, 2009). Typically, the originating electromagnetic field encompasses a distance of 300 nm from the metal surface in both directions (Mitchell, 2010).

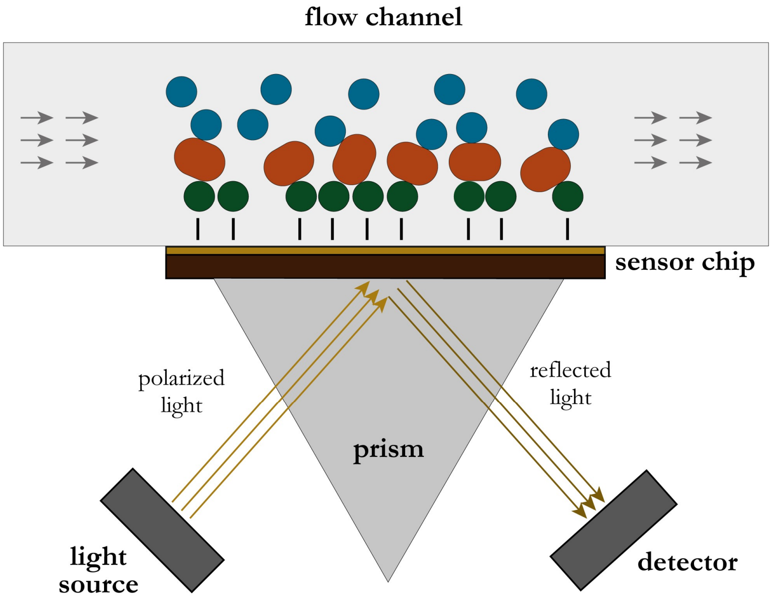

Figure 10: A schematic diagram showing the SPR setup. A specific MBP-binding VHH-antibody (green) was coupled covalently to the chip surface, to trap the antigen MBP-NLRP3 (red). The VHH-antibodies (blue) to be tested are applied in different concentrations via the flow channel. Polarized light is used to illuminate an electrically conducting surface (gold) on the sensor chip, thus inducing the excitation of surface plasmons. The resulting decrease in the intensity of reflected light is measured using a detector. Illustration prepared in accordance with Mitchell, 2010.

Consequently, molecules which are directly interacting with the metal surface interfere with the plasmons and thus result in a change of the resonance angle (Mitchell, 2010). The resulting changes in refractive index are typically measured in resonance units (RU).

In order to determine the binding affinities of NLRP3 antigens towards the generated VHH-antibodies, a Biacore S200 SPR device was used (GE Healthcare, Munich, Germany).

For the performed measurements, a commercially available MBP-binding VHH-antibody (Chromotek GmbH, Planegg, Germany) was covalently coupled to the carboxymethylated dextran matrix, attached to the gold surface of the used CM5 chip (GE Healthcare, Munich, Germany). The experimental setup is presented in Figure 10. Immobilization of the anti-MBP-VHH was performed using a amine-coupling kit (GE Healthcare, Munich, Germany), using 50 μg/mL of protein in 10 mM ammonium acetate (pH 5.5), resulting in a final immobilization response of about 5000 RU. The immobilization conditions were previously determined using the internal pH scouting method. Subsequently, the target protein (MBP-NLRP3 Peak 2 or MBP-NLRP3 N6) was captured for 240 s using a protein concentration of 20 μg/ml, resulting in a final response of 640 RU for MBP-NLRP3 Peak 2 in HBS buffer at pH 8.0 (GE Heathcare, Munich, Germany). Standard regeneration procedures were unsuccessful, thus a novel regeneration strategy was established: two consecutive injections of 10 mM glycine at pH 2.0 and 50 mM NaOH, each 45 s, were applied, respectively.

The analytes were tested using the single cycle kinetics (SCK) mode, which utilizes a sequential injection of increasing analyte concentrations, terminated by a single regeneration step, detaching the ligand from the covalently bound anti-MBP VHH (Palau & Di Primo, 2013).

As a control and reference, each measurement was performed on two flow cells in parallel, one of which including the bound analyte on the anti-MBP VHH, whereas the second cell included the VHH only. For analysis, both the active and the reference cell, were substracted. In order to reduce unspecific interaction of the VHH-antibodies to the reference cell and the system, the experiments were carried out using the following buffer system, including surfactant: 10 mM HEPES pH 8.0, 150 mM NaCl, 1 mM TCEP, 3 mM EDTA, 0.005% v/v P20. The tested VHH-antibodies were applied in eight different concentrations, in a 1:3 concentration row. The measurements were performed at a constant temperature of 25°C and a flow rate of 50 μL/min. Data analysis was performed by the internal Biacore S200 Evaluation Software edition 1.1.

The control experiments involving immobilized MBP, were performed in 10-fold dilutions (0 nM, 0.1 nM, 10 nM, 100 nM, 1000 nM), using an MBP protein concentration of 0.2 μg/mL and the following buffer: 137 mM NaCl, 2.7 mM KCl, 10 mM Na_2HPO_4, 2 mM KH_2PO_4, 0.05% (v/v) Tween 20, 1 mM TCEP, pH 7.4. The amine coupling procedure was performed using 10 mM ammonium acetate (pH 4.5). The MBP control measurements were perfomed by Dr. K. Gatterdam. In this case, a Biacore 8K was used as well as the internal evaluation software.

8 Results

8.1 Molecular and biochemical characterization of NLRP3

8.1.1 Domain architecture and sequence motifs of NLRP3

The family of NLR receptors follows a tripartite domain architecture consisting of an N-terminal PYD-domain, a central NACHT-domain, and a C-terminal LRR-domain. A sequence alignment, comparing human NLRP1 to NLRP14, distinclty indicates high sequence conservation among the PYD-domains as well as the NACHT-domains (Figure 11 A). In contrast, the LRR-domain shows a greater diversity between the investigated NLRPs. The conserved protein-fold, which is defined by the typical LxxLxLxxN/CxL motif, still allows for individual sequence variation, thus forming a potential binding motif for ligand interaction (Kobe & Kajava, 2001; Botos *et al.*, 2011).

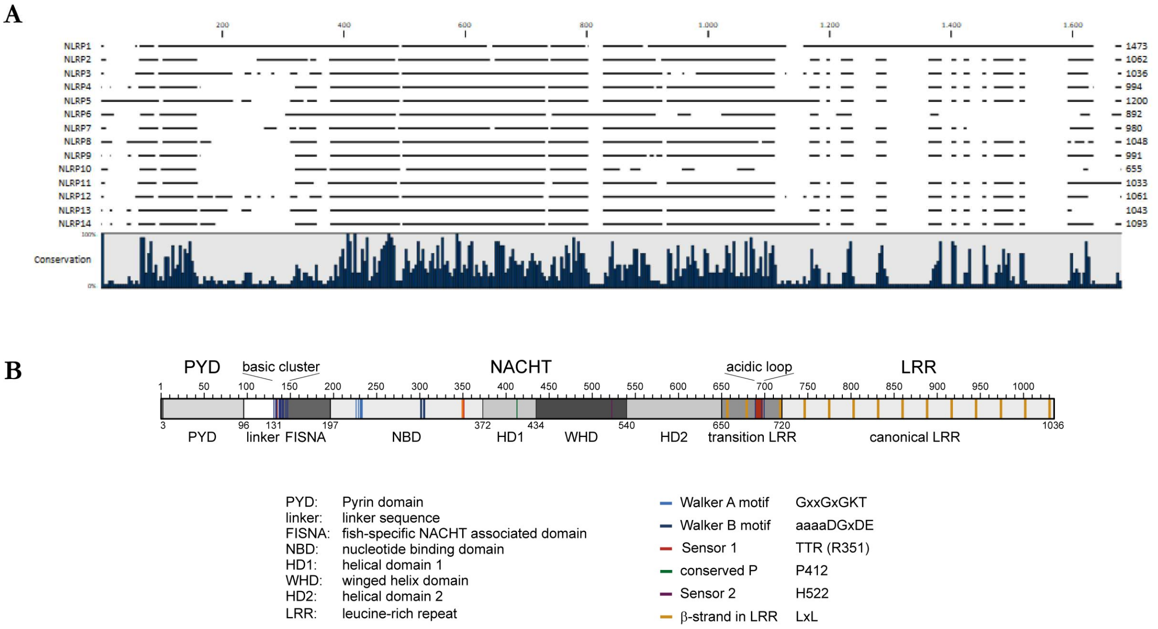

Figure 11: Domain architecture of human NLRP3. A: Sequence alignment of human NLRP 1 to 14. The degree of amino acid conservation is shown in the bar diagram below. **B:** Domain architecture of human NLRP3. The tripartite domain composition is shown on top. The predicted domain boundaries are indicated as well as conserved residues and the respective motifs.

Until now, the only structural information about NLRP3 is taken from either the NMR (PDB: 2NAQ) or the crystal structure (PDB: 3QF2) of the NLRP3 PYD-domain. Thus, in depth structural alignments of NLRP3 were performed with the published structures of the most similar immune receptors NLRC4 in its autoinhibited (PDB: 4KXF) and active conformation (PDB: 3JBL), as well as NOD2 in the ADP-bound state (PDB: 5IRN) (Figure 12). Based on these alignments, domain boundaries of NLRP3 could be defined and conserved residues and motifs have been revealed. Besides the parent tripartite domain organisation, the domain boundaries of further subdomains can be appointed (Figure 11 B). The N-terminal PYD-domain is defined to span from aa 3-96, followed by a linker region and a Fish-specific NACHT associated domain (FISNA), starting at aa 131. Both are separated by a basic cluster of residues, found in this structurally undefined region. The FISNA domain is typically associated with the NACHT domain, and was first identified in zebrafish (Stein *et al.*, 2007).

The central NACHT domain can be subdivided into four subdomains. The nucleotide-binding domain, beginning at aa 197, includes the well-predicted nucleotide binding motifs Walker A and Walker B. Further, the conserved sensor 1 motif is found in this domain at position R351, embedded in the sequence motif TTR. Typically, AAA+ ATPases include a Glu-Switch motif, mediating the orientation of a glutamate residue in the Walker B motif (Zhang & Wigley, 2008). Conventionally, in AAA+ ATPases, amino acids with polar uncharged side chains like mostly asparagine, serine and threonine fulfill this function (Zhang & Wigley, 2008). Sequence and structural alignments of NLRP3 reveal the sequence HCR (aa 260-262), at the predicted Glu-Switch motif, harbouring none of the mentioned amino acids. The central cysteine residue is strongly conserved between the members of the NLR family, thus most likely, a Glu-Switch residue is not present in the ATP-binding site of NLRP3 (Proell *et al.*, 2008). Moreover, AAA+ ATPases typically include an Arg-finger motif, which is either involved in nucleotide binding and/or facilitating complex formation (Wendler *et al.*, 2012). The Arg-finger is typically found in helix a4, following the sensor 1 motif. Computational analysis revealed, that neither arginine nor lysine is found at an equivalent position in the sequence of NLRP3.

The NBD is followed up by the HD1, which spans aa 372 until aa 434. The HD1 includes a well-conserved residue, P412, belonging to a GxP motif, identified in members of the STAND family (Proell *et al.*, 2008). Nonetheless, neither NLRP3, nor any of the other NLRP members includes the glycine residue. Further, the adenine base of ADP in the rabbit NOD2 structure (PDB: 5IRL) is located in close proximity to the respective proline, thus potentially fulfilling an important role in the ATP-binding site. The ensuing winged-helix-domain (WHD) ends approximately at aa 540 and ties in HD2, which is predicted to end at about aa 650. The WHD includes another important residue, H522. AAA+ ATPases conventionally include a conserved arginine or lysine residue, sensor 2, which is located downstream of the sensor 1 but before beta-strand 5 (Figure 26) (Wendler *et al.*, 2012). Sensor 2 is involved in ATP hydrolysis and nucleotide binding. Instead of the typical sensor 2, a conserved histidine residue is expected to fulfill this function in members of the STAND family (Proell *et al.*, 2008).

In NLRP3, the HD2 is followed by the C-terminal LRR-domain. Structure predictions and sequence alignments identified a canonical LRR motif, ranging from aa 720-1036 and including the conserved horse-shoe shaped alpha-helix/turn/beta-sheet/turn-motif (Figure 17). In total, 14 LRR-repeats have been identified with slight sequence variations in the range of aa 650-1036. Sequence variantions were especially identified in an intermediate region, with vaying length of the individual subunits of a LRR-subunit in the area of aa 650-720, that was hence termed transition LRR (Figure 11). The transition LRR-domain includes an acidic cluster, which was predicted to assemble into a loop structure between the alpha-helix and the subsequent beta-sheet of a LRR-motif (Figure 17).

Here, besides the information derived from the amino acid sequence of NLRP3, structural alignments were performed to get insight into the process of inflammasome assembly and complex formation.

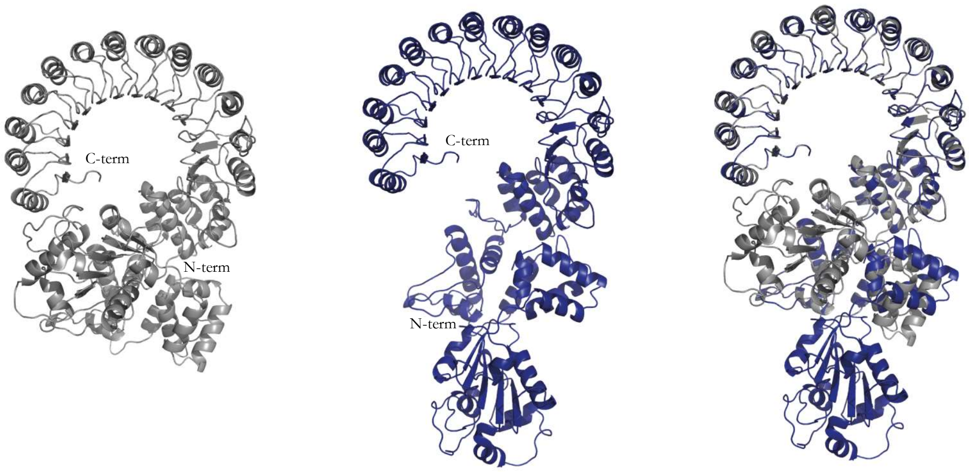

Figure 12: Model of NLRP3 in the inactive and active conformation. Structural modelling was performed using the structure of NLRC4ΔCARD in its autoinhibited (PDB: 4KXF) and the oligomeric (PDB: 3JBL) as a template, combined with the LRR-structure of procrine ribonuclease inhibitor (The inactive conformation is shown on the left, the active conformation in the middle and an overlay of both model structures on the right.

8.1.2 Characterization of the NLRP3 PYD-domain

8.1.2.1 *In silico* based interface analysis

Death domains, like the PYD-domain, were identified as the key domains, facilitating domain/domain interactions in immune receptor signalling. The formation of inflammasome signalling complexes is mediated by the recruitment of the adaptor protein ASC, via PYD/PYD interactions. Besides the homotypic interaction of inflammasome forming proteins and regulators via the PYD-domains, the formation of the inflammasome signalling platform is initiated by PYD/PYD interactions. Further, homotypic PYD-interactions have been identified for several different proteins like ASC, AIM2, Pyrin, NLRP1, NLRP2, NLRP3, NLRP7, NLRP10, NLRP12, POP1 and POP2, as well as IFI16 (Kwon *et al.*, 2012). Several PYD- and CARD-domains have been investigated structurally, but until now, only the PYD-domain of ASC was shown to form a fibrillar assembly (PDB: 3J63), mediated by three intramolecular PYD/PYD interfaces (Lu *et al.*, 2014). As the adaptor ASC only bridges the inflammasome protein and Caspase-1, it is of major interest, wether the PYD domain of inflammasome forming proteins like NLRP3 is also able to assemble into a fibrillar structure.

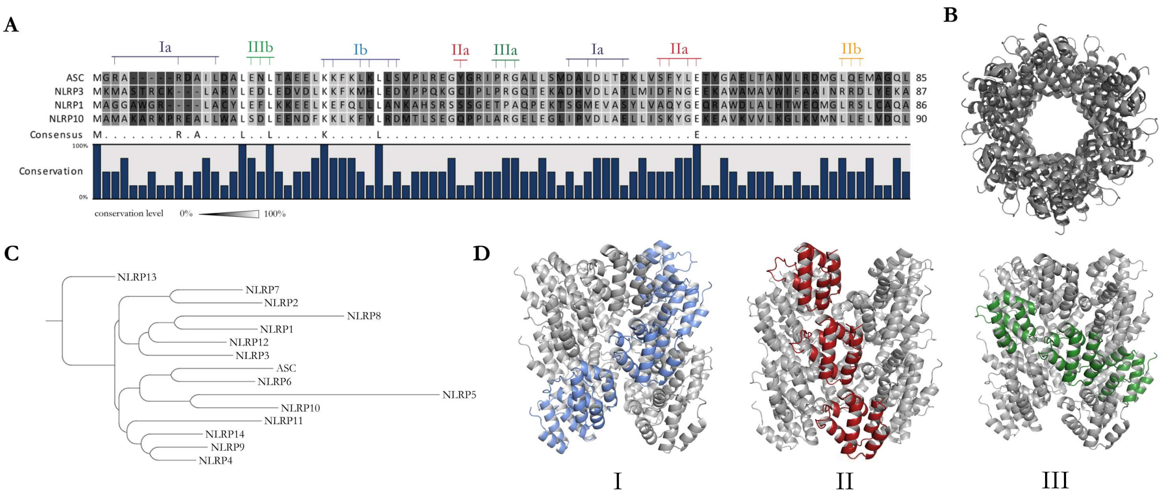

Figure 13: *In silico* analysis of the NLRP3-PYD domain. A: Alignment of the PYD-domains of human ASC, NLRP3, NLRP1 and NLRP10. The conserved residues are indicated by a color code and a bar diagram. Further, residues showing 100% conservation are listed below. Residues, which are predicted to form inter-molecular interfaces between the PYD-domains according to the ASC-PYD fibril structure (PDB: 3J63), are presented on top; Interface I in blue, Interface II in red and Interface III in green. **B:** Structural alignment of the NLRP3-PYD crystal structure (PDB: 3QF2) onto the ASC-PYD fibril structure (PDB: 3J63), top view. **C:** Phylogenetic tree of PYD-domains of human NLRP 1 to 14 (Software: CLC Sequence Viewer 8). **D:** Structural alignment of the NLRP3-PYD crystal structure (PDB: 3QF2) onto the ASC-PYD fibril structure (PDB: 3J63), side view. Intra-molecular interfaces are shown, according to the prediction, shown in A.

In silico analysis of the PYD-domains of human NLRP1, NLRP3, NLRP10 and ASC revealed, that the protein domain includes cluster of highly conserved as well as less conserved amino acid sequences, that partly go along with the three interfaces determined to mediate the assmbly of the ASC-PYD fibril (Figure 13). Interestingly, the phylogenetic relationship of the investigated PYD-sequences is diverse, thus showing three main-branches. Hence a closer relationship between the PYD domain of NLRP10 and ASC, than of NLRP3 or NLRP1 is predicted. It has been shown previously, that Interface I is the largest interface mediating the assembly of the ASC-fibril. This interface is subdivided into three further clusters of which Interface Ia mediates binding to Interface Ib on the neighbouring ASC-PYD molecule (Lu *et al.*, 2014). A similar mechanism holds true for Interface IIa/b and Interface IIIa/b, resulting in three interface axes spanning the ASC-PYD fibril. The cryo-EM structure of the ASC-PYD fibril (PDB: 3J63) was used as a template for the alignment of the crystal structure of the NLRP3-PYD (PDB: 3QF2). Due to the high homology in structure, a similar fibrillation mechanism can be assumed for the PYD-domain of NLRP3, resulting in similar interfaces and interface axes (Figure 13 D). The residues spanning Interface I can be identified as follows: Ia: M3, R7, A11, D50, V52, D53 and T56 and Ib: K23, K24, M27, H28, E30 and D31 (Figure 14 A). Again, Interface Ia and Ib are provided by two neighbouring PYD molecules, thus transmitting the interface along the PYD-fibril structure. Recently, S5 was identified as a crucial phosphorylation site in the NLRP3-PYD domain, which upon phosphorylation inhibits NLRP3 inflammasome formation (Stutz *et al.*, 2017). Among the analysed PYD domains, S5 is not conserved, whereas positive residues are found at the same position in ASC (R5) and in NLRP10 (K5). This points towards a potential impairment in interface formation in case of a phosphorylation event at Ser5 of NLRP3. Moreover, the PYD-domain of NLRP3 shows a highly polar surface, potentially mediating the fibrillar assembly by interaction of charged residue clusters (Figure 14 C).

8.1.2.2 Mutational analysis of NLRP3 PYD Interface I

In order to determine the underlying mechanism of inflammasome formation, the PYD-domain of NLRP3 was investigated in a mutational approach. Charge-reversal mutations were introduced in Interface Ia (D50K, D53K) and Ib (K23E), indicated in Figure 14 B. Additionally, the phosphorylation site S5 was included in the study, to investigate its impact on fibril formation. Thus, a phospho-mimetic mutant S5E and a charge-neutral variant S5A were generated and analysed.

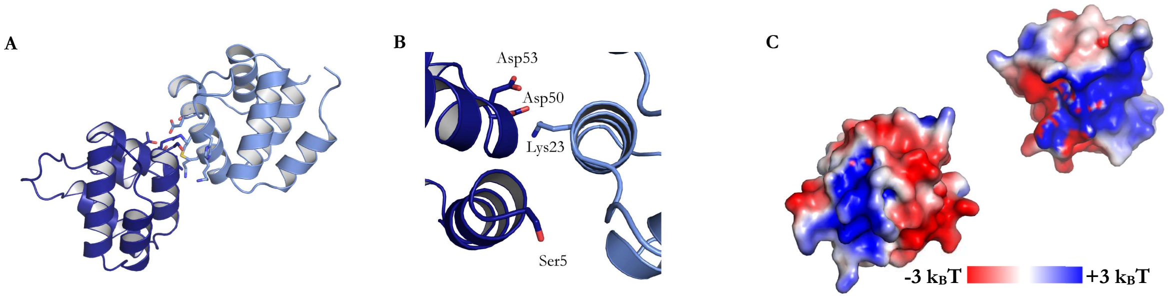

Figure 14: *In silico* analysis of NLRP3-PYD interface I. A: Structural alignment of the NLRP3-PYD crystal structure (PDB: 3QF2) onto the ASC-PYD fibril structure (PDB: 3J63), side view. Two NLRP3-PYD molecules are shown (lightblue and blue), including the interface I residues, shown in Figure 9. The color code was chosen accordingly. **B:** Detailed view on the interface shown in A. The amino acids in Interface I, which were chosen for a mutational approach are labeled. **C:** Electrostatic surface of the structural alignment shown in A, back view. The electrostatic surface is displayed in a charge range of k_BT -3 to 3.

The NLRP3-PYD variants were expressed and purified from *E.coli* cells, including an additional mutation, C108S, to avoid artificial intramolecular disulfide-bridges, previously identified in the crystal structure (PDB: 3QF2). The variants S5A, S5E, K23E and D50K, were purified to homogeneity, whereas the wt and the D53K variant showed a slight contamination of uncleaved GST-tagged protein, that was not separated from the cleaved protein during gel filtration (Figure 15). Analytical gel filtration again shows slight contamination of the WT and D53K-variant, but single peak profiles for the remaining mutants. Further, the determined size of the protein mutants deviated from the calculated molecular weight of a monomeric protein. The calculated molecular weight of the mutants ranges from 12.52 kDa (S5A,C108S) to 12.58 kDa (S5E, C108S), whereas the measured sizes of the proteins range from 16.64 kDa (D50K,C108S) to 18.23 kDa (C108S), thus pointing to either dimer or monomer formation of the PYD-domain variants. In order to further analyse the oligomeric state of the NLRP3-PYD-mutants, Native-PAGE was performed. Again, no higher oligomeric complexes were identified. In contrast, the PYD-mutants were separated according to their pI.

The proteins harbouring the mutation at either Ser5 or Lys36 were well separated by Native-PAGE, whereas it was not possible to analyse the NLRP3-PYD mutants D50K and D53K due to a pI of 6.93 (Figure 15). Thus, the pI value of both mutants resembled the pH of the running buffer. Besides the biochemical analysis, the Interface I mutants were further investigated by transmission electron microscopy, with respect to their ability to form fibrillar structures. Fibrils ranging from 9-13 nm were detectable for the wt, as well as the D50K and the D53K mutant. For both mutants, the amount of fibrils was lower when compared to the WT. Significantly smaller fibrillar structures were detected for the phosphorylation resembling mutant S5E. This mutant showed a great number of small fibrils with an average size of only 6.7 nm. In contrast, no fibrillation was detected for the K23E mutant, thus this mutation was found to fully inhibit fibrillation in the NLRP3-PYD domain.

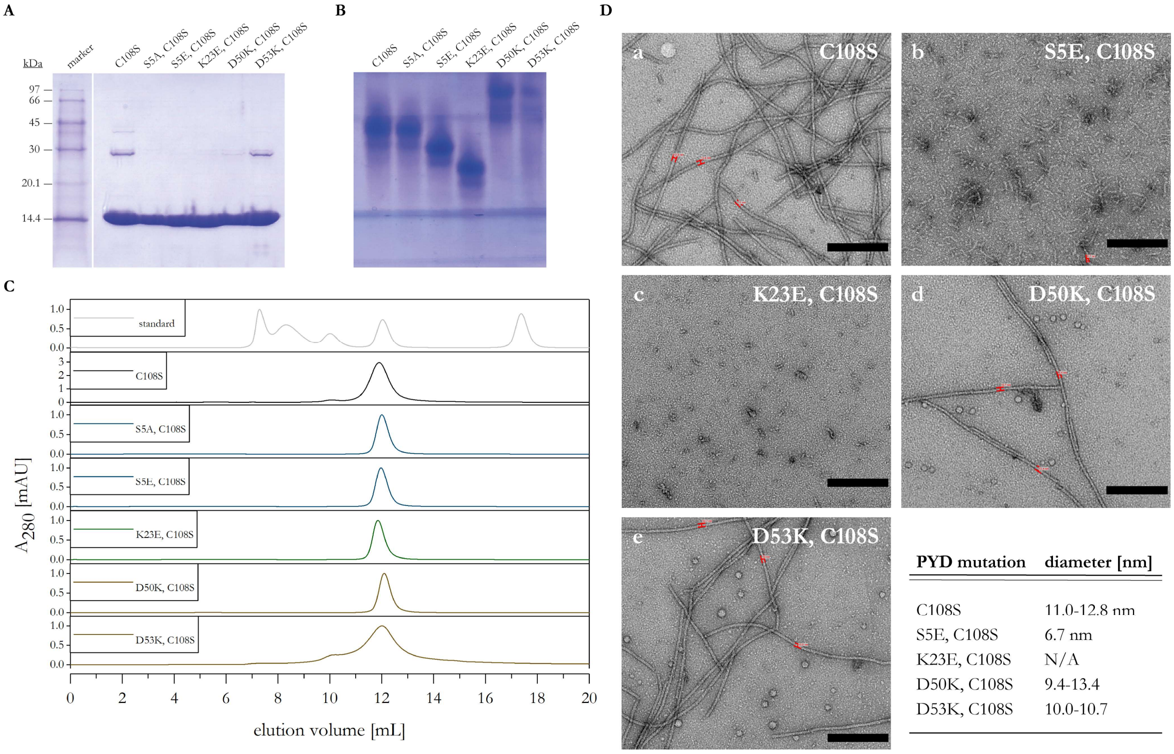

PYD mutation	diameter [nm]
C108S	11.0-12.8 nm
S5E, C108S	6.7 nm
K23E, C108S	N/A
D50K, C108S	9.4-13.4
D53K, C108S	10.0-10.7

Figure 15: Biochemical and electron microscopic analysis of NLRP3-PYD variants. A: SDS-PAGE of NLRP3-PYD variants. The proteins range from aa 3-110 and include the indicated point mutations. **B:** Native-PAGE of NLRP3-PYD variants shown in A. **C:** Analytical gel filtration runs of NLRP3-PYD variants performed on a Superdex 75 10/300 column. The molecular weight determined for each mutant is: C108S: 18.23 kDa, S5A, C108S: 17.32 kDa, S5E, C108S: 17.59 kDa, K23E, C108S: 18.59 kDa, D50K, C108S: 16.64 kDa, D53K, C108S: 17.32 kDa. The standard includes proteins of the following sizes: 670 kDa, 158 kDa, 44 kDa, 17 kDa and 1.35 kDa. **D:** Negative stain electron microscopy analysis of NLRP3-PYD variants shown in A. Further, the fibril diameter is compared. The following mutants are shown: a: C108S, b: S5E, C108S, c: K23E, C108S, d: D50K, C108S, e: D53K, C108S. The scalebar corresponds to 200 nm.

8.1.3 Characterization of the NLRP3-LRR domain

The LRR-domain of NLRP3 was previously identified as binding site, mediating protein-protein interactions. The chaperone HSP90 and its co-chaperone SGT1 were both found to interact with NLRP3 via the LRR domain (Mayor *et al.*, 2007) and also the kinase Nek7 was identified as LRR-interacting protein (He *et al.*, 2016b). As the exact mechanism underlying NLRP3-inflammasome formation is still unknown, structural information about its major protein-interaction domain is of great interest to ellucidate the underlying activation mechanism.

In order to gain structural information about the LRR-domain of NLRP3, several different constructs were designed, of which the most promising are displayed in Figure 17. So far, lacking structural information, the exact boundaries of the LRR-domain are difficult to be determined. Thus, models were generated according to the structure determined for the LRR-domain of ribonuclease inhibitor (PDB: 2Q4G) that shows the highest sequence homology to NLRP3 among the published structures of LRR-containing proteins. Aligning the LRR-domain according to the consensus sequence of a typical leucine-rich repeat motif (LxxLxLxxN/CxL), gives rise to a highly conserved region from aa 714-1036, the canonical LRR.

Figure 16: Sequence alignment of the NLRP3-LRR domain. The amino acid sequence (602-1036) was aligned according to the prediced consensus LRR sequence motif. The respective exons are marked and the sequence length is shown. The predicted secondary structure is labelled on top of the sequence. Conserved Leucine residues are marked in green, as well as Cysteines in yellow. Moreover, the amino acid residues spanning aa 689-698, which are predicted to form the acidic loop region, were excluded from the alignment (arrow). Further exon boundaries are marked in white and grey.

In the range of aa 650-718, a less conserved leucine-rich-repeat sequence is found, which we named transition LRR. The canonical LRR-fold is accompanied by exon-borders, which include two LRR-motifs each, predicted to fold into a beta-strand/loop/alpha-helix/loop motif, displayed in Figure 17 B.

Based on the alignment shown in Figure 16, construct boundaries were chosen, which included the conserved LRR-fold starting from exon 5. Additionally, constructs extending these boundaries were generated. The LRR-constructs LRR1 and LRR2 (651-1036), are deviating with respect to the predicted acidic loop-sequence spanning aa 689-698 (Figure 17 C). According to the structural prediction, the acidic loop sticks out of the LRR surface, indicating a potential impact on LRR-ligand binding. The construct MBP-F1 did result in soluble protein, but was neither stable, when expressed without the MBP-tag nor, when the tag was cleaved off (not shown). In order to increase the crystallizability of the construct MBP-LRR F1, the variants LRR1-4 have been fused N-terminally to an uncleavable mMBP-tag, thus facilitating both crystallizability and affinity purification (chapter 8.1.5.1) (Bokhove *et al.*, 2016).

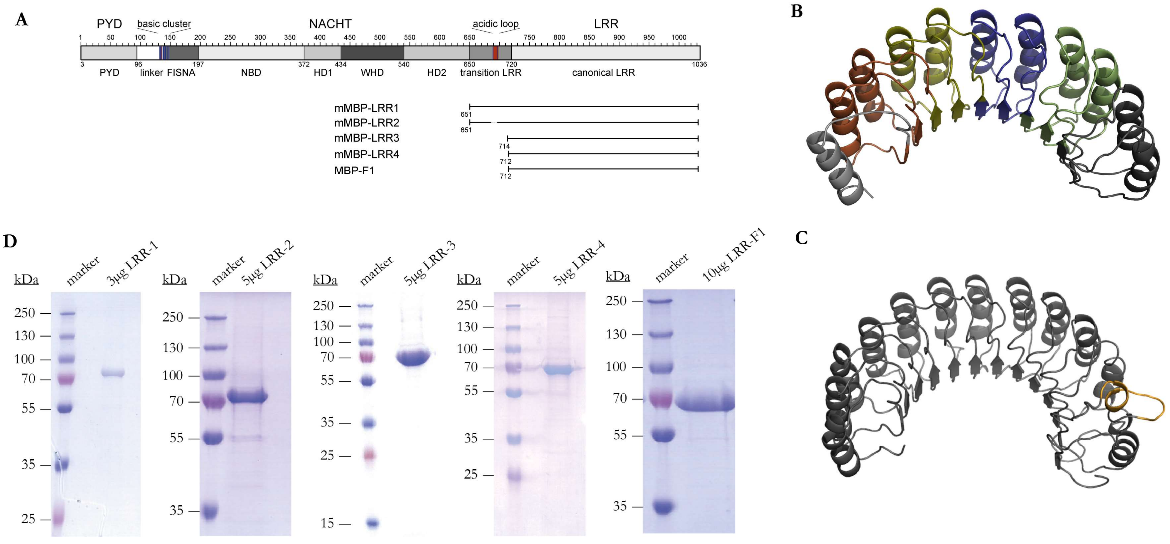

Figure 17: Purification of NLRP3-LRR constructs. A: Overview of mMBP- and MBP-NLRP3 LRR construct boundaries. The constructs mMBP-LRR 1-4 additionally included the point mutation C838S. **B,C:** NLRP3 models generated using Swiss-Model on the basis of the structure of human ribonuclease inhibitor (PDB: 2Q4G). **B:** Model of NLRP3-LRR aa 719-1026. The different exon boundaries are shown, exon 5 in darkgrey, exon 6 in green, exon 7 in blue, exon 8 in yellow, exon 9 in red and exon 10 in lightgrey. **C:** Model of NLRP3-LRR aa 647-1030. The acidic loop, presented in A is coloured in orange. **D:** SDS-PAGE of the LRR constructs shown in A. LRR-1, LRR-2, LRR-3, LRR-4 and LRR-F1 were purified to homogeneity.

The LRR-constructs have been expressed and purified to homogeneity from *Sf9* insect cells, as presented in Figure 17 D, showing a low degree of contamination and degradation. Nonetheless, when subjected to gel filtration chromatography, the tested constructs eluted in the void volume, indicating a high degree of aggregation. The proteins were tested in crystallization trials, but never resulted in successful crystal formation. Moreover, point-mutations of several cystein residues included in the canonical LRR-motif did not yield refined protein samples (not shown).

8.1.4 Characterization of the NLRP3-NACHT domain

NLRP3 harbours a central NACHT domain, ranging from the end of the predicted FISNA-domain at aa 197 to the C-terminal end of HD2 at approximately aa 650. The NACHT-domain can be further subdivided into the nucleotide-binding domain (NBD) ranging (aa 197 to 372), followed by the HD1 (aa 372-434), the winged-helix domain (WHD) (aa 434 to 540) and the HD2-domain (aa 540 to 650).

The borders defined here are predicted based on the structural model of NLRP3, which in turn is based on the structures of NOD2 (PDB: 5IRN) and NLRC4 (PDB: 3JBL) (Figure 12).

Several different domain boundaries were designed and expressed in *Sf9* cells, of which the five most promising are compared in Figure 18. NLRP3 comprises a basic- and an acidic cluster, located in the FISNA/linker region between the PYD-domain and in the LRR-domain, respectively. In order to determine whether these clusters influence protein folding and stability, the NACHT constructs were designed accordingly. Either a cleavable MBP-tag (N-series), or a non-cleavable mMBP-tag, including an Ala-Ala-Ala-linker was chosen (M-series). The constructs spanning the NACHT-domain of NLRP3 were expressed and purified successfully to homogeneity.

Purification of the recombinantly expressed NACHT-constructs, using a Superose 6 10/300 GL increase column, revealed clear differences with respect to the elution profiles. Irrespective of the C-terminal border, constructs that started at aa 159 (M1, M2 and M4), resulted in a large contamination of mMBP, pointing to unstable and intracellularly degraded protein. Furthermore, these proteins eluted in the void volume, denoting large protein complexes as well as aggregated protein sample. In contrast, the NLRP3-NACHT construct (M3) spanning both, the acidic and the basic cluster, eluted in four peaks, all of which contained the protein of interest (Figure 18). Besides one peak in the void volume, the mMBP-M3 construct eluted in two or three additional peaks in a range of 12-17 mL, indicating large variance in the composition of the homo-oligomer. Moreover, a second construct spanning both, the acidic and the basic cluster was examined, ranging from aa 131-704 (N6), including a cleavable N-terminal MBP-tag. Similar to the previously described M3 construct, this protein eluted in 2-3 peaks ranging from 12-17 mL, but did not show a peak in the void volume. In comparison to construct M3, the protein was less stable, indicated by the low protein yields. When subjected to TEV-cleavage, most of the protein aggregated, indicated again by a peak in the void volume and an excessive peak corresponding to MBP. Only a very small fraction of cleaved protein eluted at about 16-17 mL, corresponding to fraction 11, shown by SDS-PAGE (Figure 19).

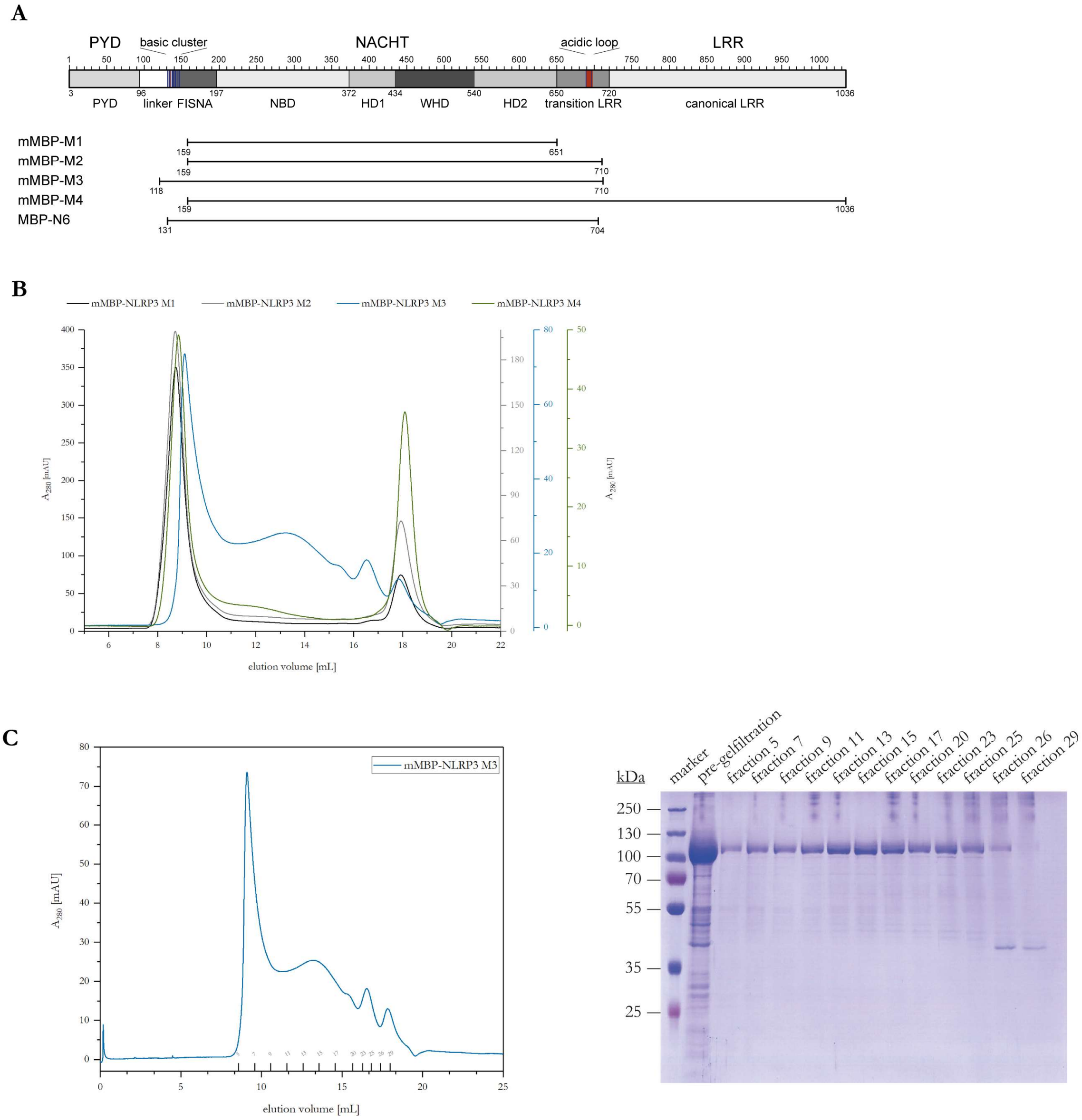

Figure 18: Biochemical analysis of NLRP3-NACHT M-series constructs. The proteins were recombinantly expressed and purified from *Sf9* insect cells. **A:** Overview of NLRP3-NACHT construct boundaries, including either a MBP-tag or an uncleavable mMBP-tag. **B:** An overlay of the chromatography profiles of mMBP-NLRP3 M1-M4 (Superose 6 10/300 GL increase) shows one peak in the void volume for the constructs M1, M2 and M4, as well as a second peak corresponding to leaky MBP. For the construct mMBP-NLRP3 M3, an additional peak is shown at about 13.5 mL and another one at about 16.5 mL. **C:** The individual gel filtration chromatogram of mMBP-NLRP3 M3 is shown, including the collected fractions. The protein mMBP-NLRP3 M3 is purified to homogeneity, as shown in the SDS-PAGE. The protein is found in each of the analysed fractions, corresponding to an elution volume of 8.5 mL to 17 mL at the corresponding size of about 106 kDa. Further leaky MBP is found in fraction 26-29, at a corresponding size of about 42 kDa.

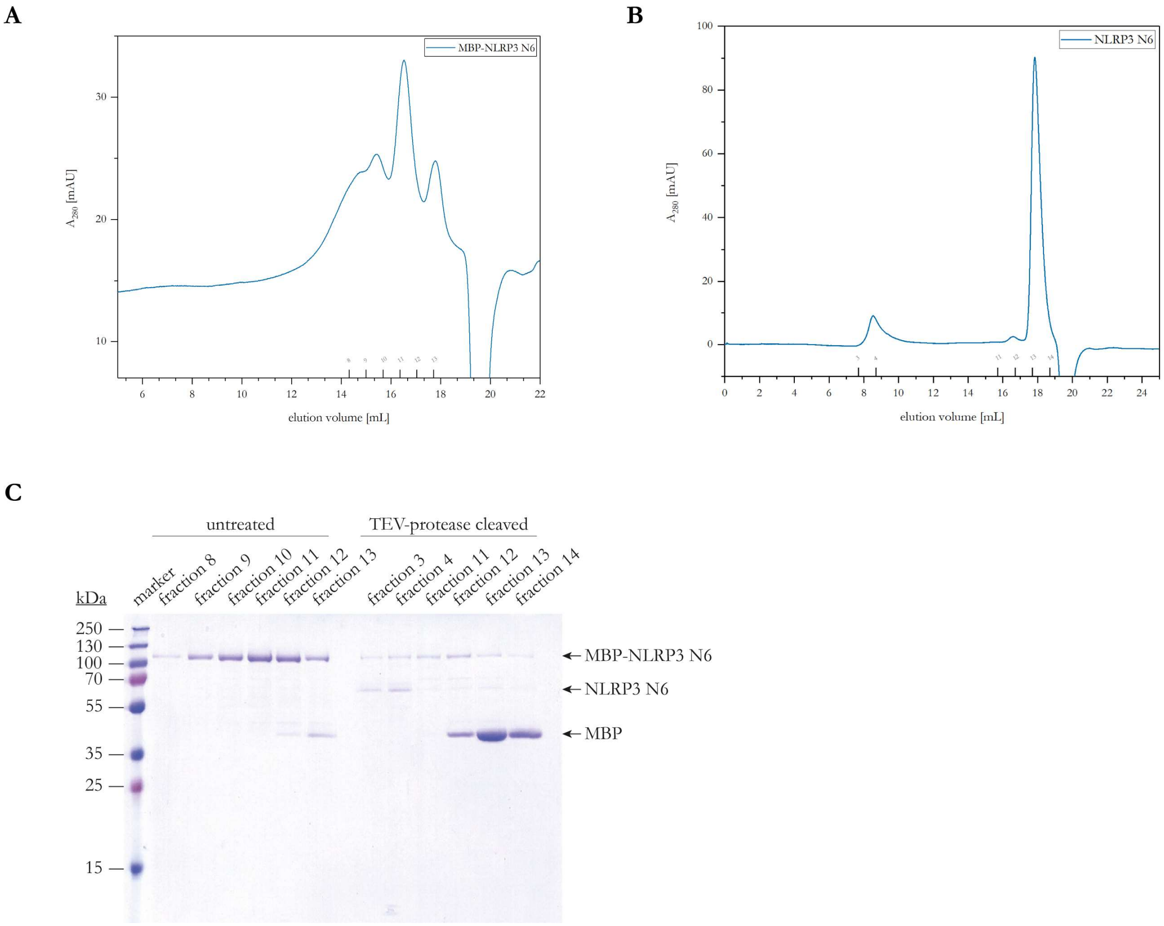

Figure 19: Biochemical analysis of NLRP3-NACHT N6 construct. The proteins were recombinantly expressed and purified from *Sf9* insect cells. The gel filtration chromatogram of MBP-NLRP3 N6 (**A**) as well as of TEV-cleaved NLRP3 N6 (**B**) is shown, including the collected fractions. The protein MBP-NLRP3 N6 elutes at about 14-17 mL, when purified using a Superose 6 10/300 GL column, whereas the TEV-treated variant shows a peak in the void colume, as well as a small portion of cleaved sample eluting at about 16 mL and further the cleaved MBP-tag at about 18 mL. The corresponding SDS-PAGE of MBP NLRP3 N6 as well as the TEV-cleaved NLRP3 N6 sample is shown in **C**.

8.1.5 Biochemical and molecular analysis of full-length NLRP3

The intracellular receptor protein NLRP3 is thought to undergo conformational changes upon ligand recognition and was further shown to form an inflammasome platform for the association with the adaptor protein ASC.

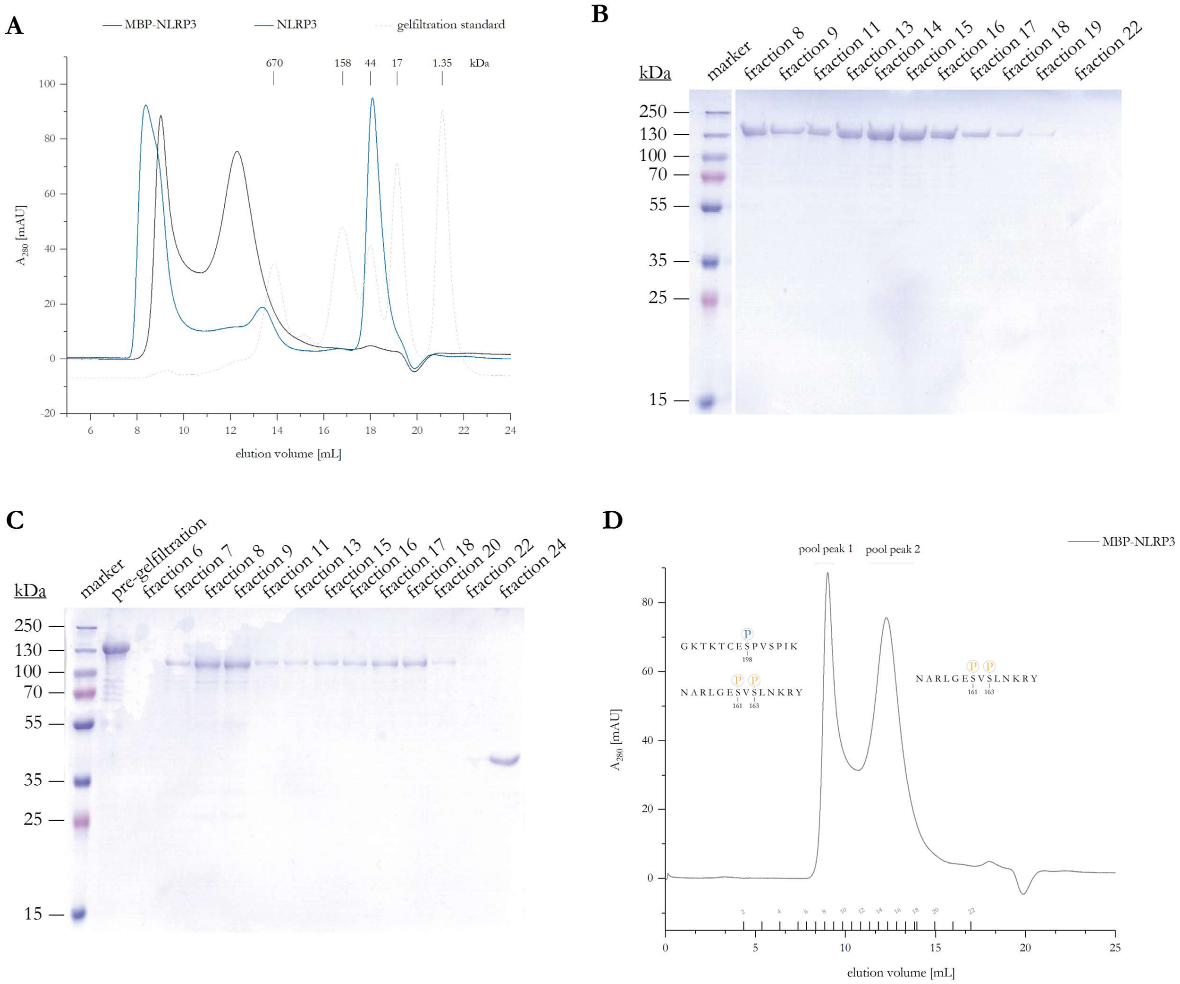

Figure 20: Purification of MBP-NLRP3. A: Gel filtration analysis (Superose 6 10/300 GL) shows a shift of TEV-protease-treated NLRP3 compared to untreated MBP-NLRP3. MBP-NLRP3 elutes in a void peak and a second peak at about 12.5 mL. In contrast, the TEV-treated sample shows a void peak, which is further shifted to about 8 mL and a second peak eluting at about 13.5 mL. The third peak eluting at about 18.5 mL corresponds to the cleaved MBP-tag. **B:** SDS-PAGE (12%) of untreated MBP-NLRP3, according to gel filtration fractions shown in D. The protein band at about 165 kDa corresponds to the theoretical MW of MBP-NLRP3. **C:** SDS-PAGE (12%) of TEV-protease-treated NLRP3 corresponding to the gel filtration profile shown in A. NLRP3 was completely cleaved, shown by one distinct band at the corresponding size of about 115 kDa. MBP eluted in a single peak in fraction 24, corresponding to the expected size of about 42 kDa. **D:** MBP-NLRP3, subjected to gel filtration (Superose 6 10/300 GL), elutes in two distinct peaks. Mass-spectrometric analysis revealed deviating phosphorylation patterns for the individual peaks. Phophorylation of S161 and S163 was shown for both peaks, whereas phosphorylation of S189 was only identified for peak 1. The corresponding fractions are indicated.

Thus, besides the structural and biochemical analysis of single domains, the full-length protein was of major interest. MBP-NLRP3 was shown to be soluble, when purified from *Sf9* insect cells (Lu *et al.*, 2014). We focussed on the expression of MBP-NLRP3 and mMBP-NLRP3 (3-1036) in *Sf9* insect cells and succeeded in the generation of soluble and pure (MBP)-NLRP3 full-length protein. MBP-NLRP3 was subjected to gel filtration chromatography using a Superose 6 column. The protein eluted in two distinct peaks. One peak (Peak 1) eluted close to the void volume and a second peak (Peak 2) at about 12.5 mL, thus corresponding to a MW >670 kDa (Figure 20). When subjected to TEV-cleavage, the majority of the protein sample aggregated and was shifted even more to the void volume. Nevertheless, a small portion of the cleaved protein was soluble in solution and eluted later, compared to the uncleaved Peak 2 sample. The purity of both samples is demonstrated by SDS-PAGE (Figure 20 B and C). Previously, post-translational modifications, especially phosphorylations, were shown to convey the inactive and active state of NLRP3. Thus the purified protein was investigated with respect to its phosphorylation pattern (Stutz *et al.*, 2017). Mass-spectrometric analysis revealed, that MBP-NLRP3 Peak 1 is phosphorylated at positions S198, S161 and S163. Strikingly, MBP-NLRP3 Peak 2 only showed phosphorylation at positions S161 and S163. Dependent on the proteolytic digest, no peptide covering the area of amino acids 1-7 could be identified, thus phosphorylation of S5 in *Sf9* cells could neither be confirmed nor rejected. Moreover, the phosphorylation of S198, as well as S161 have both been reported previously, but whether the phosphorylation of S163 is dependent on the protein expression in *Sf9* insect cells is not known (Song *et al.*, 2017; Stutz *et al.*, 2017).

In order to further analyse the influence of the phosphorylation of S198 on the generation of the two oligomeric assemblies of MBP-NLRP3 (Peak 1 and 2), two mutations were tested. On the one hand, S198 was mutated to a phospho-mimetic residue S198E and on the other hand, an alanine residue was introduced, to exclude phosphorylation at position 198. As shown in Figure 21, gel filtration analysis revealed two peaks for both mutants, eluting at the same elution volume as the wild-type protein.

Equivalent to the data obtained by mass-spectrometric analysis, the mutation of residue S198 resulted in a change of the ratio of Peak 1 to Peak 2. MBP-NLRP3 S198E resulted in Peak 1 eluting at 8.67 mL and Peak 2 at 11.90 mL. Integration of the peak areas showed a ratio of Peak 1 (73.69%) to Peak 2 (26.31%) of about 2.8:1. In contrast, MBP NLRP3 S198A, showed a much lower ratio between Peak 1 and Peak 2. MBP NLRP3 S198A Peak 1, elutes at about 8.82 mL and Peak 2 elutes at about 11.90 mL.

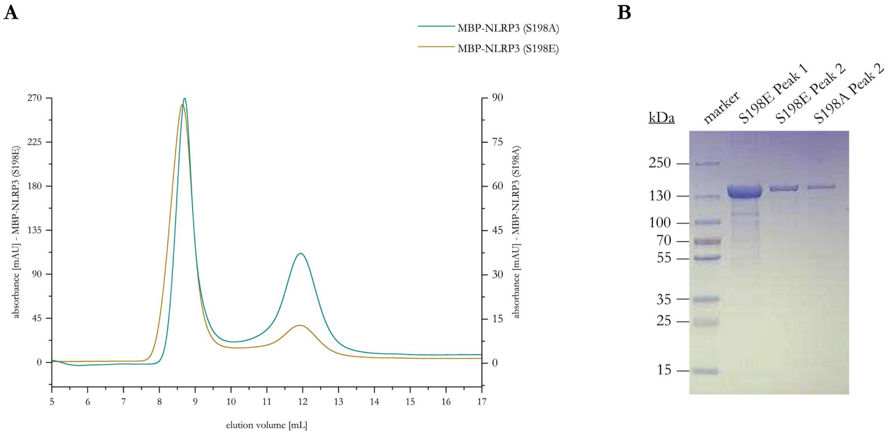

Figure 21: Phosphorylation mimicking mutation at S198 change the oligomeric assembly of MBP NLRP3. A: Gel filtration analysis (Superose 6 10/300 GL) shows a change in the ratio of MBP NLRP3 Peak 1 and Peak 2, based on the phospho-mimicking mutation on position S198. The ratio of Peak 2 : Peak 1 eluting at about 12 mL and 8.5 mL, respectively for S198A is higher compared to the mutant S198E. **B:** SDS PAGE (12%) of MBP-NLRP3 S198A and S198E, respectively.

As mutations of S198 resulted in a shifted ratio of both protein species, a different oligomeric assembly is assumed.

In order to determine the exact dimensions and sizes of these two populations, MBP-NLRP3 wild-type Peak 1 and Peak 2 were investigated by batch-DLS, Online-DLS and MALS.

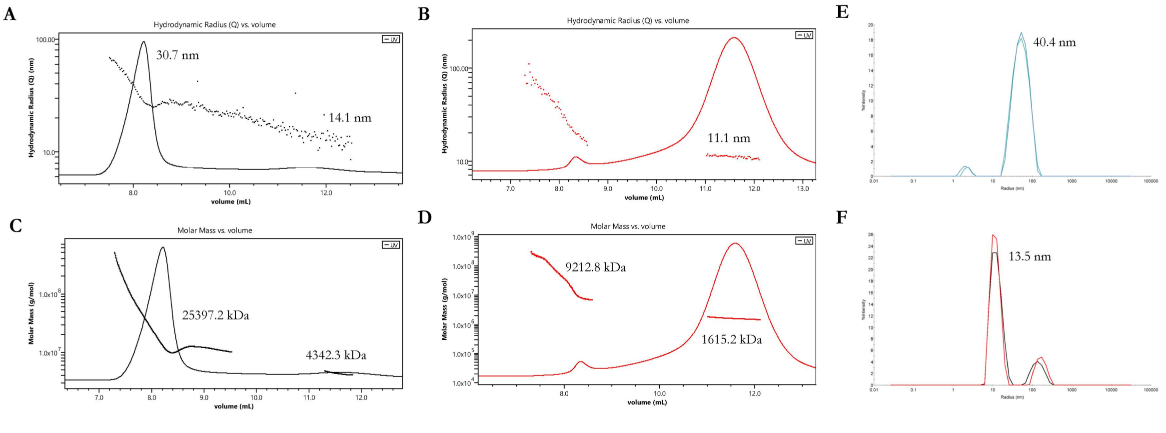

Figure 22: Online MALS and DLS of MBP-NLRP3 Peak 1 and Peak 2. A, C, E: Analysis of MBP-NLRP3 Peak 1. **A:** Plot of the online hydrodynamic radius against retention volume. The UV-traces are plotted as an overlay, showing a main peak size of ~40 nm. **C:** Plot of the molar mass against retention volume. The UV-traces are plotted as an overlay. A second peak at 12 ml might correspond to MBP-NLRP3 Peak 2. The sample shows a very high degree of aggregation. **E:** Batch DLS reveals a approx. size of about 40 nm for MBP-NLRP3 Peak 1. **B, D, F:** Analysis of MBP-NLRP3 Peak 2. **B:** Plot of the online hydrodynamic radius against retention volume. The UV-traces are plotted as an overlay, showing a main peak size of about 10 nm. **D:** Plot of the molar mass against retention volume. The UV-traces are plotted as an overlay. **F**: Batch DLS reveals a approx. size of about 13 nm for MBP-NLRP3 Peak 2.

MBP-NLRP3 Peak 1 was shown to have a hydrodynamic radius of 30.7 nm, related to a high degree in aggregation. In contrast, MBP-NLRP3 Peak 2 shows a low degree of aggregation and a hydrodynamic radius of 11.1 nm. In comparison, batch-DLS measurements revealed an average radius of 13.5 nm, corresponding to a theoretical mass of 1.47 MDa, whereas MALS analysis resulted in a molar mass of 1.62 MDa for MBP-NLRP3 Peak 2. Relative to the molecular weight of the monomer (~165 kDa), Peak 2 corresponds to a decamer. In order to further analyse the oligomeric state of MBP-NLRP3 Peak 1 and Peak 2, the protein was examined by negative-stain electron microscopy.

MBP-NLRP3 Peak 2 reveals single particle structures, without aggregate contamination, in contrast to Peak 1, which shows a higher degree of impurities, as well as vesicular structures and larger protein aggregates (Figure 23 B: b and c).

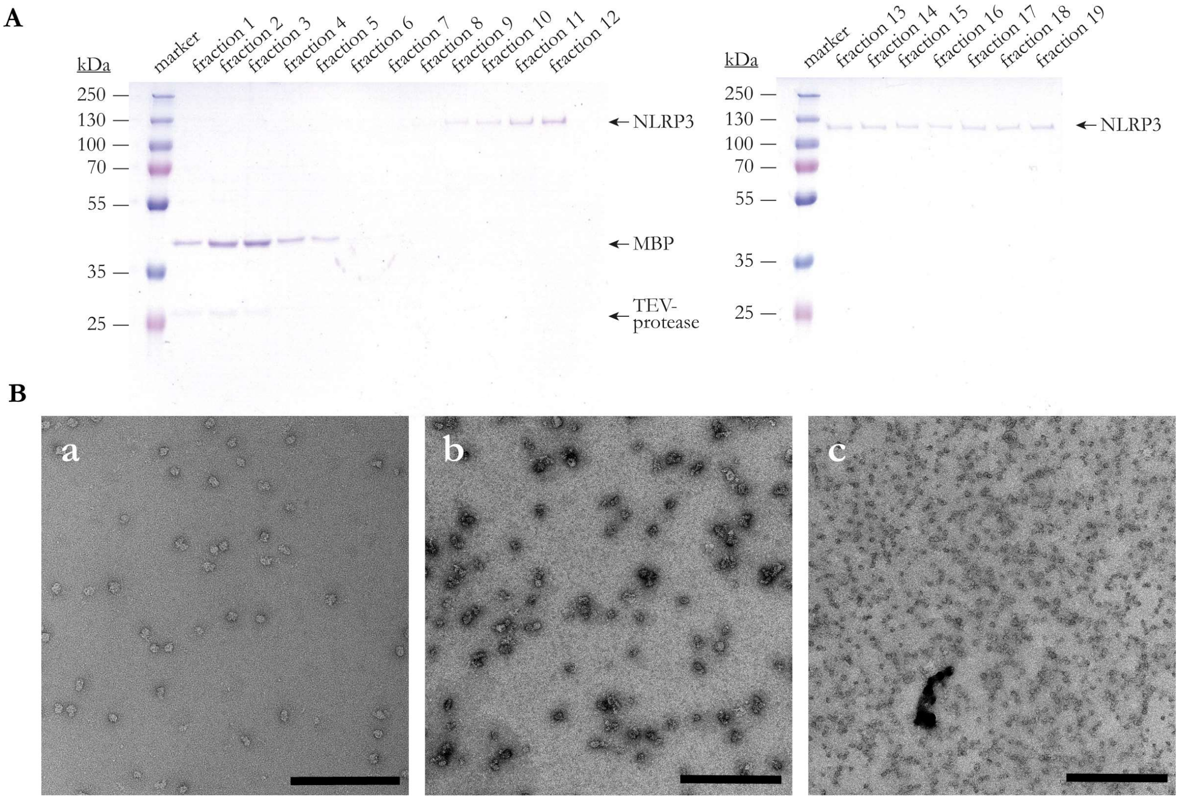

Figure 23: NLRP3 and MBP-NLRP3 is analysed by transmission EM. A: MBP-NLRP3 (800 pmol) was TEV-cleaved o/n at 4°C and subsequently subjected to a sucrose-gradient ranging from 10-40%. The SDS-PAGE (12%) shows individual 200 µL fractions of the sucrose gradient. **B:** Negative-stain EM images of MBP-NLRP3 Fraction 12, displayed in A, of TEV-cleaved NLRP3, purified by a sucrose gradient purification (a). The scalebar corresponds to 200 nm. Further, untreated MBP-NLRP3 protein Peak 1 (b), Peak 2 (c), is shown, which w previously purified by gel filtration on a Superose 6 10/300 GL increase column. The scalebar corresponds to 500 nm.

Moreover, TEV-cleaved NLRP3 Peak 2 showed single particle structures similar to the uncleaved protein sample, indicating an oligomeric state independent of the MBP-tag. Instead of purification by gel filtration, the TEV-cleaved NLRP3 sample was further subjected to a sucrose gradient of 10-40%. This alternative method allowed for gentler protein purification, resulting in clear single particle structures, without impurities and aggregates (fraction 12). According to the sucrose gradient composition, this fraction was calculated to include octameric, nonameric and decameric protein complexes. These results matched the SEC-DLS measurements, thus revealing NLRP3 to assemble into an dynamic equilibrium of octameric to decameric oligomers.

In order to further analyse the quartenary assembly of MBP-NLRP3, the thermal stability of the protein peaks was investigated in presence of potentially stabilizing reagents like ADP and ATP.

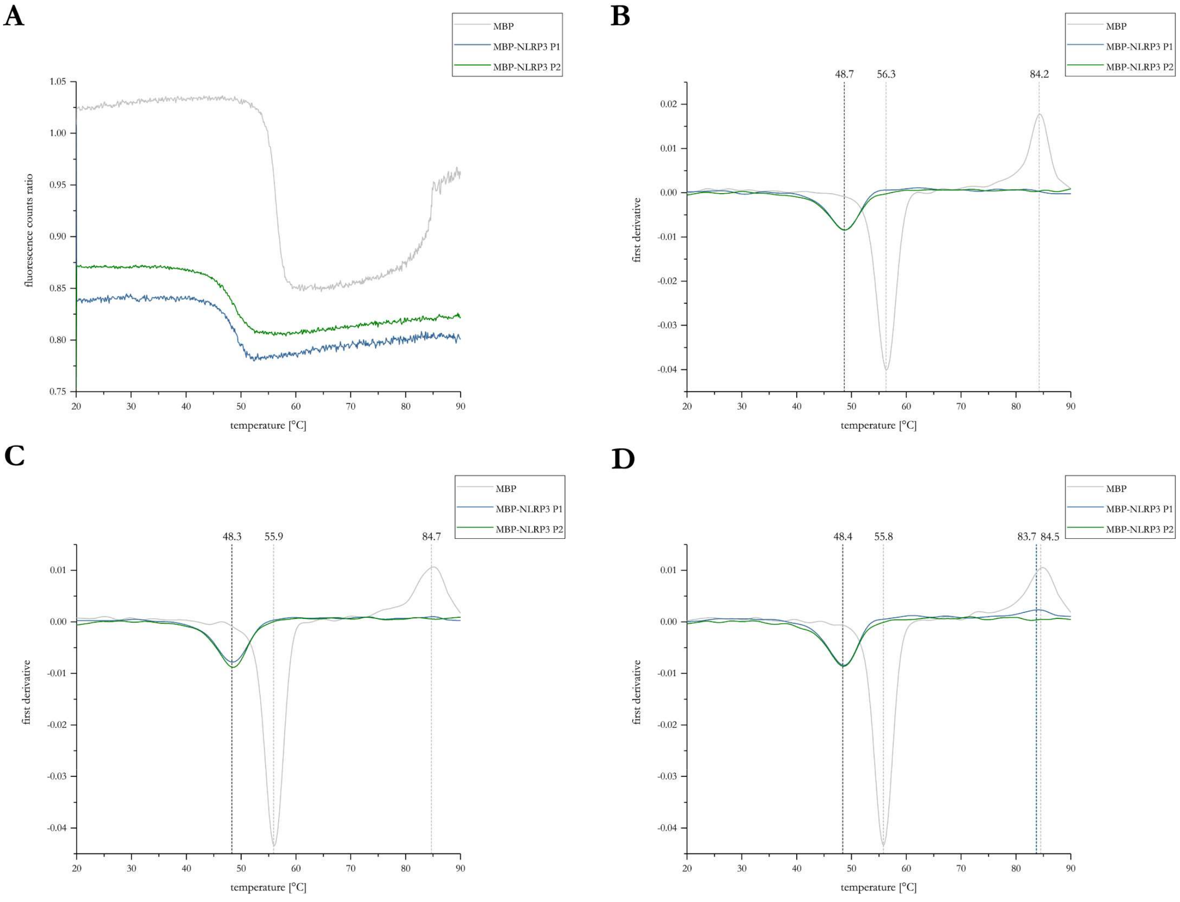

Figure 24: Thermal stability and unfolding of NLRP3 Peak 1 and Peak 2 in presence of nucleotide. A: Intrinsic fluorescence ratio (350 nm/330 nm) of MBP-NLRP3 Peak 1 (P1) and Peak 2 (P2), as well as MBP in showing thermal denaturation in a temperature range from 20°C to 90°C. **B:** First derivative of the intrinsic fluorescence ratio shown in A. The determined maxima represent the T_m, labelled in [°C] and indicated by a dashed line. **C-D:** First derivative of intrinsic fluorescence ratio (350 nm/330 nm) of MBP-NLRP3 Peak 1(P1) and Peak 2 (P2), as well as MBP in the presence of 5 mM $MgCl_2$ and 100 µM ADP **(C)** and ATP **(D)**, determined in a temperature range from 20°C to 90°C. The calculated maxima represent the respective T_m, labelled in [°C] and indicated by a dashed line.

As NLRP3 belogs to the family of STAND AAA+ ATPases, it is assumed that nuleotides like ADP and ATP could influence the protein's stability.

MBP-NLRP3 Peak 1 and Peak 2 as well as MBP were subjected to thermal denaturation in a temperature range from 20°C to 90°C using Differential Scanning Fluorimetry (nanoDSF). Independent of the elution peak, MBP-NLRP3 showed a melting temperature (T_m) of 48.7°C, whereas the control MBP, showed two distinct melting temperatures (Figure 24). The majority of the MBP sample denatured at 56.3°C, whereas a smaller fraction denatured at 84.2°C, indicating either a contamination or a second more stable MBP species being present in the sample. When incubated with the nucleotide ADP, the melting temperature of both MBP-NLRP3 peaks shifted simultaneously to 48.3°C. The control sample including MBP also showed a slight decrease in the melting temperature for the first species (T_m=55.9), when treated with ADP. The second species, present in the MBP sample slightly shifts to 84.7°C.

Interestingly, when incubated with ATP, the melting temperature of MBP-NLRP3 was nearly identical (T_m=48.4) for the main fraction of both peaks. A second melting point was determined for Peak 1 at 83.7°C, resembling the second species present in the MBP control sample (T_m=84.5°C). The majority of the MBP control sample denatured at 55.8°C, resembling the melting temperature determined in presence of ADP.

As only in the sample containing MBP-NLRP3 Peak 1, a second melting temperature was determined in the presence of ATP, a conformational change of the protein sample can be assumed, liberating the MBP and thus leading to an individual second melting curve.

8.1.5.1 Crystallographic analysis of NLRP3

Crystallographic approaches rely on protein samples that are highly pure and stable and allow for homogeneous crystal-packing. In order to optimize the crystallizing conditions of MBP-NLRP3, an mMBP fusion tag was chosen. The mMBP-tag was shown to enhance MBP solubility and thus facilitates affinity purification. Further, it was shown to provide crystal-packing interactions for increased crystallizability (Bokhove *et al.*, 2016). In total, 12 amino-acid residues have been mutated to achieve a higher protein crystallizability as well as an optimized protein purification. Moreover, a short linker sequence (Ala-Ala-Ala) was inserted between the mMBP-fusion tag and the passenger protein to reduce flexibility and facilitate fusion crystallization (Bokhove *et al.*, 2016).

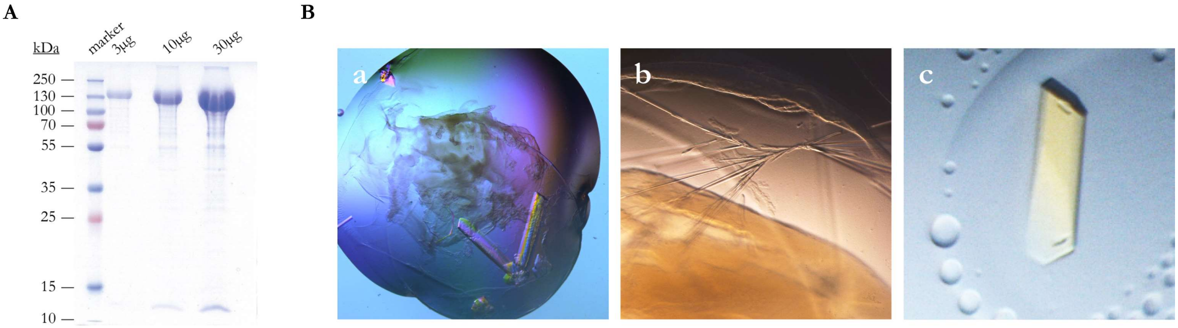

Figure 25: mMBP-NLRP3 Peak 2 was analysed in crystallographic trials. A: SDS-PAGE of mMBP-NLRP3 Peak 2, 3 µg, 10 µg and 30 µg were loaded for visualization of contaminating proteins in the sample. **B:** mMBP-NLRP3 Peak 2 was subjected to crystallization trials. Examples of generated crystals are shown (a and b). Also, the addition of ADP lead to crystal formation (c).

Based on this approach, human mMBP-NLRP3 Peak 2 was expressed and purified from *Sf9* insect cells and subsequently subjected to crystallization trials. The protein was purified to homogeneity, thus showing a low degree of either contamination or degradation. Varying conditions, like untreated protein or the addition of ADP and Mg^{2+} led to crystallization of mMBP-NLRP3 (Figure 25). Nonetheless, diffraction of the generated crystals was obtained to about 15 Å, thus the structure determination of mMBP-NLRP3 was not possible under these conditions.

8.2 ATP binding and hydrolysis of NLRP3

The activation mechanism of NLRP3 was shown to rely on ATP-binding, but the consequent fade of the ATP hydrolysis mechanism is not yet solved. Nontheless NLRP3 has been shown to exhibit ATP-hydrolysis activity (Duncan *et al.*, 2007). Also, NLRP3 inflammasome formation is abbrogated, in the presence of the specific inhibitor CY-09, for which direct interaction with the Walker A/B site in the ATP-binding site of NLRP3 was suggested (Jiang *et al.*, 2017). Moreover, decreasing intracellular ATP levels have been correlated with NLRP3 inflammasome activation (Nomura *et al.*, 2015). ATP-binding and hydrolysis of NLRP3 is of major interest in order to elucidate the underlying activation mechanism.

8.2.1 Model of the NLRP3 ATP binding site

Until now, no structural information about the NACHT-domains or ATP-binding sites of NLRP proteins is available. To overcome this problem, we designed and utilized a structural model based on the published structures of NLRC4 (PDB: 4KXF) or NOD2 (PDB: 5IRN).
The ATP-binding site of NLRP3 was modelled onto the auto-inhibited structure of NLRC4, including a bound ADP molecule (PDB: 4KXF) using the platform Swiss-Model (Waterhouse *et al.*, 2018). The predicted ATP-binding site resembles the typical fold of AAA+ ATPases, including the conserved β-strand arrangement of N-term-5-1-4-3-2-C-term (Figure 26). Further, the Walker A site, located on a loop downstream of β-strand 1 and the Sensor 1 motif, at the tip of β-strand 4, are found at the expected positions. Based on the alignment performed for NLRP1-14, the Walker A motif of NLRP proteins can be defined as GxxGxGKT, showing a small constrain to the consensus sequence of regular AAA+ ATPases A/GxxxxGKT/S (Wendler *et al.*, 2012). Typically, the Sensor 1 motif of AAA+ ATPases is formed by the residues TN at the tip of β-strand 4 (Wendler *et al.*, 2012). In contrast, members of the NLRP family show the consensus sequence LLxTxR at this position. Thus a highly variable residue is found at the equivalent position of the threonine residue and a positive residue (arginine) at the position of the polar, uncharged asparagine (N). A strong deviation in sequence conservation is found concerning the Walker B motif, located at the tip of β-strand 3. AAA+ ATPases show the consensus Walker B motif hhhhDE, whereas NLRPs show the consensus sequence LLFhhDGFDEL, in which h is corresponding to unconserved hydrophobic residues.

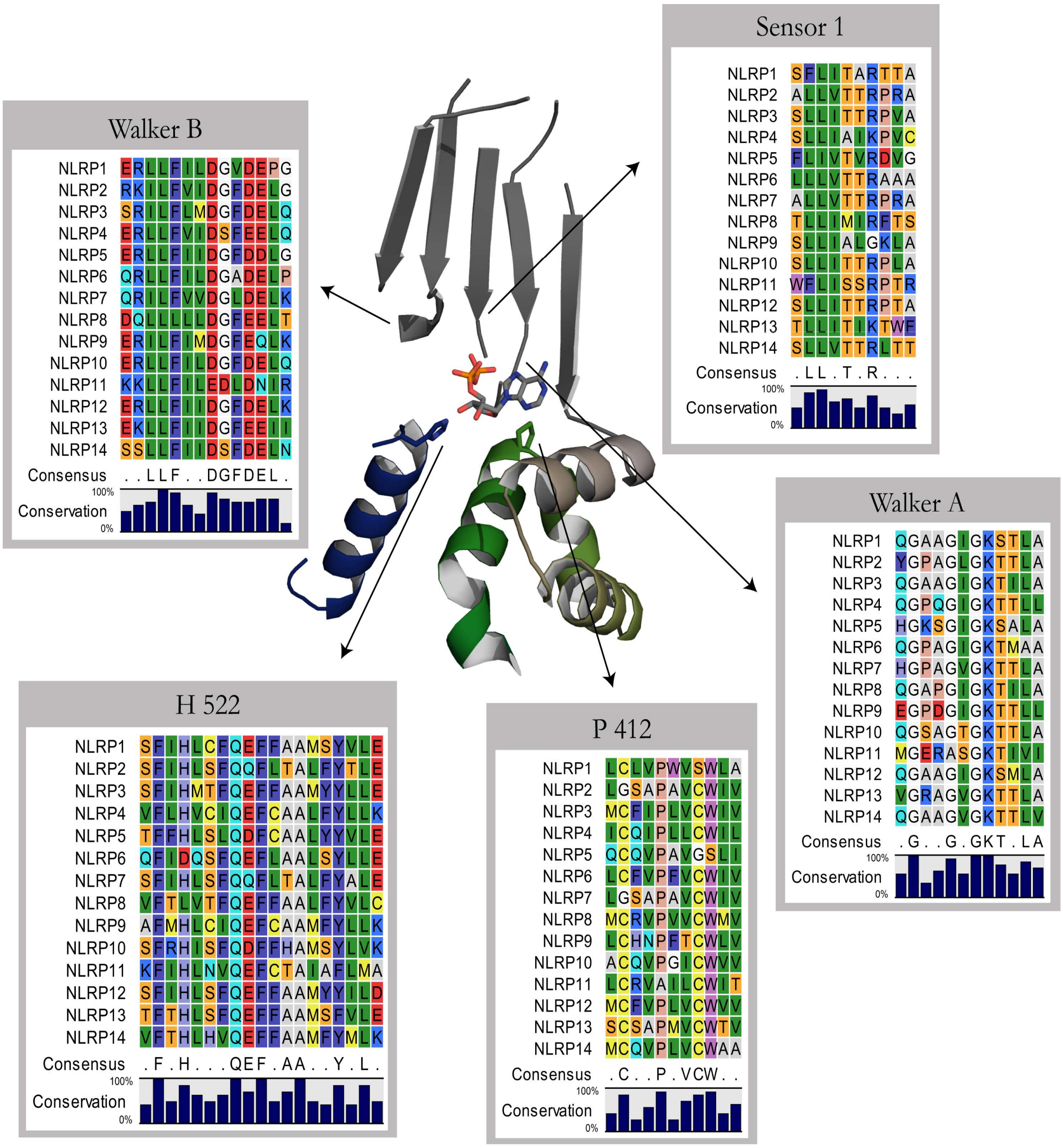

Figure 26: Model of the ATP-binding site of NLRP3. The ATP-binding site of NLRP3 is shown based on the autoinhibited structure of NLRC4 (PDB: 4KXF) including ADP. The Walker A and B motif as well as sensor 1 are shown in grey, H522 in blue (WHD), and P412 in green (HD1). Further, sequence alignments of the labelled sensor motifs and residues are shown for NLRP1-14.

Therefore, especially the investigation of the Walker B motif by point-mutations in NLRP3 is of major interest, in order to elucidate the function of the individual residues. The typical Walker B motif of AAA+ ATPases is mimicked in order to investigate the influence on the ATPase activity of NLRP3.

As the sensor 2 motif (GAR), typically located on alpha-helix 7 downstream of β-strand 6 in AAA+ ATPases, is not conserved in NLRPs, the role of the suggested sensor 2 motif H522 is investigated by point-mutations (Proell *et al.*, 2008; Wendler *et al.*, 2012). The conserved histidine residue is located at the tip of a highly conserved helix in the WHD-domains of NLRPs, suggesting a crucial role in either protein folding or ATP-hydrolysis. An additional conserved residue was identified by sequence alignment analysis: at the tip of the fourth helix in the HD1 domain of NLRPs, a conserved proline is found, which, similar to the H522 residue, is located in close proximity to the ADP moity in the predicted ATP-binding site of NLRP3.

Again, also the involved helix and the proline residue might be important for protein folding and function. In order to analyse the ATP-binding site of NLRP3, the described motifs were subjected to point-mutations. Based on the analysis by sequence alignment, point-mutations were introduced in the Walker A motif, Walker B motif, sensor 1 (R351) and a further potential sensor motif at position H522. Gel filtration of MBP-NLRP3 harbouring diverse point-mutations, respectively, resulted in elution profiles depicting one distinct peak, eluting at 8.5 mL at RT (Figure 27).

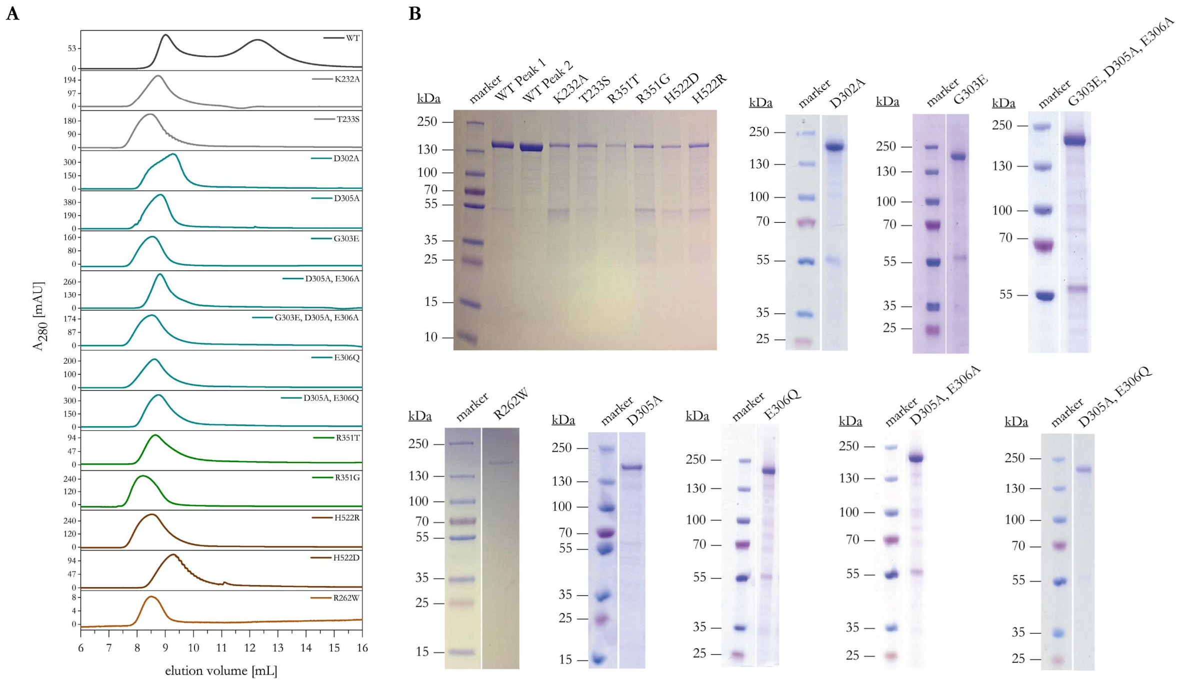

Figure 27: Gel filtration chromatograms for MBP-NLRP3 ATP-binding site mutants. A: The x-axis shows the elution volume [mL] and the y-axis displays the absorbance at 280nm in mAU units. The point mutations are indicated for each chromatogram. The chromatograms are sorted in dependence of the mutated motif, the wt is shown in black, the Walker A motif in grey, the Walker B motif in blue, sensor 1 in green, the H522 motif in brown and the CAPS mutant R262W in orange. **B:** Corresponding SDS-PAGE showing MBP-NLRP3 ATP-binding site variants analysed in A.

Two single point-mutations were introduced in the Walker A motif, K232A and T233S. Furthermore, several single point-mutations were introduced in the Walker B motif of NLRP3: D302A, G303E, D305A, E306A, E306Q, as well as the combinations: D305A/E306A and D305A/E306Q. In order to reconstitute a typical Walker B motif of AAA+ ATPases, the following triple mutation was introduced: G303E/D305A/E306A. Moreover, the sensor 1 motif (R351) was mutated to analyse the importance of this residue in NLRP3. Two substitutions were tested: R351G, which mimics the sensor 1 motif of NLRP9, as well as R351T, exchanging the polar amino acid by another polar amino acid, known to be involved in the formation of the sensor 1 motif in NLRC4 (PDB: 4KXF). Typically, an asparagine, serine, threonine or aspartate residue is found at the position of sensor 1 in AAA+ ATPases, structurally located between the Walker A and Walker B sites, assisting the glutamate residue of the Walker B site during the nucleophilic attack of the water molecule during ATP-hydrolysis (Miller & Enemark, 2016).

An additional mutated residue is H522. This position was modelled to be in a close proximity to the ATP-binding site of NLRP3. Hence, it is assumed, that this residue might also be involved in the coordination of the ATP-hydrolysis. In order to investigate the effect of this residue, two mutations were introduced (H522D and H522R) to determine the effect of charged residues on the ATP-hydrolysis reaction of NLRP3.

Within the predicted Glu-Switch region, the CAPS mutation R262W was investigated, to analyse its effect on the ATP-hydrolysis as well as to get insights into the molecular interplay and the involvement of disease mutations in the function of the protein.

As shown in Figure 27, the mutant proteins were purified to homogeneity and further analysed by gel filtration on a Superose 6 10/300 increase coloum at RT. Interestingly, the wild-type protein eluted in two distinct peaks, as described before, whereas each of the analysed NLRP3 variants eluted in a single peak only. The Walker B variant D305A, showed a deviating peak structure, as a smaller peak is eluting near the void volume of the coloum, which devolves into a shoulder-shaped second peak at about 9.5 mL. The NLRP3 variant H522D also showed a deviating elution profile: the protein eluted in a single peak which is slightly shifted towards 9.0 to 9.5 mL. Importantly, the analysed NLRP3 mutants eluted in single peaks which did not show a symmetric peak shape, hence inhomogeneous protein oligomers are expected to underly each of the purified protein species.

8.2.2 Analysis of the NLRP3 hydrolysis activity

Recombinantly expressed and purified MBP-NLRP3 (wt) was shown to elute in two distinct peaks, when subjected to gel filtration chromatography (Figure 20 A). In order to analyse the ATP hydrolysis activity of NLRP3 initial experiments were performed using the Malachite Green Phosphate Assay, thus detecting the release of P_i.

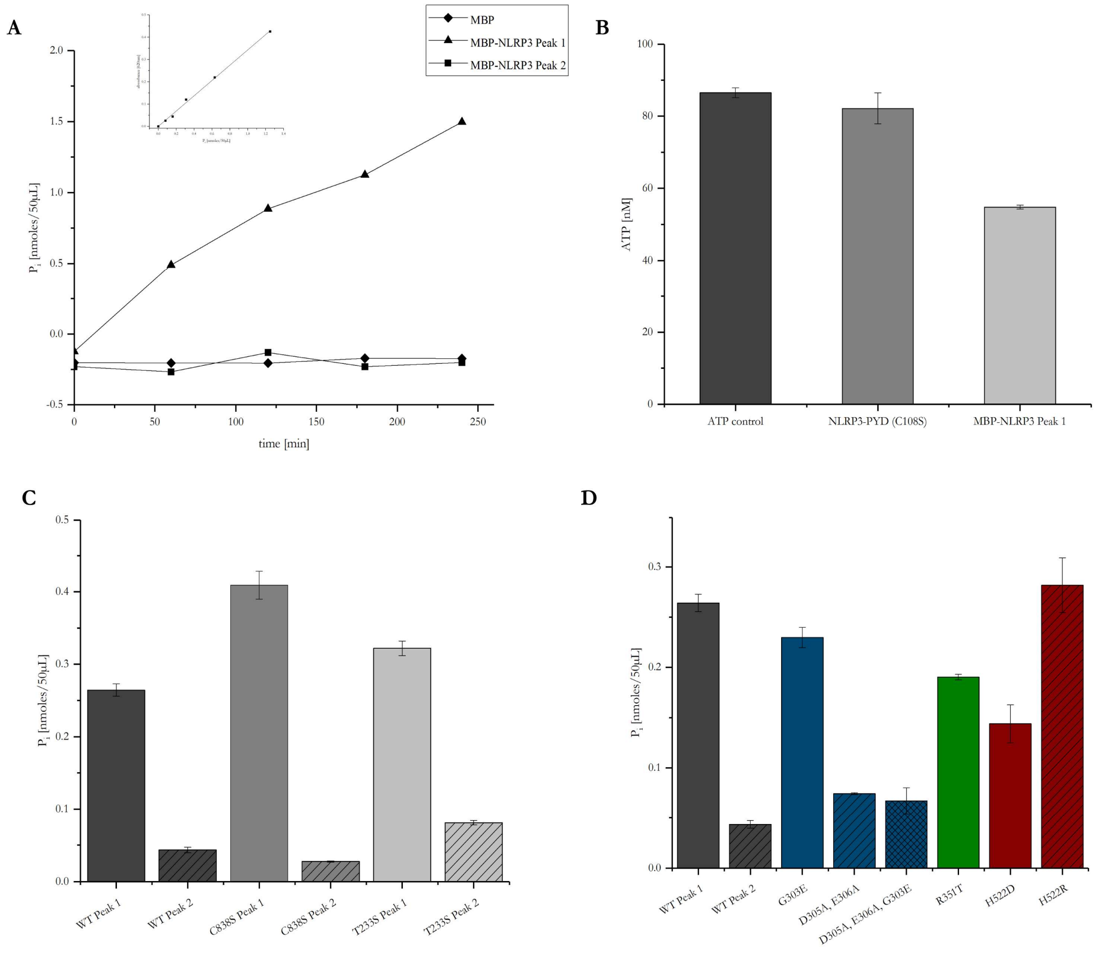

Figure 28: ATP hydrolysis activity of NLRP3. The Malachite Green Phosphate Assay (A,C,D) and the Luminescence ATP detection Assay were used to determine the ATP hydrolysis activity of MBP-NLRP3. **A:** The amount of P_i was measured over 240 min. MBP-NLRP3 Peak 1 and 2 (0.4 µM) were incubated at 20°C in the presence of 1 mM ATP and $MgCl_2$. MBP was included as control. n=1 The standard curve is included. **B:** The amount of ATP was determind over a time course of 2 hours at RT. MBP-NLRP3 and NLRP3-PYD (3-110, C108S) (0.5 µg) were incubated in the presence of 100 nM ATP and $MgCl_2$. n=1, tech. duplicates **C, D:** The amount of P_i generated in the presence of 1 mM ATP and $MgCl_2$ was determined using the Malachite Phosphate Assay after 90 min incubation at 22°C and MBP-NLRP3 mutants (0.4 µM). **C:** The ATP-hydrolysis activity of MBP-NLRP3 wt, C838S and T233S, each showing Peak 1 and Peak 2, is compared. **D:** Several point mutations in the ATP-binding site are analysed and compared to MBP-NLRP3 wt Peak 1 and Peak 2 with respect to the amount of P_i generated. N=1, tech. duplicates

Differences between the two peak species have been determined with respect to the size of the oligomer and the stability and melting temperature of the protein sample in presence of ATP and $MgCl_2$ (Figure 22 and Figure 24). Thus the ATP hydrolysis activity of the individual peaks was of major interest to further elucidate differences between the two species. ATP-hydrolysis was first determined using a Malachite Green Phosphate Assay and a Luminescence ATP Detection Assay. For both assays, the protein samples were incubated in the presence of ATP and $MgCl_2$. The Malachite Green Phosphate Assay revealed up to 1.497 nmoles/50µL (29.94 µM) of P_i for 0.4 µM of MBP-NLRP3 Peak 1 over 240 min, whereas no P_i was measurable for MBP-NLRP3 Peak 2 or the MBP control. Based on these data, a turnover rate of 0.312 ATP min^{-1} for MBP-NLRP3 Peak 1 was calculated, whereas no apparent hydrolysis could be determined for MBP-NLRP3 Peak 2. In consistance with these data, a decrease in ATP concentration of 31.72 nM was determined in a Luminescence ATP detection Assay, corresponding to a turnover rate of 0.079 ATP min^{-1} for MBP-NLRP3 Peak 1. Again, no hydrolysis activity was measurable for the NLRP3-PYD control sample. The MBP-NLRP3 point-mutants C838S and T233S both show two individual peaks when subjected to gel filtration chromatography at 4°C, were also analysed regarding the ATP hydrolysis activity of their individual peaks.

MBP-NLRP3 C838S and T233S show a similar ATP hydrolysis activity for Peak 1 compared to the wild-type MBP-NLRP3 protein, whereas Peak 2 again does not show hydrolysis activity. Additional point-mutations located within the Walker B, sensor 1 or sensor 2 (H522) residues were analysed in the Malachite Green Phosphate Assay (Figure 28 D). In contrast to the wild-type protein, these point-mutants did not show a second peak, when subjected to gel filtration chromatography, thus solely Peak 1 was analysed in the following experiments. In comparison to MBP-NLRP3 Peak 1, similar levels of Pi have been determined for the Walker B point-mutant G303E, as well as the sensor 2 mutant H522R. Slightly reduced ATP-hydrolysis was determined for the sensor 1 mutant R351T and the sensor 2 mutant H522D. Moreover, very low levels of P_i have been measured for the Walker B mutants D305A/E306A as well as G303E/D305A/E306A.

In a further approach, the ATP-hydrolysis activity of WT and mutant NLRP3 was analysed by RP-HPLC, in order to determine ATP turnover rates and to further characterize the ATP binding site of NLRP3.

By RP-HPLC the nucleotides are separated according to their charge (Figure 29) enabeling the calculation AMP/ADP/ATP ratios at given time points of the ATP hydrolysis reaction.

First, it was tested whether recombinantly expressed and purified MBP-NLRP3 Peak 2 harbours a bound nucleotide. Therefore, the protein sample was subjected to RP-HPLC. Neither the MBP control nor MBP-NLRP3 Peak 2 showed a peak corresponding to a bound nucleotide, thus MBP-NLRP3 Peak 2 is considered to have an empty nucleotide binding pocket when purified by affinity and gel filtration chromatography (Figure 29 B).

Next, the HPLC setup was used to monitor ATP hydrolysis and to determine hydrolysis rates for MBP-NLRP3 originating from Peak 1 and Peak 2, respectively. The protein samples were incubated for 60 min at 25°C in the presence of 100 µM of ATP and 5 mM $MgCl_2$. Every 10 min, a sample was injected onto the RP-HPLC column and the generated nucleotide elution profiles were detected by the absorbance at 254 nm. The peak areas were integrated and normalized to 100%, enabeling the calculation of nucleotide ratios.

Again, MBP-NLRP3 Peak 1 showed hydrolysis activity for ATP, whereas MBP-NLRP3 Peak 2 did not exhibit any hydrolysis activity (Figure 29 C and D).

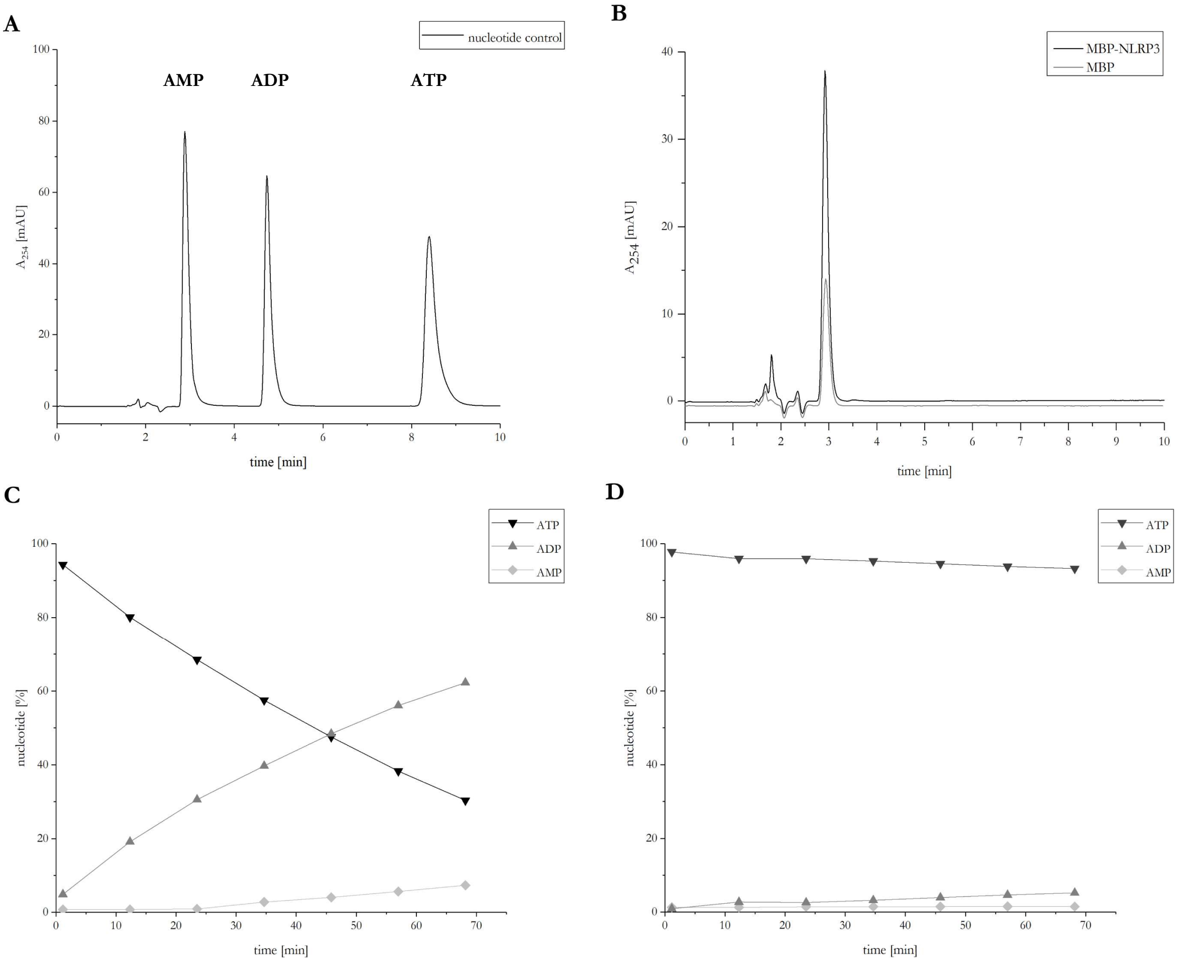

Figure 29: ATP-hydrolysis of MBP-NLRP3 is detected in Peak 1 but not in Peak 2. A: RP-HPLC measurement of nucleotide controls eluting at about 3 mL (AMP), at about 4.5 mL (ADP) and at about 8.5 mL (ATP). **B:** MBP and MBP-NLRP3 Peak have been subjected to RP-HPLC, both eluting at about 3 mL. **C,D:** MBP-NLRP3 Peak 1 **(C)** and Peak 2 **(D)** (3 µM) have been incubated at 25°C for 60 min in the presence of 5 mM $MgCl_2$ and 100 µM ATP. The amount of AMP, ADP and ATP, separated by RP-HPLC, was determined every 10 min by integration and adjusted to 100%. The nucleotide concentration is shown on the y-axis and the time is shown on the x-axis [min].

It has previously been published, that NLRP3 binds either ATP or dATP, but does not bind CTP, GTP or UTP (Duncan *et al.*, 2007). In order to ellucidate the hydrolysis activity of NLRP3 for nucleotides other than ATP, the protein MBP-NLRP3 Peak 1 was incubated with GTP, CTP and UTP in the presence of $MgCl_2$ and subjected to RP-HPLC. As shown in Figure 30, MBP-NLRP3 Peak 1 does not exhibit hydrolysis activity for the nucleotides GTP, CTP and UTP. Further, the dependence on $MgCl_2$, in the hydrolysis reaction of ATP was tested. MBP-NLRP3 Peak 1 did not show hydrolysis activity for ATP in the absence of $MgCl_2$, indicating the dependence on a Mg^{2+}-ion in the hydrolysis reaction.

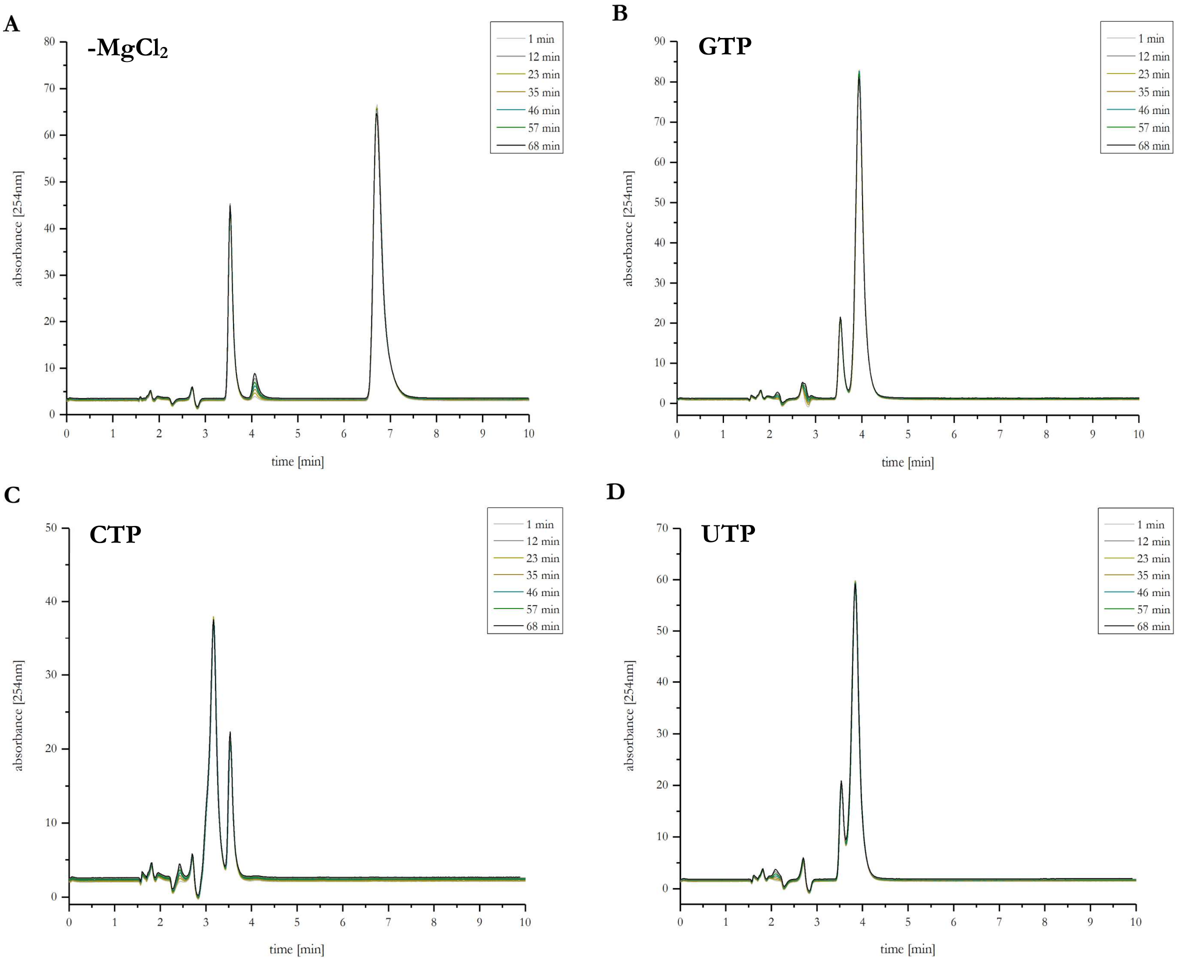

Figure 30: MBP-NLRP3 Peak 1 does not show hydrolysis activity for GTP, CTP, UTP and ATP in the absence of $MgCl_2$. A: MBP-NLRP3 Peak 1 (3 µM) was incubated at 25°C for 60 min in the presence of 100 µM ATP, but in the absence of $MgCl_2$. **B-D:** MBP-NLRP3 Peak 1 (3 µM) was incubated at 25°C for 60 min in the presence of 5 mM $MgCl_2$ and 100 µM GTP **(B)**, CTP **(C)** and UTP **(D)**. Samples were subjected to RP-HPLC every 10 min. The chromatograms show the absorbance at 254 nm on the y-axis and the time [min] on the x-axis. The peak eluting at ~ 3.5 min corresponds to the protein sample.

Alongside with the analysis of the hydrolysis activity of NLRP3, in control experiments, a potential consumption of non-hydrolysable ATP analogues was tested. MBP-NLRP3 Peak 1 was incubated in the presence of 100 µM ApNHpp and ApCH$_2$pp, respectively and subsequently analysed by RP-HPLC experiments (Figure 31). Nonhydrolysable ATP analogues like ApNHpp and ApCH$_2$pp have been shown to abolish ATP hydrolysis reactions, whereas a complete inhibition of the reaction is dependent on the protein tested. MBP-NLRP3 Peak 1 was shown to slightly utilize the ATP analogues ApNHpp and ApCH$_2$pp, whereas ApNHpp is consumed more effectively than ApCH$_2$pp. Hence, a higher binding affinity is assumed for the ATP analogue ApNHpp, compared to ApCH$_2$pp.

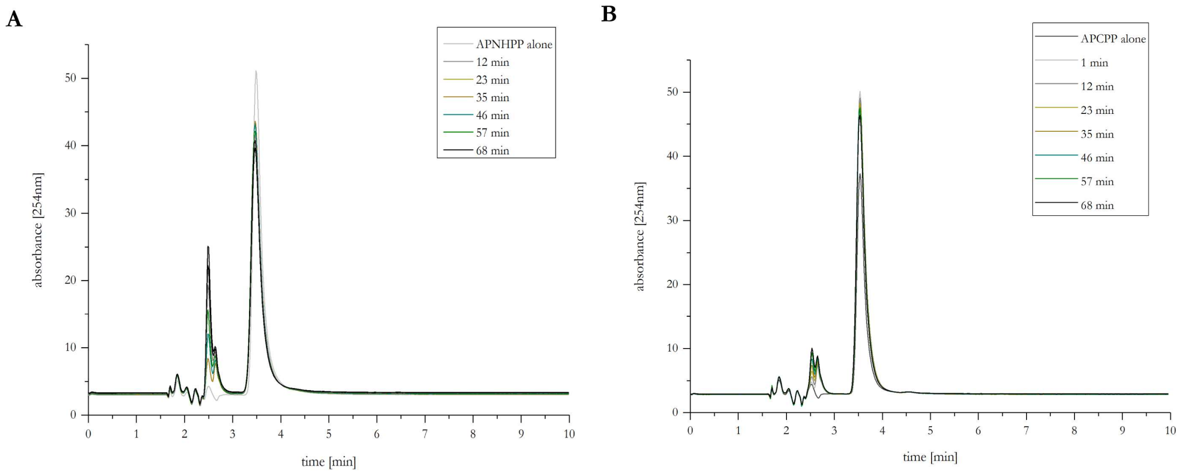

Figure 31: MBP-NLRP3 utilizes ATP analogues ApNHpp and ApCH$_2$pp. MBP-NLRP3 Peak 1 was incubated at 25°C for 60 min in the presence of 5 mM MgCl$_2$ and nonhydrolysable ATP analogue. The samples were subjected to RP-HPLC every 10 min. Overlays of each run are shown. **A:** The sample was incubates with 100 µM of ApHNpp. **B:** The sample was incubated with 100 µM of ApCH$_2$pp. The y-axis shows the absorbance at 254 nm, whereas the x-axis shows the time [min].

8.2.2.1 Influence of the binding partner Nek7 on the ATP-hydrolysis of NLRP3

The NIMA-related serine/threonine kinase Nek7, has been shown to directly interact with murine NLRP3 via the LRR-domain (He *et al.*, 2016b; Shi *et al.*, 2016). The Nek7/NLRP3 interaction was shown to be dependent on K^+ efflux, thus representing a consequence of prior NLRP3 activation (He *et al.*, 2016b; Schmid-Burgk *et al.*, 2016). The NLRP3 inflammasome assembly, including the formation of ASC-Specks, was found to be dependent on the association of Nek7 to the protein complex, but independent on its kinase activity (He *et al.*, 2016b). As Nek7 was found to influence the activity and complex formation of the NLRP3 inflammasome, its influence on the ATP hydrolysis activity of NLRP3 was analysed by RP-HPLC measurements.

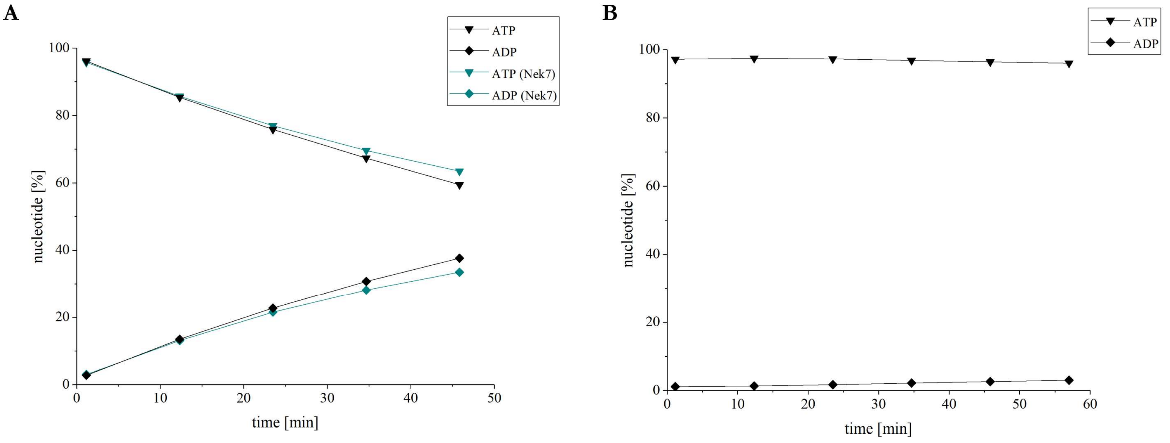

Figure 32: ATP hydrolysis activity of NLRP3 is independent of Nek7. A: MBP-NLRP3 Peak 1 (3 µM) was incubated at 25°C for 60 min in the presence of 100 µM ATP, 5 mM $MgCl_2$ and in the presence and absence of an equimolar concentration of Nek7. **B:** Nek7 (3 µM) was incubated at 25°C for 60 min in the presence of 100 µM ATP and 5 mM $MgCl_2$. Samples were subjected to RP-HPLC every 10 min. The chromatograms show the nucleotide [%] on the y-axis and the time [min] on the x-axis.

MBP-NLRP3 Peak 1 was incubated with Nek7 in a 1:1 molar ratio, in the presence of 5 mM $MgCl_2$ and 100 µM ATP and the resulting nucleotides were subsequently analysed by RP-HPLC. As shown in Figure 32 A, the presence of Nek7 does not change the ATP hydrolysis activity of MBP-NLRP3 Peak 1, as nearly identical amounts of ADP and ATP are produced by the hydrolysis reaction. In a control experiment, the kinase Nek7 was incubated in the presence of 5 mM $MgCl_2$ and 100 µM ATP, in order to test for intrinsic ATP hydrolysis. As shown in Figure 32 B, the kinase Nek7 does not exhibit ATP hydrolysis activity on its own.

8.2.2.2 Influence of small molecule inhibitors on NLRP3 ATP-hydrolysis

Small-molecule inhibitors targeting the NLRP3 inflammasome, promise a huge therapeutic benefit for a wide range of diseases, besides the known NLRP3-associated diseases like CAPS. CRID3 (MCC950) is a small molecule inhibitor, which selectively inhibits non-canonical and canonical NLRP3 activation in the nanomolar concentration range (Coll *et al.*, 2015). Therefore, the effect of CRID3 (MCC950) on the ATPase activity of NLRP3 was tested by RP-HPLC measurements, to clarify the underlying mechanism of action.

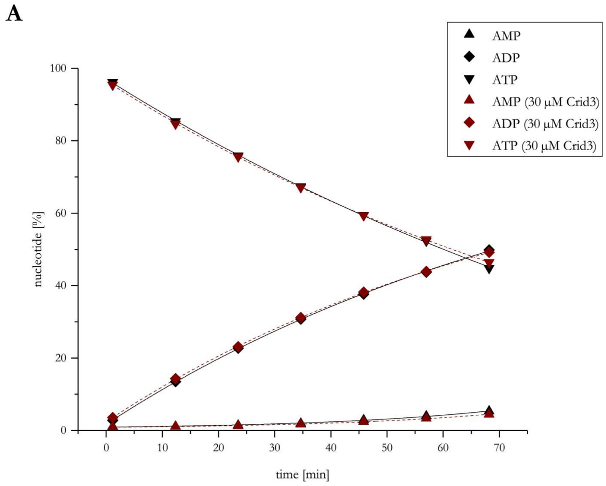

Figure 33: The small molecule CRID3 (MCC950) does not influence ATP-hydrolysis of MBP-NLRP3 Peak 1. A: MBP-NLRP3 Peak 1 (3 μM) was incubated at 25°C for 60 min in the presence of 100 μM ATP, 5 mM $MgCl_2$ and 30 μM CRID3 (MCC950). The relative nucleotide concentration [%] is shown on the y-axis, the time [min] on the x-axis.

Recombinantly expressed and purified MBP-NLRP3 Peak 1 was incubated with 100 μM ATP and 5 mM $MgCl_2$ in the presence of 30 μM CRID3 (MCC950), dissolved in DMSO. In order to monitor the shift in nucleotide abundance over time, the sample was subjected to RP-HPLC measurements (Figure 33). In presence of CRID3 (MCC950), the resulting nucleotide abundance was exactly equivalent to a DMSO control. Thus, CRID3 (MCC950) was shown not to influence the ATPase activity of MBP-NLRP3 Peak 1.

Recently, a novel small molecule inhibitor of NLRP3 has been identified: CY-09 (Jiang *et al.*, 2017). The inhibitor was shown to directly interact with NLRP3 (K_D: ~500 nM). Moreover, by a luminescent ADP detection assay CY-09 was shown to inhibit the ATPase activity of NLRP3 (Jiang *et al.*, 2017). In order to investigate the effect of CY-09 on the ATP hydrolysis activity of MBP-NLRP3 Peak 1 and Peak 2, RP-HPLC measurements were performed.

MBP-NLRP3 Peak 1 was incubated in the presence of 100 µM ATP, 5 mM $MgCl_2$ and increasing concentrations of CY-09. As shown in Figure 34 A, concentrations up to about 10 µM of CY-09 did not result in a change in ATP-hydrolysis activity of NLRP3, whereas higher concentrations up to 100 µM lead to an increase in ATP consumption. Interestingly, a time-course experiment analysing MBP-NLRP3 Peak 2 in the presence of 100 µM ATP, 5 mM $MgCl_2$ and 100 µM CY-09 did not reveal any change in ATPase activity.

Therefore, stimulating effect of the NLRP3 ATPase activity is restricted to very high concentrations and not determined for MBP-NLRP3 Peak 2. Nonetheless, a decrease in ATPase activity was not confirmed for neither of the tested MBP-NLRP3 species.

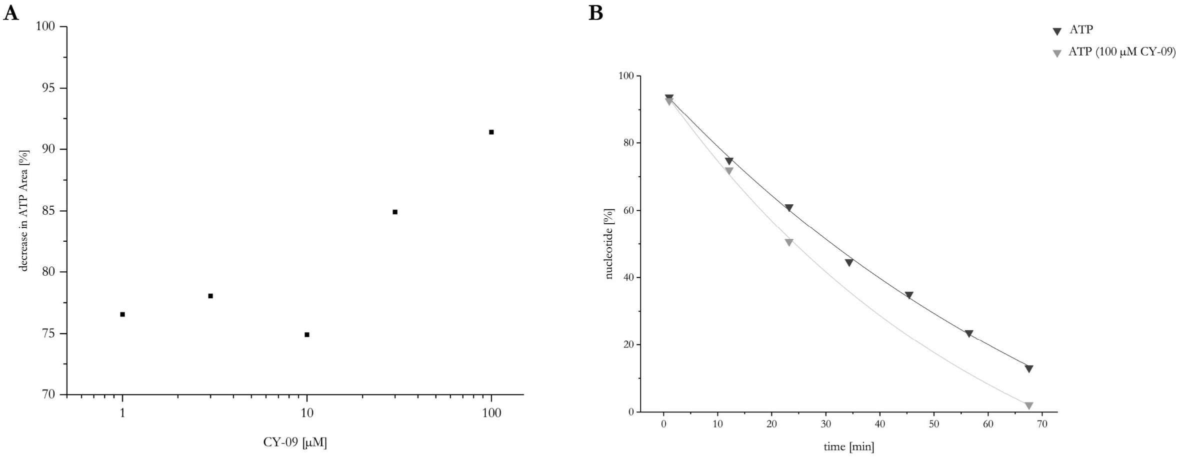

Figure 34: The small molecule CY-09 increases ATP-hydrolysis of MBP-NLRP3 Peak 1. A: MBP-NLRP3 Peak 1 (3 µM) was incubated at 25°C for 60 min in the presence of 100 µM ATP, 5 mM $MgCl_2$ and in increasing concentrations of CY-09. The relative decrease in ATP [%] is shown on the y-axis, the respective concentration of CY-09 on the x-axis. **B:** MBP-NLRP3 Peak 2 (3 µM) was incubated at 25°C for 20 min and 60 min, respectively in the presence of 100 µM ATP, 5 mM $MgCl_2$ and 100 µM CY-09. The amount of ATP present [%] is shown on the y-axis, the time [min] on the x-axis.

8.2.3 Mutational analysis of the NLRP3 ATP binding site

Sequence alignments of NLRP1 to NLRP14 revealed that the ATP-binding pocket of NLRP3 contains well conserved motifs, like the Walker A motif, but, also motifs, like the Walker B motif divergent from the consensus NLRP sequence (Figure 26). In order to determine the role of the involved motifs and sensor residues in ATP hydrolysis, MBP-NLRP3 was subjected to a mutational approach, introduced in 8.2.1.

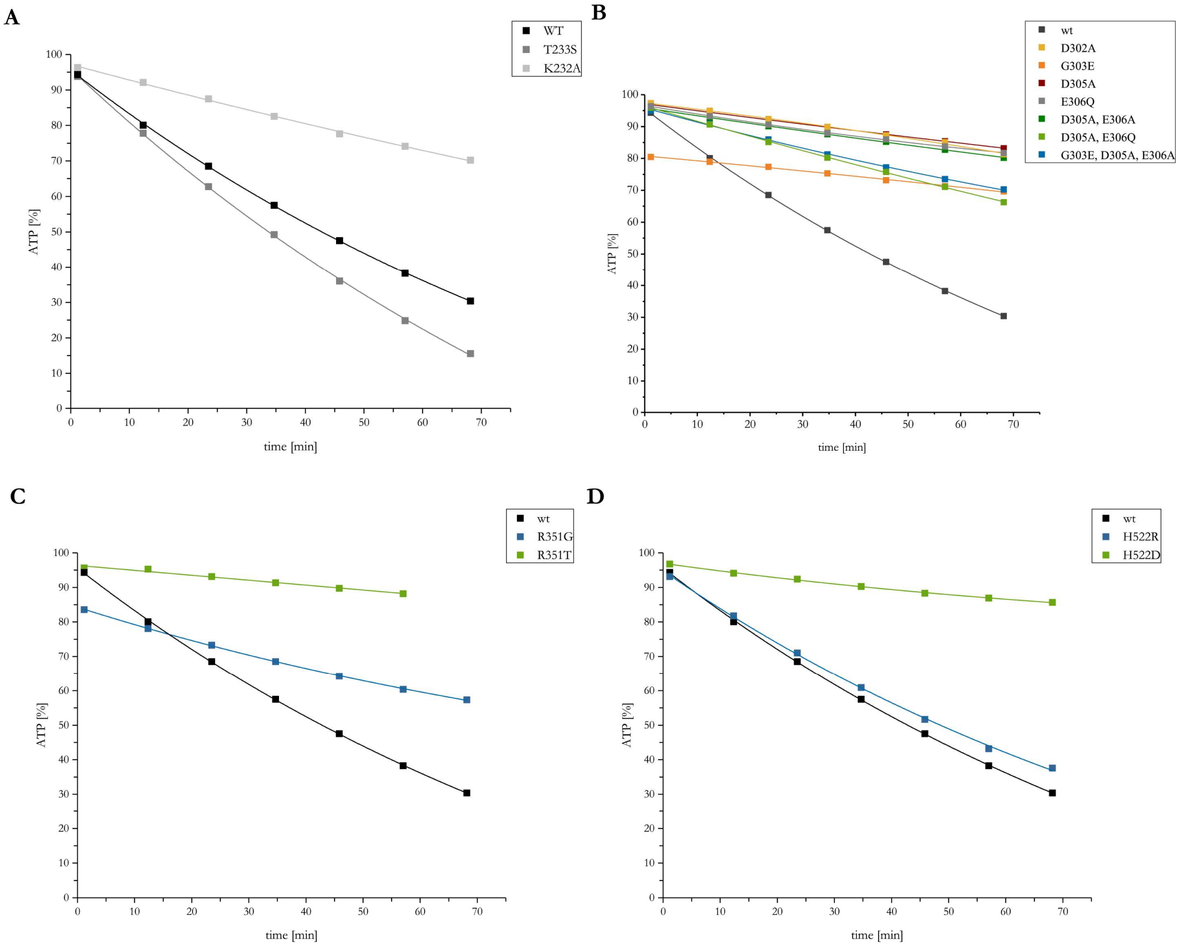

Figure 35: ATP-hydrolysis of MBP-NLRP3 ATP-binding site mutants. MBP-NLRP3 wt and point-mutants were analysed by RP-HPLC. **A-D** shows the amount of ATP [%] present on the y-axis and the time [min] on the x-axis. The protein samples [3 μM] were incubated at 25°C in the presence of 100 μM ATP and 5 mM $MgCl_2$. The amount of ATP [%] consumed is shown for MBP-NLRP3 point mutants in the Walker A motif **(A)**, Walker B motif **(B)**, the sensor 1 motif **(C)** and the residue H522 **(D)**. The amount of ATP, separated by RP-HPLC, was determined every 10 min by integration and adjusted to 100%.

In AAA+ ATPases, the Walker A lysine residue (NLRP3: K232), was shown to interact with both, the β- and the γ-phosphate of the bound ATP molecule. Mutations of the lysine residue have been shown to cause a loss in ATP binding and consequently a loss in ATP hydrolysis activity (Wendler *et al.*, 2012). In order to adress this finding, a K232 to alanine mutation in the Walker A motif was introduced.

Table 6: Nucleotide change rates resulting from ATP-hydrolysis measurements of MBP-NLRP3 variants. The ATP-hydrolysis reaction of MBP-NLRP3 Peak 1 and Peak 2, as well as of protein variants was analysed by RP-HPLC. The resulting slopes and rates [min^{-1}] are shown for the nucleotides AMP, ADP and ATP.

Mutant / nucleotide	Slope	Rate [min^{-1}]	Mutant / nucleotide	Slope	Rate [min^{-1}]
NLRP3 P1 AMP	0.104	0.035	D305A, E306A AMP	-0.009	*0.003*
NLRP3 P1 ADP	1.149	0.393	D305A, E306A ADP	0.261	0.087
NLRP3 P1 ATP	-1.156	**0.385**	**D305A, E306A ATP**	-0.252	**0.084**
NLRP3 P2 AMP	0.001	0.000	D305A, E306Q AMP	-0.004	*0.001*
NLRP3 P2 ADP	0.156	0.052	D305A, E306Q ADP	0.486	0.162
NLRP3 P2 ATP	-0.157	**0.052**	**D305A, E306Q ATP**	-0.484	**0.161**
K232A AMP	0.010	0.003	D305A, E306A, G303E AMP	-0.034	*0.011*
K232A ADP	0.387	0.129	D305A, E306A, G303E ADP	0.440	0.147
K232A ATP	-0.396	**0.132**	**D305A, E306A, G303E ATP**	-0.408	**0.136**
T233S AMP	-0.008	*0.003*	R351T AMP	0.001	0.001
T233S ADP	1.399	0.466	R351T ADP	0.152	0.051
T233S ATP	-1.391	**0.464**	**R351T ATP**	-0.112	**0.037**
D302A AMP	-0.006	*0.002*	R351G AMP	0.000	0.000
D302A ADP	0.229	0.076	R351G ADP	0.462	0.154
D302A ATP	-0.222	**0.074**	**R351G ATP**	-0.462	**0.154**
G303E AMP	-0.075	*0.025*	H522D AMP	-0.000	*0.000*
G303E ADP	0.213	0.071	H522D ADP	0.195	0.065
G303E ATP	-0.138	**0.046**	**H522D ATP**	-0.195	**0.065**
D305A AMP	-0.002	*0.001*	H522R AMP	0.006	0.002
D305A ADP	0.216	0.072	H522R ADP	0.986	0.329
D305A ATP	-0.214	**0.071**	**H522R ATP**	-0.992	**0.331**
E306Q AMP	0.002	0.001	R262W AMP	0.009	0.003
E306Q ADP	0.257	0.086	R262W ADP	0.604	0.201
E306Q ATP	-0.259	**0.086**	**R262W ATP**	-0.613	**0.204**

In contrast to the finding by Wendler et al. for AAA+ ATPases, RP-HPLC experiments of MBP-NLRP3 K232A revealed a residual ATPase activity of about 25%, rather than a complete loss of function. The consensus sequence of a typical Walker A motif in AAA+ ATPases is A/GxxxxGKT/S (Wendler *et al.*, 2012). Either a threonine or a serine residue is found in the Walker A site synonymously, thus an exchange of the corresponding residue in NLRP3 (T233) to serine is expected not have an impact on ATP hydrolysis. A mutation at this position allows for a control, which should not change ATP hydrolysis, but could show intact protein activity upon mutating the ATP binding site. In accordance with the results obtained in the Malachite Green Phophate Assay, hydrolysis activity of MBP-NLRP3 (T233S) was slightly increased (rate: 0.464 min^{-1}) compared to the wild-type NLRP3 protein.

Besides the Walker A motif, point-mutations in the Walker B motif have been investigated, as this motif shows high divergence when compared to a typical Walker B motif of AAA+ ATPases. NLRP3 harbours a degenerated Walker B motif (LLFhhDGFDEL), thus point-mutations were introduced and analysed by RP-HPLC to investigate the importance of the individual residues on ATP hydrolysis. The analysis of single point-mutations in the Walker B motif resulted in the following rates: D302A (0.074 min^{-1}), G303E (0.046 min^{-1}), D305A (0.071 min^{-1}), E306Q (0.086 min^{-1}) as well as the double mutant D305A/E306A (0.084 min^{-1}). These mutants show a reduction in ATPase activity by about 4.4-fold to 5.4-fold, compared to wild-type protein. A slightly higher hydrolysis activity was detected for the following two mutants: D305A/E306Q (0.161 min^{-1}) and G303E/D305A/E306A (rate: 0.136 min^{-1}), indicating a slight recovery in ATP hydrolysis by introduction of a glutamine residue instead of alanine and/or the typical consensus Walker B motif is generated by exchanging glycine (G303) to glutamic acid. These mutants showed a reduction in ATPase activity of about 2.4-fold and 2.8-fold, respectively. Nonetheless, none of the introduced mutations resulted in regular ATP hydrolysis, when compared to the wild-type protein. In conclusion, the residues D302, G303, D305 and E306 could been identified as critical residues, mediating ATP hydrolysis in NLRP3 and giving rise to an altered but functional Walker B motif in NLRPs.

The sensor 1 motif was found to be crucial in coordinating the attacking water molecule in ATP hydrolysis (Wendler *et al.*, 2012). Again, the corresponding residue in NLRP3 (R351) was investigated in a mutational approach, to determine its involvement in ATP hydrolysis. Sequence alignments of NLRP 1-14 revealed, that NLRP9 harbours a glycine residue at the respective position, rather than a positively charged residue, thus a corresponding variant of MBP-NLRP3 was generated to study its effect. Furthermore, an exchange of this residue to threonine was tested, to investigate the effect of the positive charge in the sensor 1 motif of NLRP3. RP-HPLC measurements revealed a decrease in ATP hydrolysis rates for both mutants (R351G and R351T). Whereas nearly no activity was measurable for the point-mutant R351T, an intermediate activity was observed for the mutant R351G, when compared to MBP-NLRP3 Peak 1. Compared to the wild-type protein, a 10-fold reduction of the ATP hydrolysis rate was determined for the mutant R351T (0.037 min^{-1}). In contrast, the ATPase activity of the variant R351G was only reduced by 2.5-fold. Therefore, also the sensor 1 residue (R351) can be confirmed as a crucial residue in the ATP hydrolysis of NLRP3.

Besides the regular motifs, which have been identified to regulate ATP hydrolysis in AAA+ ATPases and NLRPs, an additional motif is discussed to be part of the ATP binding pocket of NLRPs, termed sensor 2. The typical sensor 2 motif is not conserved in ATPases belonging to the STAND family. Here, a further residue was suggested to take over the function and being involved in nucleotide binding.

Between members of the NLRP family, a conserved histidine residue in the WHD domain was identified by sequence alignments and structural modelling, which was suggested to replace Sensor 2 in NLRP proteins (Proell *et al.*, 2008). The equivalent residue (H522) found in NLRP3 was analysed by RP-HPLC. Sequence alignments revealed, that NLRP6 harbours an Aspartic acid at the respective position, thus the point-mutation H522D was introduced into MBP-NLRP3. Further, a positive charged residue was introduced (H522R) to investigate the effect of charged residues at the suggested sensor 2 position on NLRP3 ATP hydrolysis. RP-HPLC measurements revealed a regular ATP hydrolysis rate for the point-mutation H522R (0.331 min^{-1}), whereas introduction of a negative charge abolished ATP hydrolysis activity, resulting in a rate of about 0.065 min^{-1}. The MBP-NLRP3 variant H522R showed a reduced ATPase activity of about 6-fold, when compared to the wild-type protein. Thus, H522 could be clearly identified as an important residue for the ATP hydrolysis activity of NLRP3, indicating this residue to take over the function of a typical Sensor 2 motif of AAA+ ATPases.

When comparing the different rates calculated from the slopes of each nucleotide, generated or consumed during the ATP hydrolysis reaction, three different phenomena become obvious. Besides the decrease in ATP concentration during ATP hydrolysis and the corresponding increase in ADP, also a slight increase in AMP concentration was detectable for the wild-type protein MBP-NLRP3 Peak 1. As shown in Figure 29, at a residual level of about 60% ATP and 40% ADP, the amount of generated AMP starts to increase linearilly, resulting in an AMP generation rate of about 0.035 min^{-1}. Hence, starting off from 100% ATP, the rate of AMP generation is only 10-fold lower compared to the rate of ATP-consumption. Interestingly, a single mutant shows the same ratio for the generation of AMP: the Walker B mutant D305A/E306A/G303E. This mutant shows an ATP hydrolysis rate of about 0.136 min^{-1} and also an AMP generation rate, which is about 12-fold reduced (0.011 min^{-1}). Interestingly, the single mutant G303E also shows a comparable phenomenon, but in this case, the rate of AMP generated is further reduced, though still measurable (0.025 min^{-1}), whereas the mutant shows an ATP hydrolysis rate of about 0.046 min^{-1}.

Moreover, four MBP-NLRP3 mutants do not show any AMP generation during the ATP-hydrolysis measurement: MBP-NLRP3 Peak 2, E306Q, R351G and H522D. The remaining mutants show a very reduced AMP generation rate, which is more than 10-fold reduced compared to the rate determined for MBP-NLRP3 Peak 1.

Alltogether, these phenomena indicate a second reaction, acting in parallel to the ATP hydrolysis reaction, that will be analysed in the following chapter.

8.3 Adenylate kinase activity, a novel function to NLRP3

8.3.1 NLRP3 shows adenylate kinase activity *in vitro*

The ATPase activity of NLRP3 has been linked to its activity to form active inflammasome complexes in immune cells. In accordance with its ability to bind ATP molecules, NLRP3 has beenen shown to also bind ADP, though exhibiting a lower affinity (Duncan *et al.*, 2007). Alongside with the analysis of the hydrolysis activity of NLRP3 by RP-HPLC experiments, in control experiments, a potential consumption of ADP was tested.

Interestingly, MBP-NLRP3 Peak 1 was found to consume ADP in the presence of $MgCl_2$, going along with an increase in AMP and a slight increase in ATP (Figure 36). This result clearly suggests a second mechanism, underlying the ATPase activity of NLRP3.

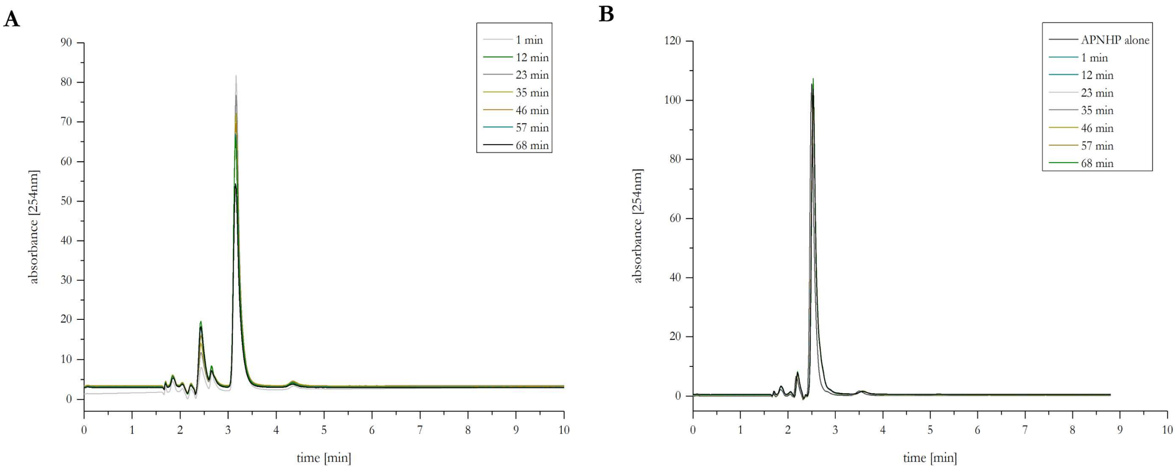

Figure 36: MBP-NLRP3 Peak 1 utilizes ADP but not ApNHp. MBP-NLRP3 Peak 1 was incubated at 25°C for 60 min, in the presence of 5 mM $MgCl_2$ and 100 µM ADP **(A)** or 100 µM of the nonhydrolysable ADP analogue ApNHp **(B)**. The samples were subjected to RP-HPLC every 10 min. The chromatograms show the absorbance at 254 nm on the y-axis, the time [min] is displayed on the x-axis.

In order to explain the observed phenomenon of AMP and ATP formation, the reaction mechanism of adenylate kinases was assumed for NLRP3. Typically, adenylate kinases (AK) convert one molecule of AMP and one molecule of ATP into two molecules of ADP (Figure 37A). As NLRP3 exhibits ATPase activity, this typical AK-reaction would hardly be detectible in the RP-HPLC assay, as the generated ATP would inevitably be hydrolyzed to ADP.

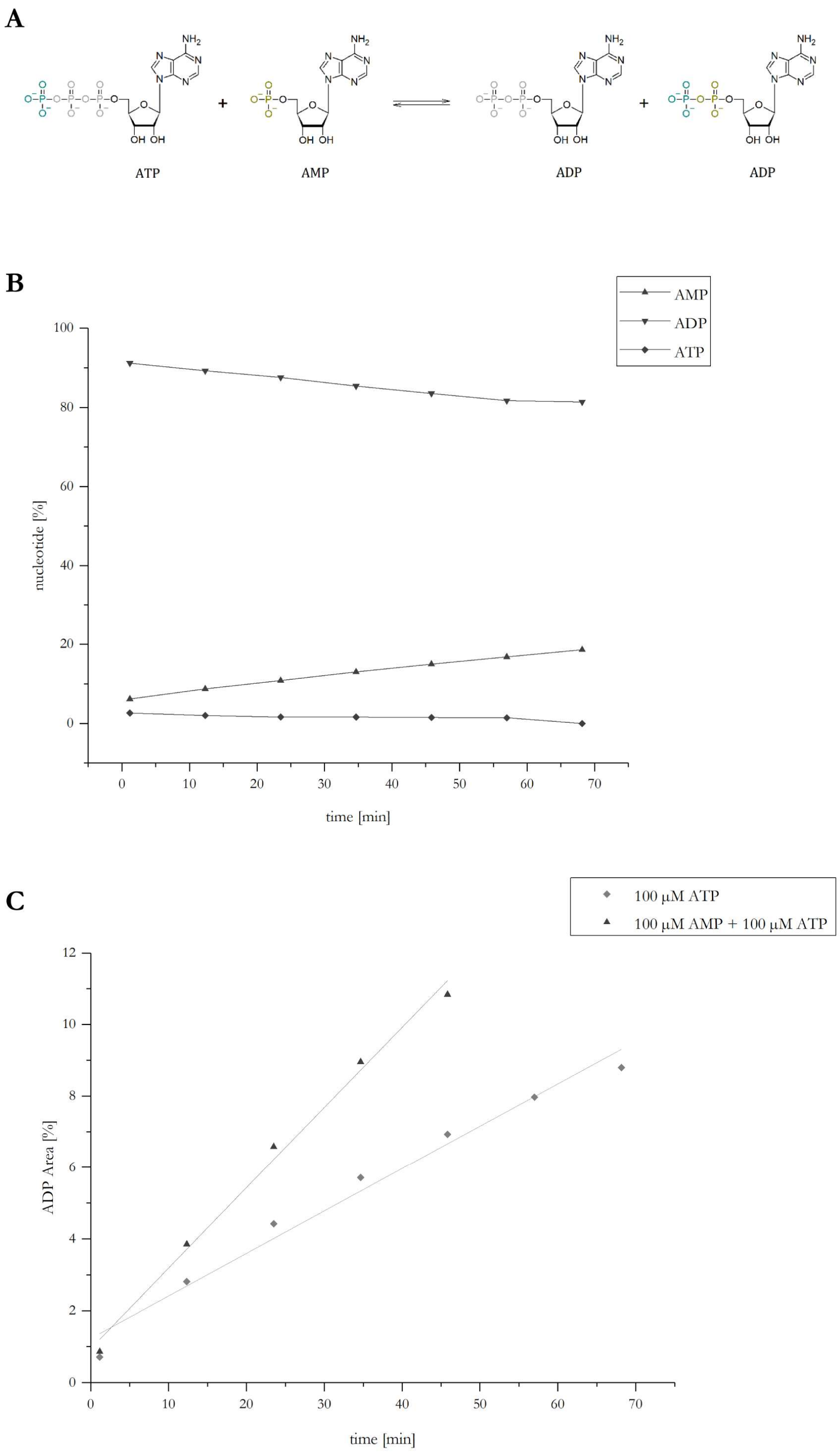

Figure 37: NLRP3 shows adenylate kinase activity. A: Forward and reverse reaction scheme of adenylate kinase activity. **B:** MBP-NLRP3 Peak 1 is incubated at 25°C for 60 min in the presence of 5 mM $MgCl_2$ and 100 µM ADP. The eluting nucleotides AMP, ADP and ATP are determined and displayed in nucleotide [%] on the y-axis, plotted against the time [min] on the x-axis. **C:** MBP-NLRP3 Peak 1 is incubated at 25°C for 60 min or 40 min in the presence of 5 mM $MgCl_2$ and 100 µM ATP as well as 100 µM AMP and ATP, respectively. The resulting amount of ADP is plotted in [%] on the y-axis, compared to the time [min] on the x-axis. Linear regression curves are plotted for both reactions, resulting in a slope of 0.119±0.008 (R^2=0.978) in the presence of ATP (ATPase) and a slope of 0.224±0.011 (R^2=0.993) in the presence of AMP and ATP (adenylate kinase).

To circumvent this problem, NLRP3 was tested for the reverse AK-reaction (ATP + AMP → 2 ADP). MBP-NLRP3 Peak 1 was incubated in 100 µM AMP and ATP each, in the presence of $MgCl_2$. The nucleotide turnover was monitored by RP-HPLC (Figure 37). Strikingly, MBP-NLRP3 Peak 1 showed an increased generation of ADP from ATP, when provided with AMP (Figure 37 C). To enable a direct comparison of nucleotide turnover in between the measurements, the relative abundance of AMP, ADP and ATP was plotted over time, and a slope was derived. For the generation of ADP from ATP only, a slope of 0.119±0.008 (R^2=0.978) was calculated. For the generation of ADP from ATP in the presence of an equimolar amount of AMP, a slope of 0.224±0.011 (R^2=0.993) was calculated. Stoichiometrically, this finding underlines the proposed assumption of NLRP3 having adenylate kinase activity.

In order to further investigate the adenylate kinase activity of NLRP3, two nucleotide analogues, Ap5A and ApNHp, were tested. The ADP analogue ApNHp was used to determine wether MBP-NLRP3 Peak 1 possesses the ability to utilize ApNHp in the adenylate kinase reaction. As shown before, MBP-NLRP3 Peak 1 was found to convert the ATP analogue ApNHpp into ApNHp (Figure 31). In contrast, the ADP analogue ApNHp is not utilized by MBP-NLRP3 Peak 1 (Figure 36).

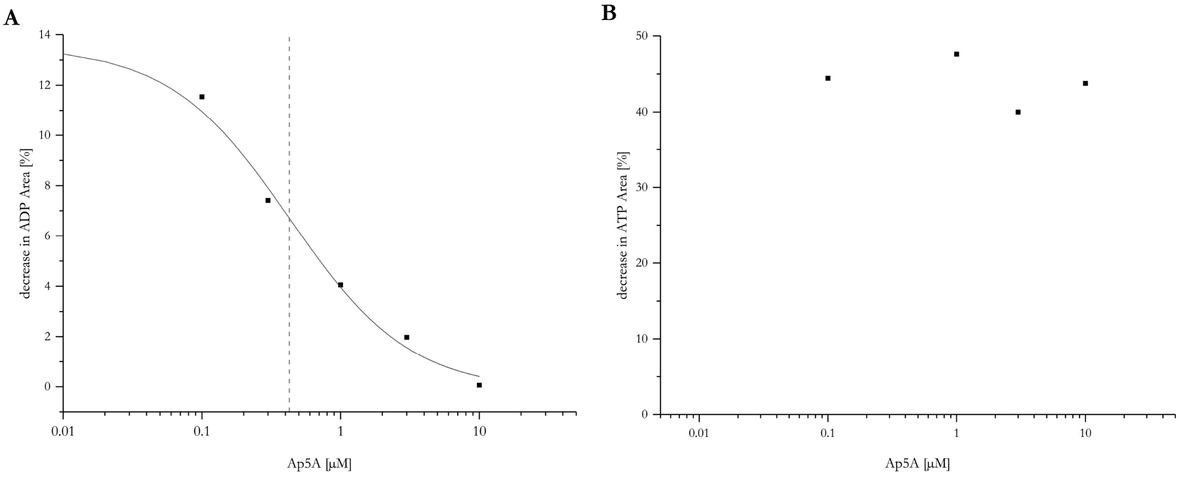

Figure 38: MBP-NLRP3 Peak 1 is inhibited by Ap5A. MBP-NLRP3 Peak 1 (3 µM) was incubated at 25°C for 60 min in the presence of 5 mM $MgCl_2$ and 100 µM AMP and ATP, respectively. The adenylate kinase inhibitor Ap5A was included in concentration ranging from 0.1 µM to 10 µM. **A:** The sample was incubated in the presence of 100 µM of ADP and Ap5A. On the y-axis, the decrease in ADP [%] is displayed; the concentration of Ap5A [µM] on the x-axis. **B:** The sample was incubated in the presence of 100 µM of ATP and Ap5A. On the y-axis, the decrease in ATP [%] is displayed; the concentration of Ap5A [µM] on the x-axis. The samples were subjected to RP-HPLC after 60 min of incubation.

The inhibitor Ap5A is known to specifically inhibit adenylate kinases, but not ATPases *in vitro* (Feldhau *et al.*, 1975). The adenylate kinase activity of MBP-NLRP3 Peak 1 was effectively inhibited the presence of 100 µM ADP, resulting in an IC_{50} value of 0.428 µM (Figure 38 A). In contrast, Ap5A did not inhibit the ATPase activity of NLRP3, when measured in the presence of 100 µM ATP (Figure 38 B).

As the adenylate kinase inhibitor Ap5A was found to effectively inhibit the AK-activity of MBP-NLRP3 Peak 1, the thermal stability of MBP-NLRP3 Peak 1 and Peak 2 was tested in presence of Ap5A.

Identical melting points were determined for MBP-NLRP3 Peak 1 and Peak 2, measured in the presence of the nucleotide ADP (Figure 24). Similar melting points were determined for both samples in the presence of ATP, whereas MBP-NLRP3 Peak 1 showed a second melting point at 83.7°C, resembling the melting point of MBP. Deviating from that, the incubation of both peaks spiecies with the inhibitor Ap5A resulted in two individual melting temperatures. MBP-NLRP3 Peak 1 showed a melting temperature of T_m=48.4°C, whereas MBP-NLRP3 Peak 2 resulted in a melting temperature of 48.7°C. Furthermore, a second melting point is implied for Peak 2, which resembles the melting point of MBP.

The occurance of a second melting point suggests a conformational change, which leads to liberation of the MBP-tag for MBP-NLRP3 Peak 2 in the presence of the inhibitor Ap5A.

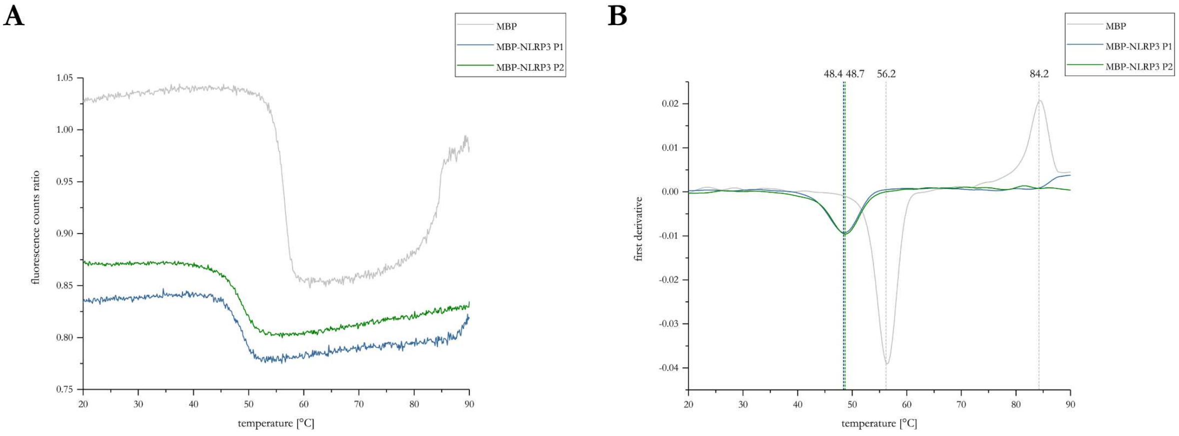

Figure 39: Thermal stability and unfolding of NLRP3 Peak 1 and Peak 2 in presence of Ap5A. A: Intrinsic fluorescence ratio (350 nm/330 nm) of MBP-NLRP3 Peak 1 (P1) and Peak 2 (P2), as well as MBP in showing thermal denaturation in a temperature range from 20°C to 90°C in the presence of 0.25 mM (MBP-NLRP3 Peak 1) and 1 mM Ap5A (MBP and MBP-NLRP3 Peak 2), respectively. **B:** First derivative of the intrinsic fluorescence ratio shown in A. The determined maxima represent the T_m, labelled in [°C] and indicated by a dashed line.

In order to further characterize the adenylate kinase activity of MBP-NLRP3 Peak 1, a second freshly expressed and purified protein sample was analysed. To compare the ATPase activity and the adenylate kinase activity of both samples, the protein was either incubated with 100 µM ATP, 100 µM AMP and ATP or 200 µM ADP in the presence of 5 mM $MgCl_2$ and subsequently subjected to RP-HPLC measurements.

As expected, the ATP hydrolysis rate determined for the second protein sample of MBP-NLRP3 Peak 1 incubated in the presence of 100 µM ATP was 0.385 min^{-1} (Table 6). Morover, the simultaneously determined ADP generation rate was 0.393 min^{-1}, whereas the rate determined for the generation of AMP was 0.035 min^{-1}.

The analysis of MBP-NLRP3 Peak 1 was shown to be inconsistent between alternating purifications. These results are summerized in the following part:

As shown in Figure 37, MBP-NLRP3 Peak 1 exhibits adenylate kinase activity, indicated by a doubled slope of ADP generated in the presence of AMP and ATP, compared to the measurement using ATP only.

Interestingly, the MBP-NLRP3 Peak 1 protein sample, originating from a second purification, revealed a deviating result. When supplied with 100 µM of AMP and ATP, the slope determined for the reduction of ATP is decreased (-0.960) compared to the measurement including ATP only (-1.156). In contrast, the slope calculated for the generation of ADP was also decreased, yielding a slope of 1.110, when incubated in the presence of AMP and ATP, compared to a slope of 1.149, determined in the presence of ATP. Furthermore, when incubated with AMP and ATP, a slope of -0.086 is determined for the reduction of AMP.
Comparing the proteins of both purification procedures and the respective slopes determined for the generation of ADP, two different results are determined.
In case of the sample originating from the first purification, yielding only a very slow ATP hydrolysis rate, the slope determined for the generation of ADP was determined as 0.119, whereas in the presence of AMP and ATP, a slope of 0.224 was determined. In case of the protein originating from the second purification, which shows a much higher hydrolysis rate, the slope of ADP generated in the presence of AMP and ATP is lowered, as described above.

Thus, the adenylate kinase activity seems to be dependent on the hydrolysis rate in general. In order to validate that the protein still possesses adenylate kinase activity, the reverse adenylate kinase reaction was tested. MBP-NLRP3 Peak 1 (second batch) was incubated in the presence of 200 µM ADP and 5 mM $MgCl_2$, resulted in a slope of 0.173 for the generation of ATP and a slope of 0.360 for the generation of AMP.
Thus, the reverse adenylate kinase reaction is measurable in both samples, irrespective of the ATP hydrolysis rate.

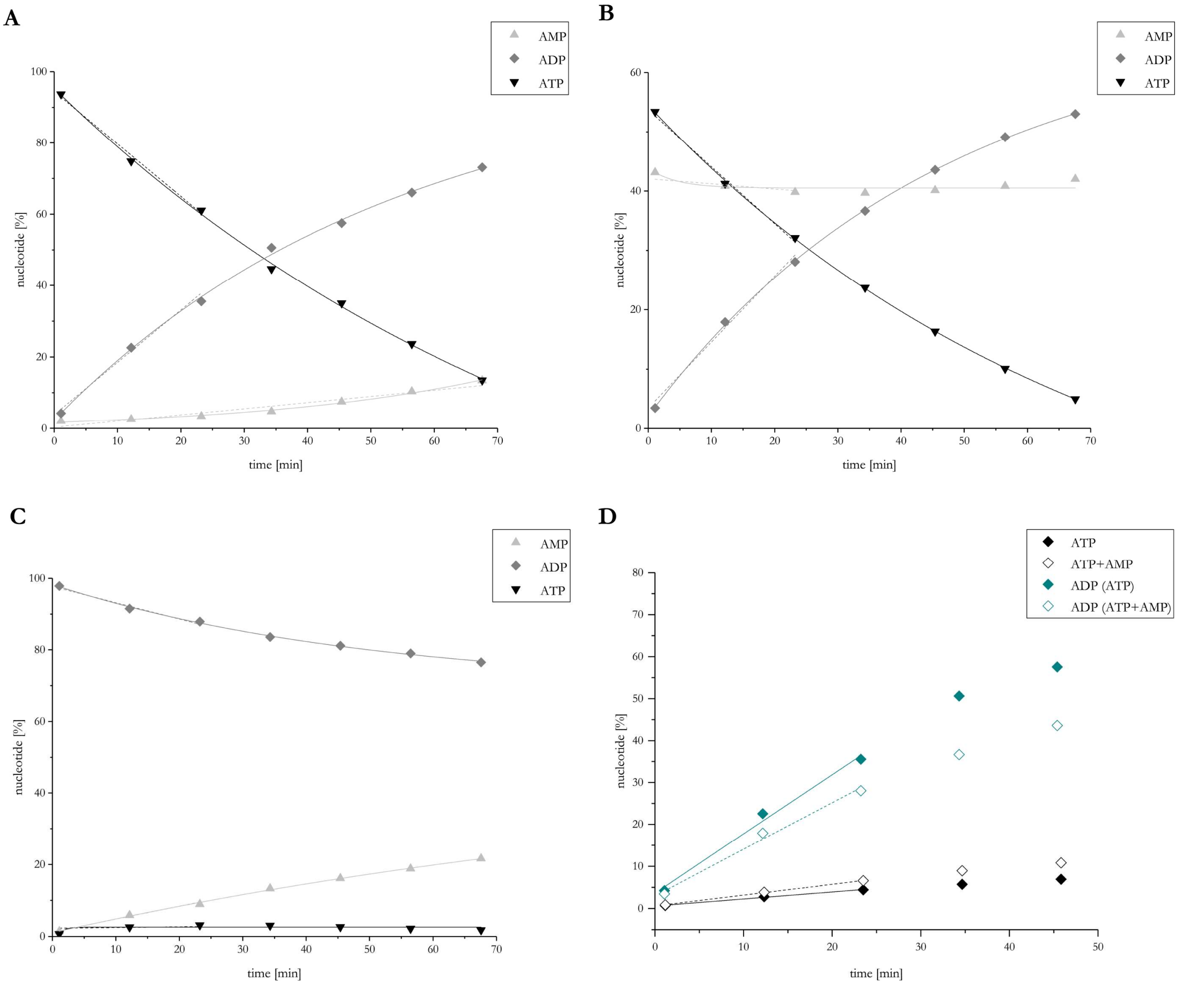

Figure 40: The adenylate kinase activity of NLRP3 is correlated with the ATP-hydrolysis rate of MBP-NLRP3 Peak 1. A: MBP-NLRP3 Peak 1 is incubated at 25°C for 60 min in the presence of 5 mM $MgCl_2$ and 100 μM ATP. The eluting nucleotides AMP, ADP and ATP are determined and displayed in nucleotide [%] on the y-axis, plotted against the time [min] on the x-axis. **B:** MBP-NLRP3 Peak 1 is incubated at 25°C for 60 min in the presence of 5 mM $MgCl_2$ and 100 μM AMP and ATP. The eluting nucleotides AMP, ADP and ATP are determined and displayed in nucleotide [%] on the y-axis, plotted against the time [min] on the x-axis. **C:** MBP-NLRP3 Peak 1 is incubated at 25°C for 60 min in the presence of 5 mM $MgCl_2$ and 200 μM ADP. The eluting nucleotides AMP, ADP and ATP are determined and displayed in nucleotide [%] on the y-axis, plotted against the time [min] on the x-axis. **D:** Two individually purified samples of MBP-NLRP3 Peak 1 are incubated at 25°C for 60 min in the presence of 5 mM $MgCl_2$ and 100 μM ATP as well as 100 μM AMP and ATP, respectively. The eluting nucleotides AMP, ADP and ATP are determined and displayed in nucleotide [%] on the y-axis, plotted against the time [min] on the x-axis. Linear regression curves are plotted, only in the linear curve area, as well as exponential curves to visualize the graph course.

8.3.2 Analysis of the NLRP3 adenylate kinase activity in a mutational approach

Previous data suggest a dual role for the ATP-binding site of NLRP3: ATP-hydrolysis activity as well as the adenylate kinase activity. In oder to further characterize the fuction and activity of NLRP3, ATP-binding site mutants, introduced in Figure 27, were generated and investigated regarding their ability to function as adenylate kinases.
Mutant MBP-NLRP3 Peak 1 was incubated in the presence of 5 mM $MgCl_2$ and either 100 µM AMP and ATP or 200 µM ADP, to analyse both directions of the adenylate kinase reaction. Changes is nucleotide ratios were monitored over time by RP-HPLC, normalized, and the slopes derived for nucleotide generation or consumption were calculated (Table 7). As the adenylate kinase reaction, going along with the underlying ATP hydrolysis reaction, does so far not allow for the calculation of a defined reaction equation, slopes rather than rates are determined to compare the different nucleotide effects, in these experiments.

Next, the AK activity of MBP-NLRP3 Peak 1 and Peak 2 was compared. For MBP-NLRP3 Peak 2, when incubated in the presence of 200 µM ADP, very low slopes were determined for the generation of the nucleotides AMP and ATP. Hence, adenylate kinase activity of MBP-NLRP3 Peak 2 is deviating from the AK activity determined for MBP NLRP3 Peak 1. When MBP-NLRP3 Peak 1 was incubated in 200 µM ADP, the resulting slopes for the generation of AMP and ATP appeared in a ratio of 2:1, thus doubled the amount of AMP was produced compared to ATP. In contrast, MBP-NLRP3 Peak 2 revealed a ratio of generated AMP to ATP of about 1:1, thus resembling the expected ratio typical for adenylate kinases.

The Walker A mutant K232A, was already found to have a reduced ATP hydrolysis rate (Figure 41). As expected, it also shows a slower adenylate kinase reaction compared to the wild-type protein: incubation in 200 µM of ADP, as well as incubation with 100 µM of AMP and ATP respectively, revealed a 3-fold reduced adenylate kinase activity.

The second Walker A mutant tested is T233S, which was shown to possess a similar hydrolysis activity as MBP-NLRP3 Peak 1 (Figure 41 and Figure 43). Interestingly, when incubated in 100 µM AMP and ATP, the slope resulting for generated ADP, was nearly halved, compared to the slope determined from the ATP hydrolysis reaction. When incubated in the presence of 200 µM ADP, the decrease is ADP only goes along with an increase in AMP. Here, no ATP generation was detectable. Therefore, either an ADP hydrolysis mechanism is assumed or an instantaneous consumption of generated ATP, based on the ATP hydrolysis activity of NLRP3.

Likewise, the adenylate kinase activity of the Walker B mutants was analysed. The mutant D302A shows nearly no adenylate kinase activity, when incubated in 100 µM of AMP and ATP, whereas the incubation in 200 µM ADP, revealed an about 6-fold reduced adenylate kinase activity, compared to the wild-type protein. Moreover, the ratio of AMP and ATP generated from ADP was again found to be 1:1. A similar result was obtained for the mutant D305A. Again, when incubated in the presence of 100 µM AMP and ATP, nealry no AMP was consumed. In contrast, the incubation in 200 µM of ADP resulted in a ratio of 1:1 of generated AMP to ATP.

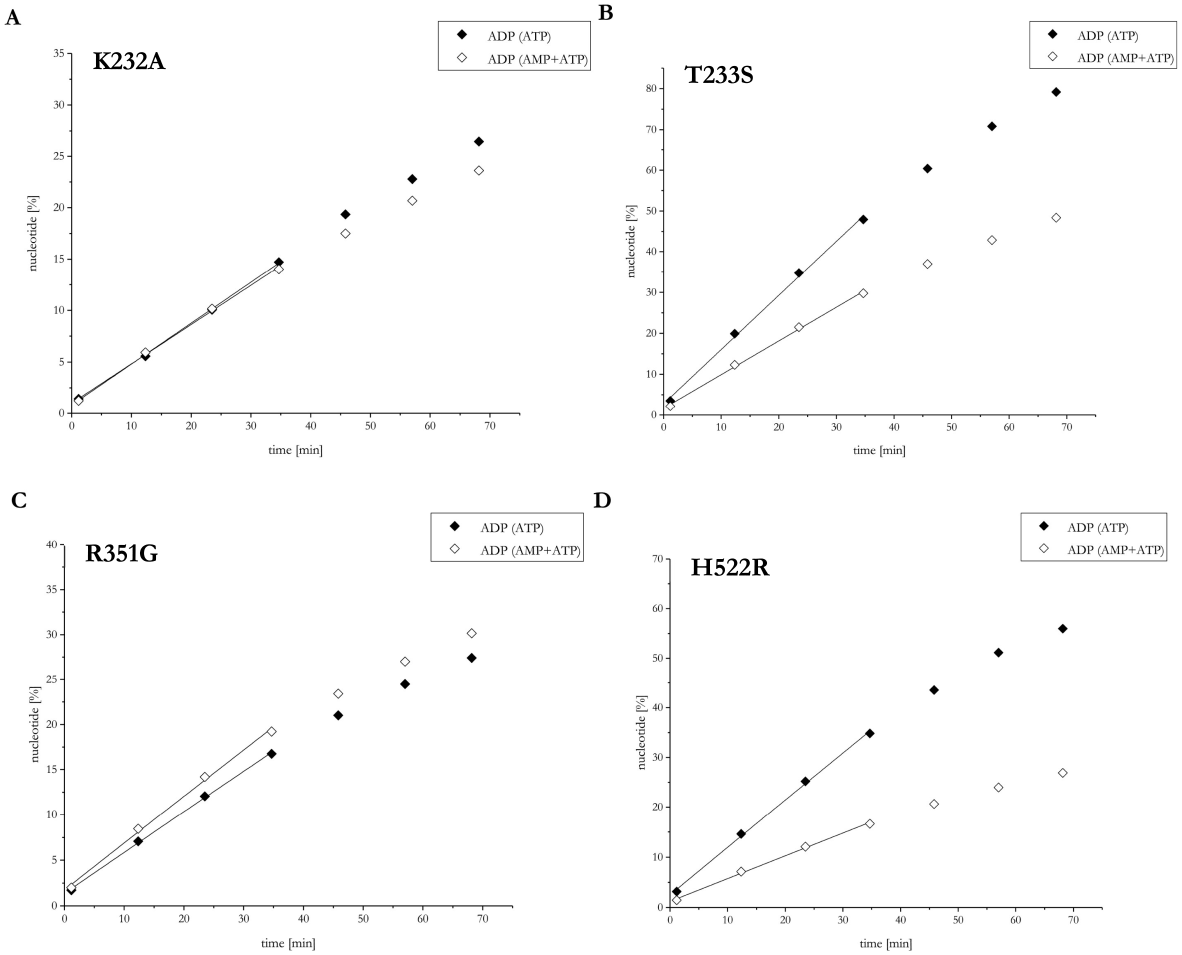

Figure 41: MBP-NLRP3 variants show reduced adenylate kinase activity and ATP-hydrolysis is partly inhibited by AMP. A: MBP-NLRP3 K232A is incubated at 25°C for 60 min in the presence of 5 mM $MgCl_2$ and 100 µM ATP and 100 µM AMP and ATP, respectively. **B:** MBP-NLRP3 T233S is incubated at 25°C for 60 min in the presence of 5 mM $MgCl_2$ and 100 µM ATP and 100 µM AMP and ATP, respectively. **C:** MBP-NLRP3 R351G is incubated at 25°C for 60 min in the presence of 5 mM $MgCl_2$ and 100 µM ATP and 100 µM AMP and ATP, respectively. **D:** MBP-NLRP3 H522R is incubated at 25°C for 60 min in the presence of 5 mM $MgCl_2$ and 100 µM ATP and 100 µM AMP and ATP, respectively. The eluting nucleotide ADP is normalized and displayed in nucleotide [%] on the y-axis, plotted against the time [min] on the x-axis. Linear regression curves are plotted, only in the linear curve area.

As expected, the mutants E306Q and the double mutant D305A/E306Q showed a similar adenylate kinase behaviour. In the presence of 100 µM of AMP and ATP, both mutants showed ATP hydrolysis activity only. Furthermore, the measurements revealed that ADP formation seems inhibited in the presence of AMP, reflected by a decrease in the slope of about 30%. In contrast, incubation in 200 µM ADP led to a ratio of generated AMP to ATP of about 7:1 (E306Q) and to a ratio of about 1.5:1 (D305A/E306Q) (Table 7).

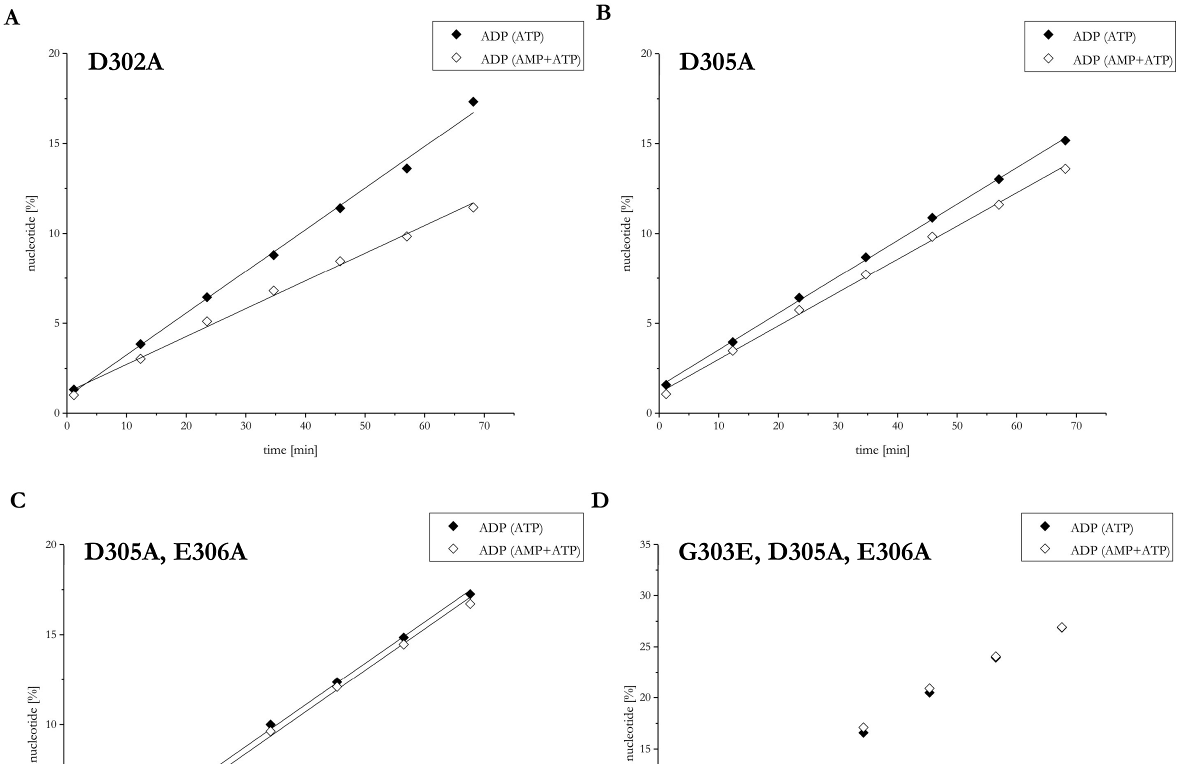

Figure 42: MBP-NLRP3 Walker B variants lack adenylate kinase activity, but ATP-hydrolysis is partly inhibited by AMP. A: MBP-NLRP3 D302A is incubated at 25°C for 60 min in the presence of 5 mM $MgCl_2$ and 100 µM ATP and 100 µM AMP and ATP, respectively. **B:** MBP-NLRP3 D305A is incubated at 25°C for 60 min in the presence of 5 mM $MgCl_2$ and 100 µM ATP and 100 µM AMP and ATP, respectively. **C:** MBP-NLRP3 D305A, E306A is incubated at 25°C for 60 min in the presence of 5 mM $MgCl_2$ and 100 µM ATP and 100 µM AMP and ATP, respectively. **D:** MBP-NLRP3 G303E, D305A, E306A is incubated at 25°C for 60 min in the presence of 5 mM $MgCl_2$ and 100 µM ATP and 100 µM AMP and ATP, respectively. The eluting nucleotide ADP is normalized and displayed in nucleotide [%] on the y-axis, plotted against the time [min] on the x-axis. Linear regression curves are plotted, only in the linear curve area.

Furthermore, the slope determined for the generation of ADP upon incubation in 100 μM AMP and ATP was reduced by half for the double mutant D305A/E306A, compared to the mutant D305A/E306Q (Table 7). Strikingly, the slope determined for the consumption of ADP was increased (ADP: -0.097).

The Walker B mutant G303E/D305A/E306A was selected in order to investigate whether the typical Walker B motif of AAA+ ATPases could be reconstituted in NLRP3. The hydrolysis activity of the triple-mutant upon incubation in 100 μM ATP was shown to be reduced by about 3-fold, compared to the wild-type protein. In contrast, the adenylate kinase reaction of this mutant shows a deviating behaviour: in the presence of 100 μM AMP and ATP, a slope of about 0.487 was determined for the generation of ADP, compared to the ATP hydrolysis reaction revealing a slope of about 0.440, determined for the generation of ADP (Table 7).

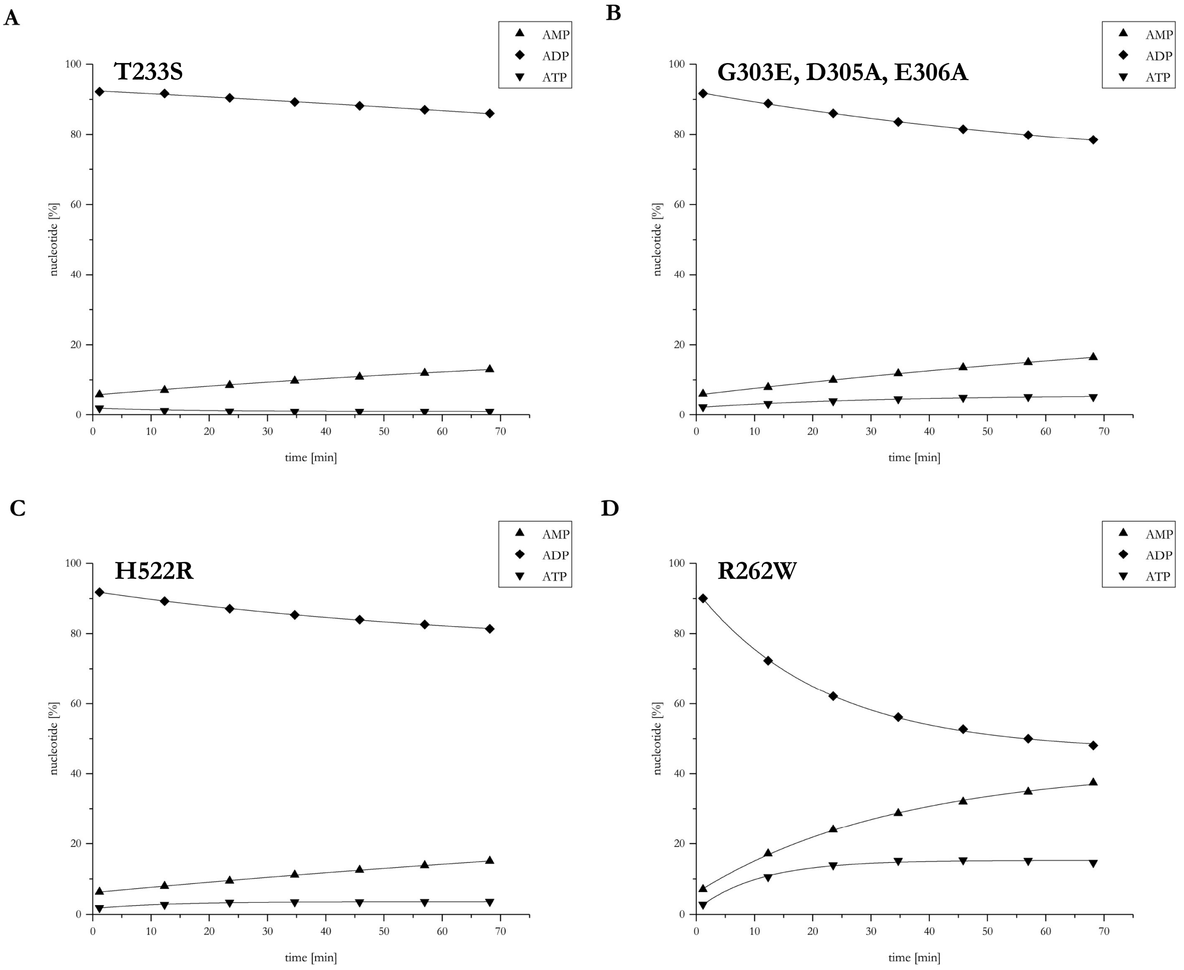

Figure 43: MBP-NLRP3 variants show slight adenylate kinase activity, in reverse reaction. **A:** MBP-NLRP3 T233S is incubated at 25°C for 60 min in the presence of 5 mM $MgCl_2$ and 200 μM ADP. **B:** MBP-NLRP3 G303E, D305A, E306A is incubated at 25°C for 60 min in the presence of 5 mM $MgCl_2$ and 200 μM ADP. **C:** MBP-NLRP3 H522R is incubated at 25°C for 60 min in the presence of 5 mM $MgCl_2$ and 200 μM ADP. **D:** MBP-NLRP3 R262W is incubated at 25°C for 60 min in the presence of 5 mM $MgCl_2$ and 100 μM ADP. The eluting nucleotides AMP, ADP and ATP are normalized and displayed in nucleotide [%] on the y-axis, plotted against the time [min] on the x-axis. Exponential curves are plotted to visualize the graph course.

Nonetheless, AMP is still consumed, yielding a slope of about 0.114. In the presence of 200 µM ADP, again AMP and ATP is produced, but in a ratio of about 2.5:1, similar to the wild-type protein.

The sensor 1 motif (R351) was found to participate in the ATP hydrolysis reaction of MBP-NLRP3 Peak 1 (chapter 8.2.3). Thus the variant R351G was also tested regarding its importance in adenylate kinase activity. The mutant protein was incubated in 100 µM AMP and ATP and subsequently analysed by RP-HPLC. The slope determined for the decrease in ATP is equivalent to the slope determined upon incubation in 100 µM ATP (Table 7). Interestingly, the slope determined for the increase in ADP was found to be higher (0.577), compared to the slope determined upon incubation in 100 µM ATP (0.462). Consequently, AMP was found to be consumed in this experiment, yielding a slope of about -0.072.

Next, the influence of residue H522 on the adenylate kinase activity was tested using two MBP-NLRP3 variants: H522D and H522R. The latter one showed ATP hydrolysis activity, similar to the wild-type protein. Incubation in 100 µM AMP and ATP resulted in a lower slope determined for ATP consumption (-0.379), compared to the slope derived upon incubation in 100 mM ATP only (-0.992). Moreover, upon incubation in 100 µM AMP and ATP, the slope determined for the generation of ADP is higher (0.476) than the decrease in ATP (Table 7), which goes along with a decrease in AMP (slope: -0.097).

In contrast, the second mutant (H522D) shows a similar behaviour, but a comparably slower turnover. Again, the slope determined for the consumption of ATP is lower (-0.122) upon incubation in 100 µM AMP and ATP, when compared to the slope derived upon incubation in 100 µM ATP, yielding a slope of about -0.195. Comparing these results to the reverse adenylate kinase reaction, both mutants show a consumption of ADP, when incubated with 200 µM ADP only. Similar to the wild-type protein, the ratio of generated AMP:ATP from ADP is shifted towards ADP, showing a ratio of about 2:1, whereas again the variant H522D shows an about 4-fold increased adenylate kinase reaction.

Besides mutants affecting the ATP-binding site of NLRP3, also the CAPS disease mutant R262W was tested with respect to a potential effect on the adenylate kinase activity. Strikingly, upon incubation in 100 µM ADP, a slope for the decrease in ADP of about -1.250, was determined. Interestingly, again a smaller ratio of the generated nucleotides AMP and ATP of about 1.5:1, was determined, compared to the wild-type protein.

When interpreting these data in order to determine the favoured direction of the adenylate kinase reaction mediated by NLRP3, it has to be considered, that the incubation with AMP and ATP to yield ADP is accompanied by the ATP hydrolysis reaction.

Furthermore, the reverse adenylate kinase reaction, (2xADP → 1xAMP+1xATP), is most probably going along with a simultaneous consumption of the freshly generated ATP.
Moreover, an an inhibitory effect of AMP could be assumed, as the comparison of slopes determined for the generation of ADP from AMP and ATP and the ones determined from the ATP hydrolysis reaction were lower for most of the tested mutants.

In summary, adenylate kinase activity was determined for each of the tested MBP-NLRP3 variants, whereas the disease mutant R262W, showed about 3-fold higher adenylate kinase activity compared to the wild-type protein. Moreover, MBP-NLRP3 Peak 1 showed a faster adenylate kinase reaction when incubated in the presence of ADP, compared to the reverse reaction, starting with AMP and ATP. Here, simultaneously, higher ATP hydrolysis rates were determined. A similar phenomenon was observed for the following mutants: T233S, D302A, D305A, the double mutant D305A/E306Q, as well as H522R and the triple-mutant G303E/D305A/E306A. In contrast, some mutants show a preference for the adenylate kinase reaction, starting with AMP and ATP, like K232A, E306Q, the double mutant D305A/E306A, as well as H522D.

Table 7: Slopes (linear regression) resulting from adenylate kinase activity measurements of MBP-NLRP3 variants. The adenylate kinase reaction of MBP-NLRP3 Peak 1 and Peak 2, as well as of protein variants was analysed by RP-HPLC. The resulting slopes are shown for the nucleotides AMP, ADP and ATP. The adenylate kinase reaction was measured using either 100 µM of AMP and ATP or 200 µM of ADP (R262W; 100 µM ADP). Variants showing higher slopes when incubated with AMP and ATP instead of ADP are labelled with an *.

Mutant / nucleotide	Slope (ADP)	Slope (AMP+ATP)	Mutant / nucleotide	Slope (ADP)	Slope (AMP+ATP)
NLRP3 P1 AMP	0.360	**-0.086**	D305A, E306A AMP *	0.070	**-0.125**
NLRP3 P1 ADP	**-0.457**	1.108	D305A, E306A ADP *	**-0.097**	0.276
NLRP3 P1 ATP	0.173	**-0.960**	D305A, E306A ATP *	0.027	**-0.152**
NLRP3 P2 AMP	0.012	n.d.	D305A, E306Q AMP	0.040	**-0.021**
NLRP3 P2 ADP	**-0.027**		D305A, E306Q ADP	**-0.064**	0.334
NLRP3 P2 ATP	0.015		D305A, E306Q ATP	0.024	**-0.313**
K232A AMP	0.123	**-0.170**	G303E, D305A, E306A AMP	0.179	**-0.114**
K232A ADP	**-0.182**	0.400	G303E, D305A, E306A ADP	**-0.253**	0.487
K232A ATP	0.059	**-0.230**	G303E, D305A, E306A ATP	0.074	**-0.239**
T233S AMP *	0.118	**-0.045**	R351T AMP	n.d.	n.d.
T233S ADP *	**-0.078**	0.865	R351T ADP		
T233S ATP *	*-0.040*	**-0.819**	R351T ATP		
D302A AMP	0.063	**-0.039**	R351G AMP	n.d.	**-0.072**
D302A ADP	**-0.115**	0.183	R351G ADP		0.577
D302A ATP	0.052	**-0.144**	R351G ATP		**-0.469**
G303E AMP	n.d.	n.d.	H522D AMP *	0.043	**-0.054**
G303E ADP			H522D ADP *	**-0.057**	0.177
G303E ATP			H522D ATP *	0.015	**-0.122**
D305A AMP	0.060	**-0.044**	H522R AMP	0.140	**-0.097**
D305A ADP	**-0.105**	0.208	H522R ADP	**-0.210**	0.476
D305A ATP	0.045	**-0.165**	H522R ATP	0.070	**-0.379**
E306Q AMP *	0.031	**0.072**	R262W AMP	0.755	n.d.
E306Q ADP *	**-0.035**	0.175	R262W ADP	**-1.250**	
E306Q ATP *	0.004	**-0.247**	R262W ATP	0.495	

8.4 Analysis of VHH antibodies directed against NLRP3

Antibodies are well-established and well-studied tools for the investigation of protein-protein interactions, protein targeting in cells as well as in functional screens.

Camelid heavy chain-only antibodies, more specifically the single variable domain fragment (VHH), are antibody fragments (about 14 kDa), which consist of only one variable region. Thus the binding to the target protein is mediated only by three complementarity determining regions (CDRs) (Helma *et al.*, 2015). Compared to conventional antibodies, VHH-antibodies show a higher stability and solubility due to framework exchanges of hydrophobic to hydrophilic residues (Helma *et al.*, 2015).

Specific VHH antibodies were generated, directed against the target proteins MBP-NLRP3 Peak 2 and the subdomain fragment mMBP-NLRP3 LRR 4 in collaboration with Dr. F. Schmidt at the Institute of Innate Immunity, University Clinics Bonn. Positively tested VHH antibodies were recombinantly expressed and purified from *E.coli* cells and subsequently tested for protein binding by analytical gel filtration and SPR measurements.

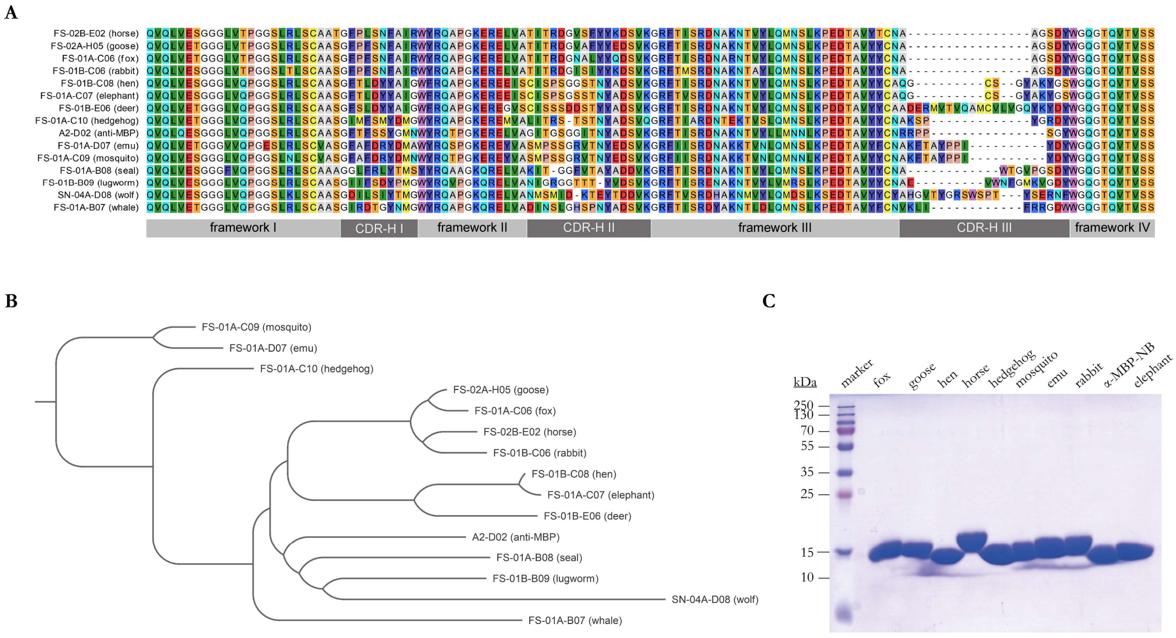

Figure 44: Phylogenetic relationship of VHH antibodies generated against MBP-NLRP3 Peak 2 and mMBP-NLRP3 LRR. A: Sequence alignment of VHH antibodies generated against NLRP3. Framework regions and coding regions of the VHH antibody are shown below. **B:** Phylogenetic tree of the VHH antibodies generated against NLRP3. The phylogenetic tree was generated using the clustering method Neighbor Joining. **C:** SDS-PAGE of recombinantly expressed and purified VHH antibodies.

The analysed VHH antibodies show a typical framework arrangement of four framework parts, interrupted by three coding regions, in which the highest variability is shown in CDR-H III (Figure 44). In order to determine an amino acid sequence based relationship between the generated VHH antibodies, a phylogenetic analysis was performed.

The VHH antibodies generated against the target MBP-NLRP3 Peak 2 and the VHH antibody SN-04A-D08 (wolf), resulting from the immunization with the target protein mMBP-NLRP3 LRR 4, were compared to a previously generated anti-MBP VHH antibody A2-D02. The resulting phylogenetic tree clearly separates the different VHH antibodies in three main subclasses. One of these includes the VHH antibodies FS-01A-C09 (mosquito) and FS-01A-D07 (emu), both generated against the target MBP-NLRP3 Peak 2. A second subclass is formed by the VHH antibody FS-01A-C10 (hedgehog). The largest class is build up by the remaining twelve VHH antibodies, including the MBP control VHH antibody A2-D02 and the VHH antibody SN-04A-D08 (wolf), raised against the target mMBP-NLRP3 LRR 4.
Among all generated VHH antibodies, the highest sequence similarity is found between the VHH antibody FS-01B-C08 (hen) and FS-01A-C07 (elephant). Furthermore, a close sequence homology of four VHH antibodies became evident for FS-02A-H05 (goose), FS-01A-C06 (fox), FS-02B-E02 (horse) and FS-01B-C06 (rabbit). The generated VHH antibodies were purified to homogeneity, as no contaminating proteins were co-purified (Figure 44 C).

8.4.1 Analysis of the VHH antibodys by analytical gel filtration

In order to determine the specificity of each VHH antibody towards the target protein NLRP3, the proteins were analsed by analytical gel filtration. Furthermore, the specificity of each VHH antibody for individual protein subdomains like the N-terminal PYD-domain and the C-terminal LRR-domain was tested. The proteins were subjected to analytical gel filtration, using a Superose 6 3.2/300 column (GE Healthcare). For each protein, the individual apparent molecular weight was derived using a gel filtration standard (BioRad). Subsequently, the target proteins were incubated with the VHH antibody of interest in a ratio of 1:10 and analysed by analytical gelfiltration, in order to determine changes in the resulting apparent molecular weight, due to complex formation.
Analytical gel filtration analysis of MBP-NLRP3 Peak 2 resulted in a large peak at an elution volume of about 1.3 mL, corresponding to an apparent molecular weight of about 1,872 kDa.

Furthermore, the gel filtrations showed a smaller peak at about 2.0 mL, corresponding to a contamination smaller than 5 kDa. A small aggregated fraction was abundant at about 0.8 mL, corresponding to the void volume of the column. Analytical gel filtration of the N-terminal PYD-domain of NLRP3 resulted in a single peak, corresponding to an apparent molecular weight of 20.03 kDa. The mMBP-tagged C-terminal LRR-domain of NLRP3 has a predicted MW of about 83 kDa, whereas the analytical gel filtration analysis indicated a larger complex, eluting in the void volume of the volumn, corresponding to an apparent molecular weight of about 25,240 kDa. The gel filtration chromatograms as well as the calculated molecular weight values are presented in Figure 45. The gel filtration standard (BioRad) was used to determine a standard curve, to calculate the corresponding K_{av} values for the proteins of intererst and the resulting apparent molecular weight. Furthermore, the generated VHH antibodies were analysed by analytical gel filtration, resulting in a MW between 8.2 to 15.0 kDa (Table 8). The strongest deviation from the predicted molecular weight was determined for the VHH antibody elephant with an apparent MW of 8.2 kDa (pred. 16.4 kDa), the VHH antibody hen with an apparent MW of about 9.3 kDa (pred. 16.2), and the VHH antibody hedgehog resulting in an apparent MW of about 9.5 kDa (pred. 16.4 kDa). Interestingly, each of the tested VHH antibodies resulted in a smaller apparent molecular weight, compared to the predicted values.

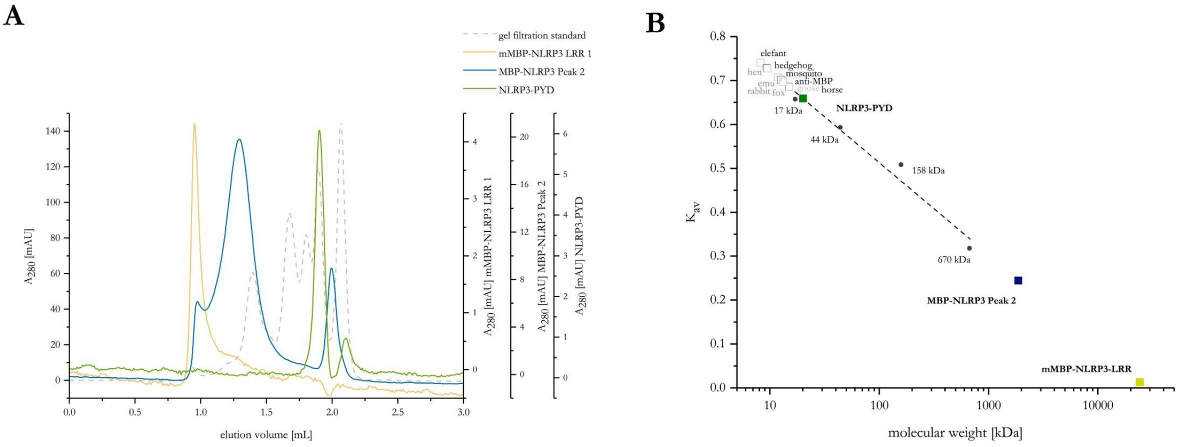

Figure 45: Analytical gel filtration analysis of VHH antibody target proteins. A: Chromatogram of analytical gel filtration analysis of MBP-NLRP3 Peak 2 (blue), mMBP-NLRP3 LRR 1 (yellow) and NLRP3-PYD (green) shown in relation to the gel filtration standard (grey, dashed line). **B:** The diagram shows the calculated K_{av} values (y-axis) in dependence of the known molecular weight standard sizes [kDa] (x-axis). The regression curve ($f(x)= 0.091\times\ln(x)+0.932$) is indicated in grey. The generated VHH antibodies are shown in grey, as well as the VHH antibody target proteins MBP-NLRP3 Peak 2 (blue), mMBP-NLRP3 LRR 1 (yellow) and NLRP3 PYD (green).

In order to determine, whether the generated VHH antibodies specifically bind to the target protein NLRP3, the target proteins and the VHH antibodies were incubated in a 10:1 molar ratio and subjected to analytical gelfiltration.

Representative gel filtration chromatograms of four VHH antibodies (anti-MBP, rabbit, emu, hedgehog) with the target proteins (MBP-NLRP3 Peak 2, mMBP-NLRP3 LRR 1 and NLRP3-PYD) are shown in Figure 46, Figure 47 and Figure 48, respectively.

The calculated apparent molecular weight values of each experiment are shown in Table 9, Table 10 and Table 11.

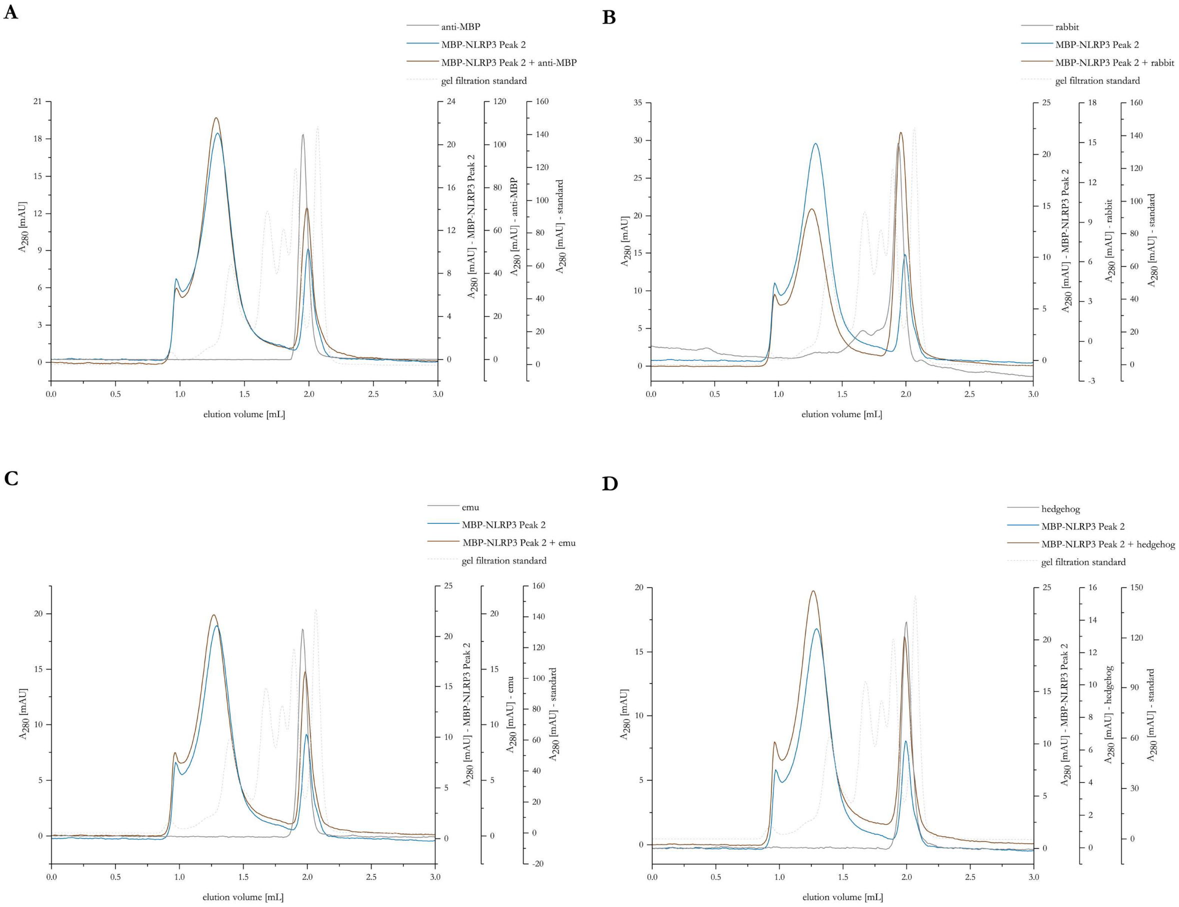

Figure 46: Analytical gel filtration analysis of VHH antibodies and MBP-NLRP3 Peak 2. A-D: Gel filtration chromatograms of representative VHH antibodies anti MBP **(A)**, rabbit **(B)**, emu **(C)** and hedgehog **(D)**. The respective proteins were applied to an analytical Superose 6 3.2/300 gel filtration column (GE Healthcare) in a molar ratio of 1:10, as well as in individual runs. The target protein MBP-NLRP3 Peak 2 is shown in blue, the respective VHH antibodies are shown in grey, the combination of both in brown and the gel filtration standard in light grey (dashed line).

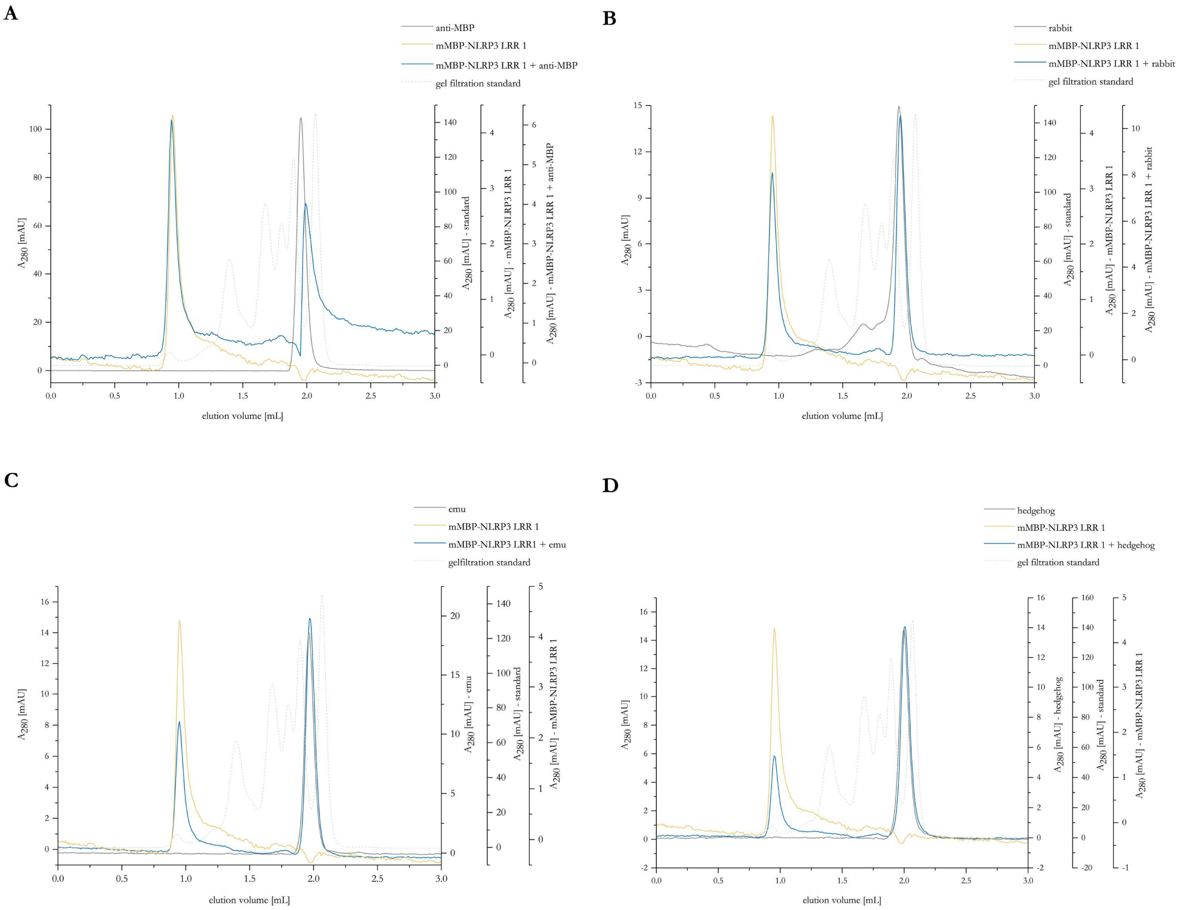

Figure 47: Analytical gel filtration analysis of VHH antibodies and mMBP-NLRP3-LRR. A-D: Gel filtration chromatograms of representative VHH antibodies anti-MBP **(A)**, rabbit **(B)**, emu **(C)** and hedgehog **(D)**. The respective proteins were applied to an analytical Superose 6 3.2/300 gel filtration column (GE Healthcare) in a molar ratio of 1:10, as well as in individual runs. The target protein mMBP-NLRP3-LRR is shown in yellow, the respective VHH antibodies are shown in grey, the combination of both in blue and the gel filtration standard in light grey (dashed line).

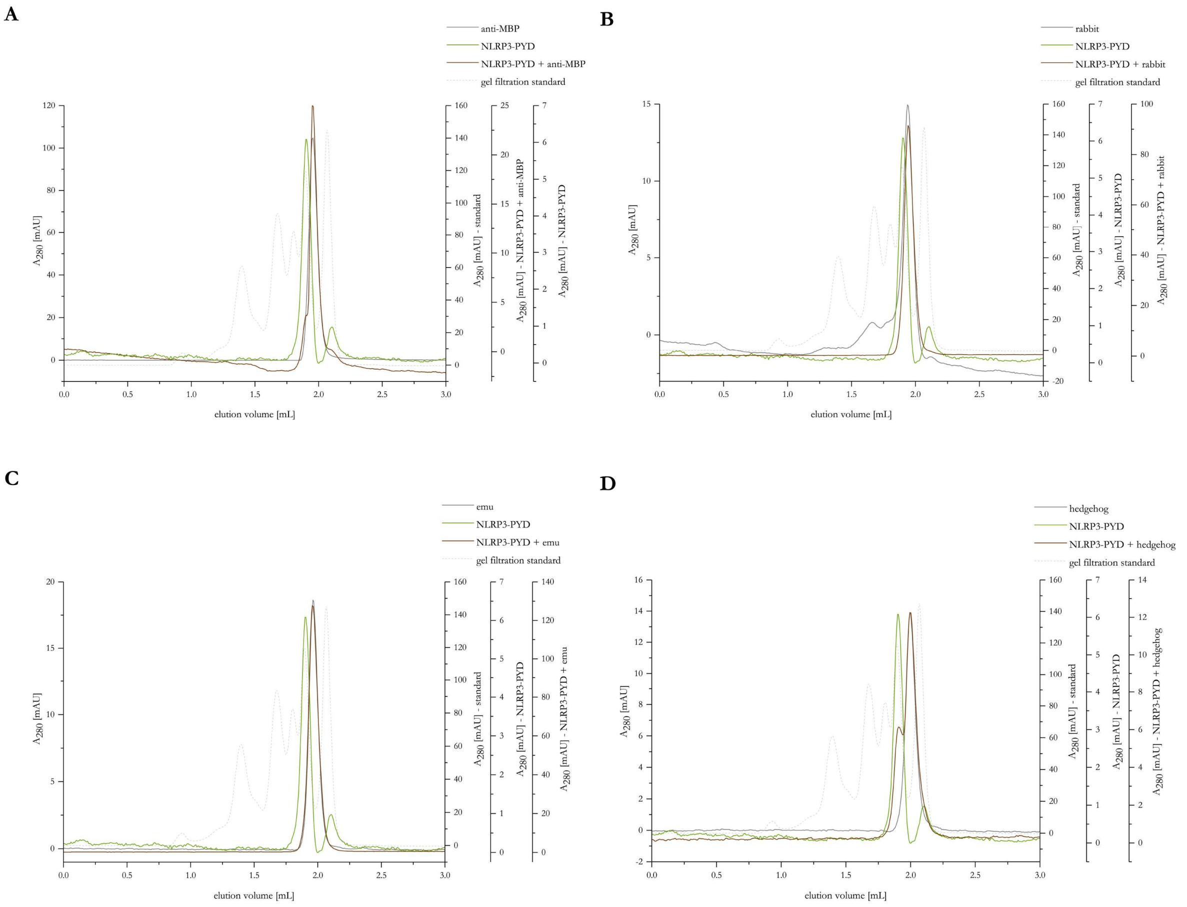

Figure 48: Analytical gel filtration analysis of VHH antibodies and NLRP3-PYD. A-D: Gel filtration chromatograms of representative VHH antibodies anti-MBP **(A)**, rabbit **(B)**, emu **(C)** and hedgehog **(D)**. The respective proteins were applied to an analytical Superose 6 3.2/300 gel filtration column (GE Healthcare) in a molar ratio of 1:10, as well as in individual runs. The target protein NLRP3-PYD is shown in green, the respective VHH antibodies are shown in grey, the combination of both in brown and the gel filtration standard in light grey (dashed line).

As the majority of the generated VHH antibodies was raised against the target protein MBP-NLRP3 Peak 2 in an individual immunization of an Alpaka animal, the VHH antibodies were tested against the full-length NLRP3 protein. The resulting apparent molecular weight values for the incubation of each VHH antibody and the target protein MBP-NLRP3 Peak 2 are shown in Table 9. Coincubation resulted in an increase in the apparent MW, for all VHHs tested. Thus, binding of each of the investigated VHH antibodies to the full-length protein was assumed. The largest increase in the apparent MW was determined in case of the VHH antibody goose, resulting in a complex of about 2,540 kDa and the VHH antibody elephant, giving rise to a complex with an apparent MW of about 2,364 kDa. The calculated theoretical complex formed by MBP-NLRP3 Peak 2 and goose has a ratio of 12:42, whereas the complex formed by MBP-NLRP3 Peak 2 and elephant corresponds to an apparent ratio of 12:62.

In general, three subclasses can be distinguished, one of which includes VHH antibodies which bind the target protein with an over-stoichiometric ratio (like hedgehog, fox, goose, elephant, and mosquito). A second subclass includes the VHH antibodies, which bind in a ratio of about 1:2 (rabbit, emu and hen). A last subclass is formed by VHH antibodies, which bind the target protein MBP-NLRP3 Peak 2 in a 1:1 ratio, like the control VHH antibody directed against the MBP-tag and the VHH antibody horse.

Table 8: Analytical gel filtration analysis of VHH antibodies and target proteins, respectively. The predicted molecular weight [kDa] of the VHH antibodies and the target proteins MBP-NLRP3 Peak 2, mMBP-NLRP3 LRR 1 and NLRP3-PYD is shown, as well as the predicted pI and the apparent molecular weight [kDa] determined by analytical gel filtration.

Protein	Pred. MW [kDa]	Pred. pI	Appar. MW [kDa]
MBP-NLRP3 Peak 2	159.41	5.84	1,871.95
mMBP-NLRP3 LRR 1	82.75	5.30	24,238.91
NLRP3-PYD	13.07	6.43	20.03
Hedgehog	16.42	7.83	9.45
Fox	16.17	8.60	14.90
Rabbit	16.08	8.57	15.02
Emu	17.10	7.81	12.58
Goose	16.16	7.83	14.50
Horse	16.08	8.95	13.19
Mosquito	17.08	7.80	11.84
Elephant	16.40	7.71	8.19
Hen	16.25	7.70	9.34
Whale	17.26	8.55	
Wolf	18.28	6.69	
Lugworm	17.40	8.52	
Seal	16.91	8.51	
Deer	18.49	6.02	
α-MBP-NB	14.11	9.00	13.19

Besides binding to the MBP-NLRP3 full-length protein, specific interactions of the VHH antibodies with individual domains of NLRP3 were investigated. Thus, it was expected to identify VHH antibodies, which show a higher affinity for individual domains. Heavy-chain-only antibodies typically form a convex paratope, which is prone to bind cavity structured epitopes, hence VHH antibodies directed against the full-length protein were expected. In order to investigate the interaction of the VHH antibodies with the C-terminal LRR-domain of NLRP3, the protein mMBP-NLRP3 LRR 1 (651-1036) was used. As the immunization procedure was performed using the mMBP NLRP3 LRR 4 variant (712-1036), encompassing a shorter sequence motif of the LRR domain, two classes of VHH antibodies were expected to be identifies: (i) one interacting with the LRR-domain, (ii) VHH antibodies, generated against the full-length protein, which interact with the short protein region, spanning residues 651-712.

Again, the VHH antibodies were incubated with the target protein mMBP-NLRP3 LRR 1 and analysed by analytical gel filtration. Representative chromatograms are shown in Figure 47. The resulting, calculated apparent molecular weight values are presented in Table 10.

Table 9: Analytical gel filtration analysis of MBP-NLRP3 Peak 2 and VHH antibodies. The predicted molecular weight [kDa] of the target protein MBP-NLRP3 Peak 2 and the VHH antibodies is shown, as well as the apparent molecular weight [kDa] determined by analytical gel filtration on an analytical Superose 6 3.2/300 column. The proteins were applied in a molar ratio of 1:10 (target:VHH antibody). Furthermore, the apparent ratio of target and VHH antibody is shown.

Protein A	Pred. MW (A) [kDa]	Appar. MW (A) [kDa]	Protein B	Pred. MW (B) [kDa]	Appar. MW (B) [kDa]	Appar. MW [kDa]	Appar. MW [kDa]	Appar. Ratio [A:B]
MBP-NLRP3	159.41	1,871.95	Hedgehog	16.42	9.45	2,277.85	10.95	12:40
MBP-NLRP3	159.41	1,871.95	Fox	16.17	14.90	2,373.94	10.66	12:33
MBP-NLRP3	159.41	1,871.95	Rabbit	16.08	15.02	2,262.14	12.87	12:24
MBP-NLRP3	159.41	1,871.95	Emu	17.10	12.58	2,172.72	10.76	12:18
MBP-NLRP3	159.41	1,871.95	Goose	16.16	14.50	2,539.65	10.06	12:42
MBP-NLRP3	159.41	1,871.95	Horse	16.08	13.19	1,970.94	10.50	12:8
MBP-NLRP3	159.41	1,871.95	Mosquito	17.08	11.84	2,279.61	10.76	12:34
MBP-NLRP3	159.41	1,871.95	Elefant	16.40	8.19	2,364.31	8.76	12:62
MBP-NLRP3	159.41	1,871.95	Hen	16.25	9.34	2,080.66	9.57	12:23
MBP-NLRP3	159.41	1,871.95	Whale	17.26				
MBP-NLRP3	159.41	1,871.95	Wolf	18.28				
MBP-NLRP3	159.41	1,871.95	Lugworm	17.40				
MBP-NLRP3	159.41	1,871.95	Seal	16.91				
MBP-NLRP3	159.41	1,871.95	Deer	18.49				
MBP-NLRP3	159.41	1,871.95	α-MBP	14.11	13.19	2,085.24	10.60	12:16

The protein mMBP-NLRP3 LRR 1 was shown to elute close to the void volume of the analytical gel filtration column (Figure 45), corresponding to an ill-defined apparent molecular weight of 24,239 kDa.

Most likely, the mMBP-NLRP3 LRR variants eluted in the void volume of the column, as the proteins were aggregated. Thus complex formation is neither ordered nor stoichoimetrically uniform. Incubation of the VHH antibodies and the mMBP-NLRP3 LRR 1 variant was performed, in order to investigate weather the heavy-chain only antibodies successfully assist proper complex formation or lead to the liberation of monomeric protein.

Analytical gel filtration analysis revealed an increase in the apparent molecular weight corresponding to mMBP-NLRP3 LRR 1 + VHH for five of the tested VHH antibodies (fox, rabbit, emu, goose and the anti-MBP control VHH). In case of the remaining VHH antibodies (hedgehog, horse, mosquito, elephant and hen), a slight decrease in the apparent molecular weight corresponding to mMBP-NLRP3 LRR 1 was seen.

The calculated, apparent ratio of the complex formed between the NLRP-LRR variant and the VHH antibodies tested, was strongly hypostoichiometric for the VHH fox, rabbit and emu, with a ratio of about 292 to <35. Furthermore, incubation with the VHH antibody goose resulted in an increase in the apparent MW to about 1,700 kDa, corresponding to a complex ratio of about 3 to 1. A similar value was determined for the control VHH antibody directed against the MBP-tag.

In conclusion, the addition of VHH antibody did not result in the generation of a peak corresponding to the size of monomeric or dimeric mMBP-NLRP3 LRR 1.

Table 10: Analytical gel filtration analysis of mMBP-NLRP3 LRR 1 and VHH antibodies. The predicted molecular weight [kDa] of the target protein mMBP-NLRP3 LRR 1 and the VHH antibodies is shown, as well as the apparent molecular weight [kDa] determined by analytical gelfiltration. The proteins were applied in a molar ratio of 1:10 (target:VHH antibody). Furthermore, the apparent ratio of target and VHH antibody is shown.

Protein A	Pred. MW (A) [kDa]	Appar. MW (A) [kDa]	Protein B	Pred. MW (B) [kDa]	Appar. MW (B) [kDa]	Appar. MW [kDa]	Appar. MW [kDa]	Appar. Ratio [A:B]
mMBP- LRR 1	82.75	24,238.91	Hedgehog	16.42	9.45	24,198.98	9.02	-
mMBP- LRR 1	82.75	24,238.91	Fox	16.17	14.90	24,714.98	14.00	292:32
mMBP- LRR 1	82.75	24,238.91	Rabbit	16.08	15.02	24,297.58	13.55	292:4
mMBP- LRR 1	82.75	24,238.91	Emu	17.10	12.58	24,415.34	11.92	292:14
mMBP- LRR 1	82.75	24,238.91	Goose	16.16	14.50	25,893.78	9.30	292:110
mMBP- LRR 1	82.75	24,238.91	Horse	16.08	13.19	23,987.18	13.65	-
mMBP- LRR 1	82.75	24,238.91	Mosquito	17.08	11.84	24,145.86	10.82	-
mMBP- LRR 1	82.75	24,238.91	Elefant	16.40	8.19	24,132.59	8.18	-
mMBP- LRR 1	82.75	24,238.91	Hen	16.25	9.34	23,819.07	9.30	-
mMBP- LRR 1	82.75	24,238.91	α-MBP	14.11	13.19	25,853.98	10.01	292:124

Besides the C-terminal LRR-domain, also the N-terminal PYD domain was tested in analytical gel filtration for the interaction with the specifically generated VHH antibodies.

The protein, spanning residues aa 3-106, was previously expressed and purified from *E.coli* cells using a C-terminal His-tag. Thus the PYD-domain construct is the only one tested, being purified with an affinity tag deviant from a MBP-tag.

Analytical gel filtration analysis of the co-incubated VHH antibody samples with the NLRP3 PYD variant, in a ratio of 1:10, resulted in a single peak corresponding to the predicted MW of the VHH antibody tested. As the NLRP-PYD protein eluted at about 1.8 mL, corresponding to an apparent MW of about 20 kDa, the specific interaction with a VHH antibody should result in an increase in the apparent MW of about 8 kDa to 15 kDa, respectively. Therefore, interaction between the NLRP-PYD domain was not assumed for any of the VHH antibodies tested.

Table 11: Analytical gel filtration analysis of NLRP3-PYD and VHH antibodies. The predicted molecular weight [kDa] of the target protein NLRP3-PYD and the VHH antibodies is shown, as well as the apparent molecular weight [kDa] determined by analytical gelfiltration. The proteins were applied in a molar ratio of 1:10 (target:VHH antibody).

Protein A	Pred. MW (A) [kDa]	Appar. MW (A) [kDa]	Protein B	Pred. MW (B) [kDa]	Appar. MW (B) [kDa]	Appar. MW [kDa]	Appar. MW [kDa]
NLRP3-PYD	13.07	20.03	Hedgehog	16.42	9.45	18.96	9.82
NLRP3-PYD	13.07	20.03	Fox	16.17	14.90	14.80	-
NLRP3-PYD	13.07	20.03	Rabbit	16.08	15.02	14.61	-
NLRP3-PYD	13.07	20.03	Emu	17.10	12.58	13.06	-
NLRP3-PYD	13.07	20.03	Goose	16.16	14.50	16.12	-
NLRP3-PYD	13.07	20.03	Horse	16.08	13.19	13.64	-
NLRP3-PYD	13.07	20.03	Mosquito	17.08	11.84	11.96	-
NLRP3-PYD	13.07	20.03	Elefant	16.40	8.19	8.80	-
NLRP3-PYD	13.07	20.03	Hen	16.25	9.34	10.05	-
NLRP3-PYD	13.07	20.03	α-MBP	14.11	13.19	13.65	-

In summary, an increase in the apparent MW of MBP-NLRP3 Peak 2 was determined for each of the VHH antibodies. In contrast, five of the tested heavy-chain only antibodies showed an increase in the apparent MW of mMBP-NLRP3 LRR 1, after co-incubation, whereas no interaction is assumed for the VHH antibodies and the C-terminal PYD-domain.

8.4.2 Analysis of the VHH antibodies by SPR

In order to determine the binding affinity of the generated VHH antibodies to the target protein NLRP3, SPR measurements were performed. SPR allows for the measurement of binding affinities (K_D), calculated from association and dissociation constants in real time.

In this case, the target protein MBP-NLRP3 Peak 2, the NACHT-domain spanning variant MBP NLRP3 N6 and the MBP control were immobilized via the MBP-tag on the surface of a CM5-chip. Sequential injections of the analytes, VHH antibodies, in increasing protein concentrations allowed for the determination of specific binding affinities. The experiments were perfomed in a single-cycle mode, using either a Biacore T200 instrument or a Biacore 8K instrument.
Binding affinities were calculated assuming a 1:1 binding model of ligand to analyte. The association constant (K_a) describes the time of complex formation between the ligand and the analyte, whereas the dissociation constant (K_d) is a measure for the complex decay.

The generated VHH antibodies were measured against the target protein MBP-NLRP3 Peak 2 (3-1036) and MBP-NLRP3 N6 (131-704). Representative SPR sensorgrams are shown in Figure 49 to Figure 52.

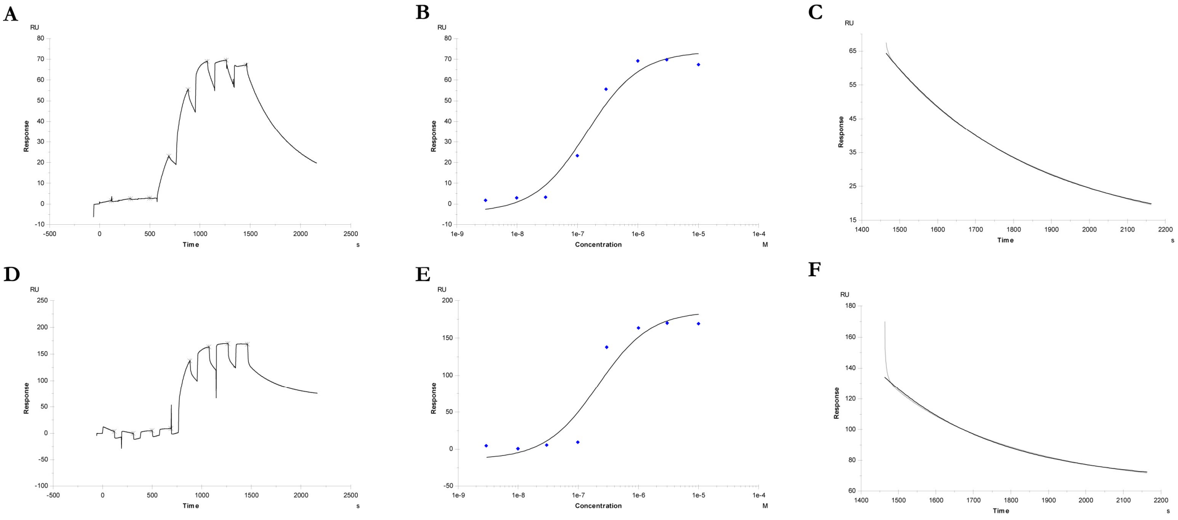

Figure 49: SPR analysis of VHH antibody FS-01A-C10 (hedgehog) and immobilized target proteins MBP-NLRP3 Peak 2 and MBP-NLRP3 N6. A-C: SPR sensorgrams of immobilized MBP-NLRP3 Peak 2 and VHH antibody FS-01A-C10 (hedgehog). **D-F:** SPR sensorgrams of immobilized MBP-NLRP3 N6 and VHH antibody FS-01A-C10 (hedgehog). Single-cycle sequential measurements of three-fold dilutions are shown (A, D). The time [s] is shown on the x-axis and the response [RU] on the y-axis. Binding affinities are calculated dependent on the regression curve shown (B, E). The concentration [M] is shown on the x-axis and the response [RU] on the y-axis. Furthermore, the dissociation is determined using the regression curve shown (C, F). Here, the time [s] is shown on the x-axis and the response [RU] on the y-axis. The experiments were performed using a Biacore T200 instrument.

SPR analysis reveald specific interaction for each of the tested VHH antibodies against the target proteins MBP-NLRP3 Peak 2 and MBP-NLRP3 N6. The determined binding and dissociation constants are displayed in Table 12.

In Figure 49, the SPR sensorgrams of the ligands MBP-NLRP3 Peak 2 and MBP-NLRP3 N6 respectively, are shown for the VHH antibody analyte hedgehog. An affinity of 143.3 nM was calculated for the full-length NLRP3 protein, whereas the shorter N6 construct (aa 131-704) showed a K_D of 210.2 nM. The equilibrium constant K_D was determined using a nonlinear calibration curve, fitting the analyte concentration in a steady-state affinity model, shown in Figure 49 B and E.

Furthermore, the analyte hedgehog showed a slower dissociation from the ligand MBP-NLRP3 Peak 2 (2.6×10^{-3} s^{-1}), compared to the NACHT-domain variant (K_d = 3.3×10^{-3} s^{-1}). A similar result was obtained for the VHH antibody analyte mosquito (Figure 50). Again, a higher binding affinity (69.2 nM) was determined for the full-length MBP-NLRP3 ligand, compared to the NACHT-domain variant (179.0 nM). The three-fold difference in the binding affinity is mainly due to a difference in the dissociation of the VHH antibody. Again, the dissociation constant determined for the ligand MBP-NLRP3 N6 was faster (3.4×10^{-3} s^{-1}), compared to MBP NLRP3 Peak 2, resulting in a K_d value of 1.6×10^{-3} s^{-1}.

In contrast, the analysis of the VHH antibody horse revealed a significantly different kinetic: the binding affinity between the ligand MBP-NLRP3 Peak 2 (521.1 nM) was smaller compared to the NACHT-domain variant (480.1 nM). Moreover, for both ligands the fastest dissociation constant of 2.3×10^{-2} s^{-1} and 3.0×10^{-2} s^{-1} respectively, was determined (Figure 53).

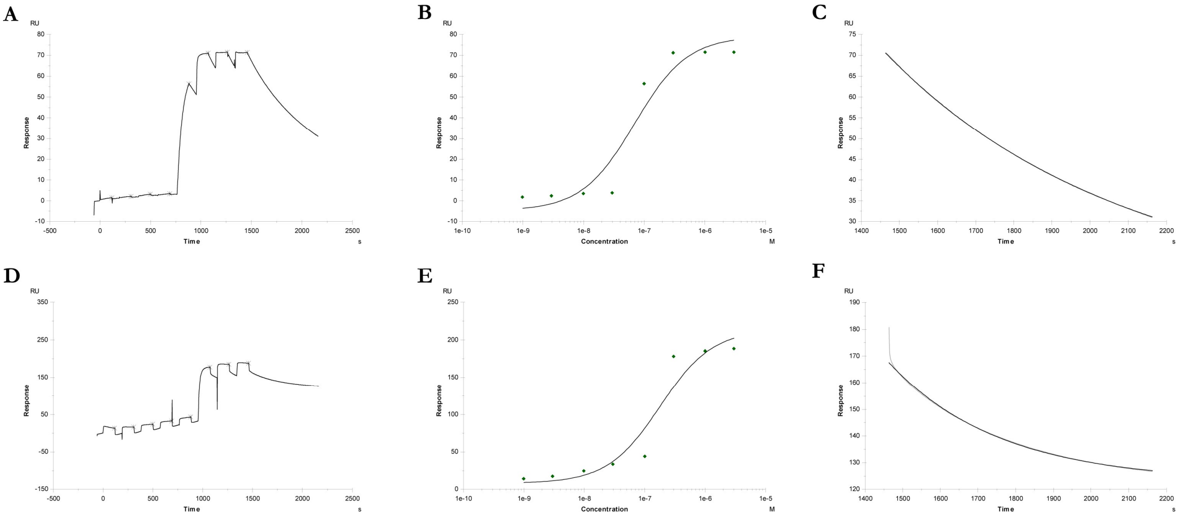

Figure 50: SPR analysis of VHH antibody FS-01A-C09 (mosquito) and immobilized target proteins MBP-NLRP3 Peak 2 and MBP-NLRP3 N6. A-C: SPR sensorgrams of immobilized MBP-NLRP3 Peak 2 and VHH antibody FS-01A-C09 (mosquito). **D-F:** SPR sensorgrams of immobilized MBP-NLRP3 N6 and VHH antibody FS-01A-C09 (mosquito). Single-cycle sequential measurements of three-fold dilutions are shown (A, D). The time [s] is shown on the x-axis and the response [RU] on the y-axis. Binding affinities are calculated dependent on the regression curve shown in B and E, respectively. The concentration [M] is shown on the x-axis and the response [RU] on the y-axis. Furthermore, the dissociation is determined using the regression curve shown in C and F, respectively. The time [s] is shown on the x-axis and the response [RU] on the y-axis. The experiments were performed using a Biacore T200 instrument.

SPR analysis of the VHH antibody SN-04A-D08 (wolf), raised against the LRR-domain of NLRP3, revealed the fastest binding kinetics, of all VHH antibodies tested. Again, a higher affinity was determined for the NLRP3 full-length construct (6.97 nM), whereas a K_D value of 146.8 nM was determined for the NACHT-domain variant. Furthermore, the analyte wolf showed strong binding to the full-length NLRP3 ligand, as nearly no dissociation was measurable ($K_d = 1.8\times10^{-5}\ s^{-1}$) (Figure 51).

In a control experiment, the generated VHH antibodies were tested against MBP as the ligand bound to the chip surface, to test for cross-interaction with the affinity-tag. In Figure 52, the SPR sensorgrams and the calibration curves generated to determine specific binding affinities are shown for the analyte horse and wolf, measured with the ligand protein MBP. Similar to the data obtained for the target proteins MBP-NLRP3 Peak 2 and MBP NLRP3 N6, the kinetics determined for the VHH antibody analyte horse were fast and showed the lowest binding affinity, compared to the remaining VHH antibodies. Again, the kinetic of the VHH antibody wolf was comparable to the measurements generated for the ligand proteins MBP-NLRP3 Peak 2 and MBP-NLRP3 N6, showing an even lower dissociation constant of $6.2\times10^{-6}\ s^{-1}$.

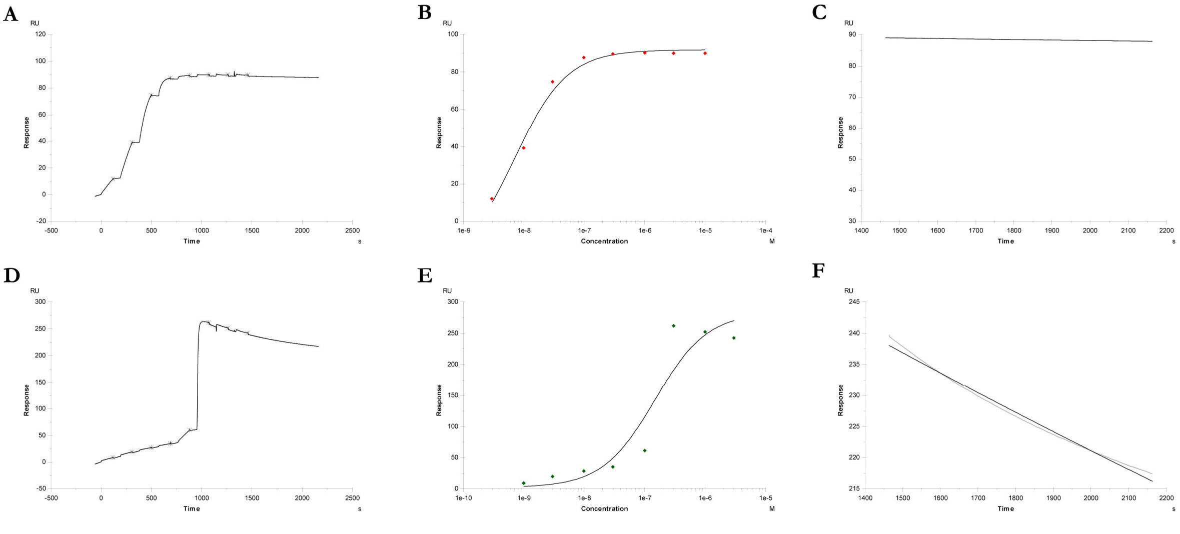

Figure 51: SPR analysis of VHH antibody SN-04A-D08 (wolf) and immobilized target proteins MBP-NLRP3 Peak 2 and MBP-NLRP3 N6. A-C: SPR sensorgrams of immobilized MBP-NLRP3 Peak 2 and VHH antibody SN-04A-D08 (wolf). **D-F:** SPR sensorgrams of immobilized MBP-NLRP3 N6 and VHH antibody SN-04A-D08 (wolf). Single-cycle sequential measurements of three-fold dilutions are shown (A, D). The time [s] is shown on the x-axis and the response [RU] on the y-axis. Binding affinities are calculated dependent on the regression curve shown in B and E, respectively. The concentration [M] is shown on the x-axis and the response [RU] on the y-axis. Furthermore, the dissociation is determined using the regression curve shown in C and F, respectively. The time [s] is shown on the x-axis and the response [RU] on the y-axis. The experiments were performed using a Biacore T200 instrument.

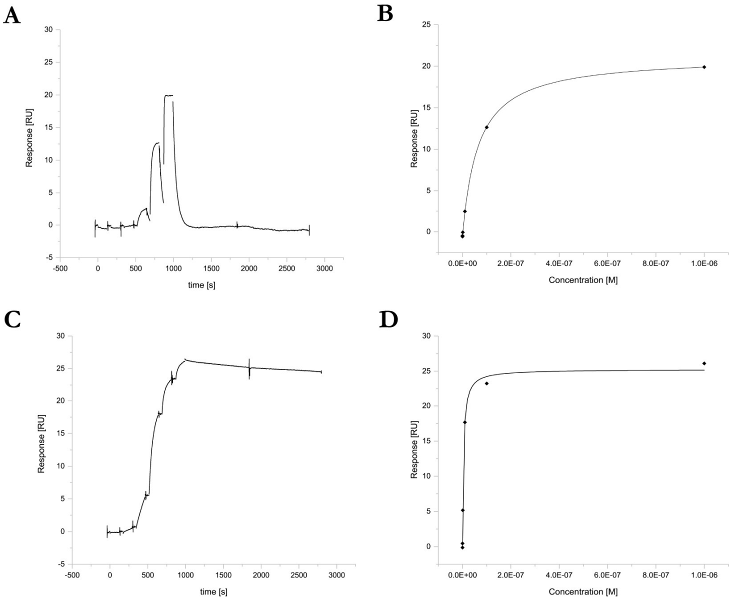

Figure 52: SPR analysis of VHH antibody FS-02B-E02 (horse) and SN-04A-D08 (wolf), respectively and the immobilized target protein MBP. A,B: SPR sensorgrams of immobilized MBP VHH antibody FS-02B-E02 (horse). **C,D:** SPR sensorgrams of immobilized MBP and VHH antibody SN-04A-D08 (wolf). Single-cycle sequential measurements of ten-fold dilutions are shown (A, C). The time [s] is shown on the x-axis and the response [RU] on the y-axis. Binding affinities are calculated dependent on the regression curve shown in B and D, respectively. The concentration [M] is shown on the x-axis and the response [RU] on the y-axis. The experiments were performed using a Biacore 8K instrument.

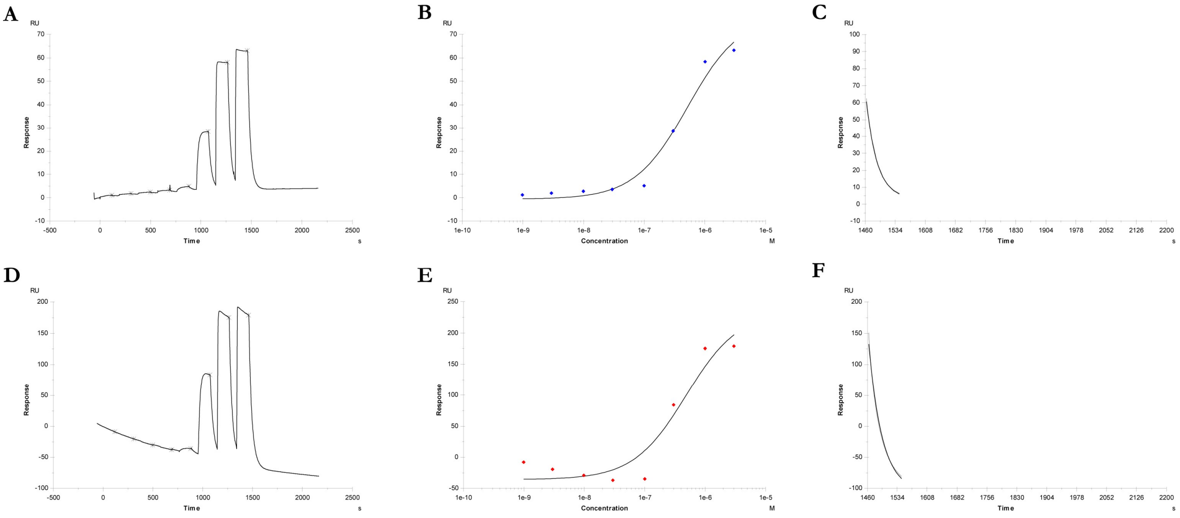

Figure 53: SPR analysis of VHH antibody FS-02B-E02 (horse) and immobilized target proteins MBP-NLRP3 Peak 2 and MBP-NLRP3 N6. A-C: SPR sensorgrams of immobilized MBP-NLRP3 Peak 2 and VHH antibody FS-02B-E02 (horse). **D-F:** SPR sensorgrams of immobilized MBP-NLRP3 N6 and VHH antibody FS-02B-E02 (horse). Single-cycle sequential measurements of three-fold dilutions are shown (A, D). The time [s] is shown on the x-axis and the response [RU] on the y-axis. Binding affinities are calculated dependent on the regression curve shown in B and E, respectively. The concentration [M] is shown on the x-axis and the response [RU] on the y-axis. Furthermore, the dissociation is determined using the regression curve shown in C and F, respectively. The time [s] is shown on the x-axis and the response [RU] on the y-axis. The experiments were performed using a Biacore T200 instrument.

Each of the analysed VHH antibodies showed a specific binding affinity for the affinity-tag MBP (Table 12). Unfortunately, the binding affinities determined were even higher, compared to the target proteins MBP-NLRP3 Peak 2 and MBP-NLRP3 N6. In order to evaluate the experimental data, two control VHH antibodies were included, which are directed against the ligand MBP. The commercially available anti-MBP VHH (Chromotek) showed a binding affinity of 800 pM for MBP and a dissociation constant of 5.0×10^{-4} s^{-1}. In contrast, an anti-MBP VHH antibody, generated in a previous screen, showed a binding affinity of 17.8 nM for MBP and a dissociation rate of 1.3×10^{-1} s^{-1}. Interestingly, the VHH antibodies emu and lugworm, raised against MBP-NLRP3 Peak 2, showed a higher affinity for MBP, compared to the commercial VHH antibody. Moreover, the VHH antibody wolf, which was raised against the target protein mMBP-NLRP3 LRR 4, resulted in a binding affinity of 5.5 pM for MBP and the slowest dissociation constant of 6.2×10^{-6} s^{-1}. Nonethless, the VHH antibody showed more than 10-fold higher affinity for MBP, than the commercial available VHH antibody, even though it was raised against a mMBP-tagged protein.

Table 12: Binding affinities (K_D) and dissociation constants (K_d) of SPR measurements. SPR measurements were performed for the immobilized target proteins MBP-NLRP3 Peak 2, MBP-NLRP3 N6 and the control MBP and the generated VHH antibodies. The binding affinities K_D are shown in nM; the dissociation constants (K_d) are shown in s^{-1}.

VHH	MBP-NLRP3 Peak 2		MBP-NLRP3 N6		MBP	
	K_D [nM]	K_d [s^{-1}]	K_D [nM]	K_d [s^{-1}]	K_D [nM]	K_d [s^{-1}]
Wolf	6.97	1.8×10^{-5}	146.8	1.4×10^{-4}	0.0055	6.2×10^{-6}
Goose	64.3	4.7×10^{-4}	429.0	1.3×10^{-3}	9.41	3.5×10^{-4}
Rabbit	102.9	8.1×10^{-4}	187.7	2.4×10^{-3}	0.95	3.6×10^{-4}
Elephant	321.3	8.6×10^{-4}	198.0	n.d.	0.97	3.3×10^{-4}
Whale	129.6	8.4×10^{-4}	236.2	9.5×10^{-4}	1.78	2.2×10^{-3}
Hen	285.4	1.6×10^{-3}	378.0	n.d.	3.71	7.8×10^{-4}
Fox	219.9	1.6×10^{-3}	274.0	2.0×10^{-3}	2.34	8.6×10^{-4}
Mosquito	69.2	1.6×10^{-3}	179.0	3.4×10^{-3}	1.63	9.6×10^{-4}
Emu	14.8	1.8×10^{-3}	209.5	1.7×10^{-3}	0.57	5.5×10^{-4}
Hedgehog	143.3	2.6×10^{-3}	210.2	3.3×10^{-3}	11.9	9.2×10^{-4}
Lugworm	209.8	2.9×10^{-3}	217.6	2.3×10^{-3}	0.42	3.2×10^{-3}
Seal	799.2	4.2×10^{-3}	706.2	5.8×10^{-3}	36.1	2.4×10^{-3}
Horse	521.1	2.3×10^{-2}	480.1	3.0×10^{-2}	68.1	2.5×10^{-2}
Anti-MBP VHH	-	-	-	-	17.8	1.3×10^{-1}
Anti-MBP NB	-	-	-	-	0.80	5.0×10^{-4}

In summary, the immunization procedure resulted in VHH antibodies, specifically binding to the affinity-tag MBP, instead of binding to the target protein NLRP3. Interestingly, three VHH antibodies were identified, which show an even higher binding affinity than the commercially available anti-MBP VHH antibody from Chromotek.

8.5 *In vitro* generation of ASC specks

8.5.1 Structural analysis of ASC oligomerization

The adaptor protein ASC is involved in the formation of several different inflammasome complexes as well as in regulatory events. ASC consists of an N-terminal PYD-domain and a C-terminal CARD-domain, connected by an intramolecular linker region. Either the PYD-domain or the CARD-domain is involved in homotypic domain-domain interactions, which facilitate and amongst others, enable the formation of the NLRP3 inflammasome by PYD-PYD interactions, as well as the formation of the NLRC4 inflammasome by CARD-CARD interactions (Kwon *et al.*, 2012). Furthermore, ASC bridges the NLR-protein to the Caspase-1 zymogen via CARD-CARD interactions, mediating the formation of an inflammasome complex.

Besides the structural investigation of inflammsomes, also the single inflammasome components like ASC and Caspase-1 are of major interest.

8.5.1.1 Electron microscopic analysis of full-length human ASC

Structural analysis by transmission electron microscopy of the N-terminal PYD-domain of human ASC (PDB: 3J63) revealed that the domain itself is able to undergo polymerization and forms filaments *in vitro* with a diameter of 9 nm (Lu *et al.*, 2014). Three intermolecular interfaces have been characterized in a mutational approach, which were identified to be responsible for filament formation (Lu *et al.*, 2014). In a similar approach, also the human ASC CARD-domain (PDB: 6NIH) was investigated by transmission electron microscopy (Li *et al.*, 2018). Also the ASC CARD-domain was shown to undergo self-oligomerization, resulting in a filamentous structure with a diameter of 8 nm. Again, three intermoelcular interfaces have been identified in a mutational approach, which facilitate fibril formation.

Furthermore, in reconstituted immortalized murine BMDMs, the PYD-domain of ASC was identified to mediate filament formation. In contrast, the CARD-domain was shown to mediate intermolecular bridging by crosslinking of single filaments, resulting in the formation of an ASC-speck upon activation of NLRP3 (Dick *et al.*, 2016). Until now, the only structural information about the ASC full-length protein is gained by a structure of monomeric human ASC (PDB: 2KN6) determined by NMR (de Alba, 2009).

Human full-length ASC was recombinantly expressed and purified from *E.coli* cells and the oligomerization and fibrillation was investigated by transmission electron microscopy.

Human wild-type ASC-mCherry$_{His}$ was recombinantly expressed in *E.coli* cells and subsequently purified from inclusion bodies, as displayed in Figure 54. The resulting protein was further purified by affinity chromatography, dialysed and subjected to ultracentrifugation and an incubation step at 37°C. Transmission electron microscopy revealed that incubation in 2 M Gdn-HCl is insufficient for the complete lysis of inclusion bodies, as vesicular structures are still detectable during this purification step (step 4. b). Nonetheless, it was sufficient to prevent fibrillation of the protein, as no fibrillar structures are detectable. Negative stain electron microscopy of the affinity purified ASC-mCherry$_{His}$ by metal affinity chromatography, resulted in short fibrillar structures in the pooled sample, shown in Figure 54, step 5, suggesting a concentration dependent initiation of fibrillation.

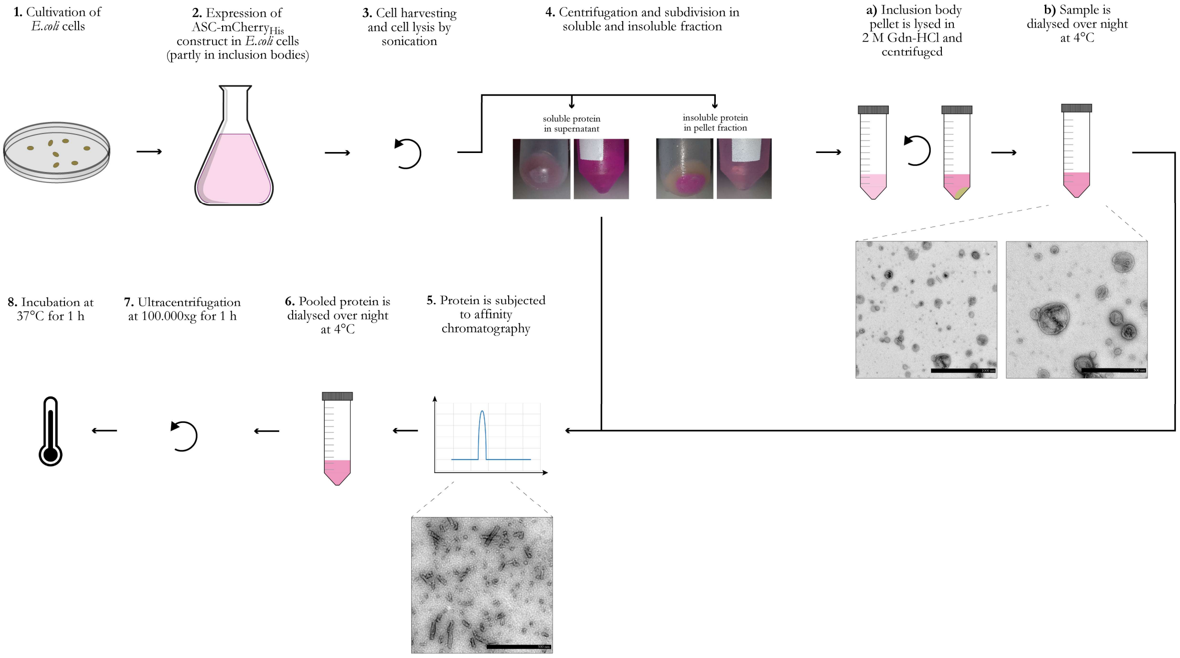

Figure 54: Workflow of ASC-mCherry$_{His}$ protein purification. Human ASC-mCherry$_{His}$ variants are recombinantly expressed in *E.coli* cells, the cells are harvested and subsequently lysed by sonication. Dependent of the protein expression compartment, the cell lysate is either directly used for affinity chromatography or the cell pellet is subjected to an inclusion body purification procedure, shown in step 4. a) and b), respectively. Following affinity chromatography, the protein is dialysed and filament formation is initiated by an ultracentrifugation step prior to incubation at 37°C for 1 h. Individual steps during the protein purification procedure have been analysed by transmission electron microscopy. The scale bars used indicate the following sizes: 1000 nm step 4. b) left and 500 nm step 4. b) right and step 5., respectively.

SDS-PAGE analysis of samples taken from purification step 4 and 5, respectively, revealed a band at about 50.41 kDa, the approximate MW of ASC-mCherry$_{\text{His}}$. Furthermore, two contaminating bands are detectable, corresponding to a MW of about 30 kDa and 20 kDa, respectively (Figure 55).

The purified protein ASC-mCherry$_{\text{His}}$ was subjected to ultracentrifugation, followed by an incubation period of 1 h at 37°C, in order to initiate fibrillation of the protein.

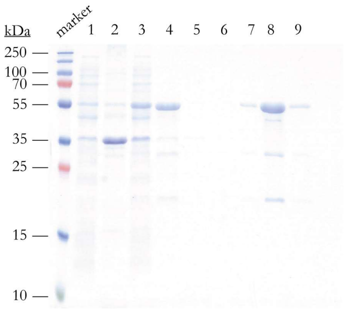

1. supernatant (step 4.)
2. pellet (step 4.)
3. supernatant (step 4. a)
4. supernatant (step 4. b)
5. flow-through fraction (step 5.)
6. wash fraction (step 5.)
7. elution fraction 7 (step 5.)
8. elution fraction 9 (step 5.)
9. elution fraction 11 (step 5.)

Figure 55: SDS-PAGE analysis of ASC-mCherry$_{\text{His}}$ purification procedure. Individual samples of the ASC-mCherry$_{\text{His}}$ purification procedure, step 4. and step 5. respectively, have been subjected to SDS-PAGE (15%) analysis. The samples show a band at about 50.41 kDa, corresponding to the approximate MW of the recombinant ASC-mCherry$_{\text{His}}$ protein.

Transmission electron microscopy was used to study the oligomeric assembly of the human full-length ASC protein. In Figure 56, representative negative stain EM images are shown.

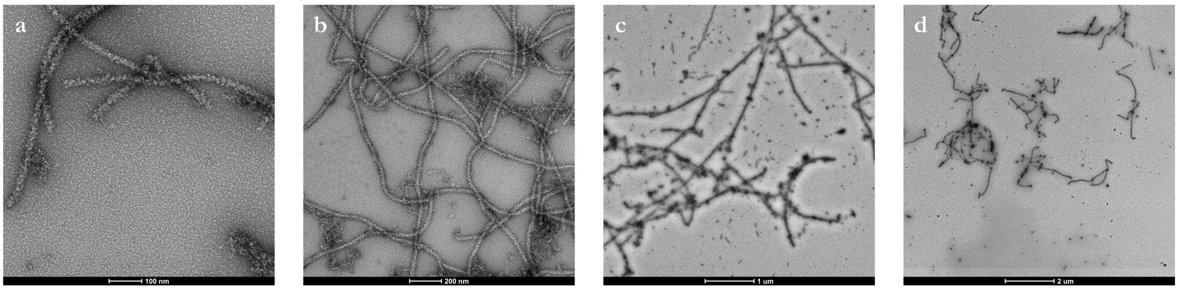

Figure 56: Transmission electron microscopic analysis of human ASC-mCherry$_{\text{His}}$. Recombinantly expressed and purified human ASC-mCherry$_{\text{His}}$ was incubated at 37°C for 1h (a-c) and for 23 h at 37°C (d) and subsequently subjected to negative stain electron microscopic analysis. The protein was used in a concentration of 0.9 mg/mL. Scale bars are shown below each image.

Transmission electron microscopy clearly revealed fibrillar structures for the mCherry-tagged human ASC protein with an average diameter of 22.7 nm. After 1 h of incubation at 37°C, long structured fibrillar structures are seen, as well as monomeric and smaller oligomeric protein structures (Figure 56 a-c). Moreover, improperly folded protein aggregates are detectable.

Compared to the incubation of 1 h, a longer incubation period of 23 h also resulted in long fibrils of ASC-mCherry$_{\text{His}}$, going along with monomeric and oligomeric protein populations. Either connection of individual fibrils as well as branching of the fibrillar structures was detectable after both time points. Thus, it was shown that the full-length human ASC-mCherry$_{\text{His}}$ protein forms fibrillar structures *in vitro* in a concentration and time-dependent manner.

8.5.1.2 Mutational studies of ASC oligomerization interfaces

In order to investigate the effect of the PYD-domain and the CARD-domain of ASC on its ability to form fibrils *in vitro*, single point-mutations were introduced in either of the two domains and the oligomeric assembly was investigated by transmission electron microscopy. Previous studies have shown, that the PYD-domain of ASC is essential for the formation of an intracellular ASC-speck upon activation of NLRP3, as it initiates fibrillation (Dick *et al.*, 2016).

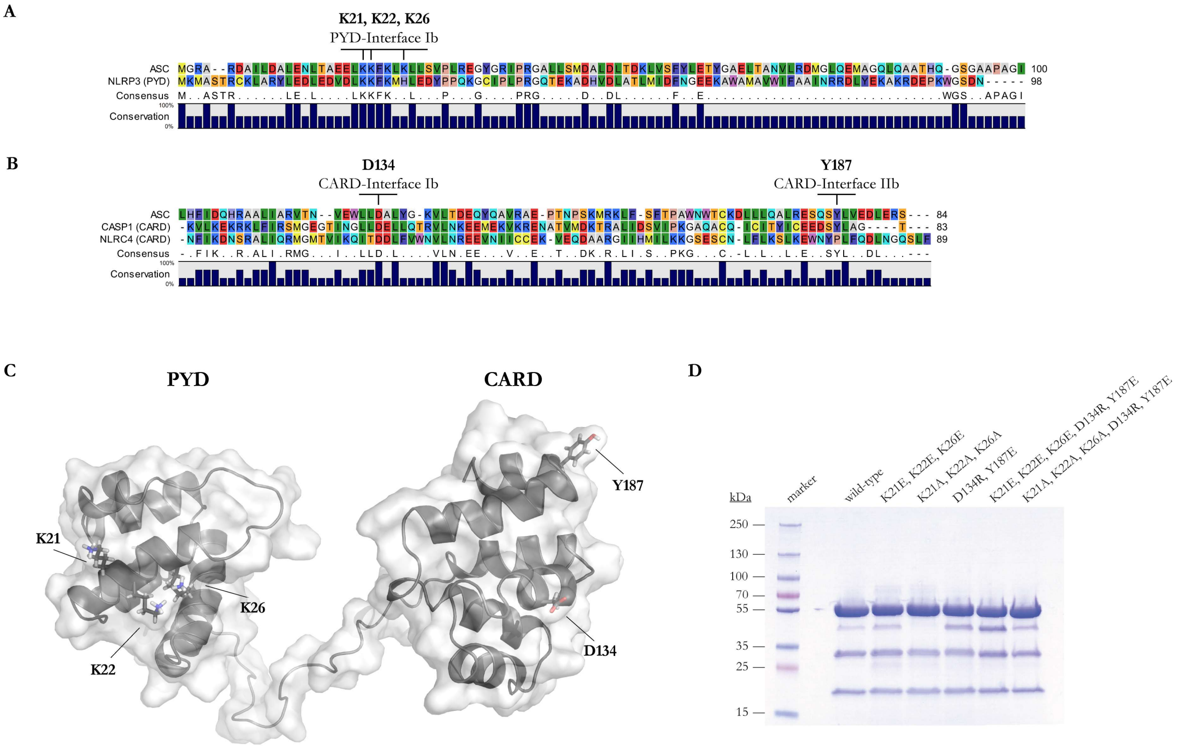

Figure 57: Analysis of ASC oligomerization interfaces. A: Sequence alignment of human ASC-PYD (1-100) and human NLRP3-PYD (1-98). The consensus sequence and the sequence conservation is shown below. The residues K21, K22 and K26 are indicated. **B:** Sequence alignment of human ASC-CARD (112-195), human Caspase 1-CARD (4-86) and human NLRC4-CARD (2-90) is shown. The consensus sequence and the sequence conservation is shown below. The residues D134 and Y187 are indicated. **C:** NMR structure of full-length human ASC (PDB: 2KN6) showing CARD and PYD domain, including surface representation (De Alba, 2009). The amino acids subjected to point-mutations are indicated. **D:** SDS-PAGE of recombinantly expressed and purified human full-length ASC-mCherry variants.

Moreover, the CARD-domain was found to facilitate speck formation by crosslinking of the individual filaments, though both individual domains were found to form fibrils *in vitro (Lu et al., 2014; Dick et al., 2016; Li et al., 2018)*. Both, the PYD-domain and the CARD-domain of ASC were found to assemble into fibrillar structures, each facilitated by three intramolecular interfaces, identified in a mutational approach (Lu *et al.*, 2014; Li *et al.*, 2018). In order to determine suitable point-mutations to study the effect of both domains on the fibrillation ability of full-length human ASC, residues which are involved in homotypic interfaces were chosen.

A sequence alignment of the human ASC PYD-domain and the PYD-domain of human NLRP3, revealed a strong conservation of residues involved in the intramolecular interfaces facilitating the fibrillar assembly of the ASC PYD-domain (Figure 13 and Figure 57). Thus, three residues, forming the main interface (Ib), were chosen for a mutational approach: K21, K22 and K26 (Lu *et al.*, 2014). Furthermore, a sequence alignment of the human ASC CARD-domain and the human Caspase-1 CARD-domain revealed two highly conserved residues (D134 and Y187), which were meanwhile identified to form the intramolecular interfaces Ib and IIb, respectively, thus facilitating fibrillation of the ASC CARD-domain (Li *et al.*, 2018). The mentioned residues were mutated in order to investigate the effect of the respective charge on the formation of the intramolecular interface. Thus K21, K22 and K26 were either mutated to an uncharged alanine residue (A) or to the negatively charged glutamic acid (E). Simillarly, the residue D134 was mutated to a positively chared arginine residue (R), whereas Y187 was substituted by the negatively charged glutamic acid residue (E).

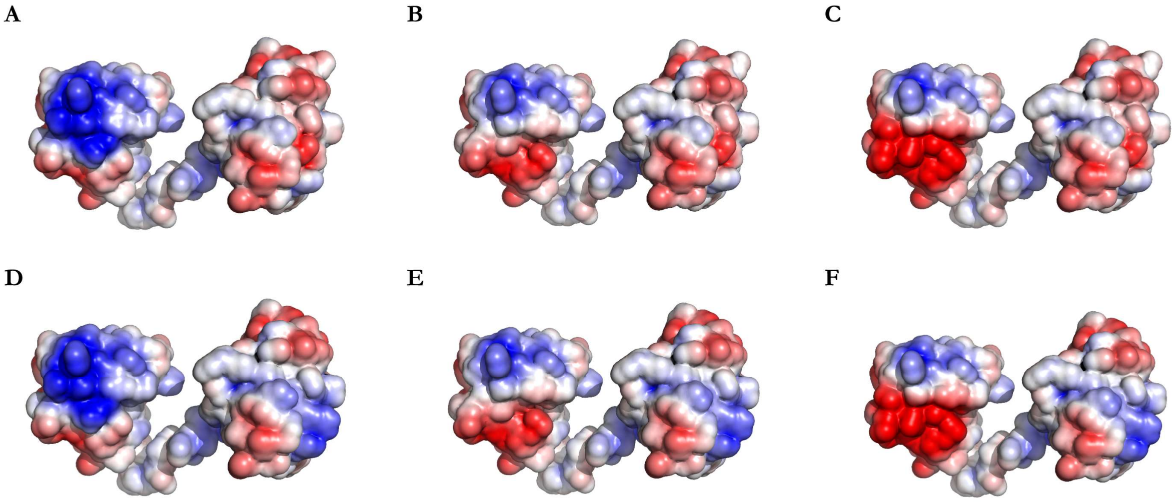

Figure 58: Electrostatic surface representation of full length human ASC (PDB: 2KN6). The wild-type protein is shown in **A** and modified accordingly, the PYD interface mutant K21A,K22A,K26A (**B**) as well as the respective charge reversal mutant K21E, K22E, K26E (**C**). Furthermore, an electrostatic surface representation of human ASC full-length, including mutations in the CARD-domain (D134R, Y187E) are shown (**D**). These mutations are also shown in combination with the PYD Interface I mutations K21A, K22A, K26A (**E**) and K21E, K22E and K26E (**F**). The electrostatic surface is displayed in a charge range of k_BT -3 to +3.

The mutations involving the PYD-domain and the CARD-domain of ASC were either introduced seperately or in combination with the residues located on the second domain, to yield ASC-mCherry$_{\text{His}}$ variants which are incapable of fibril formation *in vitro*. The respective protein variants were purified according to the workflow presented in Figure 54.

Of note, all ASC-mCherry$_{\text{His}}$ variants were purified using the inclusion body purification protocol, displayed in step 4. a and b, except for the variants K21A, K22A, K26A, D134R, Y187E and K21E, K22E, K26E, D134R, Y187E, which were expressed as soluble protein and thus directly subjected to affinity purification. An SDS-PAGE of the resulting protein variants showing the protein purity is presented in Figure 57. Introduction of charge reversal mutations leads to changes in the electrostatic surface of the protein, presented in Figure 58.

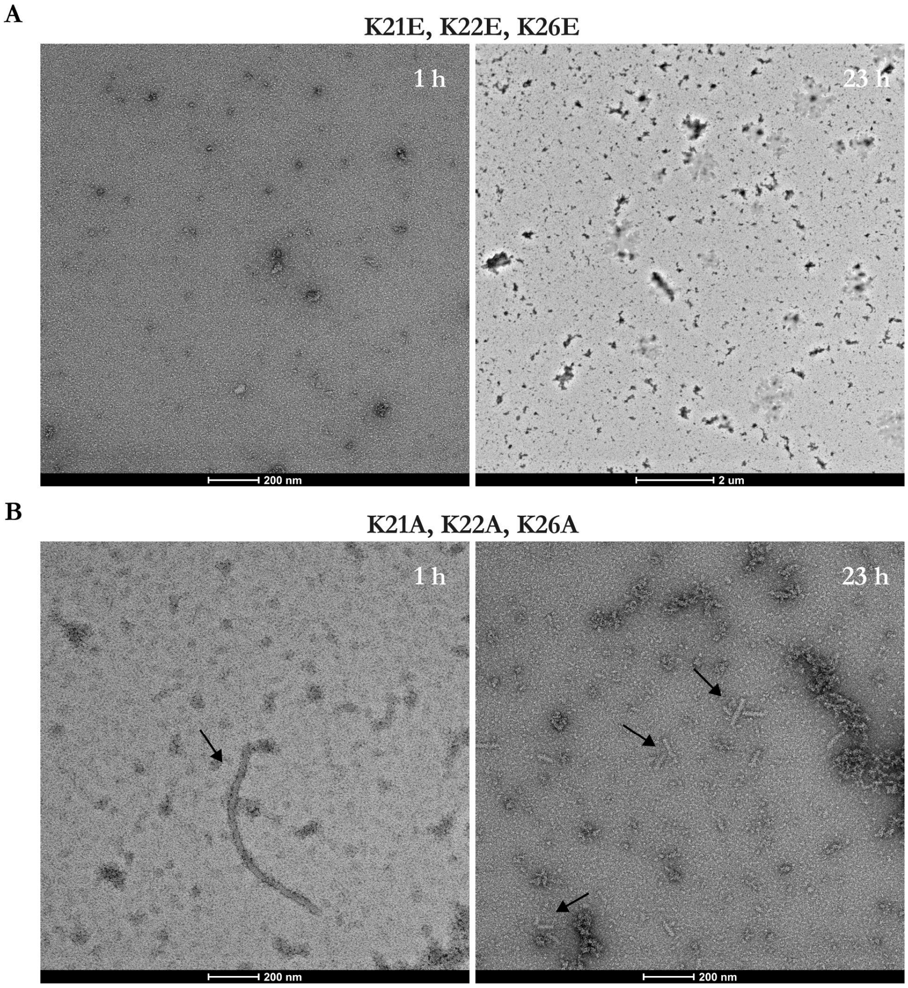

Figure 59: Transmission electron microscopic analysis of human ASC-mCherry$_{\text{His}}$ PYD-mutants. Recombinantly expressed and purified human ASC-mCherry$_{\text{His}}$ was incubated at 37°C for 1 h and for 23 h at 37°C and subsequently subjected to negative stain electron microscopic analysis. **A:** ASC-mCherry$_{\text{His}}$ K21E, K22E and K26E does not show filament formation after 1 h (0.9 mg/mL) to 23 h (0.3 mg/mL) of incubation. **B:** ASC-mCherryHis K21A, K22A and K26A shows very low filament formation after 1 h of incubation (a) (0.3 mg/mL). Short protofibrils are shown after 23 h of incubation (0.3 mg/mL) (b). Protofibrils are marked by an arrow. Scale bars are included below each image.

Either the introduction of charge-neutral or negatively charged residues in interface Ib of the ASC PYD-domain lead to a more negatively charged electrostatic surface.

In contrast, the influences of the point-mutations introduced in the CARD-domain of ASC (D134 and Y187) have a lower impact on the electrostatic surface, whereas the single Y187 to E mutation leads to the incorporation of a smaller residue in a negatively charged patch.

In order to investigate the influence of the mentioned mutations on the ability of ASC-mCherry$_{His}$ to form filamentous structures, the proteins were analysed by transmission electron microscopy.

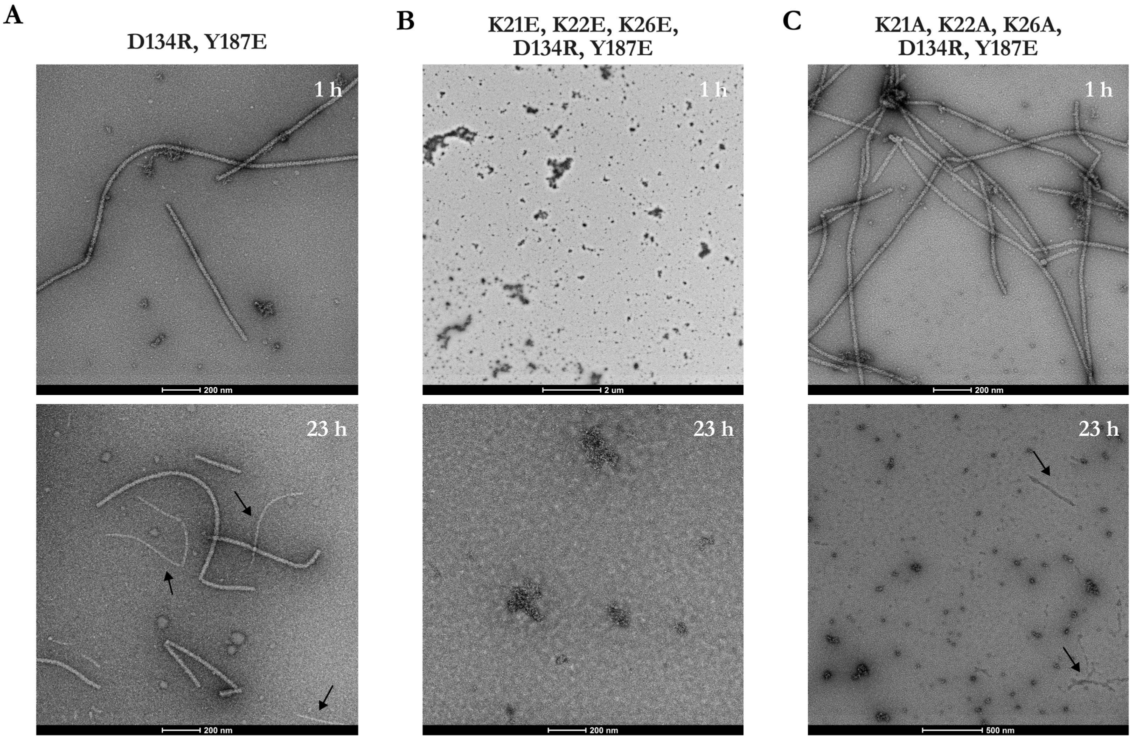

Figure 60: Transmission electron microscopic analysis of human ASC-mCherry$_{His}$ CARD-mutants. Recombinantly expressed and purified human ASC-mCherry was incubated at 37°C for 1h and for 23 h at 37°C and subsequently subjected to negative stain electron microscopic analysis. **A:** ASC-mCherry$_{His}$ D134R, Y187E shows regular filament formation after 1 h (0.9 mg/mL) and after 23 h of incubation time (0.9 mg/mL). Thinner filaments are marked by an arrow. **B:** ASC-mCherry$_{His}$ K21E, K22E, K26E, D134R, Y187E does not show filament formation during 23 h of incubation (0.9 mg/mL). **C:** ASC-mCherry$_{His}$ K21A, K22A, K26A, D134R, Y187E shows regular fibril formation after 1 h of incubation (0.9 mg/mL), but very low fibrillation after 23 h of incubation (0.9 mg/mL). Short fibrils are marked by an arrow. Scale bars are included below each image.

Either charge-neutral or charge reversal mutations of the residues K21, K22 and K26 resulted in strongly impaired filament formation of ASC-mCherry$_{His}$. Transmission electron microscopy revealed, that exchanging these residues by glutamic acid abrogates filament formation completely (Figure 59 A). In contrast, the exchange of K21A, K22A and K26A, resulted in a single fibril after 1 h of incubation and several short protofibrils after 23 h of incubation. The protofibrils were determined to have an average diameter of 22.5 nm.

Both samples showed monomeric protein as well as smaller oligomeric structures. Furthermore, aggregates were visible, caused by improper folded protein oligomers. Besides the mutations in the PYD-domain of human ASC, also mutations in the CARD-domain were investigated by transmission electron microscopy. The CARD-mutant ASC-mCherry$_{\mathrm{His}}$ D134R, Y187E showed regular fibrillation after 1 h of incubation, whereas two individual fibril species were detectable after 23 h of incubation. One of which was determined to have an average diameter of 22.6 nm, comparable to the fibril diameter of 23.1 nm, determined after 1 h of incubation. Furthermore, a second, thinner fibril species was found in these samples, with an average diameter of about 12.9 nm (Figure 60 A). Comparable to the ASC-mCherry$_{\mathrm{His}}$ K21E/ K22E/K26E mutant, the corresponding PYD and CARD mutant, did not show any fibrillation after incubation for 23 h. In contrast, the ASC-mCherry K21A/K22A/K26A/D134R/Y187E mutant showed regular fibrillation after 1 h of incubation, but only shows short fibrillar structures after 23 h of incubation, comparable to the corresponding PYD-mutant.

Mutations in the PYD-domain of ASC were shown to be sufficient to abrogate filament formation, whereas mutations in the CARD-domain resulted in the generation of a second, thinner fibril species.

8.5.1.3 ASC seeds pathogenic amyloid-β (1-42) fibrils *in vitro*

Alzheimer's disease (AD) is a common dementing illness, affecting about 150 million patients worldwide (Heneka *et al.*, 2014). Histologically, the parenchymal deposition of amyloid-β (Aβ) is an early event, followed by neuroinflammation as well as the formation of neurofibrillary tangles by the microtubule-associated protein tau (Heneka *et al.*, 2014). Amyloid-β deposition is initiated by a dysregultaion in the proteolytic cleavage of the membrane protein amyloid-precursor protein (APP), causing a peripheral amyloidoses (Vassar *et al.*, 2014). Amyloid plaques are protein aggregates formed by mis-folded proteins that arrange into β-pleated sheet structures (Vassar *et al.*, 2014).

The proteolytic cleavage of APP is a sequential process mediated by β- and γ-secretases, leading to the liberation of the 38 to 43 residue-long Aβ peptide (Vassar *et al.*, 2014). The secreted Aβ-peptides, supported by post-translational modifications, polymerize into fibrillar structures with an approximate diameter of 10 nm, which accumulate in senile plaques and at the walls of cerebral blood vessels (Roher *et al.*, 2017). Amyloid-β plaques are mainly composed of two peptide species: Aβ (1-40) and Aβ (1-42), of which Aβ (1-42) shows the fastest fibrillation kinetics *in vitro* (Roher *et al.*, 2017).

Besides the histological basis underlying AD, evidence emerged that neuroinflammation plays a crucial role in disease pathogenesis (Heneka *et al.*, 2014). It is suggested, that the process of neuroinflammation is triggered by PRRs through PAMPs and DAMPs in microglia and other cell types in the brain, like astrocytes, neurons and endothelial cells (Heneka *et al.*, 2014).

Neurodegenerative diseases like AD go along with an excessive release of pro-inflammatory cytokines like pro-IL-1β and pro-IL-18, which links AD to the NLRP3 inflammasome, as it senses a multitude of different stimuli (Heneka *et al.*, 2014). NLRP3 and Caspase-1 were shown to play an important role in AD pathogenesis, as NLRP3$^{-/-}$ or Caspase-1$^{-/-}$ mice, additionally carrying mutations, which promote familial AD were shown to be protected from spatial memory loss and also showed an enhanced Aβ clearance (Heneka *et al.*, 2013).

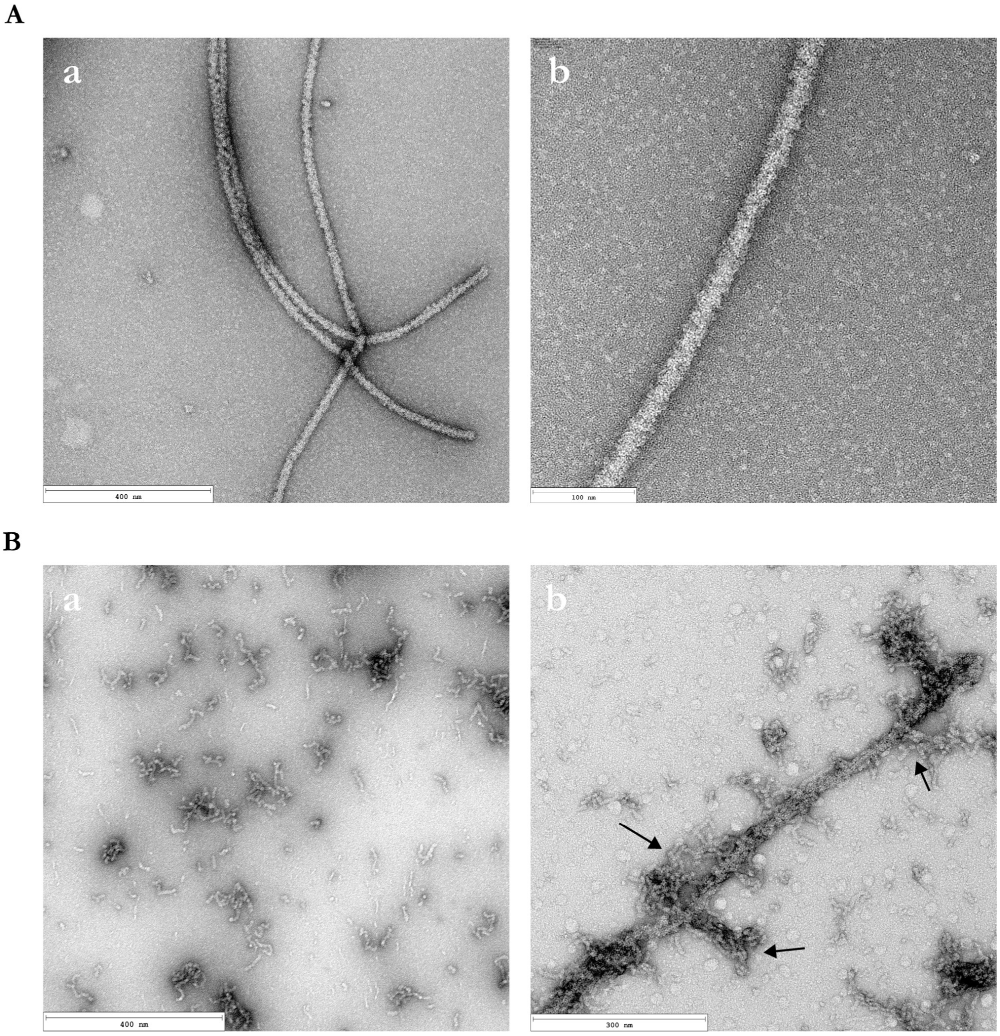

Figure 61: Transmission electron microscopic analysis of recombinantly expressed human ASC-mCherry$_{His}$ full-length and amyloid-β (1-42). A: Recombinantly expressed and purified human ASC-mCherry$_{His}$ was incubated at 37°C for 72 h (a and b) and subsequently subjected to negative stain electron microscopic analysis. **B:** EM analysis of the pathogenic peptide amyloid β (1-42) revealed small clustered fibrils after 72 h of incubation (a). The incubation of human ASC-mCherry$_{His}$ full length and amyloid β (1-42) for 72 h at 37°C resulted in a colocalization of both proteins, visualized by negative-stain electron microscopy (b).

To investigate the impact of the NLRP3 inflammasome component ASC on AD pathology, recombinant ASC-mCherry$_{\mathrm{His}}$ protein was tested in order to promote Aβ fibrillation *in vitro*, monitored by transmission electron microscopy.

Point-mutations in the PYD and CARD domain of the recombinant ASC-mCherry$_{\mathrm{His}}$ protein were tested in immunoblots in order to analyse the effect on the promotion of Aβ (1-40) and Aβ (1-42) aggregation *in vitro* (Venegas *et al.*, 2017).

The recombinant protein ASC-mCherry$_{\mathrm{His}}$ was analysed by transmission electron microscopy, as well as the synthetic peptide Aβ (1-42) (Figure 61). Moreover, recombinant ASC-mCherry$_{\mathrm{His}}$ and Aβ (1-42) were co-incubated for 72 h and analysed by negative stain electron microscopy. Transmission electron microscopy clearly revealed small clustered fibrils of synthetic Aβ (1-42) after 72 h of incubation, whereas the recombinant ASC-mCherry$_{\mathrm{His}}$ was found to form long and unbranched filaments. The co-incubation of recombinant ASC-mCherry$_{\mathrm{His}}$ and Aβ (1-42) resulted in a colocalization of both proteins. Furthermore, the association and the attachment of Aβ (1-42) fibrils onto the ASC-mCherry$_{\mathrm{His}}$ fibril was clearly shown (Figure 61 B b). Aβ (1-42) fibrils were clustered onto the ASC-mCherry$_{\mathrm{His}}$ fibril in a consistent way, thus no prefernce for branching- or end-points was detectable.

Therefore, recombinant ASC-mCherry$_{\mathrm{His}}$ fibrillation was shown to seed pathogenic Aβ deposits *in vitro*. Based on the experimental data presented in 8.5.1.2, the effect of point-mutations in the PYD- and CARD-domains of ASC-mCherry$_{\mathrm{His}}$ was tested with respect to the ability to promote Aβ (1-40) and Aβ (1-42) aggregation. The dependence of ASC-mCherry$_{\mathrm{His}}$ fibrillation on the seeding of Aβ aggregates was also analysed. A comprehensive presentation of the aquired data has been published: Venegas *et al.*, 2017, Extended data Figure 6.

In short, recombinant ASC-mCherry$_{\mathrm{His}}$ was shown to promote the aggregation of Aβ (1-40) and Aβ (1-42), with an approximate MW of about 4 kDa by immunoblot analysis. The co-incubation with recombinant ASC and Aβ (1-40) lead to an increase in higher Aβ oligomers with a size of 28 kDa to 50 kDa as well as larger oligomers with a size greater than 190 kDa. The same result was achieved for a co-incubation with Aβ (1-42), but showing a comparably higher level of aggregation. Mutations in the PYD-domain of ASC-mCherry$_{\mathrm{His}}$ (K21A, K22A, K26A), completely abolished Aβ (1-40) aggregation. These results are in accordance with the data presented in Figure 59 and Figure 60, showing that the PYD-mutant ASC-mCherry$_{\mathrm{His}}$ (K21A, K22A and K26A), was deficient in fibrillation. Thus, it is concluded, that the fibrillation of ASC underlies the aggregation of Aβ *in vitro*. Moreover, the CARD-mutant ASC-mCherry$_{\mathrm{His}}$ (D134R, Y187E), which was shown to form regular filaments, as well as thinner filament structures after 23 h of incubation (Figure 60 A), did not result in an altered Aβ (1-40) aggregation.

9 Discussion

The NLRP3 inflammasome is the most studied inflammasome to date. Nonetheless little structural and biochemical information has been gained so far. The molecular activation mechanism of NLRP3, leading to the assembly of the multi-protein complex termed NLRP3 inflammasome, is still to be elucidated. The present study aimes at the molecular characterization of NLRP3, yielding both biochemical and structural insights into the assembly of the NLRP3 inflammasome.

9.1 VHH antibodies assisting in NLRP3 crystalization trials

VHH antibodies are well studied tools to assist structure determination of proteins via crystallization, electron microscopy or NMR spectroscopy (Dmitriev *et al.*, 2016). They are used as crystallization chaperones, aiding in nucleation or potentially trapping the protein of interest in a defined conformation that allows for crystallization (Griffin & Lawson, 2011). Furthermore, the single-domain antibodies are easily applicable in crystalization trials, as they comprise a size of only about 15 kDa and are typically recombinantly expressed and purified from *E.coli* cells. Until now, structural information of NLRP3 has been gained only for the N-terminal PYD-domain, determined by both NMR spectroscopy (PDB: 2NAQ) and X-ray crystallography (PDB: 3QF2) (Bae & Park, 2011; Oroz *et al.*, 2016).

This study aimed at the elucidation of structural details of full-length human NLRP3 by electron microscopy and crystallography. Human mMBP-NLRP3 was analysed by crystallography in the presence of small molecule inhibitors like CRID3 (MCC950), Ap5A and nucleotides like ADP and ATP, yielding a resolution of about 15 Å, insuffiecient for structure determination. Hence, specific VHH antibodies targeted against MBP-NLRP3 Peak 2 and the C-terminal LRR-domain of NLRP3 were raised in alpacas. Analysis of the resulting VHH antibodies by SPR revealed a specific interaction of the VHH-antibodies with the maltose-binding protein MBP- and mMBP-affinity tag, respectively. Also, analytical gel filtration of the VHH antibodies of interest revealed no specific interaction with the N-terminal PYD-domain of NLRP3. Therefore, unfortunately, the raised VHH antibodies could neither be used as crystallization chaperones nor in electron microscopic analysis.

MBP is a widely used as fusion partner, to enhance solubility and assist protein folding in crystallization as well as to facillitate phasing (Bokhove *et al.*, 2016). Hence, the MBP-tag is friend and foe at the same time, as a high solubility impedes crystallization of the protein. For crystallization, a mutant MBP version was used, which increases the purification yield as well as the crystallisability of MBP by a shorter linker region as well as by allowing for a closer packing of intramolecular moities (Bokhove *et al.*, 2016). Though, the mutant MBP variant increased crystallizability, it did not allow for proper crystal packing of the NLRP3 fusion protein. In order to further optimize the crystallization procedure, the generated VHH antibodies, targeting the affinity tag, will be used in crystallization trials to increase the crystallizability of MBP by masking surface residues.

Several optimization strategies are well-established for the expression and of multi-domain proteins: exchange of an affinity-tag, expression system, co-expression of chaperones and single domain targeting (Smyth *et al.*, 2003). Typical large affinity tags, that increase the solubility of large multi-domain proteins besides MBP are Glutathione S-Transferase (GST), Green fluorescent protein (GFP), Galactose-binding protein (GBP) and NusA, which can be combined with short affinity tags like poly-Histidine or Streptavidin to facilitate the purification procedure. Although the switch of the expression system from *E.coli* cells to *Sf9* insect cells resulted in soluble NLRP3 protein in sufficient amounts, yielding multiple crystals at many conditions, *Sf9* cells obviously still differ from mammalian cell systems. In contrast to the bacterial expression system, insect cells permit post-translational modifications, whereas the glycosylation pattern is less complex in *Sf9* insect cells compared to mammalian cells (Druzinec *et al.*, 2013). Wether proper glycosylation patters would improve the crystallizability of NLRP3 is not known. Protein expression in a mammalian cell system, like Human Embryonic Kidney 293 cells, could enhance protein stability, functionality and quality. Alternitavely, structural information about multi-domain proteins can be gained by single domain targeting. Therefore, numerous individual variants of either the N-terminal PYD domain, the central NACHT domain and the C-terminal LRR domain of NLRP3 were expressed and purified in *E.coli* and *Sf9* cells. *In silico* analysis of the NLRP3 amino acid sequence revealed insights into the domain architecture of NLRP3. Identified subdomain borders and linker regions were used to facilitate recombinant protein expression and purification. Of note, soluble and stable protein variants were only generated when comprising two charged amino acid clusters: the basic (~ aa 140) and the acidic cluster (~ aa 690). Hence, the interaction of both clusters seems to underly the correct folding of the generated oligomeric protein variants.

The *in silico* analysis of the C-terminal protein sequence further revealed a transition LRR domain (aa 650-720), upstream of the canonical LRR domain (aa 720-1036). Unfortunately, the tested LRR constructs were partly unsoluble and formed large oligomeric and aggregated fractions.

Based on the structural information gained from the crystal structure as well as EM analysis, the NLR-receptor NLRC4 is known to undergo a conformational change from an inactive to an active conformation. The transition from the inactive to the active conformation, causes a rotation by about 21° in the NBD-HD1 segment (Diebolder *et al.*, 2015). A second rotational movement of about 49° has been observed in the LRR-domain (Diebolder *et al.*, 2015).

Hence, the hinge movement takes place in the transition LRR region, upstream of the canonical LRR-domain. Moreover, the crystal structure of mouse NLRC4 (PDB: 4KXF) indicates a critical role for the LRR-domain of NLRC4 (Hu *et al.*, 2013): The C-terminal LRR-domain conceals the NBD-domain by direct interaction and stabilizes the monomeric state of NLRC4 (Hu *et al.*, 2013). In contrast, electron microscopic analysis of NLRC4 in the activated conformation revealed a deviating arrangement of the LRR-domain (PDB: 3JBL, 6B5B) (Hu *et al.*, 2015; Zhang *et al.*, 2015). The C-terminal LRR-domain contacts the N-terminal LRR-motif of the adjacent molecule, resulting in a NAIP-initiated wheel-like assembly of 11 subunits (Hu *et al.*, 2015; Zhang *et al.*, 2015). Moreover, the structure of the LRR-domain of human NLRX1 was determined by crystallization (PDB: 3UN9) including the unique C-terminal and N-terminal helical bundles surrounding the LRR-domain (Hong *et al.*, 2012). Solely the LRR-domain of NLRP1 was crystallized twice, without any associated domains (PDB: 4IM6, 5Y3S). Taken together, in either the inactive or the active conformation, the LRR-domains form a binding interface with adjacent protein domains. Thus the expression and purification of the individual LRR-domain of NLRP3 might have been unsuccessful due to a lack in stabilizing protein domains, like the NBD-domain in the NLRC4 structure.

Besides crystallization attempts of either full-length and subdomain variants of NLRP3, the full-length protein was also analysed by transmission electron microscopy. MBP-NLRP3 Peak 2 resulted in defined single particle structures with an approximate size of 145 Å x 180 Å. In order to exclude MBP-driven oligomerization and structural artifacts caused by the affnity-tag, MBP-NLRP3 was TEV-cleaved to get rid of the MBP-tag and subsequently subjected to sucrose-gradient centrifugation. The resulting fractions were again analysed by transmission electron microscopy and showed similar single particle structures as the untreated MBP-NLRP3 sample. The resulting NLRP3 oligomer is therefore formed independent of the affinity tag. In order to determine the protein structure of NLRP3, the ensuing step is cryo-EM. Until now, the experimental setup underlying the cryo-EM measurement of NLRP3 is still improved further, to optain optimal conditions. Any structural information gained about the NLRP3 protein is of major interst for the development of small molecule inhibitors as well as to elucidate its activation mechanism.

9.2 Interdomain interactions initiating the assembly of the NLRP3 inflammasome

The NLRP3 inflammasome assembly is based on the formation of a molecular platform, initiated by NLRP3, which is thought to serve as a scaffold for the association of the adaptor protein ASC, mediated by PYD-PYD interactions (Dick *et al.*, 2016; Oroz *et al.*, 2016). The adaptor ASC itself serves as a binding platform for Caspase-1, which in turn binds the complex via CARD-CARD interactions (Dick *et al.*, 2016; Schmidt *et al.*, 2016).

One aim of the present study was to structurally analyse the homotypic PYD-domain interactions underlying the assembly of the NLRP3 initiation platform. Furthermore, the formation of an ASC-Speck and the associated fibrillation capacity of ASC was analysed *in vitro* by transmission electron microscopy. The N-terminal PYD domain (aa 3-110, C108S) of NLRP3 was successfully expressed and purified from *E.coli* cells and subsequently analysed by transmission electron microscopy. Upon incubation, the NLRP3-PYD showed unbranched fibrillar structures, with an approximate diameter of 12 nm. Hence, the homotypic PYD-domain interactions of NLRP3 could be confirmed and the molecular scaffold facilitating ASC association was visualized. *In vitro*, the ASC-PYD domain has been found to form fibrillar structures with a diameter of 12 nm determined (NMR), or 9 nm (EM analysis), respectively (de Alba, 2009; Lu *et al.*, 2014). Therefore, the dimensions determined for the NLRP3 PYD-filament match the requirements appointed by the ASC-PYD fibril.

Post-translational modifications, like phosphorylations, have been shown to influence the assembly of the NLRP3 inflammasome. Phosphorylation at position Ser5 in the PYD-domain of NLRP3 has been found to inhibit NLRP3 inflammasome activation (Stutz *et al.*, 2017). It is assumed, that electrostatic interactions are abbrogated by the phosphorylation event, which in turn prevents the formation of the molecular scaffold, essential for the association of the adaptor protein ASC (Stutz *et al.*, 2017). Here, we observed a deviating fibrillation behavious for the phospho-mimetic mutant NLRP3-PYD (S5E), compared to the wild-type NLRP3-PYD protein. The fibrils formed by the mutant were shorter and showed half of the diameter, compared to the wild-type protein. In concludion, the phosphorylation of Ser5 in the PYD-domain, leads to an altered assembly, unable to act as a platform for ASC polymerization. Accoding to *in silico* analyses Ser5 might participate in Interface Ia based on the intermolecular interfaces identified to mediate the polymerization of the ASC-PYD domain (Lu *et al.*, 2014). Further residues were assumed to form equivalent interfaces to the ASC-fibril and were thus investigated in a mutational approach.

The charge-reversal mutant K23E, located on the opposite interface (Ib) to the one containing the phosphorylation site Ser5, was shown to completely abbrogate filament formation. These results match the previously published *in vitro* data obtained for the NLRP3 PYD-NBD K23E/K24E variant, which was incapable of inducing ASC-nucleation (Lu *et al.*, 2014). In contrast, further mutants involved in Interface Ia, D50K and D53K, showed regular polymerization. The diameter determined for these filaments was about 10 nm for the mutant D53K and in a range of 9 nm to 13 nm for the mutant D50K, thus again resembling the size-requirements definded by the ASC-PYD filament. It can be concluded that the formation of a well-ordered NLRP3-PYD scaffold with an approximate diameter of 12 nm is a requirement for the association of the adaptor protein ASC. Phosphorylation at position Ser5 disrupts the Interface Ia, abrogating proper scaffold formation.

Until now, the filament structure of the ASC-PYD domain (PDB: 3J63) as well as of the ASC-CARD filament (6NIH) have been determined by electron microscopy, whereas no complex structure of the ASC full-length protein is available (Lu *et al.*, 2014; Li *et al.*, 2018). In order to elucidate the event of ASC-speck formation, the analysis of PYD-PYD interactions and CARD-domain initiated branching of full-length ASC protein filaments is required. Therefore, ASC-mCherry$_{\text{His}}$ was recombinantly expressed and purified from *E.coli* cells and subsequently analysed by transmission electron microscopy. Full-length ASC-mCherry$_{\text{His}}$ formed long and branched filaments, which arrange into bundles. *In vitro*, the filaments showed a length of up to 5 µm. Mutations in the Interface I forming residues of ASC have been found to abbrogate ASC-speck and filament formation (Lu *et al.*, 2014; Dick *et al.*, 2016). Moreover, it is assumed that the ASC CARD-domain condenses PYD-domain initiated filaments into an ASC-speck by bridging individual filaments (Dick *et al.*, 2016). In accordance with the previous finding, Interface I disrupting mutations (K21E/K22E/K26E) induced a complete loss in filament formation, irrespective of the CARD-domain. Alanine insertions at the respective positions (K21A, K22A, K26A) led to a decrease in filament formation. These results match the results obtained for the PYD-filament of NLRP3, confirming Interface I to be indespensable for intact filament formation in both proteins. In order to analyse the role of the ASC CARD-domain in filament formation, two residues were mutated (D134, Y187), recently confirmed to be crucial for both intact ASC-speck and ASC-CARD filament formation (Dick *et al.*, 2016; Li *et al.*, 2018). As expected, mutations in the ASC-CARD domain did not affect its ability to polymerize, whereas these mutations changed the morphology of the ASC-filament.

Strikingly, when mutated in the CARD-domain only, the ASC protein showed two different filament species: (i) regular filaments resembling the wild-type protein and (ii) filaments showing a much smaller diameter, but similar length. Moreover, not a single branching event was detected in the filaments resulting from CARD-mutated ASC.

In accordance with the literature, it can be assumed that the CARD-domain of ASC bridges the individual filaments, but also assists in the formation of properly assembled filaments (Dick *et al.*, 2016). Potentially, the CARD-domain is also involved in intra-molecular bridging in a single filament. Thus filaments showing a smaller diameter are generated in case of a disrupted CARD-CARD interaction. In order to adress this question, the structure of the ASC-filament of either wild-type or CARD-mutated protein should be determined by cryo-electron microscopy.

9.2.1 Alzheimer's pathology: ASC seeds pathogenic Aβ *in vitro*

NLRP3 has been identified as a sensor for the fibrillar peptide amyloid-β (Aβ) in the pathogenesis of Alzheimer's disease (Halle *et al.*, 2008; Heneka *et al.*, 2013). Also, a dependence of Alzheimer's disease on NLRP3 and Caspase-1 has been observed, thus suggesting a role for the adaptor protein ASC (Heneka *et al.*, 2013). Recently, it has been shown that homogenates from brains of Alzheimer's disease mouse models ($APP_{Swe}PSEN1_{dE9}$) failed to induce seeding and spreading of Aβ pathology in equivalent ASC-deficient mice (Venegas *et al.*, 2017). We contributed to this study by directly visualizing pathogenic Aβ-peptide (1-42) and ASC via transmission electron microscopy. In accordance with the data obtained *in vivo* and *in vitro*, transmission electron microscopy revealed filamentous ASC, forming a seed for the assembly of pathogenic Aβ (1-42). Moreover, the seeding of ASC is clearly dependent on its ability to form filaments, as Aβ (1-42) was not found to assemble on the ASC PYD mutants difficient in filament formation. Hence, the activation of an ASC-dependent inflammasome facilitates Alzheimer's pathology by seeding Aβ-aggregation. In order to elucidate the binding interface of ASC and Aβ, a mutational approached could follow on the present study. Moreover, small molecule inhibitors targeting the interaction site of Aβ and ASC would present a forward-looking goal to treat Alzheimer's disease and disease progression.

Besides Alzheimer's disease and the involved proteins Aβ and tau, known to form aggregates, the prion-like phenomenon is recognized in further neurodegenerative diseases (Hock & Polymenidou, 2016). The protein superoxide dismutase 1 (SOD-1), involved in amyotrophic lateral sclerosis (ALS), α-synuclein, involved in parkinson's disease (PD), as well as TARDBP-binding protein 43 (TDP-43), involved in both diseases, are known to cause disease progression by cell to cell spreading of aggregated protein. Hence, analysis of the regulation of these protein aggregates and a potential involvement of the innate immune system going along with ASC seeding could be of interest to unravel disease manifestation.

9.3 ATP hydrolysis activity of NLRP3

The NLRP3 inflammasome is the most studied and most challenging inflammasome as it is activated by a multitude of diverse stimuli, converging in the common mechanism of ASC-speck formation and subsequent activation of Caspase-1. The present study aimed to elucidate the biochemical characteristics of the NLRP3 sensor protein and to unravel the underlying activation mechanism.

Recombinant MBP-NLRP3 was shown to elute in two distinct peaks (Peak 1 and Peak 2), when subjected to gel filtration analysis. Both samples were analysed by MALS and DLS in order to determine the molar mass and the hydrodynamic radius of the individual protein complexes. Peak 1 was shown to elute as aggregated protein with a hydrodynamic radius of 30.7 nm. In contrast, MBP-NLRP3 Peak 2 showed a low degree of aggregation and a hydrodynamic radius of about 11.1 nm. This corresponds to a MW of about 1.62 MDa, possibly resembling a decamer of NLRP3. Also, transmission electron microscopic analysis revealed a higher level of aggregation of MBP-NLRP3 Peak 1 compared to Peak 2. It is concluded, that recombinant MBP-NLRP3 Peak 1 shows a conformation, which potentially reveals hydrophobic interaction sites, leading to a higher degree of protein aggregation in gel filtration analysis. In contrast, MBP-NLRP3 Peak 2 is concluded to consist of ordered oligomers, ranging from 8- to 10-mers. Transmission electron microscopic analysis revealed ordered structures for MBP-NLRP3 Peak 2, which did not ressemble the star-shaped conformation of active NLRC4 oligomers (PDB: 3JBL), but show a more compact organization. Still, the structure of mMBP-NLRP3 Peak 2 could not be solved in crystallographic approaches, assuming a heterogeneous oligomer assembly.
According to the results obtained from mass spectrometric analysis, MBP-NLRP3 Peak 1 is phosphorylated at residue S198, whereas Peak 2 lacks a phosphorylation at this position. The equivalent phosphorylation of S194 in murine NLRP3 has been shown to be mediated by the kinase JNK-1 and has been suggested as a precondition for NLRP3 inflammasome formation (Song *et al.*, 2017). Hence, MBP-NLRP3 Peak 1 is considered as the active protein complex, whereas MBP-NLRP3 Peak 2 is considered to be inactive, going along with the observed lack of ATP-hydrolysis activity. Therefore, a conformational change and a deviating assembly of the active NLRP3 oligomer is thought to go along with the phosphorylation of Ser198 of NLRP3.

The ability of recombinant NLRP3 to bind ATP has been shown to be indispensable for the ability to form an active inflammasome complex (Duncan *et al.*, 2007).

Moreover, recombinant NLRP showed the highest nucleotide binding specificity for ATP and dATP (IC_{50}=100 nM), whereas ADP resulted in an IC_{50} of about 5 µM, in an ATPγS competion assay (Duncan *et al.*, 2007). In comparison, the intracellular levels of peripheral blood lymphocytes have been determined as follows: ATP: 219 nM, ADP: 72 nM and AMP: 20 nM, resulting in a ratio of about 30:10:3 for ATP:ADP:AMP (Ng *et al.*, 1992).

In order to determine the effect of ATP and ADP binding on the conformation of NLRP3 Peak 1 and Peak 2, thermal denaturation experiments were performed. MBP-NLRP3 Peak 1 and Peak 2 were shown to possess an identical melting temperature of 48.7°C. In the presence of ADP and Mg^{2+} the melting temperature of both protein samples shifted to 48.3°C. In contrast, in the presence of ATP and Mg^{2+} both samples showed a similar melting temperature of 48.4°C. For MBP-NLRP3 Peak 1, a second melting temperature was determined at 83.7°C, which ressembled the melting temperature of MBP. Therefore, it is concluded, that the binding of ADP and ATP in combination with Mg^{2+} slightly destabilized the NLRP3 oligomer. Moreover, binding of ATP and Mg^{2+} caused a second melting event measured for MBP-NLRP3 Peak 1, which resembled the melting temperature of the MBP-tag. Hence, it is concluded, that MBP-NLRP3 Peak 1 undergoes a conformational change upon binding and potentially upon ATP hydrolysis, causing a liberation of the MBP-tag. Therefore, the difference in ATP hydrolysis activity of the individual peak species was of interest, in order to evaluate the differences determined in the denaturation behaviour.

9.3.1 Hydrolysis activity of MBP-NLRP3

NLRP3 is grouped into the family of AAA+ ATPases due to a high sequence conservation between known AAA+ ATPases and the NBD-domain of NLRP3. Until now, among the NLRP family members, interaction with ATP and ADP respectively, going along with an involvement in the activation, has been experimentally determined for NLRP1 (Faustin *et al.*, 2007; Harris *et al.*, 2015), NLRP3 (Duncan *et al.*, 2007), NLRP7 (Radian *et al.*, 2015), NLRP10 (Su *et al.*, 2013) and NLRP12 (Ye *et al.*, 2008). Most recently, an extensive *in silico* analysis of NLRP1 to NLRP14 was published, indicating amino acid residues which might participate in the binding of either ATP and ADP, respectively (Maharana *et al.*, 2018). Nonetheless, experimental evidence identifying the residues involved in the ATP hydrolysis of NLRP3 is still pending. Hence, the main task of the present study was to biochemically analyse the ATP binding site of NLRP3 in a mutational approach. Recombinant human MBP-NLRP3 was mutated in the Walker A, Walker B and sensor 1 motif as well as at the highly conserved position H522.

The effect of these mutations on the ability of NLRP3 to hydrolyse ATP was studied in RP-HPLC measurements and Malachite Green phosphate assays.
As shown before, gel filtration analysis of recombinant human MBP-NLRP3 revealed two distinct peak species: Peak 1 and Peak 2. Initial determination of the amount of free phosphate (P_i), resulting from the ATP-hydrolysis reaction, revealed that MBP-NLRP3 Peak 1 harbours ATPase activity, compared to Peak 2, which did not show any hydrolysis activity. In accordance with published data, MBP-NLRP3 showed negligible hydrolysis activity of GTP, whereas no hydrolysis activity was determined for CTP or UTP (Duncan *et al.*, 2007) and was further shown to be completely dependent on $MgCl_2$.

Also the influence of two small molecule inhibitors, CRID3 (MCC950) and CY-09, on the ATP hydrolysis activity of MBP-NLRP3 Peak 1, was tested. The small molecule inhibitor CRID3 (MCC950) was found to inhibit the formation of the NLRP3 inflammasome activiation in a crystal-induced kidney fibrosis mouse model (Ludwig-Portugall *et al.*, 2016). Furthermore, the inhibition of NLRP3 by CRID3 reduced hypertension in a renal inflammation and fibrosis associated mouse model (Krishnan *et al.*, 2016) and also led to reduced IL-1β secretion in a dermal and pulmonary inflammation mouse model (Primiano *et al.*, 2016). Intracellularly, CRID3 did neither inhibit K^+ efflux nor Ca^{2+} flux, but has been shown to circumvent Nigericin induced Cl^- efflux, thus an upstream target of NLRP3 activation is suggested (Coll *et al.*, 2015; Jiang *et al.*, 2017). The interaction of NLRP3 and the adaptor protein ASC has been shown to be unaffected by CRID3 (Coll *et al.*, 2015). Whether CRID3 does also influence the post-translational processing of IL-1β, similarly to CRID1 and CRID2, has not been investigated to date (Laliberte *et al.*, 2003). Recently, the serine-threonine kinase Nek7 has been identified as an upstream regulator of NLRP3 inflammasome activation (He *et al.*, 2016b; Schmid-Burgk *et al.*, 2016; Shi *et al.*, 2016). The interaction of NLRP3 and Nek7 has been shown to be dependent on the ROS-induced phosphorylation of Nek7 (Shi *et al.*, 2016). In the presence of CRID3, the phosphorylation of Nek7 has been consistent and thus the interaction of Nek7 and NLRP3 was unaffected by the small molecule inhibitor (Perera *et al.*, 2018).

In the present study, the effect of Nek7 as well as CRID3 on the ATP-hydrolysis of MBP-NLRP3 Peak 1 was analysed in RP-HPLC measurements. Neither the incubation in the presence of equimolar concentrations of Nek7, nor the incubation in presence of a 10-fold excess of CRID3 did affect the ATP-hydrolysis activity of recombinant MBP-NLRP3 Peak 1. Hence, both, the activating effect of Nek7 as well as the effect of the inhibitor CRID3 are concluded to be independent of the NLRP3 protein function.

Recently, the small molecule inhibitor CY-09 has successfully been used to treat mice suffering from the NLRP3-associated disease cryopyrin-associated autoinflammatory syndrome (CAPS) as well as type 2 diabetes (Jiang *et al.*, 2017). Moreover, CY-09 has been leading to significantly reduced human platelet aggregation, exhibiting therapeutic potential in the treatment of NLRP3 associated thrombosis (Qiao *et al.*, 2018). CY-09 has been shown to specifically target the NACHT-domain of NLRP3 and has been assumed to bind into the ATP-binding site of NLRP3 (Jiang *et al.*, 2017). ATP-hydrolysis of NLRP3, determined by measuring the amount of generated ADP, has been significantly inhibited by CY-09 in a dose-dependent manner and a reduction in ATP-binding affinity of NLRP3 has been observed (Jiang *et al.*, 2017).

In the present study, the effect of CY-09 on the ATP-hydrolysis activity of recombinant MBP-NLRP3 was tested by RP-HPLC. Here, CY-09 was shown to increase the ATP-hydrolysis in a concentration dependent manner: In the presence of 100 μM CY-09 the amount of consumed ATP was increased by more than 20% for MBP-NLRP3 Peak 1. In contrast, the identical amount of inhibitor did not affect ATP consumption by MBP-NLRP3 Peak 2. These results contradict the data published for NLRP3 in THP-1 cells by Jiang *et al.*, 2017. The recombinant proteins MBP-NLRP3 Peak 1 and Peak 2 are assumed to represent two individual states of NLRP3, differing at least in the phosphorylation status. The phosphorylation state of NLRP3 was shown to go along with its activation, thus MBP-NLRP3 Peak 1 resembles the active state, whereas MBP-NLRP3 Peak 2 is supposed to be inactive. In the analysis by Jiang *et al.*, 2017, the inhibitory effect of CY-09 has been determined from recombinantly purified protein in the presence of ATP. Thus potentially either a further activation state of NLRP3 is investigated or a combination of different states. The pre-incubation, of the recombinant Flag-tagged NLRP3 protein, with ATP during the purification procedure might have already caused a conformational change, resulting in a further state of NLRP3 activation. Moreover, the protein used in the study by Jiang *et al.*, has not been subjected to gel filtration chromatography, hence a mixture of the potentially generated Peak 1 and Peak 2 protein and further potential activation-state species was analysed. In consequence, the determination of binding affinities of either ATP, ADP and AMP in the presence and absence of CY-09, is utterly needed to rule out whether the observed effects are concentration dependent, or dependent on the different species and phosphorylation states of NLRP3.

9.3.2 Investigation of the ATP-binding site by a mutational approach

In the present study, point-mutants were generated, including mutations in the ATP binding cassette of NLRP3. When analysed at 4°C, two of these mutants, besides the wild-type protein, eluted in two distinct peaks when subjected to gel filtration: MBP-NLRP3 C838S and T233S. Again, as expected for both mutants, Peak 2 did not show any hydrolysis activity, thus supporting the model of an inactive protein complex. Peak 1 showed hyrolysis activity similar, to the wild-type protein. *In silico* analysis led to a refined demarcation of the Walker A motif of NLRP proteins: GxxGxGKT. The lysine residue located in the Walker A motif is typically forming a salt-bridge to the terminal phosphate of the bound nucleotide by interacting directly with the β- and γ- phosphate (Saraste *et al.*, 1990) and is thus essential to nucleotide binding (Traut, 1994). Hence, point-mutating K232 in human NLRP3 was expected to yield protein incapable of binding to ATP. The ATPase activity was drastically reduced (rate: 0.132 min^{-1}), but strikingly not completely abrogated, compared to the wild-type protein (rate: 0.385 min^{-1}). Surprisingly, the most recent *in silico* study has clearly identified differences between all 14 NLRP proteins, regarding the mode of nucleotide binding (Maharana *et al.*, 2018): In case of NLRP3, ATP is predicted to contact K232 via the α-, β-, and the γ-phosphate respectively. Moreover, the neighbouring residues, among others T233 (Walker A), R351 (sensor 1) and H522 are predicted to take part in the binding of the ATP nucleotide (Maharana *et al.*, 2018). Consequently, point-mutating K232A does not necessarily need to cause an abbrogation of neither ATP-hydrolysis nor ATP binding, though destabilizing the interaction. A further residue participating in the Walker A motif is the neighbouring residue T233. This residue was mutated to serine, as the consensus Walker A motif interchangeably includes the residues serine and threonine at that very position. Accordingly, MBP-NLRP3 T233S exhibited ATPase activity. In comparison to the wild-type protein, the activity was found to be slightly increased (rate: 0.464 min^{-1}). Nonetheless, these data underline the presumed exchangeability of serine and threonine at position 233.

In comparison, the less conserved Walker B motif formed by the consensus sequence (R/K)$x_{1\text{-}4}$G$x_{2\text{-}4}$hxh(D/E) in nucleotide binding proteins, is restricted to hhhhDE in AAA+ ATPases (Traut, 1994; Wendler *et al.*, 2012). In the present study, the consensus sequence of the Walker B motif in NLRP proteins was defined as the following: LLFhhDGFDEL. Thus, the determined Walker B sequence in NLRP proteins is strongly deviating from the motif identified in nucleotide binding proteins and AAA+ ATPases. Typically, the Walker B residues paricipate in the coordination of the attacking water molecule (Wendler *et al.*, 2012) and anchoring of the Mg^{2+}-ion (Albrecht *et al.*, 2003).

In silico analysis of the ATP-binding pocket and especially the Walker B motif of NLRP3 did neither indicate a direct interaction with the predicted ATP nucleotide nor the magnesium-ion, but identified the respective residues in close proximaty of max. 5 Å (Maharana *et al.*, 2018).
In order to analyse the residues which take part in the Walker B motif and participate in the ATP hydrolysis reaction, point-mutants of recombinant MBP-NLRP3 were generated and analysed by RP-HPLC. At first, the mutation G303E was introduced to mimick the consensus Walker B sequence of AAA+ ATPases, resulting in the following sequence: hhDEFDEL. Malachite Green Phosphate analysis revealed similar levels of generated P_i, compared to the wild-type protein. In contrast, when analysed by RP-HPLC, the hydrolysis reaction was strongly reduced by about 10-fold. Thus, batch-to-batch variation is assumed for this mutant and improper protein folding or aggregation is assumed for the batch tested in RP-HPLC. Hence,

the mutation G303E is supposed to not affect ATP hydrolysis in NLRP3. In contrast, the double mutant D305A/E306A (hhDGFAAL) showed a strong reduction in ATP-hydrolysis activity determined by RP-HPLC and Malachite Green Phosphate assay, respectively. Therefore, both residues are assumed to take over a prominent role in ATP hydrolysis of NLRP3, while not beeing essential to maintain hydrolysis activity. A combination of the above mentioned point-mutations (G303E/D305A/E306A) aimed at restoring the consensus Walker B motif in AAA+ ATPases. Reduction in ATP-hydrolysis acticity was compensated to about one-third compared to the individual mutants. Hence an exchange of the residue cluster DE from position D305/E306 to position D302/G303 partly restored the ATPase activity of NLRP3. Consequently, the point-mutant D302A and the mutant D305A were tested, assuming also a reduction in ATP-hydrolysis activity. As expected, the ATP-hydrolysis activity of both mutants was drastically reduced, to about 20%, compared to the wild-type protein. Hence both residues are shown to be involved in ATP hydrolysis.

Next, the effect of residue E306 was analysed, to determine whether the charge or the size of the respective residue is important for the hydrolysis activity of NLRP3. In consequence, two double mutants were generated and the effect was compared by RP-HPLC measurements: D305A/E306A and D305A/E306Q. Both mutants resulted in a decrease in hydrolysis activity. The mutant D305A/E306A showed a remaining hydrolysis activity of about 20%, whereas the double mutant D305A/E306Q showed partly restored activity with a remaining ATP hydrolysis activity of 40%, compared to the wild-type protein. Consequently, the MBP-NLRP3 mutant E306Q was tested for its effect on the ATP hydrolysis activity. Interestingly, this mutant showed a reduced ATP hydrolysis activity with remaining 20% activity, similar to the double mutant D305A/E306A. Hence, besides the size of the residue at position aa 306, also the charge is of major importance for the ATP hydrolysis activity of NLRP3.

From this data it is concluded, that the residues D302, G303, D305 and E306 participate in the ATP hydrolysis activity of NLRP3. An exchange of the negatively-charged cluster DE to position 302/303, resembling the typical Walker B motif of AAA+ ATPases, partly restored the hydrolysis activity.

These results clearly indicate that the Walker B motif of NLRP3 is spanning at least the residues D303 to E306, instead of solely being shifted to residues D305/E306. Hence, the Walker B motif in NLRP3 is not just degenerated but extended, including three negatively charged residues (D303, D305, E306) involved in ATP hydrolysis, instead of only two residues being present in the consensus sequence of typical AAA+ ATPases (hhhhDE) (Wendler *et al.*, 2012).

In AAA+ ATPases, the sensor 1 motif fulfils a crucial role in ATP hydrolsis. This residue, typically a threonine residue, located at the tip of β-strand 4, is involved in the coordination of the attacking water molecule during ATP hydrolysis (Wendler *et al.*, 2012). Moreover, this residue is supposed to sense the γ-phosphate of ATP (Proell *et al.*, 2008). In NLRP3, the equivalent residue is R351, which has been proposed to form hydrogen bonds with the terminal phosphate of the bound ATP nucleotide and the associated magnesium ion (Maharana *et al.*, 2018). In order to determine the effect of R351 on the ATPase activity of NLRP3, two mutants (R351G and R351T) were tested in the present study. For the mutant R351T, the amount of P_i determined in the Malachite Green Phosphate assay was much lower (decrease 20%) compared to the wild-type, whereas the hydrolysis rate determined by RP-HPLC showed a decrease by 90%. Hence, again a batch-to-batch effect is assumed to underly the disparity of both experiments. The recombinant protein MBP-NLRP3 R351T was hardly expressed and difficult to handle, thus improperly folded protein might have influenced the results gained. As the R351T mutation mimicks the threonine residue typically found in AAA+ ATPases the result obtained by the Malachite Green Phosphate assay rather suits the expectation based on the literature knowledge (Wendler *et al.*, 2012). In contrast, the point-muntant R351G, showed only a reduction in the rate determined for the decrease in ATP to about 40%, thus underlining the involvement of this residue in the ATP hydrolysis of NLRP3.

The sensor 2 motif, typically formed by a lysine or arginine residue in AAA+ ATPases, is absent in proteins grouped in the family of STAND ATPases (Proell *et al.*, 2008). Instead, members of the STAND family share a conserved histidine residue, which has been shown to coordinate the phosphate groups of the bound ADP in the structure of APAF-1 (Proell *et al.*, 2008). In NLR-family members, the conserved patch FxHxxQEhxA has been identified, including the characterictic histidine residue, which has been proposed to take over the function of the sensor 2 residue (Proell *et al.*, 2008). Computational analysis of the ATP binding site of NLRP3, indicated the residue H522 as a critical residue mediating polar contacts with the α- and β-phosphate of the bound ATP (Maharana *et al.*, 2018). In order to unravel the role of residue H522 on the ATP hydrolysis of NLRP3, two point-mutations were tested (H522D and H522R).

Due to a destabilization of the phosphate groups in the ATP-binding pocket, we expected to observe a reduced ATP hydrolysis activity of NLRP3, when introducing the mutation H522D. In contrast, either no effect or a stabilizing effect for the bound nucleotide was assumed for the mutant H522R, as the arginine residue mimicks the typical sensor 2 motif of AAA+ ATPases. As expected, the hydrolysis activity of NLRP3 H522R was comparable to the wild-type protein, determined in a Malachite Green Phosphate assay and by RP-HPLC. In contrast the mutant H522D, showed a reduced amount of P_i generated from ATP (Malachite Green Phosphate Assay) and a decrease in the ATP consumption rate to less than 20% (RP-HPLC), compared to the wild-type protein. Thereby, it was shown, that H522 participates in the ATP hydrolysis of NLRP3. A replacement of the histidine residue by a positively charged arginine (R) did not increase the ATP hydrolysis activity of NLRP3, whereas the exchange to a negatively charged aspartic acid (D) drastically decreased the ATP hydrolysis activity.

In conclusion, for each of the residues tested, the mutational approach revealed an involvement in the ATP hydrolysis of NLRP3. Surprisingly, none of the introduced point-mutations caused a complete loss of ATP hydrolysis activity. Hence it is concluded, that the ATP binding site of NLRP3 can partly compensate for the loss of single amino acids involved in the coordination of the bound ADP and ATP. Accordingly, in order to completely abolish ATP hydrolysis activity, a combination of several amino acid substitutions will be necessary rather than the mutation of a single amino acid like the lysine residue (K232) in the Walker A motif.

Moreover, one has to emphasize that point mutations may affect both ATP binding and ATP hydrolysis, respectively: The exchange of an amino acid residue may either have a direct effect on ATP hydrolysis, or may cause sterical changes in the arrangement of the ATP-binding site. The hydrolysis mechanism relies on the exact positioning of attacking water molecules. Point mutations, besides generating mechanistic changes, may open up space for additional water molecules or prevent the coordination of the water molecule inside the binding pocket.

Besides the already described ATP hydrolysis mechanism, human NLRP3 was also tested for its ability to utilize further nucleotide substrates. Human guanylate-binding protein 1 (hGBP1) has been shown to hydrolyse GTP to GMP in two consecutive cleavage reactions (Schwemmle & Staeheli, 1994; Praefcke *et al.*, 1999), thus in a control experiment, the ADP hydrolysis activity of NLRP3 was tested. Intriguingly, the incubation of NLRP3 in the presence of ADP and $MgCl_2$ led to the generation of ATP and AMP. Therefore, MBP-NLRP3 is assumed to possess adenylate kinase activity rather than ADP hydrolysis activity.

9.4 NLRP3 exhibits adenylate kinase activity

The previously described analysis of the ATP-hydrolysis activity of NLRP3 unravelled a secondary nucleotide-dependent hydrolysis mechanism. In the presence of ATP and $MgCl_2$, MBP-NLRP3 Peak 1 showed a reduction in ATP levels, going along with an increase in ADP levels. At a starting nucleotide level of about 60% ATP and 40% ADP, AMP was produced in a constant manner. In order to determine whether NLRP3 possesses ADP hydrolysis activity, resulting in the generation of AMP and P_i, a control experiment was performed. The incubation of NLRP3 in the presence of ADP and $MgCl_2$, led to the generation of ATP and AMP. Also, incubation in the presence of AMP and ATP, yielded the doubled amount of ADP, compared to the measurement upon incubation in ATP only. Therefore it is concluded, that NLRP3 harbours adenylate kinase activity rather than ADP-hydrolysis activity.

As shown before, NLRP3 exhibits ATPase activity. Hence, when ATP is produced by the protein, the generated ATP is supposed to be directly consumed, due to a favoured affinity towards ATP. Ideally, equal amounts of AMP and ATP are expected to be generated from ADP in the adenylate kinase reaction. Indeed, unequal levels of AMP and ATP are generated, probably due to the ATPase activity.
An equivalent phenomenon has been determined for several members of the ABC transporter family, which have been shown to possess a coupled AK-ATPase activity (Kaur et al., 2016). Herein, a coupled ATPase-AK cycle is proposed, which finally leads to the release of AMP, generated from ADP, in an active dimeric complex (Kaur et al., 2016). ABC transporters, like NLRP proteins are grouped into the family of AAA+ ATPases, suggesting an evolutionarily conserved mechanism of coupled ATPase-AK activity (Wendler et al., 2012).

In the present study, the specific adenylate kinase inhibitor Ap5A was shown to effectively inhibit the AK activity (IC_{50}=0.428 μM), but not the ATPase activity of NLRP3. The inhibitor Ap5A has been developed to specifically target adenylate kinases only, without interferring with ATPases (Feldhau *et al.*, 1975; Yegutkin & Burnstock, 2000). In contrast, Ap5A has been shown to inhibit both, the ATPase activity and the AK activity of the ABC transporter CFTR (Randak & Welsh, 2003). Hence, it is proposed that the binding affinity for Ap5A compared to ATP is lower in enzymes that possess ATPase activity only, whereas both ATPase and AK activity are blocked in enzymes that catalyze both reactions.
Ap5A was shown to induce a slightly stabilizing effect on MBP-NLRP3 Peak 2 (+0.3°C). A second melting temperature, resembling the one of the MBP tag, was determined for Peak 1

and Peak 2, respectively. This points towards an underlying conformational change induced by Ap5A, thus liberating the MBP-tag.

In the present study, recombinant MBP-NLRP3 Peak 1 showed higher slopes for the consumption of ADP, compared to the slopes determined in the measurement including AMP and ATP. Therefore, a preference for the substrate ADP over AMP and ATP is assumed, leading to the following preferred adenylate kinase reaction equation:
2 ADP → 1 AMP + 1 ATP.
To further characterize the mechanism of AK activity in NLRP3, point-mutations were introduced and their effect on AK activity was analysed. Each of the above mentioned mutations, located in the Walker A-, Walker B-, sensor 1- and His-motif respectively, impaired the adenylate kinase activity of NLRP3.

The wild-type protein showed an ATPase-dependent inhibitory effect of AMP: Only for mutants exhibiting low ATPase activity, the conversion of 1 AMP + 1 ATP to 2 ADP was detectable. Otherwise, AMP was shown to inhibit the ATPase activity rather than causing an increase in the amount of generated ADP from AMP and ATP.

Therefore, a batch-to-batch effect, potentially caused by a deviating phosphorylation status is assumed to underly the measured discrepancy. Moreover, an effect of AMP was measured in each of the performed experiments, thus clearly indicating a secondary role of AMP in the activity of NLRP3.
Two mutations in the Walker A site of NLRP3 were tested for its effect on the adenylate kinase activity: K232A and T233S. In order to determine the role of AMP, the reaction kinetics of the measurement including ATP was compared to the measurement including AMP and ATP. As discussed above, the mutant K232A showed a reduced ATP hydrolysis activity, which was nearly unaffected by the addition of the substrate AMP. In contrast, the mutant T233S showed half the activity for the generation of ADP from AMP+ATP, compared to the measurement including ATP only. Hence, similar to the wild-type protein, AMP strongly inhibited the ATPase activity of NLRP3 T233S. Moreover also the reverse adenylate kinase reaction (2 ADP→1 AMP+1 ATP) was measureable for both mutants, though markedly reduced compared to the wild-type protein. In AAA+ ATPases the consensus Walker A motif (GxxGxGK[T/S]) includes either a serine and threonine residue at the position upstream of the sensing lysine residue (Wendler *et al.*, 2012). The mutant NLRP3 T233S showed regular ATPase activity, but still an inhibitory effect in the presence of AMP. Therefore, the second nucleotide binding site seems accessible in this mutant, but still the adenylate kinase activity of NLRP3 was diminished. In order to elucidate the role of this respective residue on the adenylate kinase activity, a sequence alignment comparing the Walker A motif of human adenylate kinases, the human ABC transporter CFTR and human NLRP 1 to 14 proteins was performed (Figure 62).

As shown by the alignment of the Walker A motif in Figure 62, the adenylate kinases AK 1-5 have a deviating Walker A motif compared to the other proteins analysed, resulting in the following consensus sequence: GxxGSGKGT. Hence, the threonine residue, typically located adjacent to the lysine residue is shifted one position upstream. In contrast, the adenylate kinases AK 6-9, as well as the ABC transporter CFTR, show the consensus Walker A sequence. Interestingly, the Walker A motif of AK 6, which harbours adenylate kinase activity as well as intrinsic ATPase activity, resembles the consensus sequence determined for NLRP proteins (Drakou *et al.*, 2012). Here, a hydrophobic residue is incorporated in the Gx motif (GxxGhG) and further an additional serine or threonine residue is shown to follow the Walker A motif. Therefore it is concluded that the threonine residue in the Walker A motif of NLRP3 (T233) probably fulfils a crucial role for the adenylate kinase activity by assisting the sensing mechanism.

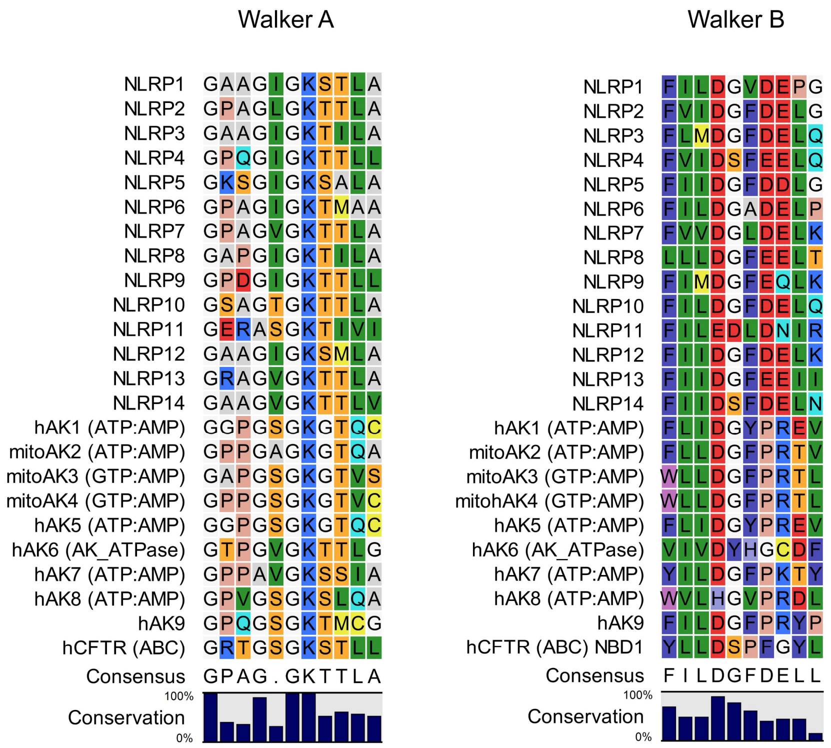
Walker A

NLRP1	GAAGIGKSTLA
NLRP2	GPAGLGKTTLA
NLRP3	GAAGIGKTILA
NLRP4	GPQGIGKTTLL
NLRP5	GKSGIGKSALA
NLRP6	GPAGIGKTMAA
NLRP7	GPAGVGKTTLA
NLRP8	GAPGIGKTILA
NLRP9	GPDGIGKTTLL
NLRP10	GSAGTGKTTLA
NLRP11	GERASGKTIVI
NLRP12	GAAGIGKSMLA
NLRP13	GRAGVGKTTLA
NLRP14	GAAGVGKTTLV
hAK1 (ATP:AMP)	GGPGSGKGTQC
mitoAK2 (ATP:AMP)	GPPGAGKGTQA
mitoAK3 (GTP:AMP)	GAPGSGKGTVS
mitoAK4 (GTP:AMP)	GPPGSGKGTVC
hAK5 (ATP:AMP)	GGPGSGKGTQC
hAK6 (AK_ATPase)	GTPGVGKTTLG
hAK7 (ATP:AMP)	GPPAVGKSSIA
hAK8 (ATP:AMP)	GPVGSGKSLQA
hAK9	GPQGSGKTMCG
hCFTR (ABC)	GRTGSGKSTLL
Consensus	GPAG.GKTTLA

Walker B

NLRP1	FILDGVDEPG
NLRP2	FVIDGFDELG
NLRP3	FLMDGFDELQ
NLRP4	FVIDSFEELQ
NLRP5	FIIDGFDDLG
NLRP6	FILDGADELP
NLRP7	FVVDGLDELK
NLRP8	LLLDGFEELT
NLRP9	FIMDGFEQLK
NLRP10	FILDGFDELQ
NLRP11	FILEDLDNIR
NLRP12	FIIDGFDELK
NLRP13	FIIDGFEEII
NLRP14	FIIDSFDELN
hAK1 (ATP:AMP)	FLIDGYPREV
mitoAK2 (ATP:AMP)	FLLDGFPRTV
mitoAK3 (GTP:AMP)	WLLDGFPRTL
mitohAK4 (GTP:AMP)	WLLDGFPRTL
hAK5 (ATP:AMP)	FLIDGYPREV
hAK6 (AK_ATPase)	VIVDYHGCDF
hAK7 (ATP:AMP)	YILDGFPKTY
hAK8 (ATP:AMP)	WVLHGVPRDL
hAK9	FILDGFPRYP
hCFTR (ABC) NBD1	YLLDSPFGYL
Consensus	FILDGFDELL

Figure 62: Sequence alignment of human NLRP-family members, human AKs and hCFTR. The amino acid sequence alignment of the human NLRP 1 to 14, human and mitochondrial AKs and the ABC transporter CFTR show a conserved Walker A motif with the following consensus sequence: GxxGxGKTT. The respective Walker B alignment elucidates a consensus sequence of: hhDGx.

In AAA+ ATPases, the Walker B motif has the following consensus sequence: hhhhDE (Wendler *et al.*, 2012). In contrast, NLRP family members, adenylate kinases, as well as the ABC transporter CFTR, show the consensus sequence: hhDGFDE, pointing to a different function of the Walker B motif in these proteins (Figure 62). In order to determine the effect of these residues on the adenylate kinase activity of NLRP3, point-mutations were analysed by RP-HPLC. Each of the mutants tested showed adenylate kinase activity, though the activity was strongly reduced compared to the wild-type protein. Two mutants (E306Q and D305A/E306A) showed a preference for the forward adenylate kinase reaction (1 AMP+1 ATP→2 ADP). Morover, the mutants D305A/E306A and G303E/D305A/E306A showed a slightly increased consumption of AMP, compared to the wild-type protein. For each of the mutants tested, except for E306Q, the generation of ADP from ATP was decreased in the presence of AMP compared to the measurement without AMP, thus again indicating an inhibitory effect of AMP. Taking together these results as well as the phenomenon, that the mutant D305A/E306Q showed the lowest slope determined for the consumption of AMP in the adenylate kinase experiment, it is concluded, that the negatively charged residues D305 and E306 might participate in the binding of both substrates AMP and/or ADP.

As indicated by the alignment shown in Figure 62, the NLRP-family members share the unique sequence motif harbouring two negatively charged residues (hhDGx[E/**DE**/D]), with only two exceptions: NLRP9 and NLRP11, which harbour only a single negative charged residue at this position. In NLRP9, the second position is occupied by a glutamine residue, resembling the situation brought about by the NLRP3 mutant E306Q. Hence, very little or no adenylate kinase activity is expected for NLRP9.

The sensor 1 motif has been shown to sense the γ-phosphate of the bound ATP and further coordinates the attacking water molecule in the ATP hydrolysis reaction (Proell *et al.*, 2008; Wendler *et al.*, 2012). As expected, the NLRP3 point-mutant R351G did not impair the adenylate kinase activity. When incubated in the presence of AMP and ATP, the amount of AMP consumed was comparable to the wild-type protein, whereas the amount of generated ADP was decreased, as discussed above. Therefore, the residue R351, sensor 1, is ruled out to interfere with the binding of AMP or ADP in the second binding pocket.

Sequence analysis revealed a conserved histidine residue (H522) that was shown to impair with the ATP hydrolysis activity of NLRP3. Two mutations, H522D and H522R were tested for its effect on the adenylate kinase activity on NLRP3. Interestingly, both mutants showed a deviating preference for directionality of the adenylate kinase reaction. The NLRP3 mutant H522R showed a preference for the forward reaction, whereas for the mutant H522D, higher slopes were determined when providing ADP as the starting nucleotide source. The ATP hydrolysis rates determined for the mutant H522R were similar to the wild-type protein. In contrast, when incubated in the presence of AMP and ATP, the resulting slopes were 3-fold reduced compared to the ATP hydrolysis reaction. In comparison, the slopes determined for the decrease in the amount of ATP for the mutant H522D are similar between the experiments including AMP and ATP as well as the ATP hydrolysis measurement. Moreover, the slope determined for the decrease in ADP, when providing ADP as the only nucleotide source, are only halved, compared to the wild-type protein. Therefore, it is assumed that H522 is involved in the sensing process of the second nucleotide in the adenylate kinase reaction of NLRP3.

A similar phenomenon has been shown to underly the adenylate kinase activity of human CINAP (AK6), which also possesses intrinsic ATPase activity (Drakou *et al.*, 2012). AK6 has been found to harbour a histidine residue, located in the Walker B motif (Figure 62), which has been shown to affect both, adenylate kinase and ATPase activity of hCINAP (Drakou *et al.*, 2012). The histidine residue is assumed to function as a structural switch, selecting for the enzymatic activity of AK6 by flipping between two positions. Either it is binding to the α-phosphate of the AMP molecule (AK-mode) or it assists in the co-ordination of the water molecule needed for the nucleophillic attack on the γ-phosphate of the bound ATP in the catalytic center (ATPase-mode) (Drakou *et al.*, 2012).

The structural model of NLRP3 (Figure 63) suggests a histidine (H522), with potentially equivalent function to the histidine residue supposed to regulate the switching mechanism between the AK-mode and the ATPase-mode of hCINAP (AK6) (Drakou *et al.*, 2012). This hypothesis is supported by computational analysis of the ATP-binding site of NLRP3, suggesting a localization of H522 in opposition to the β-phosphate of the bound ATP (Maharana *et al.*, 2018).

Therefore, it is assumed that the histidine residue (H522), which is highly conserved among the members of the NLRP-family, might fulfill a role in deciding between the enzymatic reaction catalyzed by the enzyme, by initiating a switch between the AK-mode, and the ATPase-mode.

In the present study, solely the enzymatic effect of NLRP3 on the substrates ATP, ADP and AMP was analysed, whereas cAMP should also be considered as a potential substrate. NLRP3 has been shown to directly bind cAMP but not cGMP via the NACHT domain. Interestingly, ATP binding of the NACHT domain was not inhibited in the presence of cAMP (Lee *et al.*, 2012). Thus, cAMP should be considered as a substrate for the enzymatic activity of NLRP3.

In order to unravel the function of the dual ATPase/AK activity of NLRP3, its relevance in an *in vivo* context is of major interest. Point-mutations in the NLRP3 protein are associated with several auto-immune diseases, called CAPS (Sarrauste de Menthière *et al.*, 2003). Point-mutations of the NLRP3 residue R262 have been identified in patients, suffering from severe auto-immune symptoms (Sarrauste de Menthière *et al.*, 2003).

In the present study, the point-mutant R262W, resembling a CAPS mutation identified in patients, was incubated in the presence of $MgCl_2$ and 100 μM ADP. Here, a three-fold increased slope was determined for the reduction of ADP, compared to the wild-type protein. In contrast, the ATP hydrolysis was diminished, as discussed above. Therefore, an influence of the CAPS mutation R262W in the adenylate kinase activity of NLRP3 is clearly shown. *In silico* analysis of the ATP-binding site of NLRP3 has revealed, that this residue might be located within a distance of about 5 Å of the catalytic center, close to the Walker B motif, thus elucidating a role in the enzymatic mechanism (Maharana *et al.*, 2018). As this point-mutant showed a drastic increase in the adenylate kinase activity, going along with a slight decrease in ATPase activity, the involvement of the adenylate kinase activity is assumed to underly the increased NLRP3 inflammasome activation in CAPS patients.

Point-mutations of NLRP3, which have been identified to cause the CAPS disease, are partly located in the ATP-binding pocket of NLRP3 (Figure 63). Moreover, several mutations are found on the predicted surface of the NLRP3 protein, thus suggesting a dual function of the CAPS associated mutations. Mutations might interfere with the nucleotide binding and the adenylate kinase activity of NLRP3, whereas point-mutations on the surface of the protein might interfere with homo-typic interaction sites, thus potentially favouring the active conformation or inhibiting the auto-inhibited state of NLRP3.

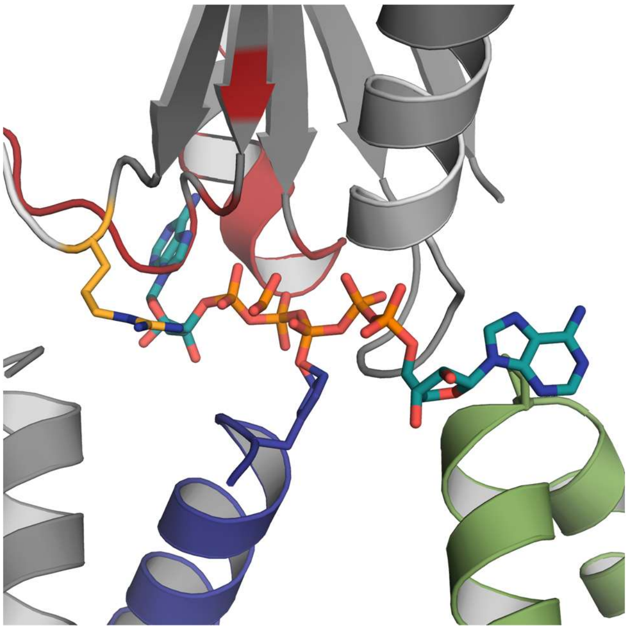

Figure 63: Model of the ATP-binding site of NLRP3 including adenylate-kinase inhibitor Ap5A. Structural model of the ATP-binding site of NLRP3 based on the structure of rabbit NOD2 bound to ADP (PDB: 3IRN). The structure of the adenylate kinases (PDB: 1ZIN) was aligned to the ATP-binding site to include the inhibitor Ap5A. The model of NLRP3 is shown in grey, Ap5A in cyan. CAPS disease associated mutations surrounding the ATP site are coloured in red, the R262W mutation is colored in yellow, whereas P412 and the according helix is coloured in green and H522 and the according helix in blue.

As shown in Figure 63, structural modelling of the ATP-binding site of NLRP3 including the adenylate kinase inhibitor Ap5A, suggests the seccond nucleotide binding site of NLRP3 to be located in close proximity of the Walker B motif and the R262 residue. Thus again a role of both motifs in the adenylate kinase activity of NLRP3 is assumed. Furthermore, CAPS associated point-mutations are preferentially located in close proximity of both motifs, shown in Figure 63 (red). Interestingly, not a single point-mutation in the Walker A motif, causing CAPS, is identified to date. Hence it is assumed that not the interference with the ATPase activity but with the adenylate kinase activity of NLRP3 causes the auto-immune reaction and an hyperactive NLRP3 inflammasome.

Without any structural information about NACHT domains of NLRP proteins, the prediction of the second nucleotide binding site is challenging. Nonethless, assumptions can be made, based on the information gained about NLRP3, AK6 and the ABC-transporter CFTR, which have been shown to possess both, ATPase and adenylate kinase activity.

Based on this knowledge, a conformational change of NLRP3 can be assumed in response to activities, thus suggesting a two-step mechanism underlying the activation of NLRP3, similar to what was determined for the ABC transporter (Randak & Welsh, 2003).

Similar to what is known for the adenylate kinase 6 (hCINAP), it can also be assumed, that based on a second stimulus, either the ATPase activity or the adenylate kinase activity of the protein is used (Drakou *et al.*, 2012).

In summary, NLRP3 was shown to exhibit adenylate kinase activity, that was drastically increased in a CAPS disease-associated mutant (R262W). Moreover, the involvement of a conserved histidine residue (H522) in the adenylate kinase activity of NLRP3 is suggested.

10 Conclusion

10.1 Model of NLRP3 inflammasome activation

The activation mechanism of the NLRP3 inflammasome is widely belived to resemble the activation mechanism determined for the NLRC4 inflammasome. Upon ligand binding and the interaction with an associated NAIP-adaptor, NLRC4 assembles into a star-shaped oligomer, forming a scaffold for the binding of either the adaptor ASC or Caspase-1. A similar mechanism is assumed for the assembly of the NLRP3 inflammasome, but until now neither a direct activator or a binding partner similar to NAIP nor a star-shaped disc formation was identified for NLRP3.

Based on the biochemical characterization of NLRP3 and the novel function identified in the present study (adenylate kinase activity), a model for the activation mechanism of the NLRP3 inflammasome was developed.

As discussed previously, the phosphorylation of Ser198 is a prerequisite for the activation of NLRP3 (Song *et al.*, 2017). Here we show that the phosphorylation event is coupled to the ability to perform ATP hydrolysis and adenylate kinase activity (Peak 1). A second species of NLRP3 was identified, which showed drastically reduced adenylate kinase activity and ATP hydrolysis and did not show phosphorylation at Ser198 (Peak 2). Furthermore, the phospho-mimicking mutation of Ser5 showed an inhibition of the fibrillation potential of the NLRP3-PYD domain. Hence it is concluded, that the phosphorylation in the PYD domain abolishes the oligomer assembly.

Besides the molecular modification by e.g. phosphorylation, changes in the intracellular nucleotide concentration have been found to correlate with the activation of the NLRP3 inflammasome. Nigericin and crystal stimulation have been shown to cause a decrease in the intracellular ATP concentration, going along with the activation of the NLRP3 inflammasome (Nomura *et al.*, 2015). Thus a role for mitochondria is suggested, as the maintenance of intracellular ATP pools might be a strategy for counteracting the activation of the NLRP3 inflammasome (Nomura *et al.*, 2015).

In order to start unravelling the activation mechanism of the NLRP3 inflammasome, a model was developed which includes the mentioned modifications and nucleotide conditions influencing the activation mechanism (Figure 64).

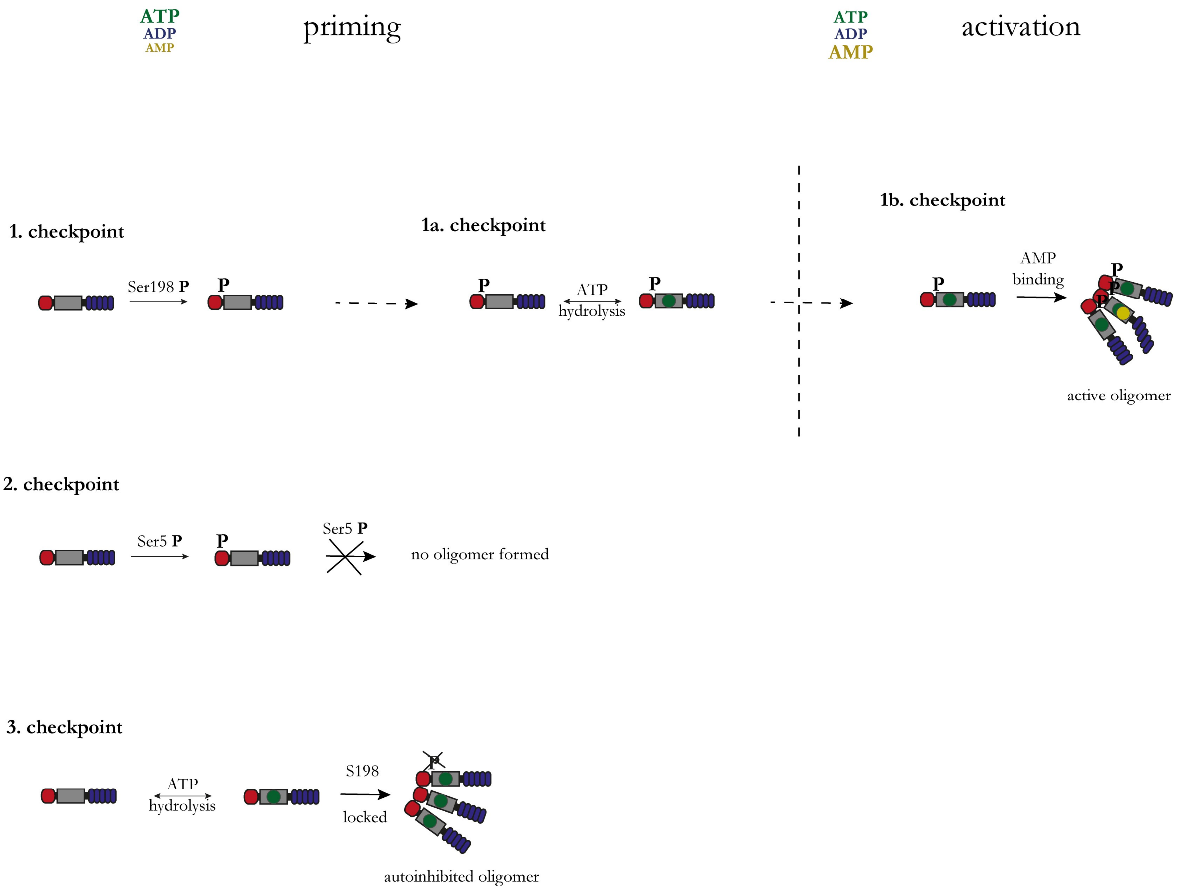

Figure 64: NLRP3 activation model. This model shows the reactivity of NLRP3 as a sensor for the nucleotide composition in the cytosol. In the priming step, the intracellular concentration of NLRP3 increases, while the ATP concentration remains at basal level. As a priming step, NLRP3 is phosphorylated at Ser198, which enables the protein to perform ATP hydrolysis. Due to the high intracellular ATP concentration, NLRP3 contineously hydrolyses ATP. The phosphorylation of Ser5 inhibits the formation of an oligomeric state (checkpoint 2). In contrast, oligomer formation without the phosphorylation of Ser198 (dephosphorylation mechanism), might lead to an autoinhibited oligomer (checkpoint 3). The NLRP3 inflammasome activation by potassium efflux or Nigericin etc. shifts the intracellular nucleotide ratios, towards higher AMP levels. In case, responsive NLRP3 recognized AMP, the protein undergoes a conformational change, initiated by its adenylate kinase activity, thus allowing for the formation of an active oligomer and further the NLRP3 inflammasome.

The developed model suggests five checkpoints, which determine the fate of the NLRP3 protein during priming and activation. The initial step of NLRP3 inflammasome activation is called priming: The transcriptional up-regulation of NLRP3, initiated by LPS stimulation (He *et al.*, 2016a). Along with priming, the kinase JNK-1 has been shown to phosphorylate NLRP3 at S198, a prerequisite for NLRP3 inflammasome assembly (1. checkpoint) (Song *et al.*, 2017). In the present study, we show that the phosphorylation event at Ser198 goes along with the proteins ability to hydrolyse ATP (NLRP3 Peak 1).

Based on the data obtained here, it is suggested, that NLRP3 continously hydrolyses ATP, rather than hydrolysing ATP in a single-event only (1a. checkpoint). The phosphorylation of Ser5 was indicated to prevent the NLRP3 oligomer formation by interferring with Interface I of the PYD-domain. Moreover, the phosphorylation of Ser5 has been shown to prevent NLRP3 inflammasome formation and has not been found simultaneously with a phosphorylation at Ser198 (Stutz *et al.*, 2017). Therefore, it is assumed, that by phosphorylation of Ser5, the activation of NLRP3 is counteracted and/or balanced (2. checkpoint).

In the present study, it was shown that NLRP3 showed a second peak species (Peak 2), which showed drastically reduced ATP hydrolysis activity. Moreover, besides the wild-type protein, also the mutant T233S showed the second peak species, when purified at 4°C. Since both proteins exhibit regular hydrolysis activity, it is assumed, that the "autoinhibited oligomer" is formed upon ATP hydrolysis in the absence of phosphorylation of Ser198 (3. checkpoint). Whether Ser198 is dephosphorylated or the protein oligomer is formed although it was not primerily phosphorylated at Ser198 remains to be elucidated. It has been pubished, that the activation of NLRP3 is accompanied by a change in the intracellular ATP concentration (Nomura *et al.*, 2015). While the priming-step is assumed to happen during regular intracellular ATP concentrations, the activation of NLRP3 by either nigericin or crystals has been shown to cause a decrease in intracellular ATP levels (Nomura *et al.*, 2015). In the present study, we have shown that in the presence of high levels of ATP, NLRP3 hydrolyses the ATP to ADP and P_i. In contrast, while AMP was present or the amount of ADP exceeded ATP, NLRP3 made use of its adenylate kinase activity. Therefore, it is proposed that NLRP3 senses an imbalance of the ATP concentration in the cell, by sensing for the nucleotides AMP, ADP and ATP, respectively. The adenylate kinase activity of NLRP3 is therefore thought to underly the activation mechanism of NLRP3 inflammasome formation by potentially inducing a conformational change. In consequence, an oligomer is formed, which functions as a scaffold for the assembly of the adaptor ASC (1b. checkpoint).

This goes along with the finding that the CAPS-disease mutant R262W showed a drastically increased adenylate kinase activity, thus potentially explaining this hyperactive NLRP3 mutant. Here it was shown that, NLRP3 R262W utilized ADP already at lower concentrations, compared to the wild-type protein. Thus it is suggested, that the CAPS mutant has a stronger affinity towards ADP and is thus already activated at resting ADP and ATP levels.

Moreover, in the present study, a concentration dependent inhibitory effect of AMP on the ATP hydrolysis activity of NLRP3 was observed. Therefore, besides the adenylate kinase activity, a mechanism in which AMP locks the protein in an ATP bound state is assumed, which initiates the NLRP3 inflammasome formation. In a model, suggesting NLRP3 to continously hydrolyse ATP, two potential pathways are possible: (i) the first binding site is still occupied by the hydrolysis product ADP and the second binding site recognizes an additional ADP molecule, (ii) the first binding site is occupied by an ATP molecule and the second binding site recognized an AMP molecule.

Both possibilities allow for the adenylate kinase reaction and elucidate a mechanism to sense for an imbalaced nucleotide ratio of AMP, ADP and ATP underlying the activation of the NLRP3 inflammasome. The intracellularly favoured adenylate kinase reaction pathway is still to be elucidated. Moreover, the exact nucleotide levels, present in immune cells in response to each known activation factor have to be determined in order to either confirm or disprove the mechanism proposed here. Additionally, the role of interaction partners like chaperones or Nek7 by potentially stabilizing one of the mentioned states of NLRP3 or inhibition of others, remains to be elucidated.

11 Erklärung

An Eides statt versichere ich, dass
die vorgelegte Arbeit – abgesehen von den ausdrücklich bezeichneten Hilfsmitteln – persönlich, selbständig und ohne Benutzung anderer als der angegebenen Hilfsmittel angefertigt wurde,
die aus anderen Quellen direkt oder indirekt übernommenen Daten und Konzepte unter Angabe der Quelle kenntlich gemacht sind, die vorgelegte Arbeit oder ähnliche Arbeiten nicht bereits anderweitig als Dissertation eingereicht worden ist bzw. sind, kein früherer Promotionsversuch unternommen worden ist, für die inhaltlich-materielle Erstellung der vorgelegten Arbeit keine fremde Hilfe, insbesondere keine entgeltliche Hilfe von Vermittlungs- bzw. Beratungsdiensten (Promotionsberater oder andere Personen) in Anspruch genommen wurde sowie keinerlei Dritte vom Doktoranden unmittelbar oder mittelbar geldwerte Leistungen für Tätigkeiten erhalten haben, die im Zusammenhang mit dem Inhalt der vorgelegten Arbeit stehen, die vorgelegte Dissertation an der nachstehend aufgeführten Stelle vollständig/auszugsweise veröffentlicht worden ist.

Datum: ____________________ Unterschrift: ___________________________

Teile dieser Dissertation sind in den folgenden Publikationen enthalten:

Stutz, A., Kolbe, C.C., Stahl, R., Horvath, G.L., Franklin, B.S., van Ray, O., **Brinkschulte, R.**, Geyer, M., Meissner, F. & Latz, E. (2017) NLRP3 inflammasome assembly is regulated by phosphorylation of the pyrin domain. *J Exp Med*, 214, 1725-1736.

Venegas, C., Kumar, S., Franklin, B.S., Dierkes, T., **Brinkschulte, R.**, Tejera, D., Vieira-Saecker, A., Schwartz, S., Santarelli, F., Kummer, M.P., Griep, A., Gelpi, E., Beilharz, M., Riedel, D., Golenbock, D.T., Geyer, M., Walter, J., Latz, E. & Heneka, M.T. (2017) Microglia-derived ASC specks cross-seed amyloid-β in Alzheimer's disease. *Nature*, 552, 355-361.

12 Danksagung

Zuallererst möchte ich Herrn Prof. Dr. Matthias Geyer danken, für die stets motivierende Betreuung und die Unterstützung während der Bearbeitung meines Projekts, sowie für die Übernahme des Erstgutachtens.
Auch Frau Prof. Dr. Irmgard Förster möchte ich herzlich für die Übernahme des Zweitgutachtens danken.
Herrn Prof. Dr. Eicke Latz gilt mein herzlicher Dank für die Möglichkeit an mehreren Retreats teilzunehmen, sowie für die Teilnahme an meiner Prüfungskommission.
Auch Herrn Prof. Dr. Hasenauer möchte ich herzlich für die Teilnahme an meiner Prüfungskommission als vierter Prüfer danken.

Des Weiteren gilt mein Dank allen Beschäftigten des Instituts für Strukturbiologie für ein freundliches Arbeitsklima und eine tolle Zeit. Im Besonderen danke ich:

- Melanie für die Hilfe im Labor und die tatkräftige Unterstützung
- Kanchan für die wissenschaftlichen Diskussionen und die unermüdliche Unterstützung auf der Suche nach Kristallen
- Robert für zahlreiche Diskussionen und den Austausch von Blickwinkeln
- Heide und Inga für die Anfertigung von elektronenmikroskopischen Aufnahmen
- Karl für die Durchführung von SPR-Messungen

sowie allen anderen Mitarbeitern und Doktoranden: Anke, Sofia, Ines, Michael und Juliane.

Mein Dank gilt auch den folgenden Mitarbeitern des caesar, für ihre Unterstützung und die Bereitstellung eines inspirierenden Arbeitsumfeldes sowie für zahlreiche wissenschaftliche Diskussionen: Toni, Volkmar, Christian, Max, Maren, Martina, Yvonne, Vera, Hannes und Mareike.

Auch möchte ich den Arbeitskollegen Andrea, Pia, Olivia, Juan, Mario, Christian, Florian und Eike am Institut für Angeborene Immunität für die wissenschaftlichen Diskussionen und für die freundliche Aufnahme am Universitätsklinikum in Bonn danken.

Im Besonderen möchte ich den Kollaborationspartnern Dr. Florian Schmidt mit Alice und June, Dr. Dietmar Riedel und Dr. Sathish Kumar für die wissenschaftliche Zusammenarbeit danken:

Mein ganz persönlicher Dank gilt meinem Freund David, für unermüdliche wissenschaftliche Diskussionen und seine stetige Unterstützung beim Anfertigen dieser Arbeit und darüber hinaus.

Mein Dank gilt im Besonderen meinen Eltern, die mich stets unterstützt haben und mir den Weg zu dieser Arbeit geebnet haben. Danke!

Zuletzt danke ich Freddy und Mo für die schöne Atmosphäre während des Schreibens dieser Arbeit.

13 References

Akira, S., Uematsu, S. & Takeuchi, O. (2006) Pathogen recognition and innate immunity. *Cell*, **124**, 783-801.

Albrecht, M., Domingues, F.S., Schreiber, S. & Lengauer, T. (2003) Structural localization of disease-associated sequence variations in the NACHT and LRR domains of PYPAF1 and NOD2. *FEBS Lett*, **554**, 520-528.

Ammelburg, M., Frickey, T. & Lupas, A.N. (2006) Classification of AAA+ proteins. *J Struct Biol*, **156**, 2-11.

Areschoug, T. & Gordon, S. (2008) Pattern recognition receptors and their role in innate immunity: focus on microbial protein ligands. *Contrib Microbiol*, **15**, 45-60.

Arnoult, D., Soares, F., Tattoli, I., Castanier, C., Philpott, D.J. & Girardin, S.E. (2009) An N-terminal addressing sequence targets NLRX1 to the mitochondrial matrix. *J Cell Sci*, **122**, 3161-3168.

Bae, J.Y. & Park, H.H. (2011) Crystal structure of NALP3 protein pyrin domain (PYD) and its implications in inflammasome assembly. *J Biol Chem*, **286**, 39528-39536.

Barrow, A.D. & Trowsdale, J. (2006) You say ITAM and I say ITIM, let's call the whole thing off: the ambiguity of immunoreceptor signalling. *Eur J Immunol*, **36**, 1646-1653.

Benkő, S., Kovács, E.G., Hezel, F. & Kufer, T.A. (2017) NLRC5 Functions beyond MHC I Regulation-What Do We Know So Far? *Front Immunol*, **8**, 150.

Beutler, B., Jiang, Z., Georgel, P., Crozat, K., Croker, B., Rutschmann, S., Du, X. & Hoebe, K. (2006) Genetic analysis of host resistance: Toll-like receptor signaling and immunity at large. *Annu Rev Immunol*, **24**, 353-389.

Bi, D., Wang, Y., Gao, Y., Li, X., Chu, Q., Cui, J. & Xu, T. (2018) Recognition of Lipopolysaccharide and Activation of NF-κB by Cytosolic Sensor NOD1 in Teleost Fish. *Front Immunol*, **9**, 1413.

Bokhove, M., Sadat Al Hosseini, H., Saito, T., Dioguardi, E., Gegenschatz-Schmid, K., Nishimura, K., Raj, I., de Sanctis, D., Han, L. & Jovine, L. (2016) Easy mammalian expression and crystallography of maltose-binding protein-fused human proteins. *J Struct Biol*, **194**, 1-7.

Botos, I., Segal, D.M. & Davies, D.R. (2011) The structural biology of Toll-like receptors. *Structure*, **19**, 447-459.

Boucher, D., Monteleone, M., Coll, R.C., Chen, K.W., Ross, C.M., Teo, J.L., Gomez, G.A., Holley, C.L., Bierschenk, D., Stacey, K.J., Yap, A.S., Bezbradica, J.S. & Schroder, K. (2018) Caspase-1 self-cleavage is an intrinsic mechanism to terminate inflammasome activity. *J Exp Med*, **215**, 827-840.

Coll, R.C., Robertson, A.A., Chae, J.J., Higgins, S.C., Muñoz-Planillo, R., Inserra, M.C., Vetter, I., Dungan, L.S., Monks, B.G., Stutz, A., Croker, D.E., Butler, M.S., Haneklaus, M., Sutton, C.E., Núñez, G., Latz, E., Kastner, D.L., Mills, K.H., Masters, S.L., Schroder, K., Cooper, M.A. & O'Neill, L.A. (2015) A small-molecule inhibitor of the NLRP3 inflammasome for the treatment of inflammatory diseases. *Nat Med*, **21**, 248-255.

Compan, V., Baroja-Mazo, A., López-Castejón, G., Gomez, A.I., Martínez, C.M., Angosto, D., Montero, M.T., Herranz, A.S., Bazán, E., Reimers, D., Mulero, V. & Pelegrín, P. (2012) Cell volume regulation modulates NLRP3 inflammasome activation. *Immunity*, **37**, 487-500.

Cruz, C.M., Rinna, A., Forman, H.J., Ventura, A.L., Persechini, P.M. & Ojcius, D.M. (2007) ATP activates a reactive oxygen species-dependent oxidative stress response and secretion of proinflammatory cytokines in macrophages. *J Biol Chem*, **282**, 2871-2879.

D'Osualdo, A., Weichenberger, C.X., Wagner, R.N., Godzik, A., Wooley, J. & Reed, J.C. (2011) CARD8 and NLRP1 undergo autoproteolytic processing through a ZU5-like domain. *PLoS One*, **6**, e27396.

de Alba, E. (2009) Structure and interdomain dynamics of apoptosis-associated speck-like protein containing a CARD (ASC). *J Biol Chem*, **284**, 32932-32941.

Deng, L.W., Malik, P. & Perham, R.N. (1999) Interaction of the globular domains of pIII protein of filamentous bacteriophage fd with the F-pilus of Escherichia coli. *Virology*, **253**, 271-277.

Dick, M.S., Sborgi, L., Rühl, S., Hiller, S. & Broz, P. (2016) ASC filament formation serves as a signal amplification mechanism for inflammasomes. *Nat Commun*, **7**, 11929.

Diebolder, C.A., Halff, E.F., Koster, A.J., Huizinga, E.G. & Koning, R.I. (2015) Cryoelectron Tomography of the NAIP5/NLRC4 Inflammasome: Implications for NLR Activation. *Structure*, **23**, 2349-2357.

Dmitriev, O.Y., Lutsenko, S. & Muyldermans, S. (2016) Nanobodies as Probes for Protein Dynamics in Vitro and in Cells. *J Biol Chem*, **291**, 3767-3775.

Drakou, C.E., Malekkou, A., Hayes, J.M., Lederer, C.W., Leonidas, D.D., Oikonomakos, N.G., Lamond, A.I., Santama, N. & Zographos, S.E. (2012) hCINAP is an atypical mammalian nuclear adenylate kinase with an ATPase motif: structural and functional studies. *Proteins*, **80**, 206-220.

Dranoff, G. (2004) Cytokines in cancer pathogenesis and cancer therapy. *Nat Rev Cancer*, **4**, 11-22.

Druzinec, D., Salzig, D., Brix, A., Kraume, M., Vilcinskas, A., Kollewe, C. & Czermak, P. (2013) Optimization of insect cell based protein production processes - online monitoring, expression systems, scale up. *Adv Biochem Eng Biotechnol*, **136**, 65-100.

Duncan, J.A., Bergstralh, D.T., Wang, Y., Willingham, S.B., Ye, Z., Zimmermann, A.G. & Ting, J.P. (2007) Cryopyrin/NALP3 binds ATP/dATP, is an ATPase, and requires ATP binding to mediate inflammatory signaling. *Proc Natl Acad Sci U S A*, **104**, 8041-8046.

Elliott, J.M., Rouge, L., Wiesmann, C. & Scheer, J.M. (2009) Crystal structure of procaspase-1 zymogen domain reveals insight into inflammatory caspase autoactivation. *J Biol Chem*, **284**, 6546-6553.

Erzberger, J.P. & Berger, J.M. (2006) Evolutionary relationships and structural mechanisms of AAA+ proteins. *Annu Rev Biophys Biomol Struct*, **35**, 93-114.

Faustin, B., Lartigue, L., Bruey, J.M., Luciano, F., Sergienko, E., Bailly-Maitre, B., Volkmann, N., Hanein, D., Rouiller, I. & Reed, J.C. (2007) Reconstituted NALP1 inflammasome reveals two-step mechanism of caspase-1 activation. *Mol Cell*, **25**, 713-724.

Feldhau, P., Fröhlich, T., Goody, R.S., Isakov, M. & Schirmer, R.H. (1975) Synthetic inhibitors of adenylate kinases in the assays for ATPases and phosphokinases. *Eur J Biochem*, **57**, 197-204.

Finger, J.N., Lich, J.D., Dare, L.C., Cook, M.N., Brown, K.K., Duraiswami, C., Bertin, J., Bertin, J.J. & Gough, P.J. (2012) Autolytic proteolysis within the function to find domain (FIIND) is required for NLRP1 inflammasome activity. *J Biol Chem*, **287**, 25030-25037.

Gargano, N. & Cattaneo, A. (1997) Rescue of a neutralizing anti-viral antibody fragment from an intracellular polyclonal repertoire expressed in mammalian cells. *FEBS Lett*, **414**, 537-540.

Gay, N.J., Symmons, M.F., Gangloff, M. & Bryant, C.E. (2014) Assembly and localization of Toll-like receptor signalling complexes. *Nat Rev Immunol*, **14**, 546-558.

Griffin, L. & Lawson, A. (2011) Antibody fragments as tools in crystallography. *Clin Exp Immunol*, **165**, 285-291.

Hafner-Bratkovič, I., Sušjan, P., Lainšček, D., Tapia-Abellán, A., Cerović, K., Kadunc, L., Angosto-Bazarra, D., Pelegrín, P. & Jerala, R. (2018) NLRP3 lacking the leucine-rich repeat domain can be fully activated via the canonical inflammasome pathway. *Nat Commun*, **9**, 5182.

Halle, A., Hornung, V., Petzold, G.C., Stewart, C.R., Monks, B.G., Reinheckel, T., Fitzgerald, K.A., Latz, E., Moore, K.J. & Golenbock, D.T. (2008) The NALP3 inflammasome is involved in the innate immune response to amyloid-beta. *Nat Immunol*, **9**, 857-865.

Hanson, P.I. & Whiteheart, S.W. (2005) AAA+ proteins: have engine, will work. *Nat Rev Mol Cell Biol*, **6**, 519-529.

Harris, P.A., Duraiswami, C., Fisher, D.T., Fornwald, J., Hoffman, S.J., Hofmann, G., Jiang, M., Lehr, R., McCormick, P.M., Nickels, L., Schwartz, B., Wu, Z., Zhang, G., Marquis, R.W., Bertin, J. & Gough, P.J. (2015) High throughput screening identifies ATP-competitive inhibitors of the NLRP1 inflammasome. *Bioorg Med Chem Lett*, **25**, 2739-2743.

Hauenstein, A.V., Zhang, L. & Wu, H. (2015) The hierarchical structural architecture of inflammasomes, supramolecular inflammatory machines. *Curr Opin Struct Biol*, **31**, 75-83.

He, Y., Hara, H. & Núñez, G. (2016a) Mechanism and Regulation of NLRP3 Inflammasome Activation. *Trends Biochem Sci*, **41**, 1012-1021.

He, Y., Zeng, M.Y., Yang, D., Motro, B. & Núñez, G. (2016b) NEK7 is an essential mediator of NLRP3 activation downstream of potassium efflux. *Nature*, **530**, 354-357.

Heid, M.E., Keyel, P.A., Kamga, C., Shiva, S., Watkins, S.C. & Salter, R.D. (2013) Mitochondrial reactive oxygen species induces NLRP3-dependent lysosomal damage and inflammasome activation. *J Immunol*, **191**, 5230-5238.

Helma, J., Cardoso, M.C., Muyldermans, S. & Leonhardt, H. (2015) Nanobodies and recombinant binders in cell biology. *J Cell Biol*, **209**, 633-644.

Heneka, M.T., Kummer, M.P. & Latz, E. (2014) Innate immune activation in neurodegenerative disease. *Nat Rev Immunol*, **14**, 463-477.

Heneka, M.T., Kummer, M.P., Stutz, A., Delekate, A., Schwartz, S., Vieira-Saecker, A., Griep, A., Axt, D., Remus, A., Tzeng, T.C., Gelpi, E., Halle, A., Korte, M., Latz, E. & Golenbock, D.T. (2013) NLRP3 is activated in Alzheimer's disease and contributes to pathology in APP/PS1 mice. *Nature*, **493**, 674-678.

Hock, E.M. & Polymenidou, M. (2016) Prion-like propagation as a pathogenic principle in frontotemporal dementia. *J Neurochem*, **138 Suppl 1**, 163-183.

Hoffman, H.M., Mueller, J.L., Broide, D.H., Wanderer, A.A. & Kolodner, R.D. (2001) Mutation of a new gene encoding a putative pyrin-like protein causes familial cold autoinflammatory syndrome and Muckle-Wells syndrome. *Nat Genet*, **29**, 301-305.

Hofmann, A., Simon, A., Grkovic, T. & Jones, M. (2014) Methods of Molecular Analysis in the Life Sciences. Cambridge University Press.

Homola, J. (2008) Surface plasmon resonance sensors for detection of chemical and biological species. *Chem Rev*, **108**, 462-493.

Hong, M., Yoon, S.I. & Wilson, I.A. (2012) Structure and functional characterization of the RNA-binding element of the NLRX1 innate immune modulator. *Immunity*, **36**, 337-347.

Hsieh, V.H. & Wyatt, P.J. (2017) Measuring proteins with greater speed and resolution while reducing sample size. *Sci Rep*, **7**, 10030.

Hu, Q., Wu, D., Chen, W., Yan, Z., Yan, C., He, T., Liang, Q. & Shi, Y. (2014) Molecular determinants of caspase-9 activation by the Apaf-1 apoptosome. *Proc Natl Acad Sci U S A*, **111**, 16254-16261.

Hu, S., Du, X., Huang, Y., Fu, Y., Yang, Y., Zhan, X., He, W., Wen, Q., Zhou, X., Zhou, C., Zhong, X.P., Yang, J., Xiong, W., Wang, R., Gao, Y. & Ma, L. (2018) NLRC3 negatively regulates CD4+ T cells and impacts protective immunity during Mycobacterium tuberculosis infection. *PLoS Pathog*, **14**, e1007266.

Hu, Z., Yan, C., Liu, P., Huang, Z., Ma, R., Zhang, C., Wang, R., Zhang, Y., Martinon, F., Miao, D., Deng, H., Wang, J., Chang, J. & Chai, J. (2013) Crystal structure of NLRC4 reveals its autoinhibition mechanism. *Science*, **341**, 172-175.

Hu, Z., Zhou, Q., Zhang, C., Fan, S., Cheng, W., Zhao, Y., Shao, F., Wang, H.W., Sui, S.F. & Chai, J. (2015) Structural and biochemical basis for induced self-propagation of NLRC4. *Science*, **350**, 399-404.

Iyer, L.M., Leipe, D.D., Koonin, E.V. & Aravind, L. (2004) Evolutionary history and higher order classification of AAA+ ATPases. *J Struct Biol*, **146**, 11-31.

Jiang, H., He, H., Chen, Y., Huang, W., Cheng, J., Ye, J., Wang, A., Tao, J., Wang, C., Liu, Q., Jin, T., Jiang, W., Deng, X. & Zhou, R. (2017) Identification of a selective and direct NLRP3 inhibitor to treat inflammatory disorders. *J Exp Med*, **214**, 3219-3238.

Jo, E.K., Kim, J.K., Shin, D.M. & Sasakawa, C. (2016) Molecular mechanisms regulating NLRP3 inflammasome activation. *Cell Mol Immunol*, **13**, 148-159.

Joly, N., Zhang, N., Buck, M. & Zhang, X. (2012) Coupling AAA protein function to regulated gene expression. *Biochim Biophys Acta*, **1823**, 108-116.

Juliana, C., Fernandes-Alnemri, T., Wu, J., Datta, P., Solorzano, L., Yu, J.W., Meng, R., Quong, A.A., Latz, E., Scott, C.P. & Alnemri, E.S. (2010) Anti-inflammatory compounds parthenolide and Bay 11-7082 are direct inhibitors of the inflammasome. *J Biol Chem*, **285**, 9792-9802.

Kato, H. & Fujita, T. (2015) RIG-I-like receptors and autoimmune diseases. *Curr Opin Immunol*, **37**, 40-45.

Kesavardhana, S. & Kanneganti, T.D. (2017) Mechanisms governing inflammasome activation, assembly and pyroptosis induction. *Int Immunol*, **29**, 201-210.

Kingeter, L.M. & Lin, X. (2012) C-type lectin receptor-induced NF-κB activation in innate immune and inflammatory responses. *Cell Mol Immunol*, **9**, 105-112.

Kobe, B. & Kajava, A.V. (2001) The leucine-rich repeat as a protein recognition motif. *Curr Opin Struct Biol*, **11**, 725-732.

Krishnan, S.M., Dowling, J.K., Ling, Y.H., Diep, H., Chan, C.T., Ferens, D., Kett, M.M., Pinar, A., Samuel, C.S., Vinh, A., Arumugam, T.V., Hewitson, T.D., Kemp-Harper, B.K., Robertson, A.A., Cooper, M.A., Latz, E., Mansell, A., Sobey, C.G. & Drummond, G.R. (2016) Inflammasome activity is essential for one kidney/deoxycorticosterone acetate/salt-induced hypertension in mice. *Br J Pharmacol*, **173**, 752-765.

Kwon, D., Yoon, J.H., Shin, S.Y., Jang, T.H., Kim, H.G., So, I., Jeon, J.H. & Park, H.H. (2012) A comprehensive manually curated protein-protein interaction database for the Death Domain superfamily. *Nucleic Acids Res*, **40**, D331-336.

Laemmli, U.K. (1970) Cleavage of structural proteins during the assembly of the head of bacteriophage T4. *Nature*, **227**, 680-685.

Laliberte, R.E., Perregaux, D.G., Hoth, L.R., Rosner, P.J., Jordan, C.K., Peese, K.M., Eggler, J.F., Dombroski, M.A., Geoghegan, K.F. & Gabel, C.A. (2003) Glutathione s-transferase omega 1-1 is a target of cytokine release inhibitory drugs and may be responsible for their effect on interleukin-1beta posttranslational processing. *J Biol Chem*, **278**, 16567-16578.

Lee, G.S., Subramanian, N., Kim, A.I., Aksentijevich, I., Goldbach-Mansky, R., Sacks, D.B., Germain, R.N., Kastner, D.L. & Chae, J.J. (2012) The calcium-sensing receptor regulates the NLRP3 inflammasome through Ca2+ and cAMP. *Nature*, **492**, 123-127.

Leipe, D.D., Koonin, E.V. & Aravind, L. (2004) STAND, a class of P-loop NTPases including animal and plant regulators of programmed cell death: multiple, complex domain architectures, unusual phyletic patterns, and evolution by horizontal gene transfer. *J Mol Biol*, **343**, 1-28.

Li, Y., Fu, T.M., Lu, A., Witt, K., Ruan, J., Shen, C. & Wu, H. (2018) Cryo-EM structures of ASC and NLRC4 CARD filaments reveal a unified mechanism of nucleation and activation of caspase-1. *Proc Natl Acad Sci U S A*.

Liedberg, B., Nylander, C. & Lundström, I. (1995) Biosensing with surface plasmon resonance--how it all started. *Biosens Bioelectron*, **10**, i-ix.

Liu, X., Zhang, Z., Ruan, J., Pan, Y., Magupalli, V.G., Wu, H. & Lieberman, J. (2016) Inflammasome-activated gasdermin D causes pyroptosis by forming membrane pores. *Nature*, **535**, 153-158.

Loo, Y.M. & Gale, M. (2011) Immune signaling by RIG-I-like receptors. *Immunity*, **34**, 680-692.

Lu, A., Li, Y., Schmidt, F.I., Yin, Q., Chen, S., Fu, T.M., Tong, A.B., Ploegh, H.L., Mao, Y. & Wu, H. (2016) Molecular basis of caspase-1 polymerization and its inhibition by a new capping mechanism. *Nat Struct Mol Biol*, **23**, 416-425.

Lu, A., Magupalli, V.G., Ruan, J., Yin, Q., Atianand, M.K., Vos, M.R., Schröder, G.F., Fitzgerald, K.A., Wu, H. & Egelman, E.H. (2014) Unified polymerization mechanism for the assembly of ASC-dependent inflammasomes. *Cell*, **156**, 1193-1206.

Lu, B., Nakamura, T., Inouye, K., Li, J., Tang, Y., Lundbäck, P., Valdes-Ferrer, S.I., Olofsson, P.S., Kalb, T., Roth, J., Zou, Y., Erlandsson-Harris, H., Yang, H., Ting, J.P., Wang, H., Andersson, U., Antoine, D.J., Chavan, S.S., Hotamisligil, G.S. & Tracey, K.J. (2012) Novel role of PKR in inflammasome activation and HMGB1 release. *Nature*, **488**, 670-674.

Ludwig-Portugall, I., Bartok, E., Dhana, E., Evers, B.D., Primiano, M.J., Hall, J.P., Franklin, B.S., Knolle, P.A., Hornung, V., Hartmann, G., Boor, P., Latz, E. & Kurts, C. (2016) An NLRP3-specific inflammasome inhibitor attenuates crystal-induced kidney fibrosis in mice. *Kidney Int*, **90**, 525-539.

Maekawa, S., Ohto, U., Shibata, T., Miyake, K. & Shimizu, T. (2016) Crystal structure of NOD2 and its implications in human disease. *Nat Commun*, **7**, 11813.

Maharana, J., Panda, D. & De, S. (2018) Deciphering the ATP-binding mechanism(s) in NLRP-NACHT 3D models using structural bioinformatics approaches. *PLoS One*, **13**, e0209420.

Mangan, M.S.J., Olhava, E.J., Roush, W.R., Seidel, H.M., Glick, G.D. & Latz, E. (2018) Targeting the NLRP3 inflammasome in inflammatory diseases. *Nat Rev Drug Discov*, **17**, 688.

Martinon, F., Burns, K. & Tschopp, J. (2002) The inflammasome: a molecular platform triggering activation of inflammatory caspases and processing of proIL-beta. *Mol Cell*, **10**, 417-426.

Matusiak, M., Van Opdenbosch, N. & Lamkanfi, M. (2015) CARD- and pyrin-only proteins regulating inflammasome activation and immunity. *Immunol Rev*, **265**, 217-230.

Mayor, A., Martinon, F., De Smedt, T., Pétrilli, V. & Tschopp, J. (2007) A crucial function of SGT1 and HSP90 in inflammasome activity links mammalian and plant innate immune responses. *Nat Immunol*, **8**, 497-503.

McPherson, A. & Gavira, J.A. (2014) Introduction to protein crystallization. *Acta Crystallogr F Struct Biol Commun*, **70**, 2-20.

Miller, J.M. & Enemark, E.J. (2016) Fundamental Characteristics of AAA+ Protein Family Structure and Function. *Archaea*, **2016**, 9294307.

Misawa, T., Takahama, M., Kozaki, T., Lee, H., Zou, J., Saitoh, T. & Akira, S. (2013) Microtubule-driven spatial arrangement of mitochondria promotes activation of the NLRP3 inflammasome. *Nat Immunol*, **14**, 454-460.

Mishra, B.B., Rathinam, V.A., Martens, G.W., Martinot, A.J., Kornfeld, H., Fitzgerald, K.A. & Sassetti, C.M. (2013) Nitric oxide controls the immunopathology of tuberculosis by inhibiting NLRP3 inflammasome-dependent processing of IL-1β. *Nat Immunol*, **14**, 52-60.

Mitchell, J. (2010) Small molecule immunosensing using surface plasmon resonance. *Sensors (Basel)*, **10**, 7323-7346.

Mitoma, H., Hanabuchi, S., Kim, T., Bao, M., Zhang, Z., Sugimoto, N. & Liu, Y.J. (2013) The DHX33 RNA helicase senses cytosolic RNA and activates the NLRP3 inflammasome. *Immunity*, **39**, 123-135.

Monroe, N. & Hill, C.P. (2016) Meiotic Clade AAA ATPases: Protein Polymer Disassembly Machines. *J Mol Biol*, **428**, 1897-1911.

Mortimer, L., Moreau, F., MacDonald, J.A. & Chadee, K. (2016) NLRP3 inflammasome inhibition is disrupted in a group of auto-inflammatory disease CAPS mutations. *Nat Immunol*, **17**, 1176-1186.

Murphy, K. & Weaver, C. (2012) *Janeway's Immunobiology*. New York, NY, USA : Garland Science, Taylor & Francis Group, LLC.

Murphy, M.P. (2009) How mitochondria produce reactive oxygen species. *Biochem J*, **417**, 1-13.

Negroni, A., Pierdomenico, M., Cucchiara, S. & Stronati, L. (2018) NOD2 and inflammation: current insights. *J Inflamm Res*, **11**, 49-60.

Ng, A. & Xavier, R.J. (2011) Leucine-rich repeat (LRR) proteins: integrators of pattern recognition and signaling in immunity. *Autophagy*, **7**, 1082-1084.

Ng, M., Blaschke, T.F., Arias, A.A. & Zare, R.N. (1992) Analysis of free intracellular nucleotides using high-performance capillary electrophoresis. *Anal Chem*, **64**, 1682-1684.

Nomura, J., So, A., Tamura, M. & Busso, N. (2015) Intracellular ATP Decrease Mediates NLRP3 Inflammasome Activation upon Nigericin and Crystal Stimulation. *J Immunol*, **195**, 5718-5724.

Ogura, T. & Wilkinson, A.J. (2001) AAA+ superfamily ATPases: common structure--diverse function. *Genes Cells*, **6**, 575-597.

Okada, M., Matsuzawa, A., Yoshimura, A. & Ichijo, H. (2014) The lysosome rupture-activated TAK1-JNK pathway regulates NLRP3 inflammasome activation. *J Biol Chem*, **289**, 32926-32936.

Oroz, J., Barrera-Vilarmau, S., Alfonso, C., Rivas, G. & de Alba, E. (2016) ASC Pyrin Domain Self-associates and Binds NLRP3 Protein Using Equivalent Binding Interfaces. *J Biol Chem*, **291**, 19487-19501.

Palau, W. & Di Primo, C. (2013) Simulated single-cycle kinetics improves the design of surface plasmon resonance assays. *Talanta*, **114**, 211-216.

Park, H.H. (2011) Structural analyses of death domains and their interactions. *Apoptosis*, **16**, 209-220.

Park, H.H., Lo, Y.C., Lin, S.C., Wang, L., Yang, J.K. & Wu, H. (2007) The death domain superfamily in intracellular signaling of apoptosis and inflammation. *Annu Rev Immunol*, **25**, 561-586.

Park, K., Shen, B.W., Parmeggiani, F., Huang, P.S., Stoddard, B.L. & Baker, D. (2015) Control of repeat-protein curvature by computational protein design. *Nat Struct Mol Biol*, **22**, 167-174.

Perera, A.P., Fernando, R., Shinde, T., Gundamaraju, R., Southam, B., Sohal, S.S., Robertson, A.A.B., Schroder, K., Kunde, D. & Eri, R. (2018) MCC950, a specific small molecule inhibitor of NLRP3 inflammasome attenuates colonic inflammation in spontaneous colitis mice. *Sci Rep*, **8**, 8618.

Praefcke, G.J., Geyer, M., Schwemmle, M., Robert Kalbitzer, H. & Herrmann, C. (1999) Nucleotide-binding characteristics of human guanylate-binding protein 1 (hGBP1) and identification of the third GTP-binding motif. *J Mol Biol*, **292**, 321-332.

Primiano, M.J., Lefker, B.A., Bowman, M.R., Bree, A.G., Hubeau, C., Bonin, P.D., Mangan, M., Dower, K., Monks, B.G., Cushing, L., Wang, S., Guzova, J., Jiao, A., Lin, L.L., Latz, E., Hepworth, D. & Hall, J.P. (2016) Efficacy and Pharmacology of the NLRP3 Inflammasome Inhibitor CP-456,773 (CRID3) in Murine Models of Dermal and Pulmonary Inflammation. *J Immunol*, **197**, 2421-2433.

Proell, M., Riedl, S.J., Fritz, J.H., Rojas, A.M. & Schwarzenbacher, R. (2008) The Nod-like receptor (NLR) family: a tale of similarities and differences. *PLoS One*, **3**, e2119.

Py, B.F., Kim, M.S., Vakifahmetoglu-Norberg, H. & Yuan, J. (2013) Deubiquitination of NLRP3 by BRCC3 critically regulates inflammasome activity. *Mol Cell*, **49**, 331-338.

Pétrilli, V., Papin, S., Dostert, C., Mayor, A., Martinon, F. & Tschopp, J. (2007) Activation of the NALP3 inflammasome is triggered by low intracellular potassium concentration. *Cell Death Differ*, **14**, 1583-1589.

Qi, S., Pang, Y., Hu, Q., Liu, Q., Li, H., Zhou, Y., He, T., Liang, Q., Liu, Y., Yuan, X., Luo, G., Wang, J., Yan, N. & Shi, Y. (2010) Crystal structure of the Caenorhabditis elegans apoptosome reveals an octameric assembly of CED-4. *Cell*, **141**, 446-457.

Qiao, J., Wu, X., Luo, Q., Wei, G., Xu, M., Wu, Y., Liu, Y., Li, X., Zi, J., Ju, W., Fu, L., Chen, C., Wu, Q., Zhu, S., Qi, K., Li, D., Li, Z., Andrews, R.K., Zeng, L., Gardiner, E.E. & Xu, K. (2018) NLRP3 regulates platelet integrin αIIbβ3 outside-in signaling, hemostasis and arterial thrombosis. *Haematologica*, **103**, 1568-1576.

Radian, A.D., Khare, S., Chu, L.H., Dorfleutner, A. & Stehlik, C. (2015) ATP binding by NLRP7 is required for inflammasome activation in response to bacterial lipopeptides. *Mol Immunol*, **67**, 294-302.

Randak, C. & Welsh, M.J. (2003) An intrinsic adenylate kinase activity regulates gating of the ABC transporter CFTR. *Cell*, **115**, 837-850.

Rathinam, V.A., Vanaja, S.K., Waggoner, L., Sokolovska, A., Becker, C., Stuart, L.M., Leong, J.M. & Fitzgerald, K.A. (2012) TRIF licenses caspase-11-dependent NLRP3 inflammasome activation by gram-negative bacteria. *Cell*, **150**, 606-619.

Raturi, A. & Simmen, T. (2013) Where the endoplasmic reticulum and the mitochondrion tie the knot: the mitochondria-associated membrane (MAM). *Biochim Biophys Acta*, **1833**, 213-224.

Reyes Ruiz, V.M., Ramirez, J., Naseer, N., Palacio, N.M., Siddarthan, I.J., Yan, B.M., Boyer, M.A., Pensinger, D.A., Sauer, J.D. & Shin, S. (2017) Broad detection of bacterial type III secretion system and flagellin proteins by the human NAIP/NLRC4 inflammasome. *Proc Natl Acad Sci U S A*, **114**, 13242-13247.

Richens, J.L., Urbanowicz, R.A., Lunt, E.A., Metcalf, R., Corne, J., Fairclough, L. & O'Shea, P. (2009) Systems biology coupled with label-free high-throughput detection as a novel approach for diagnosis of chronic obstructive pulmonary disease. *Respir Res*, **10**, 29.

Riedl, S.J., Li, W., Chao, Y., Schwarzenbacher, R. & Shi, Y. (2005) Structure of the apoptotic protease-activating factor 1 bound to ADP. *Nature*, **434**, 926-933.

Roher, A.E., Kokjohn, T.A., Clarke, S.G., Sierks, M.R., Maarouf, C.L., Serrano, G.E., Sabbagh, M.S. & Beach, T.G. (2017) APP/Aβ structural diversity and Alzheimer's disease pathogenesis. *Neurochem Int*, **110**, 1-13.

Saraste, M., Sibbald, P.R. & Wittinghofer, A. (1990) The P-loop--a common motif in ATP- and GTP-binding proteins. *Trends Biochem Sci*, **15**, 430-434.

Sarrauste de Menthière, C., Terrière, S., Pugnère, D., Ruiz, M., Demaille, J. & Touitou, I. (2003) INFEVERS: the Registry for FMF and hereditary inflammatory disorders mutations. *Nucleic Acids Res*, **31**, 282-285.

Schlee, M., Hartmann, E., Coch, C., Wimmenauer, V., Janke, M., Barchet, W. & Hartmann, G. (2009) Approaching the RNA ligand for RIG-I? *Immunol Rev*, **227**, 66-74.

Schmid-Burgk, J.L., Chauhan, D., Schmidt, T., Ebert, T.S., Reinhardt, J., Endl, E. & Hornung, V. (2016) A Genome-wide CRISPR (Clustered Regularly Interspaced Short Palindromic Repeats) Screen Identifies NEK7 as an Essential Component of NLRP3 Inflammasome Activation. *J Biol Chem*, **291**, 103-109.

Schmidt, F.I., Lu, A., Chen, J.W., Ruan, J., Tang, C., Wu, H. & Ploegh, H.L. (2016) A single domain antibody fragment that recognizes the adaptor ASC defines the role of ASC domains in inflammasome assembly. *J Exp Med*, **213**, 771-790.

Schwemmle, M. & Staeheli, P. (1994) The interferon-induced 67-kDa guanylate-binding protein (hGBP1) is a GTPase that converts GTP to GMP. *J Biol Chem*, **269**, 11299-11305.

Shenoy, A.R., Wellington, D.A., Kumar, P., Kassa, H., Booth, C.J., Cresswell, P. & MacMicking, J.D. (2012) GBP5 promotes NLRP3 inflammasome assembly and immunity in mammals. *Science*, **336**, 481-485.

Shi, H., Wang, Y., Li, X., Zhan, X., Tang, M., Fina, M., Su, L., Pratt, D., Bu, C.H., Hildebrand, S., Lyon, S., Scott, L., Quan, J., Sun, Q., Russell, J., Arnett, S., Jurek, P., Chen, D., Kravchenko, V.V., Mathison, J.C., Moresco, E.M., Monson, N.L., Ulevitch, R.J. & Beutler, B. (2016) NLRP3 activation and mitosis are mutually exclusive events coordinated by NEK7, a new inflammasome component. *Nat Immunol*, **17**, 250-258.

Shi, J., Zhao, Y., Wang, Y., Gao, W., Ding, J., Li, P., Hu, L. & Shao, F. (2014) Inflammatory caspases are innate immune receptors for intracellular LPS. *Nature*, **514**, 187-192.

Shim, D.W. & Lee, K.H. (2018) Posttranslational Regulation of the NLR Family Pyrin Domain-Containing 3 Inflammasome. *Front Immunol*, **9**, 1054.

Shimada, K., Crother, T.R., Karlin, J., Dagvadorj, J., Chiba, N., Chen, S., Ramanujan, V.K., Wolf, A.J., Vergnes, L., Ojcius, D.M., Rentsendorj, A., Vargas, M., Guerrero, C., Wang, Y., Fitzgerald, K.A., Underhill, D.M., Town, T. & Arditi, M. (2012) Oxidized mitochondrial DNA activates the NLRP3 inflammasome during apoptosis. *Immunity*, **36**, 401-414.

Smyth, D.R., Mrozkiewicz, M.K., McGrath, W.J., Listwan, P. & Kobe, B. (2003) Crystal structures of fusion proteins with large-affinity tags. *Protein Sci*, **12**, 1313-1322.

Snider, J. & Houry, W.A. (2008) AAA+ proteins: diversity in function, similarity in structure. *Biochem Soc Trans*, **36**, 72-77.

Soe, K.C., Devaiah, B.N. & Singer, D.S. (2013) Transcriptional coactivator CIITA, a functional homolog of TAF1, has kinase activity. *Biochim Biophys Acta*, **1829**, 1184-1190.

Song, N., Liu, Z.S., Xue, W., Bai, Z.F., Wang, Q.Y., Dai, J., Liu, X., Huang, Y.J., Cai, H., Zhan, X.Y., Han, Q.Y., Wang, H., Chen, Y., Li, H.Y., Li, A.L., Zhang, X.M., Zhou, T. & Li, T. (2017) NLRP3 Phosphorylation Is an Essential Priming Event for Inflammasome Activation. *Mol Cell*, **68**, 185-197.e186.

Spalinger, M.R., Kasper, S., Gottier, C., Lang, S., Atrott, K., Vavricka, S.R., Scharl, S., Raselli, T., Frey-Wagner, I., Gutte, P.M., Grütter, M.G., Beer, H.D., Contassot, E., Chan, A.C., Dai, X., Rawlings, D.J., Mair, F., Becher, B., Falk, W., Fried, M., Rogler, G. & Scharl, M. (2016) NLRP3 tyrosine phosphorylation is controlled by protein tyrosine phosphatase PTPN22. *J Clin Invest*, **126**, 4388.

Stein, C., Caccamo, M., Laird, G. & Leptin, M. (2007) Conservation and divergence of gene families encoding components of innate immune response systems in zebrafish. *Genome Biol*, **8**, R251.

Stutz, A., Kolbe, C.C., Stahl, R., Horvath, G.L., Franklin, B.S., van Ray, O., Brinkschulte, R., Geyer, M., Meissner, F. & Latz, E. (2017) NLRP3 inflammasome assembly is regulated by phosphorylation of the pyrin domain. *J Exp Med*, **214**, 1725-1736.

Su, M.Y., Kuo, C.I., Chang, C.F. & Chang, C.I. (2013) Three-dimensional structure of human NLRP10/PYNOD pyrin domain reveals a homotypic interaction site distinct from its mouse homologue. *PLoS One*, **8**, e67843.

Subramanian, N., Natarajan, K., Clatworthy, M.R., Wang, Z. & Germain, R.N. (2013) The adaptor MAVS promotes NLRP3 mitochondrial localization and inflammasome activation. *Cell*, **153**, 348-361.

Sysoeva, T.A. (2017) Assessing heterogeneity in oligomeric AAA+ machines. *Cell Mol Life Sci*, **74**, 1001-1018.

Takeuchi, O. & Akira, S. (2010) Pattern recognition receptors and inflammation. *Cell*, **140**, 805-820.

Tenthorey, J.L., Haloupek, N., López-Blanco, J.R., Grob, P., Adamson, E., Hartenian, E., Lind, N.A., Bourgeois, N.M., Chacón, P., Nogales, E. & Vance, R.E. (2017) The structural basis of flagellin detection by NAIP5: A strategy to limit pathogen immune evasion. *Science*, **358**, 888-893.

Ting, J.P., Lovering, R.C., Alnemri, E.S., Bertin, J., Boss, J.M., Davis, B.K., Flavell, R.A., Girardin, S.E., Godzik, A., Harton, J.A., Hoffman, H.M., Hugot, J.P., Inohara, N., Mackenzie, A., Maltais, L.J., Nunez, G., Ogura, Y., Otten, L.A., Philpott, D., Reed, J.C., Reith, W., Schreiber, S., Steimle, V. & Ward, P.A. (2008) The NLR gene family: a standard nomenclature. *Immunity*, **28**, 285-287.

Tran, T.A. (2017) Muckle-Wells syndrome: clinical perspectives. *Open Access Rheumatol*, **9**, 123-129.

Traut, T.W. (1994) The functions and consensus motifs of nine types of peptide segments that form different types of nucleotide-binding sites. *Eur J Biochem*, **222**, 9-19.

Urbach, J.M. & Ausubel, F.M. (2017) The NBS-LRR architectures of plant R-proteins and metazoan NLRs evolved in independent events. *Proc Natl Acad Sci U S A*, **114**, 1063-1068.

Vanaja, S.K., Rathinam, V.A. & Fitzgerald, K.A. (2015) Mechanisms of inflammasome activation: recent advances and novel insights. *Trends Cell Biol*, **25**, 308-315.

Vassar, R., Kuhn, P.H., Haass, C., Kennedy, M.E., Rajendran, L., Wong, P.C. & Lichtenthaler, S.F. (2014) Function, therapeutic potential and cell biology of BACE proteases: current status and future prospects. *J Neurochem*, **130**, 4-28.

Venegas, C., Kumar, S., Franklin, B.S., Dierkes, T., Brinkschulte, R., Tejera, D., Vieira-Saecker, A., Schwartz, S., Santarelli, F., Kummer, M.P., Griep, A., Gelpi, E., Beilharz, M., Riedel, D., Golenbock, D.T., Geyer, M., Walter, J., Latz, E. & Heneka, M.T. (2017) Microglia-derived ASC specks cross-seed amyloid-β in Alzheimer's disease. *Nature*, **552**, 355-361.

Volonté, C., Apolloni, S., Skaper, S.D. & Burnstock, G. (2012) P2X7 receptors: channels, pores and more. *CNS Neurol Disord Drug Targets*, **11**, 705-721.

Walker, J.E., Saraste, M., Runswick, M.J. & Gay, N.J. (1982) Distantly related sequences in the alpha- and beta-subunits of ATP synthase, myosin, kinases and other ATP-requiring enzymes and a common nucleotide binding fold. *EMBO J*, **1**, 945-951.

Waterhouse, A., Bertoni, M., Bienert, S., Studer, G., Tauriello, G., Gumienny, R., Heer, F.T., de Beer, T.A.P., Rempfer, C., Bordoli, L., Lepore, R. & Schwede, T. (2018) SWISS-MODEL: homology modelling of protein structures and complexes. *Nucleic Acids Res*, **46**, W296-W303.

Wendler, P., Ciniawsky, S., Kock, M. & Kube, S. (2012) Structure and function of the AAA+ nucleotide binding pocket. *Biochim Biophys Acta*, **1823**, 2-14.

Wilkins, M.R., Gasteiger, E., Bairoch, A., Sanchez, J.C., Williams, K.L., Appel, R.D. & Hochstrasser, D.F. (1999) Protein identification and analysis tools in the ExPASy server. *Methods Mol Biol*, **112**, 531-552.

Xu, T., Du, Y., Fang, X.B., Chen, H., Zhou, D.D., Wang, Y. & Zhang, L. (2018) New insights into Nod-like receptors (NLRs) in liver diseases. *Int J Physiol Pathophysiol Pharmacol*, **10**, 1-16.

Ye, Z., Lich, J.D., Moore, C.B., Duncan, J.A., Williams, K.L. & Ting, J.P. (2008) ATP binding by monarch-1/NLRP12 is critical for its inhibitory function. *Mol Cell Biol*, **28**, 1841-1850.

Yedidi, R.S., Wendler, P. & Enenkel, C. (2017) AAA-ATPases in Protein Degradation. *Front Mol Biosci*, **4**, 42.

Yegutkin, G.G. & Burnstock, G. (2000) Inhibitory effects of some purinergic agents on ecto-ATPase activity and pattern of stepwise ATP hydrolysis in rat liver plasma membranes. *Biochim Biophys Acta*, **1466**, 234-244.

Yuan, Y.Y., Xie, K.X., Wang, S.L. & Yuan, L.W. (2018) Inflammatory caspase-related pyroptosis: mechanism, regulation and therapeutic potential for inflammatory bowel disease. *Gastroenterol Rep (Oxf)*, **6**, 167-176.

Zhang, L., Chen, S., Ruan, J., Wu, J., Tong, A.B., Yin, Q., Li, Y., David, L., Lu, A., Wang, W.L., Marks, C., Ouyang, Q., Zhang, X., Mao, Y. & Wu, H. (2015) Cryo-EM structure of the activated NAIP2-NLRC4 inflammasome reveals nucleated polymerization. *Science*, **350**, 404-409.

Zhang, X. & Wigley, D.B. (2008) The 'glutamate switch' provides a link between ATPase activity and ligand binding in AAA+ proteins. *Nat Struct Mol Biol*, **15**, 1223-1227.

Zhang, Z., Meszaros, G., He, W.T., Xu, Y., de Fatima Magliarelli, H., Mailly, L., Mihlan, M., Liu, Y., Puig Gámez, M., Goginashvili, A., Pasquier, A., Bielska, O., Neven, B., Quartier, P., Aebersold, R., Baumert, T.F., Georgel, P., Han, J. & Ricci, R. (2017) Protein kinase D at the Golgi controls NLRP3 inflammasome activation. *J Exp Med*, **214**, 2671-2693.

Zhong, Z., Zhai, Y., Liang, S., Mori, Y., Han, R., Sutterwala, F.S. & Qiao, L. (2013) TRPM2 links oxidative stress to NLRP3 inflammasome activation. *Nat Commun*, **4**, 1611.

Zhou, R., Yazdi, A.S., Menu, P. & Tschopp, J. (2011) A role for mitochondria in NLRP3 inflammasome activation. *Nature*, **469**, 221-225.